uOttawa

L'Université canadienne
Canada's university

FACULTÉ DES ÉTUDES SUPÉRIEURES ET POSTOCTORALES

uOttawa

L'Université canadienne
Canada's university

FACULTY OF GRADUATE AND POSDOCTORAL STUDIES

Adam Donaldson
AUTEUR DE LA THÈSE / AUTHOR OF THESIS

Ph.D. (Chemical Engineering)
GRADE / DEGREE

Department of Chemical and Biological Engineering
FACULTÉ ÉCOLE, DÉPARTEMENT / FACULTY, SCHOOL, DEPARTMENT

Characterization of Air-Water Flow in Mini-Scale Serpentine Geometries

TITRE DE LA THÈSE / TITLE OF THESIS

Arturo Macchi
DIRECTEUR (DIRECTRICE) DE LA THÈSE / THESIS SUPERVISOR

Deepak Kirpalani
CO DIRECTEUR (CO DIRECTRICE) DE LA THÈSE / THESIS CO SUPERVISOR

B. Kruczek

P. Mehrani

M. Kawaji
University of Toronto

D. Taylor

Gary W. Slater
Le Doyen de la Faculte des etudes superieures et postdoctorales / Dean of the Faculty of Graduate and Postdoctoral Studies

Characterization of air-water flow in mini-scale serpentine geometries

By

Adam Donaldson

Thesis submitted to the Faculty of Graduate and Postdoctoral Studies

In Partial Fulfillment of the Requirements for the Degree of

Doctoral of Philosophy in Chemical Engineering

Department of Chemical and Biological Engineering

University of Ottawa

August 2010

Your file Votre référence
ISBN: 978-0-494-74247-1
Our file Notre référence
ISBN: 978-0-494-74247-1

Statement of Contribution of Collaborators

I, Adam Donaldson, hereby declare that I am the sole author of this thesis. The hydrodynamic studies, as well as the development of computer codes in ImageJ, Excel, MATLAB® and OpenFOAM for image analysis, mass transfer estimates and diffuse-interface two-phase computational fluid dynamic simulations were performed by me. The manufacturing technique used to construct each of the serpentine geometries was co-developed with David Smith, of the M4 machine shop at the National Research Council in Ottawa.

My supervisors, Dr. Arturo Macchi of the Department of Chemical and Biological Engineering, University of Ottawa, and Deepak Kirpalani of the Institute for Chemical Process and Environmental Technology, National Research Council, Ottawa, supervised my work during the Ph.D. program and provided editorial corrections.

Abstract

Advancements in chemical engineering processing focused on miniaturization of reactor flow systems has led to the adoption of mixing arrangements commonly employed in single phase applications into multi-phase systems. The planar serpentine channel is one such arrangement, found in compact heat exchangers, turbines, mini/micro-reactors and fuel cells. While extensive literature is available for serpentines with single phase flow, a limited understanding of the hydrodynamics and mass transfer characteristics of two phase flow exists. The curvature-induced flow pattern transitions, pressure drop, potential enhancement of mass transfer and suitability of common multi-phase CFD approaches were studied in this work for 1 mm circular channels with serpentine configurations consisting of consecutive return bends with radii of curvature of 3 and 6 mm.

The flow patterns generated by a 1 mm circular cross-flow T-junction were analyzed using high-speed imaging and compared to those observed within the serpentine geometries. The variation in flow behavior was illustrated in bubble breakup maps identifying the shifts in flow pattern transition boundaries and the onset of bubble breakup. The interactions between the interface and curvature-induced secondary flow were described by a combination of the Weber number and the characteristic length for single-phase flow in curved geometries, where critical values of $We_{LG}L_C = 3$, $We_{LG}L_C = 10$ and $We_{LG}L_C = 15$ are proposed for the onset of deformation, intermittent breakup, and continuous breakup, respectively.

Pressure drop measurements obtained for single and two-phase flow in straight and serpentine geometries were used to develop a semi-empirical separated flow model to predict two-phase friction factors. Five operating regions were identified, each having distinct

friction factor dependencies on We_{LG}, L_C and ε_G. The transitions between these regions depended on the phase holdup and/or the critical $We_{LG}L_C$ observed for the onset of deformation and continuous breakup.

The parametric dependency of gas-liquid inter-phase mass transfer in idealized Taylor flow was numerically investigated. The relative contributions of film and cap mass transfer at conditions suitable to industrial applications indicate that neither mechanism can be neglected when concentration polarization within the bubble film and mass transfer resistance between the slug film and bulk are accounted for. The introduction of curvature is predicted to increase overall mass transport through shear-induced deformation and secondary flow by up to 7% based on highly conservative assumptions.

Finally, the diffuse interface (DI) CFD model is introduced as a suitable interface tracking technique for modeling immiscible fluids in surface tension dominated flow. Key modifications are proposed to eliminate fundamental issues of the traditional DI approach, relaxing numerical constraints responsible for limiting practical applications to highly structured 2D and axisymmetric geometries. The new methodology proposed in this thesis was implemented in OpenFOAM®, and validated for benchmark simulations including scalar transport, free surface flow and droplet deformation in shear.

Sommaire

Les progrès en génie chimique axés sur la miniaturisation des écoulements ont conduit à l'utilisation de systèmes de mélange conçus pour les applications monophasées lors d'opérations polyphasés. Une conduite planaire en forme de serpentin est un mélangeur de ce genre, trouvée dans les échangeurs de chaleur compacts, turbines, mini/micro-réacteurs et piles à combustible. Bien que vaste littérature soient disponibles pour les conduites en serpentin ayant de grandes longueurs entre l'alternance des coudes de 180°, il manque d'informations sur l'hydrodynamique et les phénomènes d'échanges lorsque cette distance est réduite. Les régimes d'écoulement, la chute de pression, le transfert de matière et la pertinence des approches communes en CFD ont donc été étudiés pour un système diphasé air-eau s'écoulant dans des conduites circulaires de 1 mm de diamètre en serpentin ayant des coudes avec des rayons de courbure de 3 et 6 mm.

En utilisant l'imagerie à haute vitesse, les morphologies des écoulements gaz-liquide générés par une jonction en T circulaire ont été analysées et comparées à celles observées dans le serpentin. Les différents types d'écoulement ont été illustrés sur une carte identifiant les limites des régimes d'écoulement ainsi que les conditions de bris de bulles. Les interactions entre l'interface gaz-liquide et les écoulements secondaires induites par les courbes de la conduite ont été décrits par une combinaison du nombre de Weber et la longueur caractéristique d'un écoulement monophasé dans des géométries courbées, où les valeurs critique $We_{LG}L_C = 3$, $We_{LG}L_C = 10$ et $We_{LG}L_C = 15$ sont respectivement proposées pour le début de la déformation, la rupture intermittente, et la rupture continue des bulles.

Les chutes de pression obtenues lors d'écoulements mono- et diphasé dans des conduites en ligne droite et en serpentin ont été utilisées pour développer un model semi-empirique qui estime les coefficients de frottement. Cinq régions d'opérations ont été identifiées, chacune ayant des dépendances distinctes du coefficient de frottement sur We_{LG}, L_C et ε_G. Les transitions entre ces régions dépendent de la rétention des phases et/ou de $We_{LG}L_C$ critique observée pour le début de la déformation et la rupture continue des bulles.

La dépendance paramétrique du transfert de matière entre le gaz et le liquide pour un régime d'écoulement piston idéalisé a été étudiée numériquement. Les contributions relatives de transfert de matière par la paroi et le cap de la bulle lors de conditions typiquement obtenues en industrie indiquent que ni mécanisme peut être négligé lorsque la polarisation de la concentration dans le film à la paroi de la bulle et la résistance de transfert de matière entre le film du piston liquide et son milieu sont considérées. L'introduction de courbure dans la conduite augmentera le taux de transfert de matière due à la déformation de l'interface et aux écoulements secondaires d'un maximum de 7% basé sur des hypothèses très conservatrices.

Enfin, le modèle d'interface diffuse (DI) utilisé en CFD est présenté comme une méthode potentielle de suivre l'interface pour la modélisation de fluides non-miscibles lors d'écoulements dominés par la tension de surface. Des modifications clés sont proposées afin d'éliminer les problèmes fondamentaux de l'approche traditionnelle du DI, ce qui assouplie les contraintes numériques responsables des limites d'applications pratiques à des géométries 2D très structurées et axisymétriques. La méthode proposée a été mise en œuvre dans OpenFOAM ®, et validée pour des simulations de références, incluant le transport scalaire, l'écoulement à surface libre et la déformation d'une gouttelette en cisaillement.

Acknowledgements

I would like to express my gratitude to Dr. Arturo Macchi and Deepak Kirpalani for giving me the opportunity to work on this project, and for the valuable guidance they have provided throughout this program.

I would like to thank the Department of Chemical and Biological Engineering for the opportunities and experience I've obtained over the course of my Ph.D., and for the funding awarded by the University, NSERC CGS-M and PGS-D, and NRC GSSSP.

I would also like to thank the people at the National Research Council who have helped me during my time there. Special thanks go to Floyd Toll at M-12 and David Smith in the M-4 machine shop.

Finally, I would like to thank my family and friends for their support.

Table of Contents

Statement of Contribution of Collaborators ii
Abstract iii
Sommaire v
Acknowledgements vii
Table of Contents viii
List of Tables xi
List of Figures xii

Chapter 1. Introduction 1
1.1 Conventional, mini and micro-scale flow 2
1.2 Enhancing mixing within mini/micro channels 3
1.3 Fundamentals principles of the serpentine passive mixer 4
1.4 Research objectives 6
1.5 Operating conditions and geometric parameters 6
1.6 Research outline 7
Nomenclature 9
References 10

Chapter 2. Curvature induced flow pattern transitions in serpentine mini-channels 14
Abstract 15
2.1 Introduction 16
2.2 Experimental configuration 17
2.3 Inlet bubble size distribution and flow pattern map 20
2.3.1 Inlet bubble size distribution 21
2.3.2 Inlet flow pattern 28
2.4 Flow pattern transitions within the serpentine geometry 31
2.5 Critical conditions for bubble breakup 38
2.6 Conclusions 42
Acknowledgments 43
Nomenclature 44
References 46

Chapter 3. Single and two-phase pressure drop characteristics in serpentine mini-channels 51
Abstract 52
3.1 Introduction 53
3.2 Experimental configuration 54
3.3 Single phase pressure drop 57
3.3.1 Straight channel pressure drop 58
3.3.2 Serpentine channel pressure drop 59
3.4 Two-phase phase pressure drop 63
3.4.1 Homogeneous fluid and separated flow models 63
3.4.2 Inlet bubble and slug size distribution 65

3.4.3 Two-phase pressure drop in a straight channel 68
3.4.4 Two-phase pressure drop in serpentine channels 72
3.5 Conclusions 80
Acknowledgments 82
Nomenclature 82
References 85

Chapter 4. Numerical simulation of inter-phase mass transfer for idealized Taylor flow: A comparison of numerical frameworks and the effects of cap deformation in elevated shear 88
Abstract 89
4.1 Introduction 90
4.2 Homogeneous mixture model for idealized Taylor flow 92
4.3 Numerical simulation of inter-phase mass transfer 95
4.3.1 Perfectly mixed model 96
4.3.2 Slug film model 99
4.3.3 Circulating slug model 103
4.4 Results and discussion 110
4.4.1 Numerical approximations of $k_L a$ 110
4.4.2 Film vs. cap mass transfer 115
4.4.3 Effects of deformation on cap mass transfer 121
4.5 Conclusions 126
Acknowledgments 127
Nomenclature 128
References 132

Chapter 5. Diffuse interface tracking of immiscible fluids: Improving phase continuity through free energy density selection 135
Abstract 136
5.1 Introduction 138
5.2 Free energy theory for interface tracking 141
5.2.1 Equations of state (EOS) 142
5.2.2 Simplified energy density functions 144
5.2.3 Temperature-variant simplified energy density (TVSED) 146
5.2.4 Normalized excess free energy comparison 147
5.3 Equations of motion 148
5.3.1 Convective Cahn-Hilliard equation 148
5.3.2 Momentum Equation 151
5.4 Numerical procedure 151
5.4.1 Temporal discretization and solution procedure 151
5.4.2 Limiting diffusive flux to prevent non-physical variations in ϕ 153
5.5 Results and discussion 155
5.5.1 Spontaneous shrinkage of quiescent droplets 155
5.5.2 Metastable thermodynamics and phase separation 158
5.5.3 Interface tracking and phase continuity 161
5.5.4 Spurious currents and pressure rise 166

5.5.5 Free surface flow: collapse of a liquid column 170
5.5.6 Droplet in shear 177
5.6 Concluding remarks 184
Acknowledgements 186
Nomenclature 187
References 190
5.A Appendix material: Initial conditioning continuity loss 194
5.A.1 Proposed form of the 2D solution 194
5.A.2 Conditions for equilibrium 195
5.A.3 Graphical representation of instability region 197
5.A.4 Numerical implementation 198
5.A.5 Results: Validation of the 2D equilibrium profile 199
5.A.6 Continuity loss results and convergence testing 201
5.A.7 Conclusion 202

Chapter 6. Conclusions and future research 203
6.1 Conclusions 203
6.2 Future research 208

Appendices:
A.1 Manufacturing technique for the serpentine geometries

List of Tables

Table 3.1 Fitted parameters and boundary conditions for each of the four regimes identified for plug/unstable plug/slug flow. 77

Table 5.1 Maximum velocity and pressure rise obtained after 200 time steps ($\Delta t = 10^{-5}$ s) using Kim's formulation, Eq. (5.5.7), at T_R = 1 (a) and T_R = 0 (b), and using a linearized interfacial profile with n = 1.75, Eq. (5.5.8), at T_R = 0 (c). 168

Table 5.2 Mesh dependence of the deformation parameter and the angle between the major droplet axis and x-axis at t = 9 seconds for T_R = 0. 179

Table 5.A.1 Initial gain/loss in continuity resulting from the use of the 1D solution to initialize the equilibrium profile of a 2D droplet. 201

List of Figures

Figure 1.1 Serpentine channel schematic, where L_1 and L_2 are distances between sequential and alternating curves respectively, and r_C is the radius of curvature. 4

Figure 2.1 Schematic of geometry with r_c = 3 mm and 3.5 repeating serpentine unit cells. 18

Figure 2.2 Schematic of geometry with r_c = 6 mm and 4.5 repeating serpentine unit cells. 19

Figure 2.3 Experimental configuration 19

Figure 2.4 Image analysis results for U_L = 63 cm^3/min and U_G = 40 cm^3/min STP. Background correction was applied to raw images (top), and the results (middle) analyzed for individual particle identification (bottom). The population distributions for bubble length (left), bubble velocity (middle) and liquid slug length (right) were then obtained via particle tracking analysis. 21

Figure 2.5 Comparison of the measured bubble velocities and those predicted by Liu et al. (2005). Error bars represent one standard deviation, as determined from the velocity distribution for each operating condition. 24

Figure 2.6 Comparison of the bubble length predicted by Qain and Lawal (2006) to experimentally obtained values for each geometry, denoted by the radius of curvature (3 mm or 6 mm). 25

Figure 2.7 Comparison of the average bubble size predicted by the proposed correlations and experimentally obtained values. Error bars represent one standard deviation, obtained from number frequency distributions of the measured bubble length. 27

Figure 2.8 Comparison of current flow conditions and the proposed bubbly to plug transition to flow pattern transitions from previous literature. 29

Figure 2.9 Flow patterns observed for the given gas and liquid velocity, (U_D, U_C), at a location 27 to 45 channel diameters downstream of the T-junction. 30

Figure 2.10 Flow pattern observed 27 to 45 channel diameters downstream of the T-junction. Qualitatively determined transitions between flow patterns are shown as shaded regions. 31

Figure 2.11 Breakup map and flow pattern transitions within a serpentine geometry with r_c = 3 mm. Conditions where breakup was observed are indicated by open markers. 33

Figure 2.12 Breakup map and flow pattern transitions within a serpentine geometry with r_c = 6 mm. Conditions where breakup was observed are indicated by open markers. 34

Figure 2.13 Sequential images of air-water flow through the r_c = 3 mm geometry for different flow patterns, deformations, and breakup extents at (Q_C,Q_D) flow rates (cm^3/min). 35

Figure 2.14 Overlay of flow pattern transitions observed following the T-junction, and within the r_c = 6 mm and r_c = 3 mm geometries. Breakup was observed above the indicated boundary for breakup for each r_c. 36

Figure 2.15 Flow pattern within the serpentine vs. $We_{CD}L_C$ for r_c = 6 mm and r_c = 3 mm. Breakup was observed for all points above the horizontal dotted line. 39

Figure 2.16 Breakup map and flow pattern transitions for r_c = 3 mm, with the proposed breakup boundary shown ($We_{CD}L_C$ = 10). 40

Figure 2.17 Breakup map and flow pattern transitions for r_c = 6 mm, with the proposed breakup boundary shown ($We_{CD}L_C$ = 10). 41

Figure 3.1 Schematic of straight geometry. 55

Figure 3.2 Schematic of geometry with r_c = 3 mm and 3.5 repeating serpentine unit cells. 55

Figure 3.3 Schematic of geometry with r_c = 6 mm and 4.5 repeating serpentine unit cells. 56

Figure 3.4 Experimental configuration. 57

Figure 3.5 Comparison of experimentally obtained friction factors for single phase flow through the straight geometry and conventional correlations for circular pipes. 58

Figure 3.6 Comparison of experimentally obtained friction factors for single phase flow through the serpentine geometries and conventional correlations for circular pipes, log-log axis. 60

Figure 3.7 Comparison of experimentally obtained friction factors for single phase flow through the serpentine geometries and conventional correlations for circular pipes. 61

Figure 3.8 f_{serp}, f_S and $f_{helical}$ vs. Reynolds number for r_c = 3 mm and r_c = 6 mm. 62

Figure 3.9 Schematic of idealized Taylor flow, where shaded regions represent the liquid phase. 63

Figure 3.10 Comparison of the average bubble size predicted by Eq. (3.4.5) and experimentally obtained values. Error bars represent one standard deviation, obtained from number frequency distributions of the measured bubble length. 66

Figure 3.11 Average liquid slug length and variation exiting the cross-flow T-junction. Error bars represent one standard deviation, obtained from number frequency distributions of the slug length. 67

Figure 3.12 Comparison of measured slug length to that predicted using the bubble length and gas holdup. Error bars represent one standard deviation of the measured average slug length. 68

Figure 3.13 Comparison of predicted and measured pressure drop along a 179mm straight channel. 70

Figure 3.14 Dependence of b_1 on We_{LG} and gas holdup for a straight channel. 72

Figure 3.15 Predicted pressure drop obtained using Eq. (3.4.4) with a_1 = 0.17 for r_c = 3 mm. 74

Figure 3.16 Predicted pressure drop obtained using Eq. (3.4.4) with a_1 = 0.17 for r_c = 6 mm. 74

Figure 3.17 Four regimes of plug/slug flow in serpentine channels, identified by the variation in error associated to pressure drop predictions made using a single set of C_A through C_E to fit all of the experimental data. 76

Figure 3.18 Predicted pressure drop obtained for r_c = 3 mm using Eq. (3.4.12), a_1 = 0.17, and c_1 determined from Eqs. (3.4.22) and (3.4.23). 78

Figure 3.19 Predicted pressure drop obtained for r_c = 6 mm using Eq. (3.4.12), a_1 = 0.17, and c_1 determined from Eqs. (3.4.22) and (3.4.23). 79

Figure 4.1 Schematic of idealized Taylor flow, where shaded regions represent the liquid phase. For a moving frame of reference, the velocity at the capillary wall is set to $-U_b$, corresponding to movement from left to right. 91

Figure 4.2 Liquid flow region used in the derivation of the perfectly mixed model. 97

Figure 4.3 Liquid flow regions used in the derivation of the slug film model. 99

Figure 4.4 Liquid flow regions used in the derivation of the circulating slug model. 104

Figure 4.5 Circulating slug model indexing structure and boundary conditions applied within the bubble film. 105

Figure 4.6 Variation in k_La predicted by the circulating slug model with mesh refinement. 109

Figure 4.7 Comparison of Bercic & Pintar (1997) correlation to k_La values predicted by the four models discussed in this work. 111

Figure 4.8 Comparison of CFD results by van Baten & Krishna (2004) to k_La values predicted by the four models discussed in this work. Unless otherwise specified simulations were carried out at L_{UC}=0.04m, d=3mm, L_{film}=5.321mm, D=1x10-9m^2/s, U_b=0.45m/s, and $\delta_b = 45\mu m$. 114

Figure 4.9 Percentage of total mass transport attributed to the film at different bubble and slug film lengths for $D = 2x10^{-9}$ m^2/s, $Ca_{LG} = 0.004$, $d = 1mm$, $\sigma = 0.072$ N/m, and $\mu = 0.001$ kg/(m s). 118

Figure 4.10 Percentage of total mass transport attributed to the film at different bubble film lengths and capillary numbers for $D = 2x10^{-9}$ m^2/s, $(L_{UC} - L_{film})/d - 1 = 3$, $d = 1mm$, $\sigma = 0.072$ N/m, and $\mu = 0.001$ kg/(m s). 118

Figure 4.11 Percentage of total mass transport attributed to the film at different bubble film lengths and capillary numbers for D=2x10^{-9} m^2/s, L_{film}/d=8, d=1mm, $\sigma = 0.072$ N/m, and $\mu = 0.001$ kg/(m s). 119

Figure 4.12 Contours of percentage film contributions to total mass transport in 1mm (left) and 3mm (right) circular capillaries for D=2x10^{-9} m^2/s, $\sigma = 0.072$ N/m, and $\mu = 0.001$ kg/(m s). 121

Figure 4.13 Serpentine geometry illustrating the bend radius of curvature, r_c, and localized stationary frame of reference. 123

Figure 4.14 Predicted enhancement of $k_{L,cap}A_{cap}$ due to shear-induced deformation of air/water flow within a serpentine geometry. 124

Figure 4.15 Variation in path length per unit surface area due to shear-induced deformation of air/water flow within a serpentine geometry. 125

Figure 5.1 Normalized excess free energy (a) and thermodynamic regions (b) for the double-well, double-obstacle, vdW EOS ($a = 1$, $b = 1$), and TVSED energy functions. 147

Figure 5.2 Temperature dependency of the radial variation in total free energy for a 2-D droplet with initial radius, $r_o = 0.1$ m. $\psi = 0.04164$ m, $\sigma = 0.05$ n m^{-1}. 157

Figure 5.3 Phase separation of an initially random distribution of ϕ in the meta-stable region (middle) for $T_R = 0$ (left) and $T_R = 1$ (right). 159

Figure 5.4 Effect of T_R on the non-physical adsorption of an adjacent droplet arising from transport through the meta-stable region. Transient behaviour and ϕ profiles obtained for simulation parameters: $\varphi = 0.05$, $\psi = 6$ cells, $C_\Gamma = 0.001$, $\Delta t = 0.001$ s and $\sigma = 1$ N m^{-1}. 160

Figure 5.5 Continuity loss of a circular region during relaxation and diagonal convection at $T_R = 0$. Other simulation parameters: 128x128 mesh, $r_o = 16$ m, $\varphi = 0.05$, $\psi = 6$ m, $C_\Gamma = 0.001$, $C_U = 0.001$, $\sigma = 1$ N m^{-1}. 161

Figure 5.6 Continuity loss of a circular region during partial (inset) and full relaxation, and diagonal convection at $T_R = 1$. Other simulation parameters: 128x128 mesh, $r_o = 16$ m, $\varphi = 0.05$, $\psi = 6$ m, $C_\Gamma = 0.001$, $C_U = 0.001$, $\sigma = 1$ N m^{-1}. 163

Figure 5.7 Effect of T_R and conditioning on continuity loss during advection for $C_\Gamma = 0.001$. Other simulation parameters: 128x128 mesh, $r_o = 16$ m, $\varphi = 0.05$, $\psi = 6$ m, $C_U = 0.001$, $\sigma = 1$ N m^{-1}. 164

Figure 5.8 Effect of low ($C_\Gamma = 0.001$) and high ($C_\Gamma = 0.01$) mobility on continuity loss during diagonal convection of fully and partially conditioned systems. Other simulation parameters: 128x128 mesh, $r_o = 16$ m, $\varphi = 0.05$, $\psi = 6$ m, $C_U = 0.001$, $\sigma = 1$ N m^{-1}. 164

Figure 5.9 Velocity profiles obtained for $h = 1/64$ and $\psi = 0.1875\sqrt{32h}$ m after 200 time steps ($\Delta t = 10^{-5}$ s) using Kim's formulation (5.7) at $T_R = 0$ (a) and $T_R = 1$ (b); and using (5.8) with $n = 0.5$ (c), $n = 0.75$ (d), $n = 1.25$ (e), and $n = 1.75$ (f). Contours represents $\phi = \varphi$ (outside), 0.5 (center), and $1 - \varphi$ (inside). 169

Figure 5.10 Case description of a collapsing column of water ($\phi = 1$) in air ($\phi = 0$) with initial width, $L = 0.114$ m, and aspect ratio, $A_R = H / L = 2$. 171

Figure 5.11 Dimensionless leading edge position, X / L, of a collapsing water column with aspect ratio, $A_R = 2$, obtained using the TVSED function and a VOF method with a high air viscosity, 0.001 Pa s (HV), and a low air viscosity, 0.00001 Pa s (LV). 172

Figure 5.12 Dimensionless height, Y / L, of a collapsing water column at $X = 0$ m. 173

Figure 5.13 Dimensionless height, Y / L, of a collapsing water column at $X = 0.27$ m. 173

Figure 5.14 Dimensionless height, Y / L, of a collapsing water column at $X = 0.42$ m. 174

Figure 5.15 Temporal evolution of ϕ following the contact of a collapsing column with a wall at $X = 0.42$ m for VOF (left), $T_R = 0$ (middle) and $T_R = 1$ (right). 175

Figure 5.16 Predicted deformation of an air droplet suspended in corn syrup due to simple shear: $r_o = 0.001$ m, $\lambda_\eta = 7.3 \times 10^{-8}$, $Ca = 0.6429$, $\mathrm{Re} = 3.82 \times 10^{-6}$. 180

Figure 5.17 Contours of ϕ at $t = 9$ s for the simulation of an air bubble under shear, carried out using the TVSED function at $T_R = 0$ (right) and $T_R = 1$ (left). 181

Figure 5.18 The relaxation of an air bubble's shape after shear flow is ceased for VOF and TVSED simulations: $r_o = 0.001$ m, $\lambda_\eta = 7.3 \times 10^{-8}$, $Ca = 0.6429$, $\mathrm{Re} = 3.82 \times 10^{-6}$. Predicted values are based on the empirical fit to experimental data reported by Rust & Manga (2002). 182

Figure 5.19 Continuity loss during droplet deformation in shear and subsequent relaxation for VOF and TVSED based simulations of an air bubble suspended in corn syrup. 183

Figure 5.A.1 Linear fit applied in the central region of the 2D equilibrium profile of ϕ. 198

Figure 5.A.2 Comparison of the deviation from the 1D equilibrium profile obtained from CFD simulations and from the proposed analysis. 200

Chapter 1

Introduction

Reactions involving gas-liquid or gas-liquid-solid contacting are encountered in a broad range of industrial applications, where a number of reactor designs are adopted based on the reaction chemistry, design complexity and mass transfer characteristics. The most common types include slurry bubble columns / fluidized beds, stirred tank slurry reactors, and packed-bed reactors; each with advantages and limitations inherent to their design. Slurry reactors contain small catalyst particles with excellent mass transfer characteristics and solid-liquid contacting, but necessitate the use of downstream filtration for particle recovery and are prone to catalyst deactivation through attrition. Packed-bed reactors are able to eliminate the need for downstream catalyst recovery while mitigating particle attrition, at the expense of increased inter-particle diffusion resistance, higher pressure drop, and potential maldistribution of reactants. Phase contacting within a packed bed can be improved through the use of random or structured packing, of which monolith structures have received considerable attention over the last decade for industrial applications.

Comprised of many thin vertical channels, these structures are impregnated or coated with a solid catalyst layer over which process fluids flow and react. Pressure drop is reduced relative to conventional packed-bed arrangements, and heat and mass transfer is enhanced by the smaller diffusion path between the fluids and catalyst surface and a high surface-to-volume ratio. The resulting potential for process intensification has led to the recent development of mini and micro-scale reactors for mass-transfer limited and/or highly exothermic reactions. While single-phase flow in mini-scale reaction systems is well defined

in existing literature, multi-phase flow characterization and optimization is an ongoing area of research as additional applications are explored for mini and micro scale configurations.

1.1 Conventional, mini and micro-scale flow

The transition between conventional, mini and micro-scale flow is defined by a shift in dominant forces acting on the fluids as the channel diameter decreases. In conventional flow, gravity is the predominant force acting on a multi-phase system, where buoyancy has a significant effect on the flow pattern and hydrodynamics. In smaller geometries, the relative magnitude of surface forces increase until gravitational forces no longer have a significant impact on the hydrodynamics of the system. The ratio of these forces is characterized by the Bond number, $Bo = d_h^2 \bar{g} \Delta\rho / \sigma$, where d_h is the hydraulic diameter, $\Delta\rho$ is the density difference between fluids, σ is the surface tension, and $\bar{g}$ is acceleration due to gravity. The exact value of the Bond number for the transition between gravitationally dominated and surface force dominated flow is still a subject of debate, with most estimates being on the order of O(1) (Kandlikar & Grande 2002, Günther & Jensen 2006).

The applicability of existing empirical correlations describing hydrodynamic behavior in conventional geometries is limited at mini and micro-scales due to the shift in predominant forces affecting the formation of flow instabilities. The relative magnitude of surface forces to gravitational (Bond number) and inertial forces (Weber number) increases rapidly as the hydraulic diameter decreases, while viscous forces remain a function of the fluid properties and velocity (Capillary number). Three size classifications have been proposed for air/water to delineate between the different scales of flow systems (Kandlikar & Grande 2002): Conventional ($d_h > 3$ mm), Mini-Channels (200 μm $< d_h <$ 3 mm), and Micro-Channels (10 μm $< d_h <$ 200 μm).

1.2 Enhancing mixing within mini/micro channels

Single-phase flow through mini and micro-channels is primarily laminar, with viscous effects dominating over inertial forces. As a result, radial mixing becomes diffusion limited, where the smaller geometric scales make it difficult to implement active mixing arrangements (i.e. mechanical stirrers). Pressure drop considerations also limit the ability to improve mixing and mass transfer by increasing velocity and turbulence. As the need for better mixing has increased, a number of passive mixing arrangements have been developed, where changes in the geometry are used to produce secondary flows that enhance radial mixing (Steinke & Kandlikar 2004). Examples include wavy channels (Nishimura & Matsune 1996), serpentine channels (Popiel & Wojtkowiak 2000; Mees *et al.* 1996; Rosaguti *et al.* 2005), splitting and recombining geometries (Sudarsan & Ugaz 2006), and cross-flow mixers (Dodge *et al.* 2004).

Due to the dominance of surface forces, gas-liquid flow in mini/micro channels is typically characterized by a train of bubbles and plugs with internal recirculation patterns in the axial direction (Taylor 1961; Cox 1963, 1964; Thulasidas *et al.* 1997; Günther *et al.* 2004). While the recirculation is known to enhance inter-phase mass transport and axial mixing within each phase, radial mixing is still diffusion limited. Recent literature has explored the use of a number of passive mixing arrangements to improve radial mixing and mass transport in multi-phase flow (Vashisth & Nigam 2008; Fries & von Rohr 2009); however, the geometric effects on flow patterns, pressure drop and mass transfer have yet to be fully characterized.

1.3 Fundamentals principles of the serpentine passive mixer

Planar serpentine passive mixing arrangements are found in many industrial applications involving mini-channels; including compact heat exchangers, turbines, mini/micro reactors and fuel cells (Martin *et al.* 2005; Xiong & Chung 2007; Huh *et al.* 2007). For a typical configuration illustrated in Fig. 1.1, flow through the curved regions produces secondary (radial) flows, referred to as Dean's vortices, which enhance radial mixing and heat transfer in single phase applications. The intensity and number of vortices formed within a curved geometry can be characterized by two dimensionless parameters: the curvature ratio, $L_C = d/2r_c$; and the Dean's number, $D = (\rho Ud/\mu)L_C^{0.5}$ (Berger *et al.* 1983; Nandakumar & Masliyah 1986; Bara *et al.* 1992). The radius of curvature, r_C, and length between sequential curves, L_1, control the maximum strength of the vortices; while the length between alternating curves, L_2, affects the dissipation between curves. While numerous experimental and computational studies have explored the effect of the serpentine

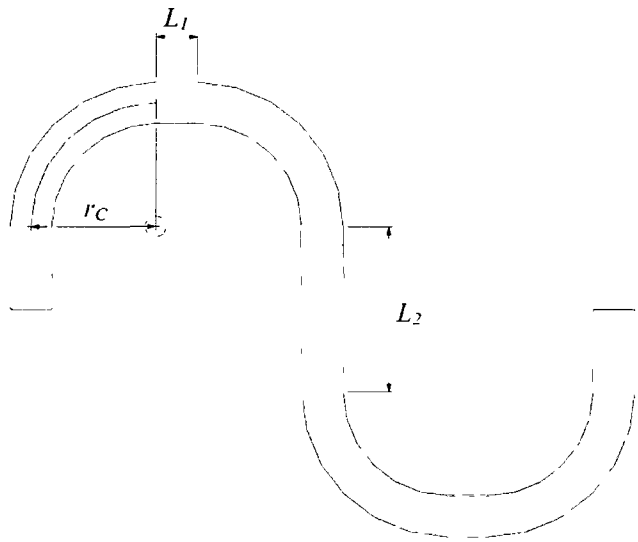

Figure 1.1 Serpentine channel schematic, where L_1 and L_2 are distances between sequential and alternating curves respectively, and r_C is the radius of curvature.

channel geometry on mixing, pressure drop and heat transfer for single phase flows (Mees *et al.* 1996; Popiel & Wojtkowiak 2000; Liu *et al.* 2000; Rosaguti *et al.* 2005); limited information is available in published literature regarding the fundamental fluid mechanics in multi-phase applications.

The fluid dynamics of two-phase flow in straight channels are well defined in literature (see review by Kreutzer *et al.* 2005c): with correlations existing for pressure drop (Kreutzer *et al.* 2005a,b), heat and mass transfer (Irandoust et al. 1992; Kreutzer 2003; van Baten & Krishna 2004), liquid film thickness (Aussilous and Quére 2000), and steady-state circulation patterns (Thulasidas *et al.* 1997; Aussilous & Quére 2000; Fujioka & Grotberg 2004). The extension of these correlations to curved geometries is non-trivial; complicated by the interaction between axial and Dean's vortices, flow pattern transitions, flow inversions induced by centrifugal forces, and bubble deformation and breakup. While recent literature is starting to explore the effects of curvature on mini/micro-scale two-phase flow (Kirpalani *et al.* 2008; Kulkarni & Kalyani 2009; Tung *et al.* 2009; Fries & von Rohr 2009), there is still a significant gap in our understanding of flow transitions, pressure drop, mixing characteristics, mass transfer rates and bubble breakup mechanisms within the serpentine geometry.

1.4 Research objectives

The dynamic behaviour of the flow pattern generated by a cross-flow T-junction as it travels through a planar serpentine arrangement is considered in this work. The serpentine is selected for its simplicity of design and frequent use in planar reactors as a method of increasing the reactor volume within a given geometric footprint. Air and water are chosen as process fluids due to their high surface tension, low miscibility, minimal safety requirements and predominance in related literature. The research program specific objectives are to:

1) Characterize the effects of the serpentine geometry and radius of curvature on pressure drop, mass transfer, flow pattern transitions, bubble size distributions and the onset of bubble breakup

2) Develop a multi-phase computational fluid dynamic (CFD) approach suitable for simulating complex topological changes in surface tension dominated flow

1.5 Operating conditions and geometric parameters

Each of the geometries used in this work were constructed from cast acrylic for optical clarity, with a channel hydraulic diameter of 1 mm corresponding to mini-scale flow for air-water mixtures. Two radii of curvature (3 mm and 6 mm) were selected, where the smallest radius of curvature was dicited by the ability to seal the contacting faces between adjacent bends during manufacturing, and the larger radius of curvature was governed by pressure drop limitations. The geometries were operated at flow rates commensurate with the capabilities of the centrifugal pump and/or a maxium pressure drop of 20 psig, above which the risk of damaging the acrylic piece became significant.

1.6 Research outline

Evaluation of the effects of curvature on the flow pattern transitions and bubble breakup is precluded by an analysis of the flow pattern generated by the cross-flow T-junction and the subsequent effects of pressure drop on the compressible gas phase.

High-speed video analysis was used to study the flow pattern and bubble size distribution generated by a circular cross-flow T-junction operating at $0.0058 < Ca_{LG} = \mu_L(U_L + U_G)/\sigma < 0.041$ and $545 < \mathrm{Re}_{LG} = \rho_L(U_L + U_G)d/\mu_L < 4675$. Models for the bubble length and bubbly to plug transition boundary were constructed from scaling laws describing the dominant forces affecting bubble generation in square micro-channels. With the developed models and flow pattern maps derived from experimental observation, the curvature induced variation in flow pattern transitions were considered for r_c = 3mm and r_c = 6mm. The critical conditions necessary for bubble breakup were defined, and guidelines presented for maintaining stable plug flow when return bends are introduced into the flow path. This work is entitled as **"Curvature induced flow pattern transitions in serpentine mini-channels"**, and is presented in Chapter 2.

The successful extension of straight-channel plug-flow pressure drop models to curved flow is limited by the unsteady nature of the flow pattern within the geometry. After having studied the flow pattern variations in Chapter 2, single and two-phase pressure drop measurements were carried out for straight and serpentine geometries operating at $400 < \mathrm{Re}_L = \rho_L U_L d/\mu_L < 3600$ (single-phase) and $500 < \mathrm{Re}_{LG} < 6500$ (two-phase). There is no data or correlation available in literature for two-phase pressure drop in a serpentine geometry operating at these conditions. A model was thus assembled to predict the experimentally observed two-phase pressure drop, and is described in Chapter 3 in the paper

entitled **"Single and two-phase pressure drop characteristics in serpentine mini-channels"**.

Flow pattern variations and elevated shear within the serpentine arrangement can enhance inter-phase mass transfer by increasing the mass transfer coefficient, k_L, and redistributing/increasing the cap and film interfacial areas, A_C and A_F. The relative importance of cap and film mass transport and the impact of common simplifications applied to mass transfer analysis of plug flow in straight channels is explored in Chapter 4; entitled **"Numerical simulation of inter-phase mass transfer for idealized Taylor flow: A comparison of numerical frameworks and the effects of cap deformation in elevated shear"**. With the important mechanisms of mass transport identified, penetration theory and semi-empirical descriptions of droplet deformation in shear were applied to explore the implications of bubble deformation and flow distribution on overall mass transfer within the serpentine.

Preliminary computational fluid dynamics (CFD) simulations of bubble deformation and breakup within the serpentine geometry led to the identification of key limitations within the Volume of Fluid interface tracking technique when applied to surface tension dominated flow. The diffuse interface approach was identified as suitable alternative, provided that a solution to the spontaneous drop shrinkage phenomena could be found which did not entail excessive mesh refinement. By defining a temperature-variant simplified energy density expression for use in the Cahn-Hilliard equation, the fundamental mechanism responsible for spontaneous drop shrinkage and interfacial smearing was identified and eliminated. This was achieved within a computational framework of comparable complexity to that of double-well energy function currently used in most diffuse interface tracking applications. The numerical approach was implemented in OpenFOAM®, and validated using a number of

benchmark simulations to illustrate the accuracy and performance of the proposed approach as an interface tracking technique for immiscible fluids. The paper associated with this work is entitled **"Diffuse interface tracking of immiscible fluids: Improving phase continuity through free energy density selection"**, and is presented in Chapter 5.

Finally, Chapter 6 summarizes conclusions and potential future research.

Nomenclature

r_C Radius of curvature of the serpentine bend (m)

d Channel diameter (m)

Re_L Reynolds number, based on liquid properties

Re_{LG} Reynolds number for the liquid slug, based on combined gas and liquid velocities

Ca_{LG} Capillary number, based on liquid properties and combined gas and liquid velocities

U_L Superficial liquid velocity (m s^{-1})

U_G Superficial gas velocity at experimental conditions (m s^{-1})

ρ_L Liquid density (kg m^{-3})

μ_L Liquid viscosity (kg m^{-1} s^{-1})

σ Surface tension (N m^{-1})

References

Aussilous, P., Quére, D., 2000. Quick deposition of a fluid on the wall of a tube. Phys. Of Fluids 12, 2367-2371.

Bara, B., Nandakumar, K., Masliyah, J.H., 1992. An experimental and numerical study of the Dean problem: flow development towards two-dimensional multiple solutions. J. Fluid Mech. 244, 339-376.

Berger, S.A., Talbot, L., Yao, L.S., 1983. Flow in curved pipes. Ann. Rev. Fluid Mech. 15, 461-512.

Cox, B.G., 1963. On driving a viscous fluid out of a tube. J. of Fluid Mech. 14, 81-96.

Cox, B.G., 1964. An experimental investigation of the streamlines in viscous fluid expelled from a tube. J. of Fluid Mech. 20, 193-200.

Dodge, A., Jullien, M.C., Lee, Y.K., Niu, X., Okkels, F., Tabeling, P., 2004. An example of a chaotic micromixer: the cross-channel micromixer, C.R. Physique, 5, 557-563.

Fries, D.M. and von Rohr, P.R., 2009. Liquid mixing in gas-liquid two-phase flow by meandering microchannels. Chem. Eng. Sci. 64, 1326-1335.

Fujioka, H., Grotberg, J.B., 2004. Steady propagation of a liquid plug in a two-dimensional channel. J. of Biomech. Eng. 126 (5), 567-577.

Günther, A., Khan, S.A., Thalmann, M., Trachsel, F., Jensen, K.F., 2004. Transport and reaction in microscale segmented gas liquid flow. Lab on a Chip 4, 278-286.

Günther, A., and Jensen, K.F., 2006. Multiphase microfluidics: from flow characteristics to chemical and materials synthesis. Lab Chip 6, 1487-1503.

Huh, C., Kim, J., Kim, M.H., 2007. Flow pattern transition instability during flow boiling in a single microchannel. Int. J. Of Heat and Mass Trans. 50, 1049-1060.

Irandoust, S., Ertlé, S., Andersson, B., 1992. Gas liquid mass transfer of Taylor flow through a capillary. Canadian J. of Chem. Eng. 70, 115.

Kandlikar, S.G., and Grande, W.J., 2002. Evolution of microchannel flow passages–thermohydraulic performance and fabrication technology, Proc. of the International Mechanical Engineering Conference and Exposition, Nov. 17–21, 2002, New Orleans, LA, Paper No. IMECE2002–32043.

Kirpalani, D.M., Patel, T., Mehrani, P., Macchi, A., 2008. Experimental analysis of the unit cell approach for two-phase flow dynamics in curved flow channels. Int. J. of Heat and Mass Trans. 51, 1095-1103.

Kreutzer, M.T., Heiszwolf, J.J., Kapteijn, F., Moulijin, J.A., 2003. Pressure drop of Taylor flow in capillaries: impact of slug length. In: Proceedings of the First Int. Conf. on Microchannels and Minichannels. A.S.M.E., Rochester NY, U.S.A., pp. 153-159.

Kreutzer, M.T., Bakker, J.J.W., Kapteijn, F., Moulijn, J.A., Verheijen, P. J.T., 2005a. Scaling–up multiphase monolith reactors: Linking residence time distribution and feed maldistribution using isobars. Ind. and Eng. Chem. Res. 44, 4898-4913.

Kreutzer, M.T., Kapteijn, F., Moulijn, J.A., Kleijn, C.R., 2005b. Inertial and interfacial effects on pressure drop of Taylor flow in capillaries. A.I.Ch.E. 51 (9), 2428-2440.

Kreutzer, M.T., Kapteijn, F., Moulijn, J.A., Heiszwolf, J.J., 2005c. Multiphase monolith reactors: Chemical reaction engineering of segmented flow in microchannels. Chem. Eng. Sci. 60, 5895-5916.

Kulkarni, A.A., and Kalyani, V.S., 2009. Two-phase flow in minichannels: hydrodynamics, pressure drop, and residence time distribution. Ind. Eng. Chem. Res. 48, 8193-8204.

Liu, R.H., Stremler, M.A., Sharp, K.V., Olsen, M.G., Santiago, J.G., Adrian, R.J., Aref, H., Beebe, D.J., 2000. Passive Mixing in a Three-Dimensional Serpentine Microchannel, J. of Microelectromechanical Sys., 9, 190-197.

Martin, J., Oshkai, P., Djilali, N., 2005. Flow structures in a U-shaped fuel cell flow channel: quantitative visualization using particle image velocimetry. J. Of Fuel Cell Sci. and Tech. 2, 70-80.

Mees, P.A.J., Nandakumar, K., Masliyah, J.H., 1996. Instability and transitions of flow in a curved square duct: the development of two pairs of Dean vortices, J. Fluid Mech., 314, 227-246.

Nandakumar, K., and Masliyah, J.H., 1986. Swirling flow and heat transfer in coiled and twisted pipes. In Advances in Transport Processe (ed. A.S. Mujumdar & R.A. Mashelkar), pp. 49-112. New Delhi: Wiley Eastern.

Nishimura, T., Matsune, S., 1996. Mass transfer enhancement in a sinusoidal wavy channel for pulsatile flow, Heat and Mass Transfer, 32, 65-72.

Popiel, C.O., and Wojtkowiak, J., 2000. Friction Factor in U-Type Undulated Pipe Flow, ASME J. of Fluid Eng., 122, 260-263

Rosaguti, N.R., Fletcher, D.F., Haynes, B.S., 2005. Laminar flow and heat transfer in a periodic serpentine channel, Chemical Eng. & Tech., 28, 353-361.

Steinke, M.E., Kandlikar, S.G., 2004. Single-phase heat transfer enhancement techniques in microchannel and minichannel flows, Microchannels and Minichanells, June 17-19, 2004, New York, NY, Paper No. ICMM2004-2328.

Sudarsan, A.P., Ugaz, V.M., 2006. Multivortex micromixing, PNAS, 103, 7228-7233.

Taylor, G.I., 1961. Deposition of viscous fluid on the wall of a tube. J. of Fluid Mech. 10, 161-165.

Thulasidas, T.C., Abraham, M.A., Cerro, R.L., 1997. Flow patterns in liquid slugs during bubble-train flow inside capillaries. Chem. Eng. Sci. 52, 2947-2962.

Tung, K-Y, Li, C-C, Yang, J-T, 2009. Mixing and hydrodynamic analysis of a droplet in a planar serpentine micromixer. Microfluid Nanofluid 7, 545-557.

van Baten, J.M., Krishna, R., 2004. CFD simulations of mass transfer from Taylor bubbles rising in circular capillaries. Chem. Eng. Sci. 59, 2535-2545.

Vashisth, S., Nigam, K.D.P., 2008. Experimental investigation of void fraction and flow patterns in coiled flow inverter. Chem. Eng. And Proc. 47, 1281-1291.

Xiong, R., Chung, J.N., 2007. Flow characteristics of water in straight and serpentine micro-channels with miter bends. Exp. Therm. And Fluid Sci. 31, 805-812.

Chapter 2

Curvature induced flow pattern transitions in serpentine mini-channels

A.A. Donaldson [1,2], D.M. Kirpalani [1,*], A. Macchi [2]

Submitted for consideration to the International Journal of Multiphase Flow
April 29, 2010.

1 Institute for Chemical Process and Environmental Technology
National Research Council Canada
M-12, 1200 Montreal Road
Ottawa, Ontario, K1A 0R6, Canada

2 Dept. of Chemical and Biological Engineering
University of Ottawa
161 Louis Pasteur Street
Ottawa, Ontario, K1N 6N5, Canada

* Corresponding author: Deepak Kirpalani, Tel: +1 (613) 991-6958,
Fax: +1 (613) 991-2384, e-mail: Deepak.kirpalani@nrc-cnrc.gc.ca

Abstract

Experimental investigation of the phase interactions in two-phase mini-channel serpentine systems is performed with a focus on determining the effect of radius of curvature of the serpentine on two-phase flow pattern transitions. The initial formation of two-phase flow patterns in T-junction contactors and the resulting effect on the flow through serpentine geometries are studied to predict the initiation of bubble breakup and/or coalescence in planar serpentine arrangements. Bubble breakup maps are developed for each of the serpentine geometries, identifying curvature-induced shifts in the transitions between flow patterns.

Single phase dimensionless analysis for curved geometries is extended to two-phase flow to identify the geometric dependence of critical bubble breakup. Further analysis performed shows that the characteristic length for curved geometries encountered in the Dean number for single-phase flow is suitable for capturing the effects of curvature on the initiation of bubble breakup. The dependence of Weber number on the characteristic length is reported and a critical $We_{CD}L_C = 10$ is identified for predicting bubble breakup inception in the serpentine system.

Keywords: T-junction, Circular mini-channel, Serpentine, Curvilinear, passive mixer, two-phase flow pattern, coalescence, breakup, bubble size distribution.

2.1 Introduction

The flow patterns generated by gas-liquid distributors for mini-scale contactors and reactor systems (diameter, $d \sim 1$mm) have been investigated extensively in the past for a variety of cross-sectional geometrical shapes and lengths (Suo and Griffith, 1964; Barnea *et al.*, 1983; Damianides and Westwater, 1988; Barajas and Panton, 1993; Fukano and Kariyasaki, 1993; Mishima *et al.*, 1995, 1996; Triplett *et al.*, 1999a; Coleman and Garimella, 1999; Shekarriz, 2000; Yang and Shieh, 2001; Zhao and Bi, 2001; Akbar *et al.* 2003). While conducted with model fluids, air and water, these studies are often extended to process fluids for engineering applications. Fundamental studies of this nature usually produce two-phase flow regime maps and semi-analytically determined regime transitions, providing insight into the hydraulic behavior and heat and mass transfer properties of two-phase mixtures flowing through a straight channel (Triplett *et al.*, 1999b; Kawahara *et al.*, 2002; Angeli and Gavriilidis, 2008, Niu *et al.*, 2009). Limited information is available in literature regarding the impact of complex downstream flow configurations on the flow patterns formed initially. With the continued development of new applications for process flow systems at this scale, the incorporation of downstream phase contactors that enhance heat and mass transfer is inevitable.

Planar serpentine mixing arrangements are found in many industrial applications involving mini-channels; including compact heat exchangers, turbines, mini/micro reactors and fuel cells (Martin *et al.*, 2005; Xiong and Chung, 2007; Huh *et al.*, 2007). Noted for their ability to enhance heat transfer and radial mixing in single phase flow through the formation Dean vortices, serpentine geometries are frequently used to increase the reaction time within a given geometric footprint by connecting long mini-channels with alternating

U-shaped return bends. While previous studies have characterized the variation in flow patterns resulting from a single return bend (Wang *et al.*, 2003, 2004, 2005; Kirpalani *et al.*, 2008), a detailed analysis of the two-phase flow patterns developed in multiple mini-channel serpentine unit cells in series has yet to be reported in published literature.

In this work, air-water flow was examined in a serpentine system. Bubbly, plug, unstable plug and slug flow patterns were generated by a cross-flow T-junction and introduced into planar serpentine arrangements to study the impact of radius of curvature on flow pattern transitions and the initiation of bubble interactions such as inception, growth, breakup and coalescence. The objectives of this study were to: (a) determine the effects of the serpentine geometry on the two-phase flow pattern generated by a cross-flow T-junction, with a focus on the shift in flow pattern transitions between bubbly, plug, unstable plug and slug flow; (b) identify the mechanisms leading to bubble breakup, grouping and coalescence before and within the serpentine geometry; and (c) extend single-phase dimensionless analysis for curved geometries to multi-phase flow for the purpose of identifying the geometric dependence of critical conditions necessary for bubble breakup to occur.

2.2 Experimental configuration

Two geometries were manufactured from cast acrylic to allow for visual observation of the flow patterns before, within, and after a series of serpentine unit cells. Semi-circular grooves were CNC-machined into two 9.5 mm thick acrylic plates to create mirror patterns that formed the serpentine geometry when bonded together using dichrolormethane (solvent). The flow path of the serpentine system consists of a cross-flow T-junction contactor for blending the two phases followed by a 47.5 mm straight channel where the gas-liquid flow pattern is further developed. The straight channel leads to a series of serpentine unit cells

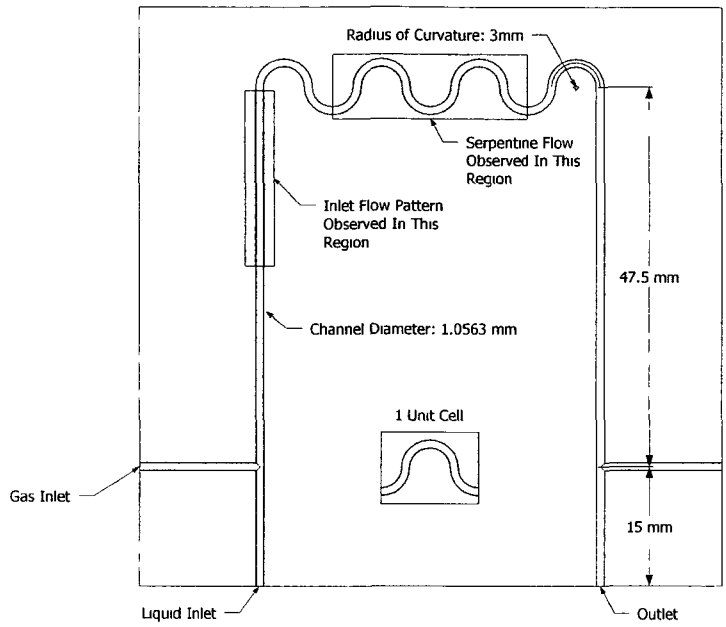

Figure 2.1 Schematic of geometry with r_c = 3 mm and 3.5 repeating serpentine unit cells.

with a radius of curvature, r_c, of 3 mm or 6 mm. Exit flow effects from the geometry were reduced by adding a 47.5 mm straight channel after the last semi-circular curve of the serpentine. At the exit, an additional T-junction was fabricated for monitoring the outlet pressure. CNC-machining of the acrylic plates introduced minimal groove depth variation. Schematics of the fabricated serpentine geometries and their dimensions are provided in Fig. 2.1 and Fig. 2.2.

The experimental setup, shown in Fig. 2.3, illustrates the operation of the serpentine mini-channel for air-water mixtures. The gas (dry air) was supplied from a cylinder through a pressure reducing valve (PRV) and a needle valve used to regulate flow. The gas flow rate, at standard conditions, was measured using an electronic mass flow meter (Omega FMA-1812). Pressure was measured at the gas inlet and channel outlet using a water manometer at low flow rates (0-11 kPa, 0-1.6 psig), and a pressure transducer at high flow rates (PSI-Tronix 68920-30, 0-30psig). Deionized water was introduced using a magnetically driven

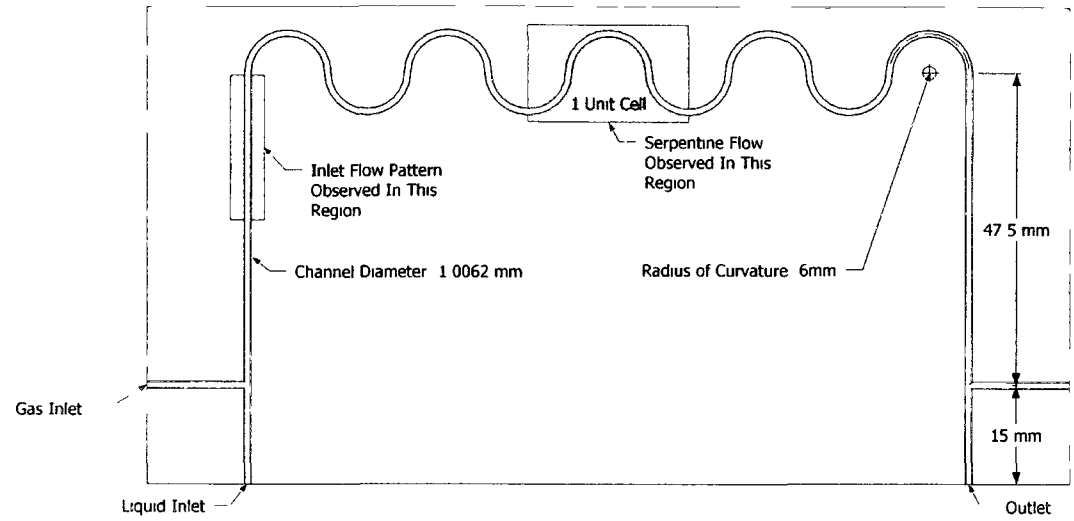

Figure 2.2 Schematic of geometry with r_c = 6 mm and 4 5 repeating serpentine unit cells

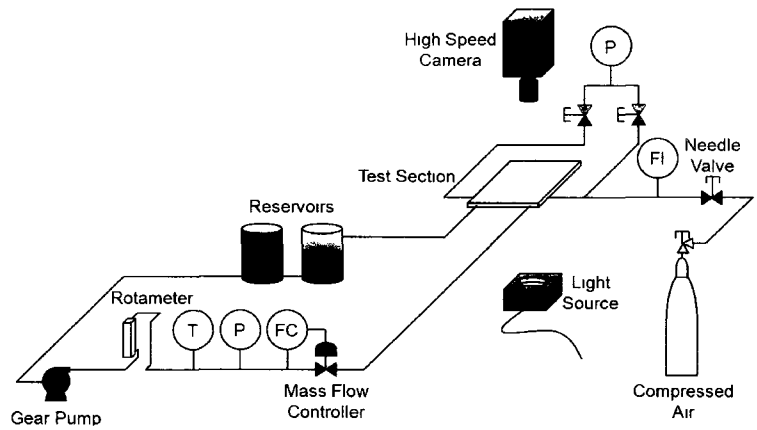

Figure 2.3 Experimental configuration

low flow rate gear pump (Micropump Series 200 P35, 1.17 mL/rev, 4.2 bar max ∇P) regulated using an electronic mass flow controller (Omega FLV-4619A). The liquid temperature was also monitored at the mass flow controller to determine the liquid viscosity at each operating condition.

The two-phase flow patterns were photographed at the inlet and within the serpentine region of each geometry using a high-speed CMOS camera (Nanosense MKIII) and custom-built pulsed-LED backlighting module synchronized with the frame rate of the camera for

visualization without raising the temperature of the process fluids. The system allowed for full-resolution image recording (1280x1024 pixels) at frame rates up to 2000 Hz, with higher frame rates achieved at reduced resolutions. A constant exposure of 20μs was used for all captured images. The equivalent pixel size was determined prior to each experiment with typical values on the order of 18 μm/pixel.

2.3 Inlet bubble size distribution and flow pattern map

An analysis of the effects of the serpentine passive mixing arrangement on two-phase air-water flow patterns was necessarily precluded by the characterization of flow patterns and bubble size distributions generated by the upstream T-junction contactor. Visual identification of these flow patterns can be highly subjective, leading to multiple classifications for similar flow regimes and the definition of flow pattern transitions as a range of operating conditions (as opposed to well defined sharp boundaries). Of significant interest in this study was the bubbly to plug flow transition, which can be difficult to determine visually due to the capillary-number dependence of the thickness of the liquid film surrounding a fully developed plug. The inlet bubble size distribution was thus used as a measurable parameter for defining a sharp boundary between these two flow patterns.

The bubble length and velocity and trailing slug length were measured in both geometries for liquid and gas flow rates ranging from 10 to 100 cm^3/min (0.2 to 2.1 m/s) and 10 to 180 cm^3/min (0.2 to 3.8 m/s) at standard conditions, respectively. Ten thousand images were collected at each operating condition, at a frame rate sufficient to capture a minimum of 10 instances of the same bubble as it traveled along the region 25 to 47 diameters downstream of the T-Junction. The location, projected area and length of each bubble within an image were measured using

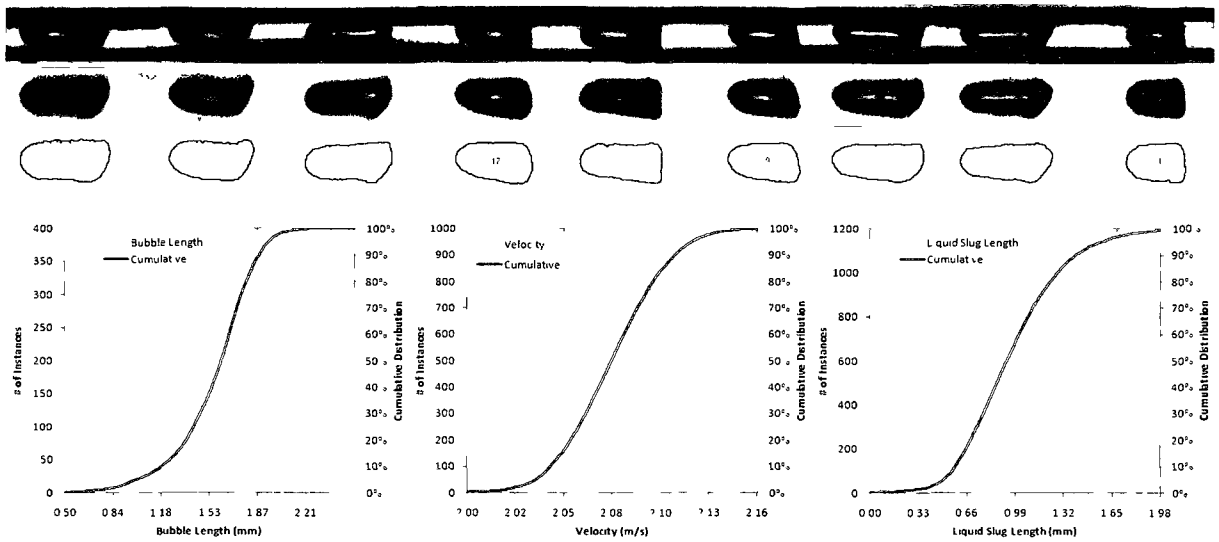

Figure 2.4 Image analysis results for U_L = 63 cm^3/min (1.32 m/s) and U_G = 40 cm^3/min STP (0.83 m/s). Background correction was applied to raw images (top), and the results (middle) analyzed for individual particle identification (bottom). The population distributions for bubble length (left), bubble velocity (middle) and liquid slug length (right) were then obtained via particle tracking analysis.

ImageJ®software, from which number-based distributions and arithmetic averages of the bubble length, velocity and trailing liquid slug length were determined. Typical results are presented in Fig. 2.4 for a liquid and gas flow rate of 63 cm^3/min and 40 cm^3/min STP, respectively. Note that the bubbles were approximated as ellipsoids and their length was defined as the major axis of the ellipsoid.

2.3.1 Inlet bubble size distribution

Scaling laws for droplet and bubble formation in T-Junctions are reported in existing literature for a range of operating conditions and channel dimensions (Laborie *et al.*, 1999; Thorsen *et al.*, 2001; Nisisako *et al.*, 2002; Tice *et al.*, 2003; Cristini & Tan, 2004; Garstecki *et al.*, 2006; Xu *et al.*, 2006 a, b, c; Qian and Lawal, 2006; Menech *et al.*, 2008; Xu *et al.*,

2008). In a recent review by Xu *et al.* (2008), three regimes of bubble and plug formation were identified, where the transition between the mechanism responsible for breakup was dependent on the capillary number for the continuous phase, $Ca_C = \mu_C U_C / \sigma$. At values of $Ca_C < 0.002$, interfacial forces are considered dominant over shear forces from cross-flow of the continuous phase, and plug formation is dependent on the pressure drop across the plug as it forms (Garstecki *et al.*, 2006). For $Ca_C > 0.01$, cross-flow shear becomes dominant, bubbly flow is observed, and the size of the bubbles is highly dependent on the geometry confinement (Menech *et al.*, 2008). Intermediate values of Ca_C between 0.002 and 0.01 correspond to a transient regime between bubbly and plug flow, where the dynamics of break-up are dependent on both shear and interfacial forces (Xu *et al.*, 2008).

The scaling laws proposed by Xu *et al.* (2008) for square micro-channels (200 μm) operating in each of the aforementioned regimes are expressed in a modified form in Eqs. (2.3.1) to (2.3.3):

$$\frac{L_b}{d} \approx \begin{cases} A/Ca_C & for \quad Ca_C > 0.01 \quad (2.3.1) \\ kCa_{D,\mu_C}^{\alpha} Ca_C^{\beta-\alpha} & for \ 0.002 < Ca_C < 0.01 \quad (2.3.2) \\ \varepsilon + \omega\left(Ca_{D,\mu_C}/Ca_C\right) & for \ 10^{-4} < Ca_C < 0.002 \quad (2.3.3) \end{cases}$$

In these expressions, the bubble length, L_b, channel width, d, and modified dispersed phase capillary number determined using the continuous phase viscosity, $Ca_{D,\mu_C} = \mu_C U_D / \sigma$, are critical in the determination of the bubble lengths. When shear forces are dominant ($Ca_C > 0.01$), the fitted parameter, A, corresponds to a correction factor for the continuous phase velocity as a bubble occupies part of the channel cross-section. For a rectangular channel, Xu *et al.* (2008) proposed a value of $A = dh/\left(dh - 0.785L_b^2\right)$, where h is the channel height. A similar constant can be derived for circular channels, resulting in a value of

$A = d^2/\left(d^2 - L_b^2\right)$. When interfacial forces are dominant ($Ca_C < 0.002$), ε and ω have ranged in magnitude from $\varepsilon = 1$ and $\omega = 1$ for Garstecki *et al.* (2006), $\varepsilon = 1.38$ and $\omega = 2.52$ for Xu and Luo (2006), and $\varepsilon = 1.9$ and $\omega = 1.46$ for Tice *et al.* (2003). In the transient regime, Xu *et al.* (2008) proposed values of $k = 0.75$, $\alpha = 1/3$ and $\beta = -1/5$ for a T-junction contactor.

Since the aforementioned correlations were developed for 200 μm channels with square cross sections, the findings cannot be directly applied to circular 1mm capillaries. Nonetheless, the force balances used to derive these scaling laws are still applicable to mini-scale geometries, and provide a basis for analyzing the empirical data for developing flow transition maps. Alternatively, a scaling law has been proposed for circular T-junctions by Qian and Lawal (2006) for gas and liquid superficial velocities from 0.01 to 0.25 m/s, gas holdups of $0.09 < \varepsilon_D \approx U_D/\left(U_C + U_D\right) < 0.91$, bubble-based Reynolds numbers of $15 < \mathrm{Re}_b = \rho_C U_b d/\mu_C < 1500$, and bubble-based capillary numbers of $0.000278 < Ca_b = \mu_C U_b/\sigma < 0.01$.

$$\frac{L_b}{d} = 1.637\varepsilon_D^{0.107}\left(1-\varepsilon_D\right)^{-1.05}\mathrm{Re}_b^{-0.075}\,Ca_b^{-0.0687} \tag{2.3.4}$$

Note that Eq. (2.3.4) requires an approximation for the bubble velocity, U_b, for which the expression proposed by Liu *et al.* (2005) is known to provide reasonable values for $2\times10^{-4} < Ca_{CD} = \mu_C\left(U_C + U_D\right)/\sigma < 0.39$.

$$\frac{U_b}{\left(U_C + U_D\right)} = \frac{1}{1 - 0.61Ca_{CD}^{0.33}} \tag{2.3.5}$$

Fig. 2.5 compares the bubble velocities predicted by Eq. (2.3.5) to the arithmetic mean of the experimentally obtained number frequency distribution of velocities for

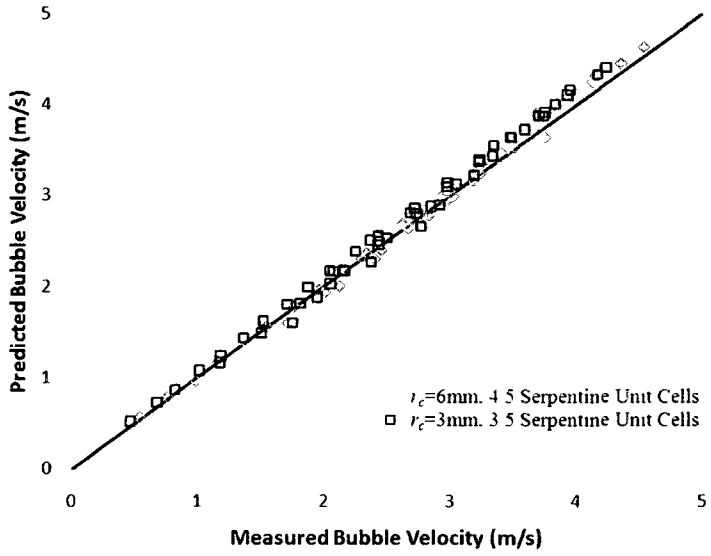

Figure 2.5 Comparison of the measured bubble velocities and those predicted by Liu *et al.* (2005). Error bars represent one standard deviation, as determined from the velocity distribution for each operating condition.

$0.0058 < Ca_{CD} < 0.041$, $545 < \mathrm{Re}_{CD} = \rho_C (U_C + U_D) d/\mu_C < 4675$. The reasonable agreement between the experimental and predicted values for U_b validates the image analysis algorithm used to determine the bubble sizes, velocities, and slug lengths.

The bubble lengths predicted by Eq. (2.3.4) are shown in Fig. 2.6 for the cross-flow T-junction operating at $0.0058 < Ca_{CD} < 0.041$, $545 < \mathrm{Re}_{CD} = \rho_C (U_C + U_D) d/\mu_C < 4675$, where the experimentally measured bubble velocity was used when determining Re_b and Ca_b. Note that a limited number of experimental conditions fell within the range of Re_b and Ca_b values for which Eq. (2.3.4) was developed, leading to overestimates of the bubble lengths at higher liquid and gas velocities where shear and inertial forces become dominant. It should also be noted that for $\varepsilon = 0.9$ and $\omega = 1.28$, Eqs. (2.3.3) and (2.3.4) yield

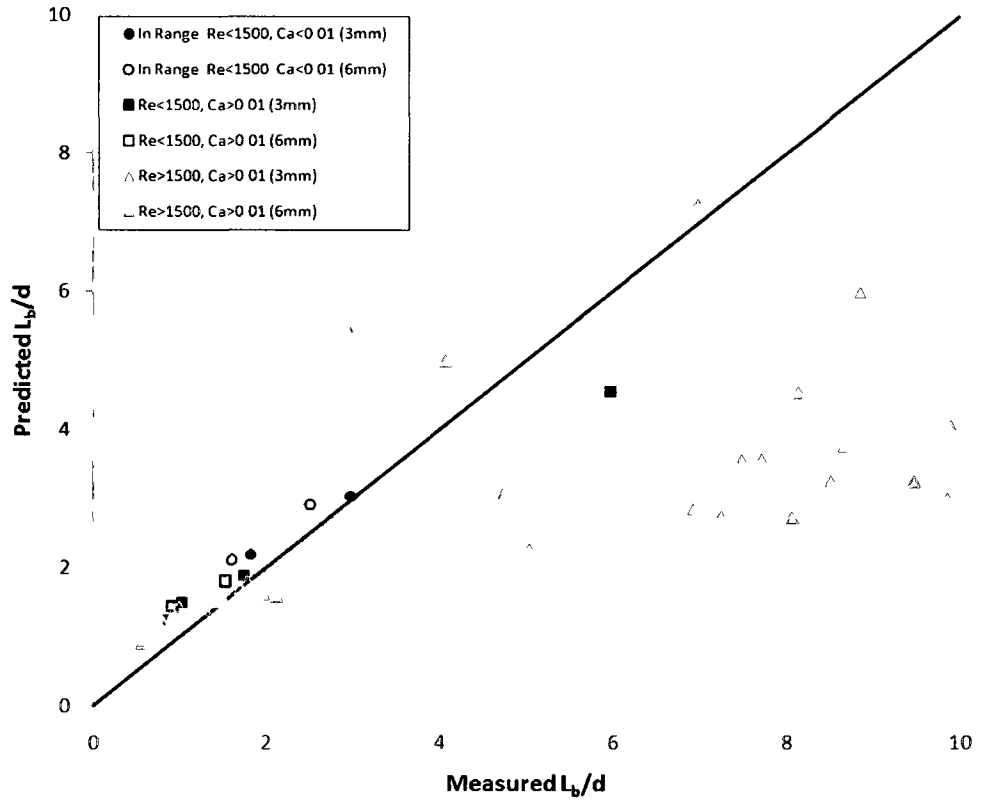

Figure 2.6 Comparison of the bubble length predicted by Qain and Lawal (2006) to experimentally obtained values for each geometry, denoted by the radius of curvature (3 mm or 6 mm). Triangle symbols represent experimental conditions outside of the valid range for Qain and Lawal.

comparable predictions for bubble length; thus confirming the similarity between the two scaling laws for bubble formation dominated by interfacial forces.

In an attempt to correlate the inlet bubble size distribution, the scaling laws proposed by Xu *et al.* (2008) for the transient and shear-based regimes were explored. For $Ca_C > 0.01$, the use of $A = d^2/\left(d^2 - L_b^2\right)$ resulted in the following expression for bubble length:

$$\frac{L_b}{d} = \frac{-Ca_C + \sqrt{Ca_C^2 + 4}}{2} \tag{2.3.6}$$

Note that Eq. (2.3.6) consistently predicts a bubble length approximately equivalent to the channel diameter. Since the experimental bubble lengths varied with Ca_{D,μ_C} and Ca_C for all operating conditions tested, an alternative expression for A was required. The scaling law for the transient regime was thus applied for all experimental data, where $\beta - \alpha$ was expected to approach -1 at higher capillary numbers.

Two distinct regimes were observed when the measured bubble lengths were fitted to Eq. (2.3.2): one applying to bubbly flow, and the other to plug/unstable plug flow. The boundary between these regimes was assumed to occur when $L_b/d = 1 - 2\delta/d$, where δ is the width of the liquid film that would surround a fully developed plug at equivalent conditions.

$$\frac{L_b}{d} = \max\begin{cases} 0.844 Ca_{D,\mu_C}^{0.285} Ca_C^{-0.384} & (Bubbly) \\ 9.721 Ca_{D,\mu_C}^{1.232} Ca_C^{-1} & (Plug/Unstable\ Plug) \end{cases} \tag{2.3.7}$$

The Ca_C^{-1} dependency noted by Xu *et al.* (2008) was observed for the plug/unstable plug flow regime, where A was a function of Ca_{D,μ_C}. The maximum operator was proposed to simplify the prediction of the bubble length when the flow pattern is not known. Based on experimental observations, the bubbly and plug/unstable plug expressions were consistently dominant in their respective flow regimes, only overlapping as $L_b/d \to 1 - 2\delta/d$. Under these transitional conditions, the larger of the predicted bubble lengths was consistently closer to those observed experimentally.

In developing these scaling laws, an approximation of δ was needed to identify the bubbly to plug flow transition. Based on the work of Aussilous and Quéré (2000) for $10^{-3} < Ca_b < 1.4$, the following expression was used:

$$\frac{2\delta}{d} = \frac{1.34Ca_b^{2/3}}{1+3.34Ca_b^{2/3}} \tag{2.3.8}$$

Assuming that the bubble velocity is well approximated by Eq. (2.3.5), this can be further expanded to provide the transition point for bubbly to plug flow, where the bubble length predicted by Eq. (2.3.7) must be less than the following critical value:

$$\left(\frac{L_b}{d}\right)_{Transition} = \frac{\left(1-0.61Ca_{CD}^{0.33}\right)^{2/3}+2Ca_{CD}^{2/3}}{\left(1-0.61Ca_{CD}^{0.33}\right)^{2/3}+3.33Ca_{CD}^{2/3}} \tag{2.3.9}$$

The bubble lengths predicted by Eq. (2.3.7) are compared to experimental values in Fig. 2.7, where reasonable agreement is observed for air-water flow in 1 mm circular

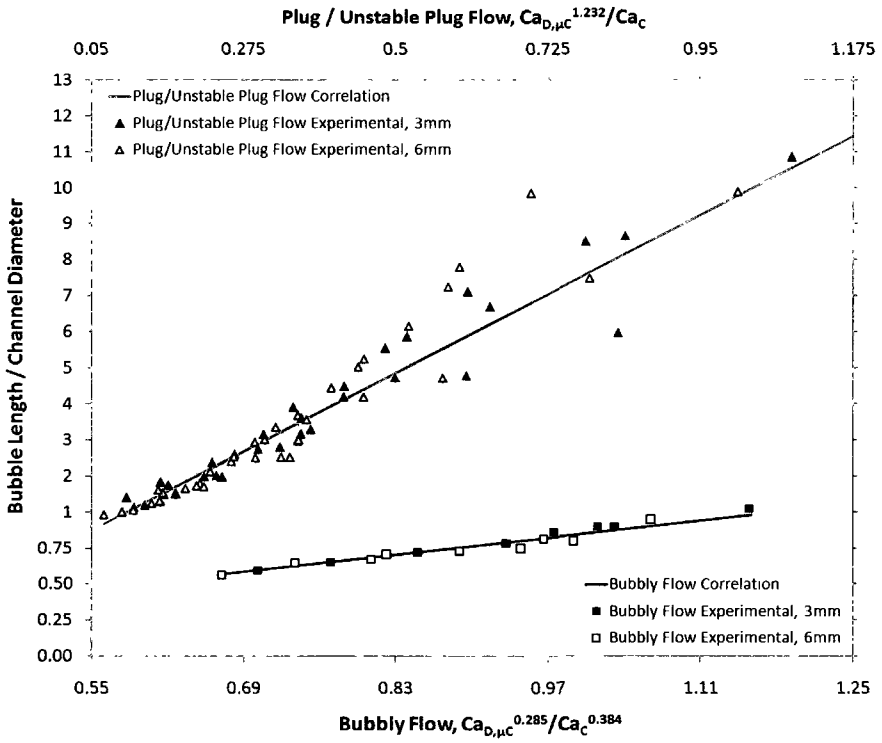

Figure 2.7 Comparison of the average bubble size predicted by the proposed correlations and experimentally obtained values. Error bars represent one standard deviation, obtained from number frequency distributions of the measured bubble length.

T-junctions operated at $545 < \mathrm{Re}_{CD} = \rho_C (U_C + U_D) d/\mu_C < 4675$, $0.0035 < Ca_C < 0.025$ and $0.0015 < Ca_{D,\mu_C} < 0.03$.

2.3.2 Inlet flow pattern

The flow patterns generated by different inlet distributor designs (T-junctions, Y-junctions, flow-focusing devices) have been extensively studied in previous literature, with multiple published works describing the criteria for transitions between bubbly, plug, slug and annular flow for different channel shapes, process fluids and channel orientations. However, a universal flow map has yet to be developed due to the strong dependency of the pattern obtained on a multitude of parameters including: viscosity, density and surface tension; channel shape, orientation and length scale; upstream and downstream configurations and pressure fluctuations; and even the interpretation of the flow patterns in transition regions. Nonetheless, a number of correlations have been developed to describe the transitions between flow patterns. A detailed review of all potential flow maps for a circular 1mm T-junction with air-water flow is beyond the scope of this work, but can be found in reviews and articles by Triplett *et al.* (1999a), Kawahara *et al.* (2002), Akbar *et al.* (2003), and Hassan *et al.* (2005).

For comparison purposes, the flow patterns observed at a distance 25 to 47 diameters downstream of the T-junction were compared in Fig. 2.8 to existing flow patterns transitions for air-water flow in circular channels, along with the proposed bubbly-plug transition relationship given by Eqs. (2.3.7) and (2.3.9). Example images of the four different flow patterns observed are provided in Fig. 2.9 for the indicated gas and liquid velocities. Note that the transition from plug to unstable plug flow was characterized by a grouping of the gas

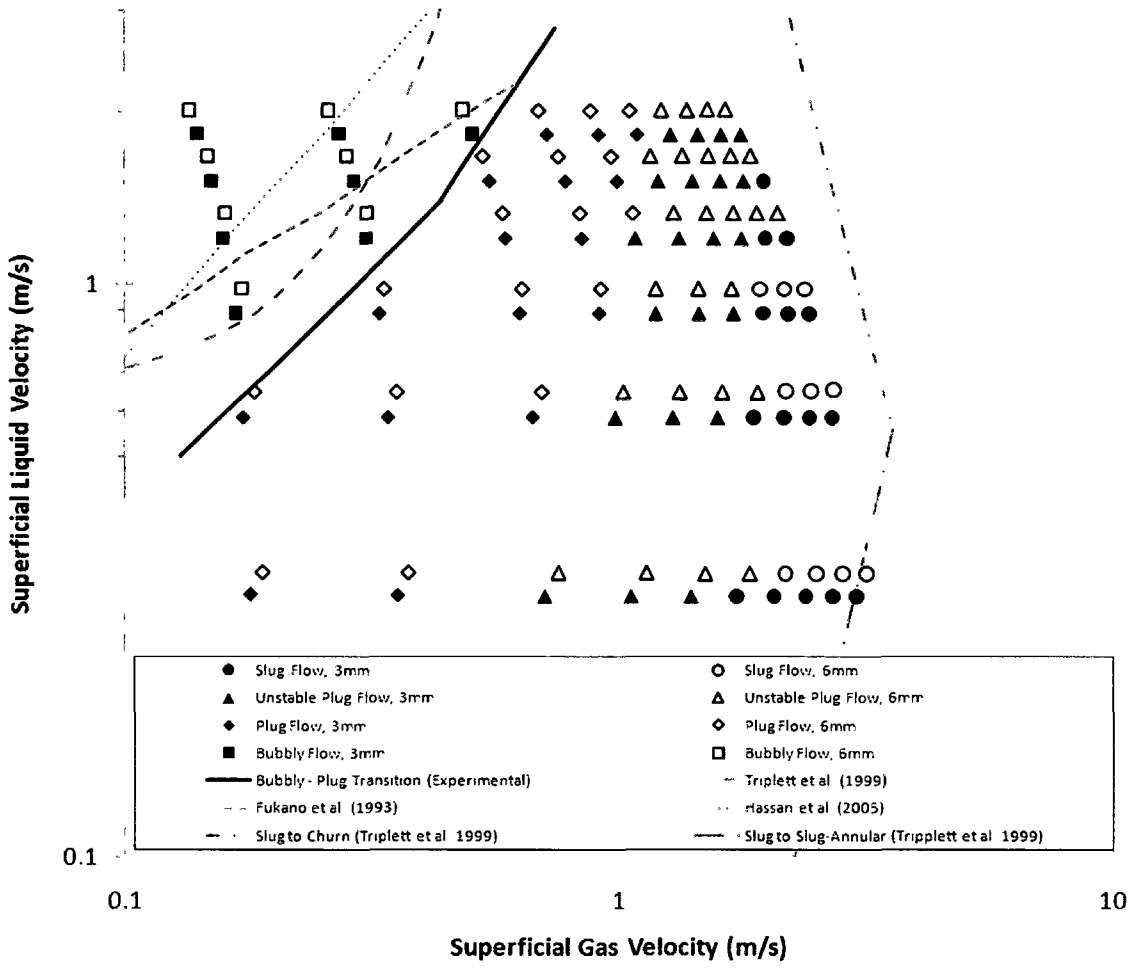

Figure 2.8 Comparison of current flow conditions and the proposed bubbly to plug transition to flow pattern transitions from previous literature.

plugs, while the transition to slug flow required the formation and entrainment of numerous small bubbles within the liquid slug.

The discrepancy between the proposed bubbly/plug transition line and previous literature was primarily attributed to differences in wetting properties and gas densities within the T-junction, and potential variances in the method by which the transition was identified. Visual determination of the transition between bubbly and plug flow is extremely subjective, especially when the film thickness surrounding a developing plug is difficult to

Figure 2.9 Flow patterns observed for the given gas and liquid velocity, (U_D, U_C), at a location 27 to 45 channel diameters downstream of the T-junction.

quantify. An approach using Eqs. (2.3.7) and (2.3.9) is considered more consistent, as it inherently accounts for the variation in film thickness and uses a measureable quantity (bubble length) to define the bubbly to plug transition. For the two geometries in this work, the flow pattern transitions occurred under similar conditions, enabling the subsequent analysis of the effects of radius of curvature on flow patterns and bubble size distributions.

In section 2.4, breakup maps are constructed using the Weber numbers for each phase to account for the presence of pseudo-turbulent flow in the serpentine arrangement. The proposed correlation for the bubbly to plug flow transition was dependent only on the capillary number, necessitating an approximation of the gas density at each point along the transition line to determine the value of the dispersed phase Weber number, $We_D = \rho_D U_D^2 d/\sigma$. This was achieved through the interpolation of the gas density at inlet conditions from the experimental data. As a result of this conversion, the bubbly to plug transition line for the two serpentine geometries no longer overlap, as the r_c = 6 mm and r_c = 3 mm geometries have different diameters and inlet pressures. The Weber-based equivalent of Fig. 2.8 is provided in Fig. 2.10, along with the boundary proposed by Akbar *et al.* (2003) for the shift from surface tension dominated flow (bubbly, plug, slug) to transitional flow (wavy annular, froth, churn), given in Eq. (2.3.10). Note that the

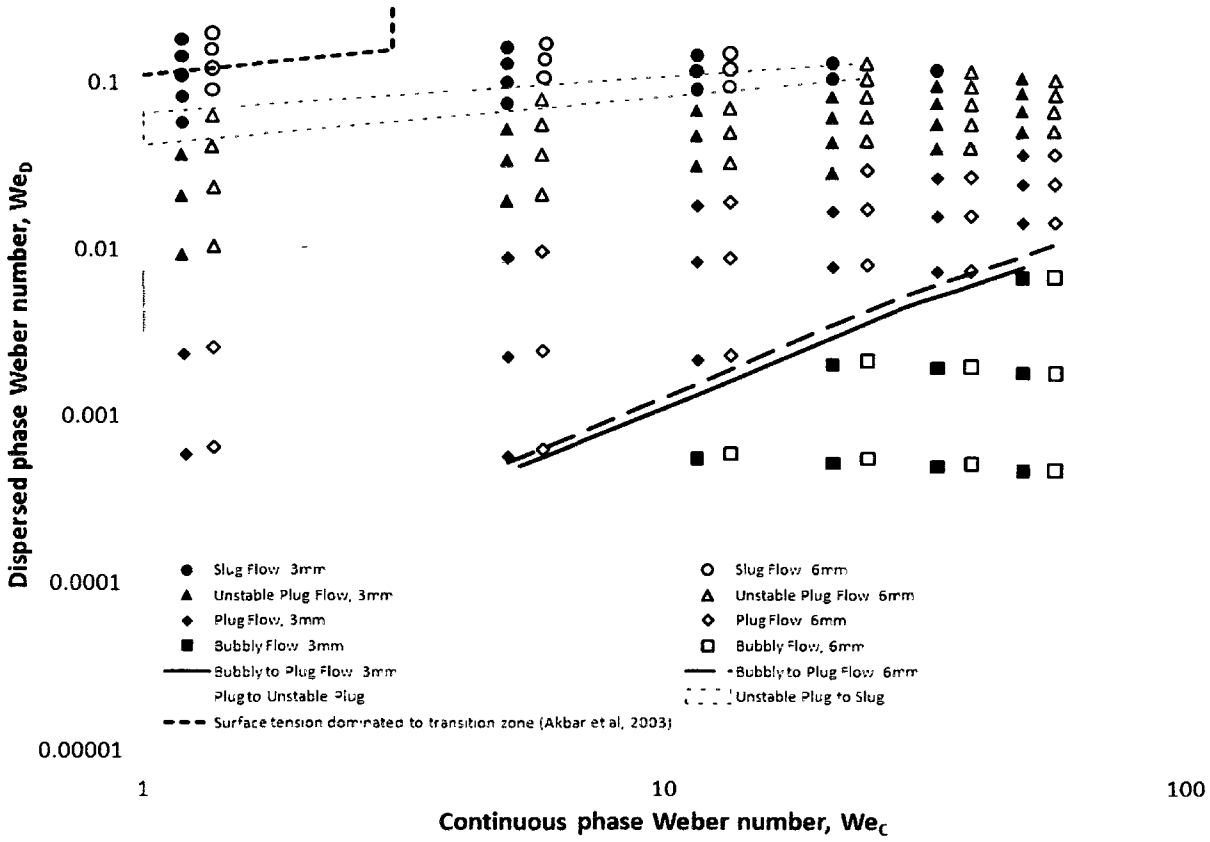

Figure 2.10 Flow pattern observed 27 to 45 channel diameters downstream of the T-junction. Qualitatively determined transitions between flow patterns are shown as shaded regions.

continuous phase (water) is plotted on the horizontal axis for consistency with previously published We-based flow pattern maps.

$$We_D \leq \begin{cases} 0.11 We_C^{0.315} & for \ We_C \leq 3 \\ 1 & for \ We_C > 3 \end{cases} \qquad (2.3.10)$$

2.4 Flow pattern transitions within the serpentine geometry

The serpentine geometry is commonly employed to enhance heat transfer and radial mixing in single-phase applications through the formation of Dean vortices, and to maximize the flow path length within a given geometric footprint. In multi-phase applications, the

serpentine geometry alters the centerline of the circulation patterns within the liquid slug (Fries and von Rohn, 2009), and is known to cause discrepancies between the entering and exiting flow patterns at larger diameters (Kirpalani *et al.*, 2008). The presence of curvature has two distinct effects on the flow pattern and bubble size distribution: coalescence due to draining of the liquid slug between adjacent bubbles; and breakup due to increased shear resulting from secondary flow formation within the liquid slug. As the liquid phase flows between two alternating curves in the serpentine arrangement, it must cross over to the opposite side of the channel, creating higher shear rates on preceding bubble and intense secondary flows. The effect of the radius of curvature on coalescence and breakup, and the critical conditions necessary to induce bubble breakup have yet to be characterized.

High frame rate videos of the dynamic behavior of gas bubbles travelling through serpentine channels were collected over a wide range of operating conditions and two radii of curvature (r_c = 6 mm and r_c = 3 mm). An assessment of flow patterns formed, nature of the bubble movement, extent of interfacial deformation, and presence or absence of breakup / coalescence within the serpentine unit cells was made from the video images. From this information, breakup maps were constructed for each radius of curvature and are presented in Figs. 2.11 and 2.12 for r_c = 3 mm, and r_c = 6 mm, respectively. The breakup boundaries formed, shown in Figs. 2.11 and 2.12, represent the conditions above which notable bubble breakup was observed. Sequential images of a bubble travelling through the 3mm serpentine geometry are provided in Figs. 2.13(a) through 2.13(l) for each of the regions identified.

The images in Figs. 2.13(a) through 2.13 (l) are grouped by flow pattern and the extent of deformation and breakup observed. Figs. 2.13(a) through 2.13(c) illustrate the two-phase flow at the onset of deformations, where small deformations or wave instabilities (seen as striations) are observed at the trailing edge of the bubble. Larger deformations and the

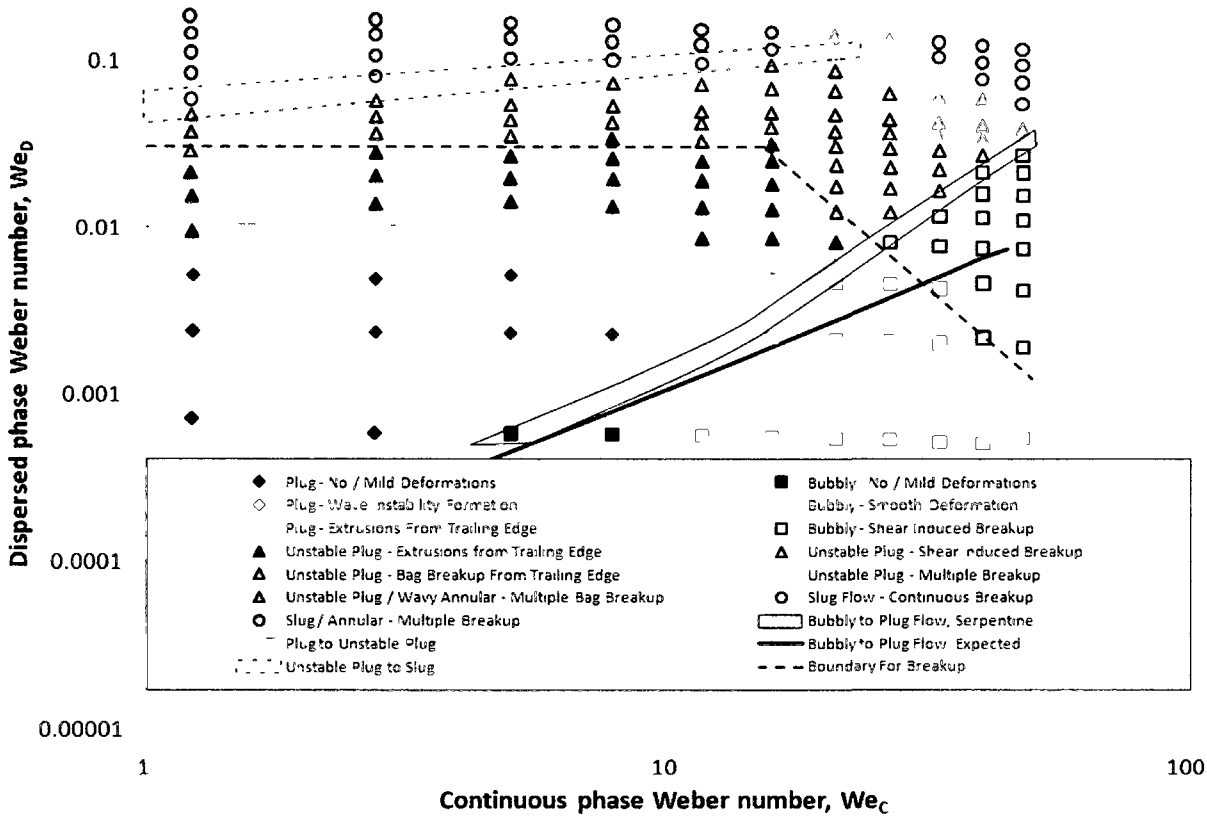

Figure 2.11 Breakup map and flow pattern transitions within a serpentine geometry with r_c = 3 mm. Conditions where breakup was observed are indicated by open markers.

wavy-annular flow regime are described in Figs. 2.13(d) through 2.13(f), followed by the various individual breakup mechanisms in Figs. 2.13(g) through 2.13(i). A distinction was made between "bag type bubble breakup" and "shear induced bubble breakup" for unstable plug flow, shown in Figs. 2.13(g) and 2.13(i)): "bag type bubble breakup" is characterized by the fracture of an extruded interface as it rapidly snaps back to the bubble bulk upon the removal of shear; whereas "shear induced bubble breakup" occurs when a smooth pinching motion is observed throughout the breakup process. Subsequent increases in gas and liquid flow rates led to multiple degrees of breakup, Figs. 2.13(j) through 2.13(l), where the

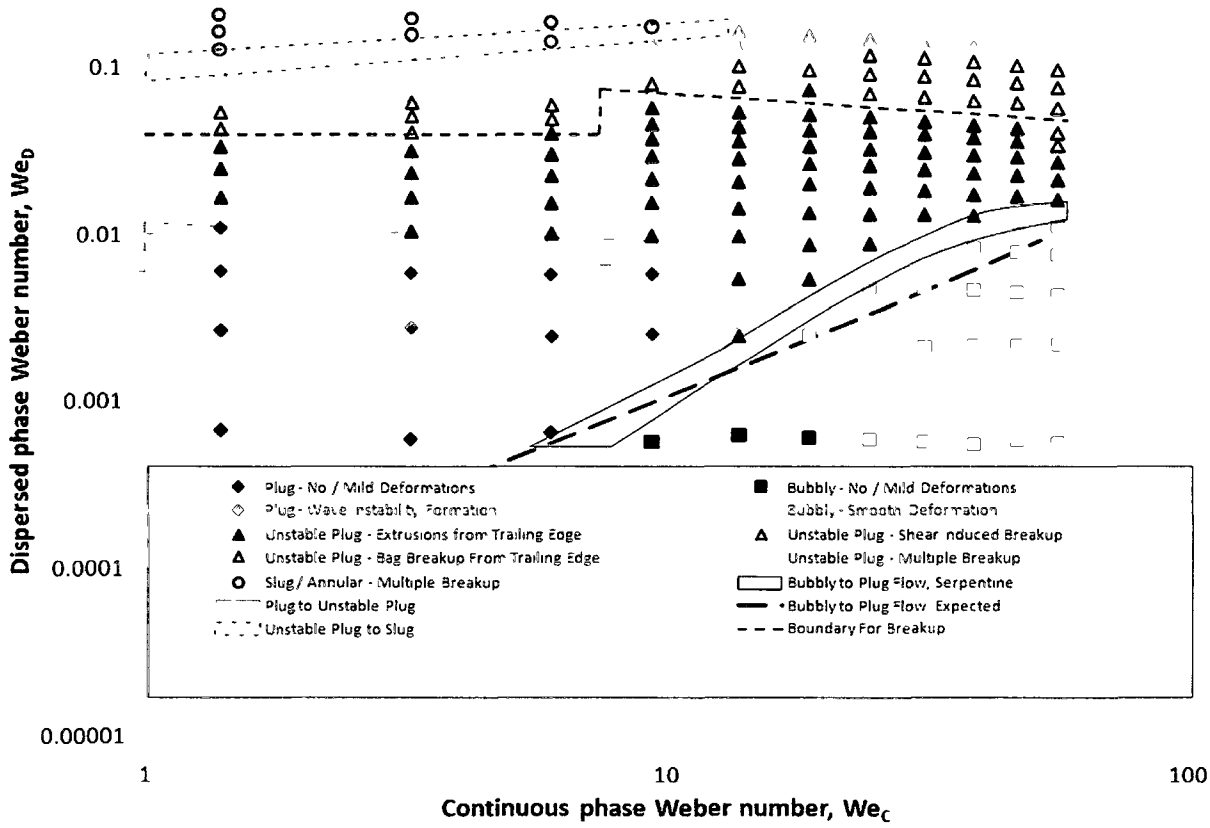

Figure 2.12 Breakup map and flow pattern transitions within a serpentine geometry with r_c = 6 mm. Conditions where breakup was observed are indicated by open markers.

transition from unstable plug to slug flow was distinguished by the presence of a large number of bubbles entrained in the liquid slug and multiple instances of breakup.

The Weber numbers in Figs. 2.11 and 2.12 for air, $We_D = \rho_D U_D^2 d/\sigma$, and water, $We_C = \rho_C U_C^2 d/\sigma$, were determined using the densities and superficial gas and liquid velocities at the point in the serpentine geometry where the images were collected (see Figs. 2.1 and 2.2). In order to provide a comparison to the inlet flow patterns (Fig. 2.10), the expected bubbly to plug transition line was calculated by estimating the ideal-gas expansion that would be expected for the measured pressure drop, $\rho_{D,s}/\rho_{D,i} = P_s/P_i$, and determining

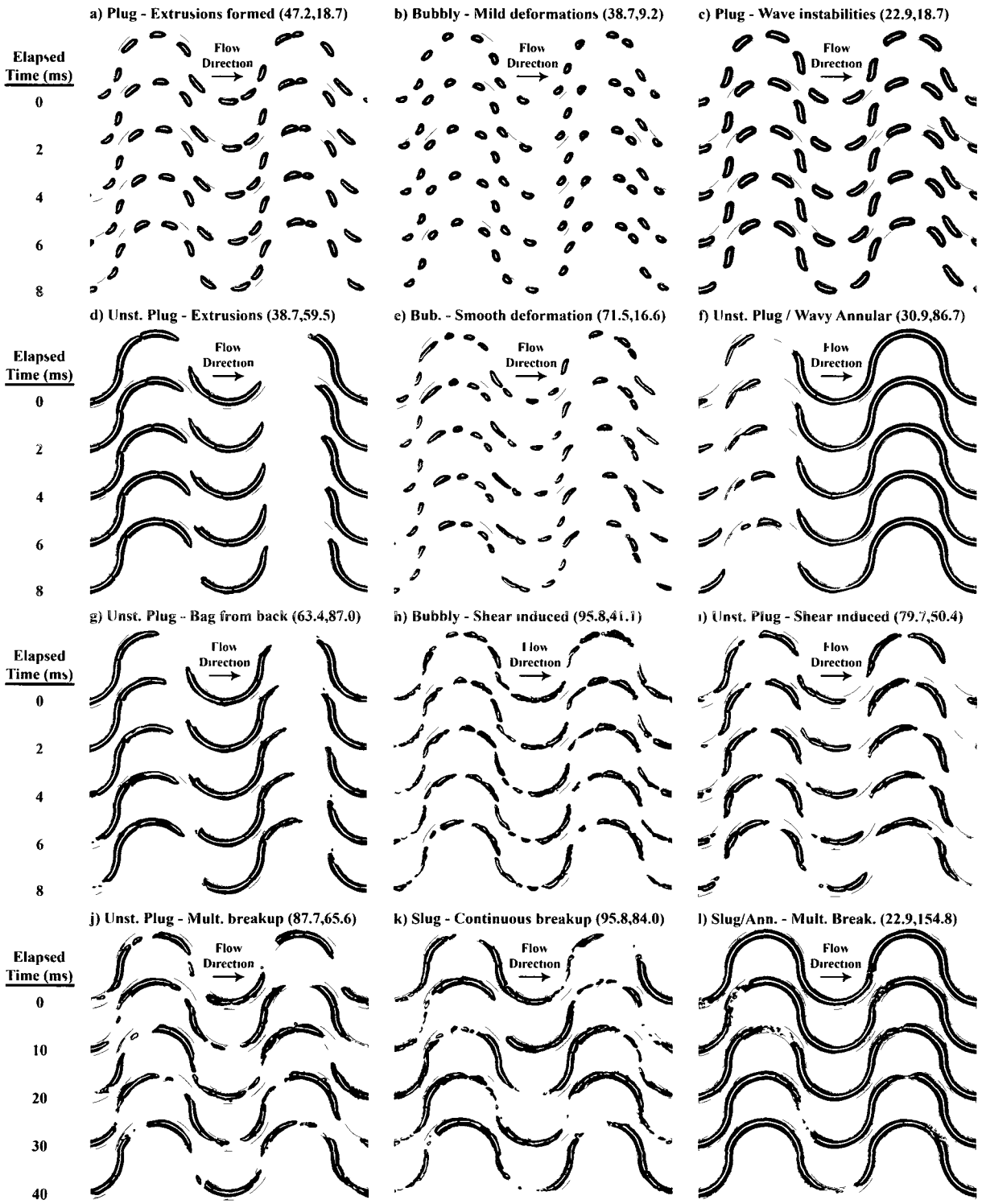

Figure 2.13 Sequential images of air-water flow through the r_c = 3 mm geometry for different flow patterns, deformations, and breakup extents at (Q_C,Q_D) flow rates (cm^3/min).

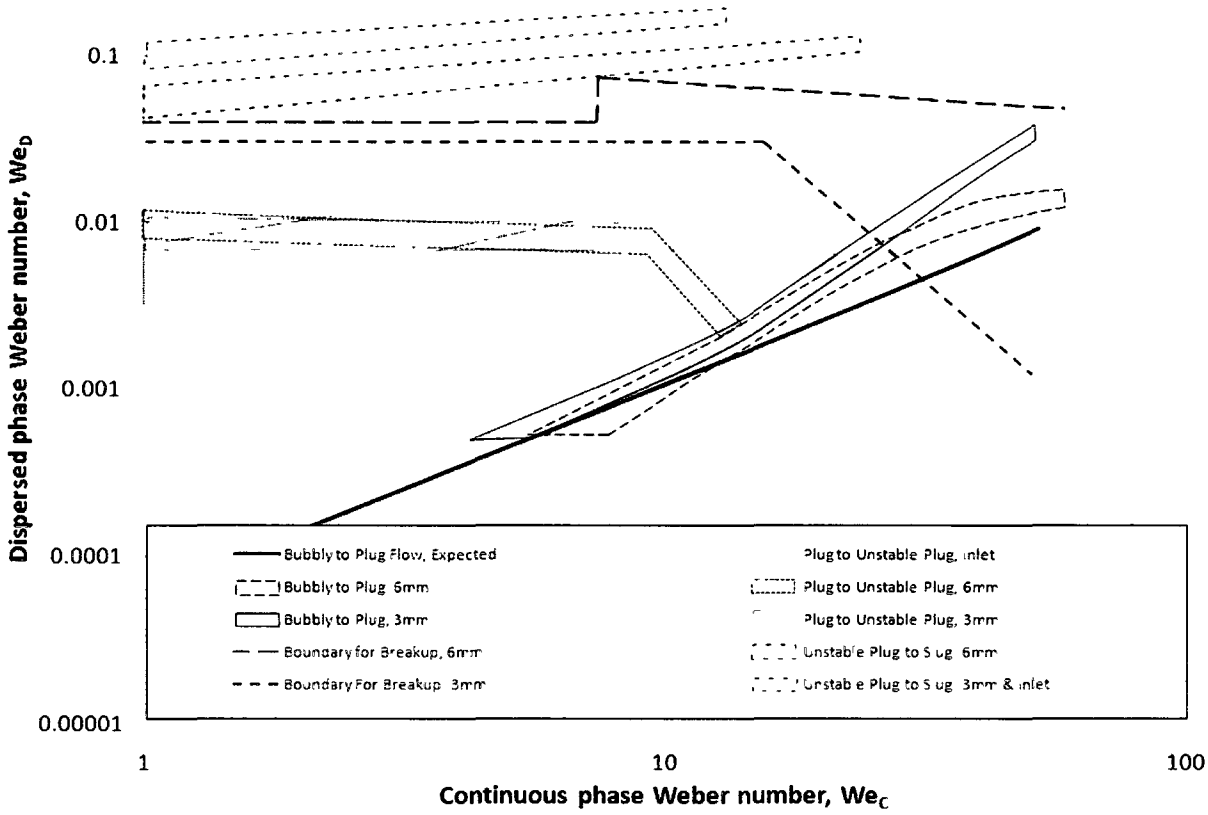

Figure 2.14 Overlay of flow pattern transitions observed following the T-junction, and within the r_c = 6 mm and r_c = 3 mm geometries. Breakup was observed above the indicated boundary for breakup for each r_c.

the maximum bubble size at the inlet which would result in $L_b/d = (1-2\delta/d)(\rho_{D,s}/\rho_{D,i})^{1/3}$. Note that $\rho_{D,s}$, $\rho_{D,i}$, P_s, and P_i are the air densities and absolute pressures within the serpentine (s) and inlet (i). Fig. 2.14 provides an overlay of each of these breakup maps and the expected bubble-plug transition point.

The inlet flow pattern and those observed in the r_c = 6 mm and r_c = 3 mm serpentine unit cells were similar for $We_C < 8$. At higher liquid flow rates, the bubbly flow regime was extended to increasing values of We_D, while a combination of bubble grouping, coalescence

and breakup shifted the transitions between plug and unstable plug flow. In single phase flow, a smaller radius of curvature leads to the development of stronger Dean vortices and increased shear rates. As a result, it can be deduced that the earlier onset of breakup and the greater extension of the bubbly flow pattern observed for r_c = 3 mm may also be a result of similar vortices formed. As the two phase mixture travels through each serpentine unit cell, the gas phase decelerates and the liquid phase migrates to the outside of each curve due to centrifugal forces. At the point where the direction of curvature alternates, the liquid must flow across the center of the channel to reach the opposing wall, exerting shear on the bubbles and completely separating the bubble from the channel wall at higher liquid flow rates. This corresponded to an apparent increase in We_C and decrease in We_D within the serpentine geometry, resulting in an upward shift of the transition boundary between bubbly and plug flow. The elevated shear rates at these conditions could potentially be used to modify the bubble size distribution and significantly increase inter-phase mass transfer.

The discrepancies between the plug to unstable plug flow transitions observed at the inlet and within the two serpentine geometries has significant implications to reactor design and flow pattern management. Almost all bubble grouping and coalescence observed in these experiments occurred within the first 180° return bend of the serpentine geometry, suggesting that similar behaviour would be observed when U-bends are used to increase the length of a flow path. The deceleration of the gas phase as it travels through the curved geometry led to two initially separated bubbles coming into contact as the liquid between them was drained by centrifugal force. The higher intensity of centrifugal forces present at the lower radius of curvature would imply that the liquid slug between bubbles would drain away quicker, resulting in an earlier onset of bubble grouping and unstable plug flow. As

can be seen in Fig. 2.14, it is actually the larger radius of curvature which first transitions to unstable plug flow. The longer curvature length of the r_c = 6 mm geometry extended the time for the liquid slug between two bubbles to drain, eventually leading to an increased rate of bubble grouping and coalescence over that observed for the r_c = 3 mm geometry. Based on this observation, the engineering design of a serpentine must take into account the curvature for a mini-scale reactor/contactor system, especially when a change in the flow pattern is undesirable. A smaller radius of curvature appears to deter bubble grouping and coalescence, and should be considered when U-bend arrangements are used to increase the reactor volume within a given geometric footprint.

2.5 Critical conditions for bubble breakup

The extent of secondary flow formation in single phase flow through curved channels is frequently characterized by the Dean number, $D = (\rho U d/\mu)(d/2r_c)^{1/2}$, derived from an approximate solution to the Navier-Stokes equations for steady, axially uniform flow in a helical coil. While the Dean number is not directly applicable to multiphase flow, the scaling used in its derivation may be useful in quantifying the effects of secondary flows in the serpentine channel. In formulating the Dean number, the cross-flow velocities are scaled by the root of a characteristic length parameter for curved geometries, $L_C = d/2r_c$. A similar scaling approach was applied for the combined gas and liquid velocities to account for the formation of secondary flows within the liquid slugs traveling through the curved channel. The following dimensionless number for curved flow is proposed for characterizing the onset of bubble breakup at elevated liquid flow rates:

$$We_{CD} L_C = \frac{\rho_C (U_C + U_D)^2 d}{\sigma} (d/2r_c) \qquad (2.5.1)$$

The near horizontal boundaries for breakup observed in Fig. 2.11 for $We_C < 16$ (r_c = 3 mm) and Fig. 2.12 for $We_C < 8$ (r_c = 6 mm) led to the assumption that breakup under these conditions was part of the natural transition from unstable plug to slug flow, with minimal dependence on the presence of a curved flow path. Determination of the onset of breakup due to the serpentine configuration thus focused on the transition between deformation and breakup at higher values of We_C, where a marked difference was observed for the location of the breakup boundary for r_c = 6 mm and r_c = 3 mm. The flow regime and

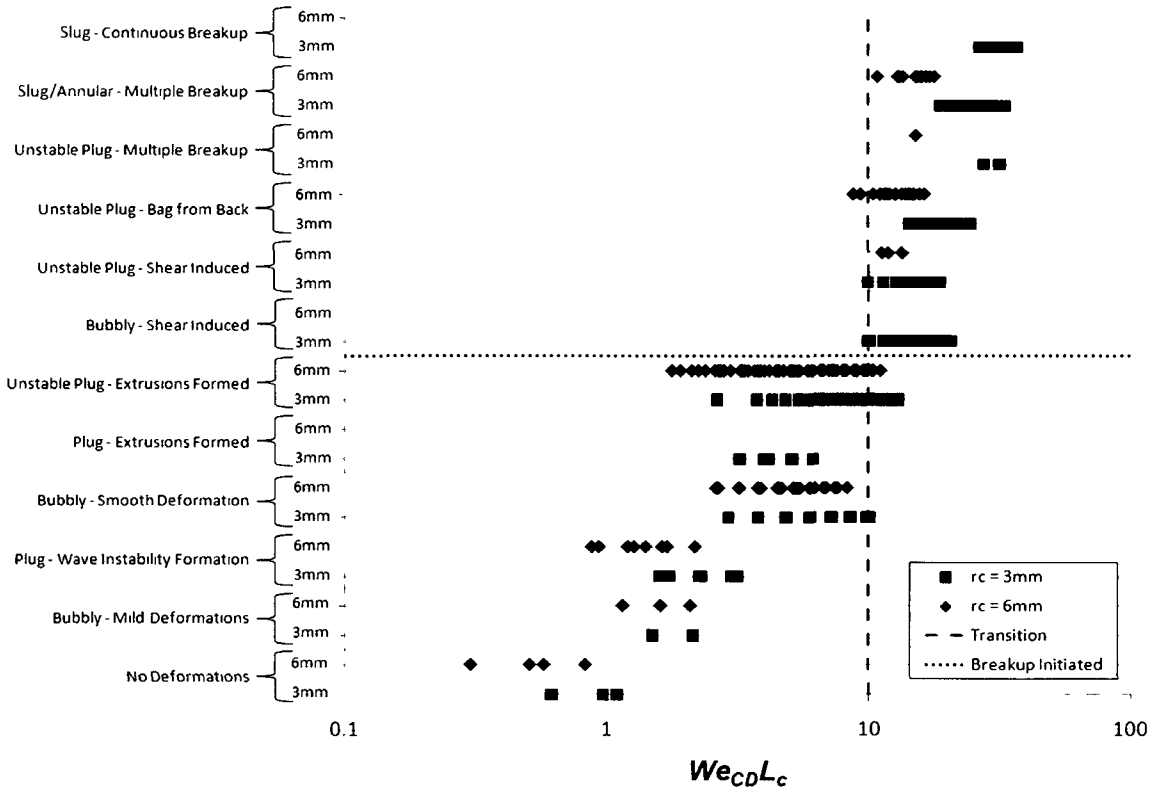

Figure 2.15 Flow pattern within the serpentine vs. $We_{CD}L_C$ for r_c = 6 mm and r_c = 3 mm. Breakup was observed for all points above the horizontal dotted line.

deformation/breakup extent at each operating condition was plotted against $We_{CD}L_C$ for both geometries, and is given in Fig. 2.15. With the exception of a few data points, the transition between deformation and breakup occurs at a critical value of $We_{CD}L_C \approx 10$.

The breakup boundary predicted by $We_{CD}L_C = 10$ was reconstructed for each of the two radii of curvatures, and presented in Figs. 2.16 and 2.17. Based on the agreement of the resulting breakup boundary with experimentally observed flow patterns, $We_{CD}L_C$ was considered an effective parameter for characterizing the intensity of secondary flows induced

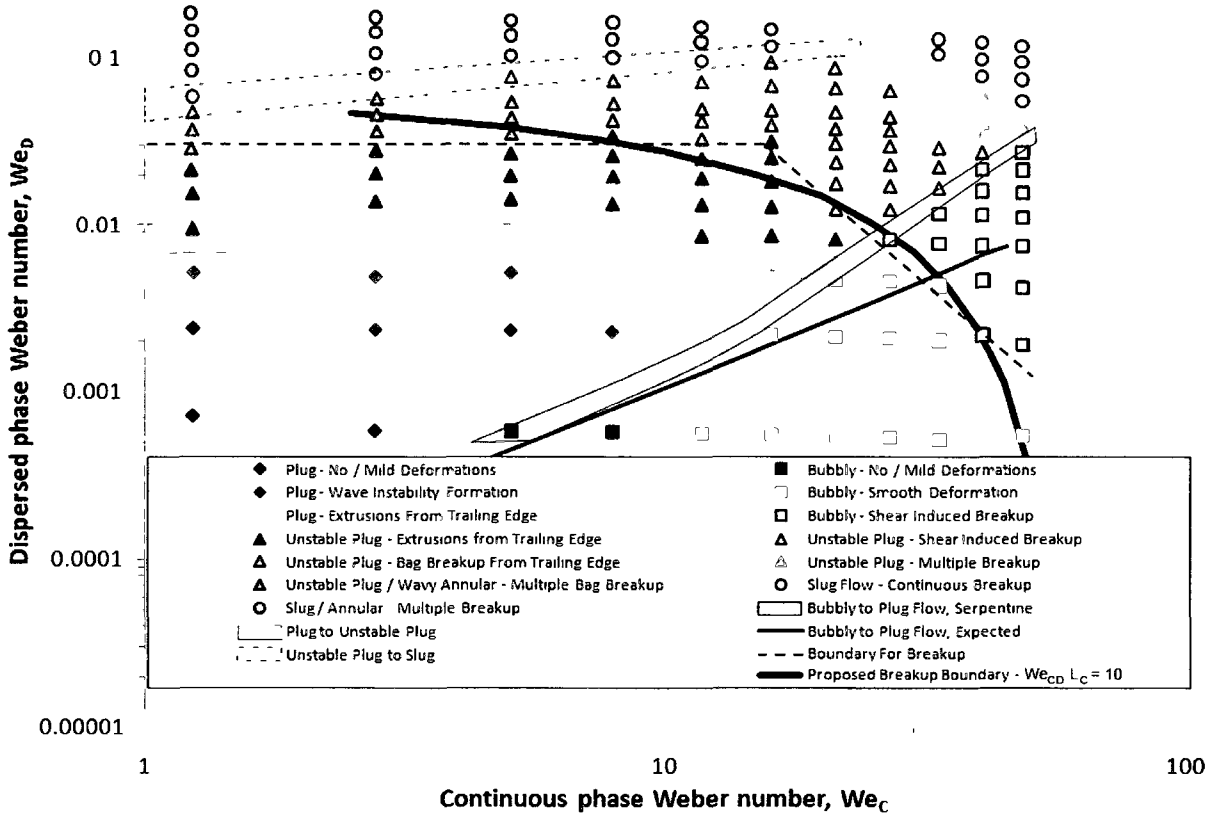

Figure 2.16 Breakup map and flow pattern transitions for r_c = 3 mm, with the proposed breakup boundary shown ($We_{CD}L_C$ = 10).

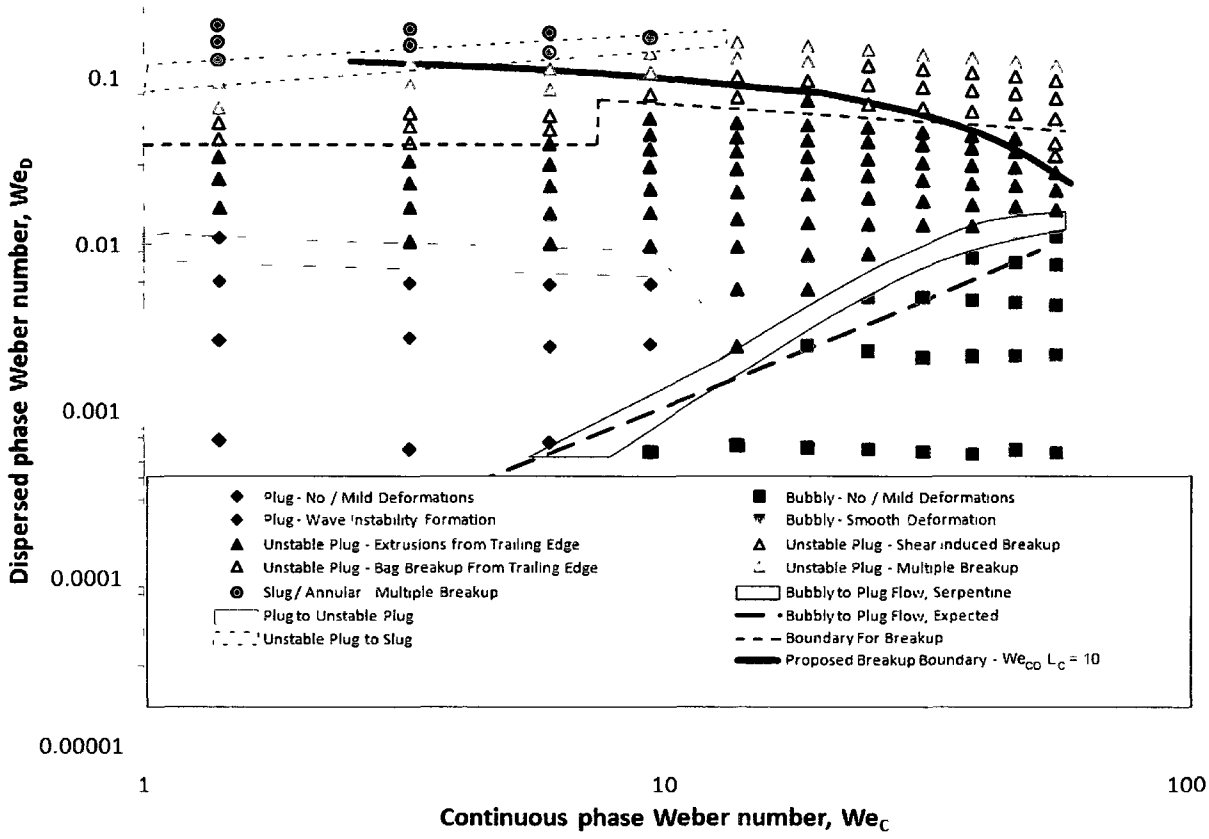

Figure 2.17 Breakup map and flow pattern transitions for r_c = 6 mm, with the proposed breakup boundary shown ($We_{CD}L_C = 10$).

in the liquid slug by curvature, relative to the surface forces maintaining the shapes of the leading and trailing bubble interfaces. Due to the limited variation of channel diameter and fluid physical properties used in this work, additional experimentation would be required to confirm the generalization of the $We_{CD}L_C = 10$ condition for the onset of bubble breakup in mini-scale curved geometries. Nonetheless, this work has demonstrated that the single phase dimensionless analysis for curved flow can be extended to the continuous phase to quantify the intensity of secondary flow formation and its effects on bubble deformation and breakup.

2.6 Conclusions

In this work, the effects of radius of curvature on two-phase flow pattern transitions and the initiation of bubble breakup/coalescence in planar serpentine arrangements were studied as a composite system. To summarize the findings in this work, an investigation of the flow patterns formed and bubble size distributions generated by the T-junction are discussed in relation to previous findings. The flow patterns and transition regions generated by the T-junction were visually identified for subsequent comparison to those present within the serpentine geometry. Scaling laws derived for square micro T-junctions were extended to a mini-scale circular T-junction operating at $545 < \mathrm{Re}_{CD} < 4675$, $0.0035 < Ca_C < 0.025$ and $0.0015 < Ca_{D,\mu_C} < 0.03$; successfully predicting bubble lengths for bubbly and plug/unstable-plug flow and enabling the use of an analytical expression to describe the transition between bubbly and plug flow.

Bubble breakup maps were developed for each of the serpentine geometries, identifying curvature-induced shifts in the transitions between flow patterns. The mechanisms of bubble breakup, grouping and coalescence are discussed, with particular emphasis placed on the relevance to reactor design. Finally, single phase dimensionless analysis for curved geometries is extended to multi-phase flow to identify the geometric dependence of the critical bubble breakup. The first bend in the serpentine geometry induced bubble grouping and coalescence, resulting in a permanent transition from plug to unstable plug flow. To maintain fully developed plug flow, r_c should be minimized whenever curvature is introduced into a design for enhancing radial mixing or increasing the reaction time within a given geometric footprint.

For the purpose of quantifying the intensity of curvature induced secondary flow in the continuous phase, the characteristic length for curved geometries encountered in the derivation of the Dean number for single-phase flow successfully captured the effects of curvature on the initiation of bubble breakup. A critical value of $We_{CD}L_C = 10$ was found for the given air-water system, above which varying degrees of bubble breakup were observed.

The generation of similar bubble breakup maps for different process fluids and serpentine designs could lead to the eventual development of a more universally applicable characteristic parameter describing not only the effects of radius of curvature, but also fluid properties and distance between alternating serpentine bends.

Acknowledgements

One of the authors (A.A. Donaldson) would like to acknowledge the support of the National Research Council of Canada (NRC) and the Natural Sciences and Engineering Research Council of Canada (NSERC).

Nomenclature

A Fitted parameter for Eq. (2.3.1)

Ca_b Bubble capillary number

Ca_C Continuous phase capillary number

Ca_{CD} Combined phase capillary number

Ca_{D,μ_C} Modified dispersed phase capillary number

d Diameter [m]

D Dean number

h Height of channels with square cross-sections [m]

k Fitted parameter for Eq. (2.3.2)

L_b Bubble length [m]

L_C Dimensionless characteristic length for curved geometry

P_i Absolute pressure at the inlet of the geometry [Pa]

P_s Absolute pressure at visualization point within the serpentine [Pa]

Q_C Volumetric flow rate of continuous phase [$cm^3\ min^{-1}$]

Q_D Volumetric flow rate of dispersed phase [$cm^3\ min^{-1}$ STP]

r_c Radius of curvature [m]

Re_b Bubble Reynolds number

Re_{CD} Combined phase Reynolds number

U_b Velocity of the bubble [$m\ s^{-1}$]

U_C Continuous phase superficial velocity [$m\ s^{-1}$]

U_D Dispersed phase superficial velocity [$m\ s^{-1}$]

We_C Continuous phase Weber number

We_{CD} Combined phase Weber number

We_D Dispersed phase Weber number

α Fitted parameter for Eq. (2.3.2)

β Fitted parameter for Eq. (2.3.2)

δ Bubble film thickness [m]

ε Fitted parameter for Eq. (2.3.3)

ε_D Volumetric holdup of the dispersed phase.

μ_C Continuous phase viscosity [kg m^{-1} s^{-1}]

ρ_C Continuous phase density [kg m^{-3}]

ρ_D Dispersed phase density [kg m^{-3}]

$\rho_{D,i}$ Dispersed phase density at the inlet of the geometry [kg m^{-3}]

$\rho_{D,s}$ Dispersed phase density at the visualization point within the serpentine [kg m^{-3}]

σ Surface Tension [N m^{-1}]

ω Fitted parameter for Eq. (2.3.3)

References

Akbar, M.K., Plummer, D.A., Hgiaasiaan, S.M., 2003. On gas-liquid two-phase flow regimes in microchannels. Int. J. Multiphase Flow 29, 855-865.

Angeli, P., and Gavriilidis, A., 2008. Hydrodynamics of taylor flow in small channels: a review. Proc. IMechE Vol. 222 Part C: J. Mech. Eng. Sci., 737-751.

Aussilous, P. and Quéré, D., 2000. Quick deposition of a fluid on the wall of a tube. Phys. Fluids 12(10), 2367-2371.

Barajas, A.M., Panton, R.L., 1993. The effect of contact angle on two-phase flow in capillary tubes. Int. J. Multiphase Flow 19, 337–346.

Barnea, D., Luninski, Y., Taitel, Y., 1983. Flow in small diameter pipes. Can J. Chem. Engng. 61, 617–620.

Coleman, J.W., Garimella, S., 1999. Characteristics of two-phase patterns in small diameter round and rectangular tubes. Int. J. Heat Mass Transfer 42, 2869–2881.

Cristini, V. and Tan, Y.C., 2004. Theory and numerical simulation of droplet dynamics in complex flows–a review. Lab Chip 4,257-264.

Damianides, C.A., Westwater, J.W., 1988. Two-phase flow patterns in a compact heat exchanger and in small tubes. In: Proc. Second UK National Conf. On Heat Transfer, Glasgow, 14–16 September. Mechanical Engineering Publications, London, pp. 1257–1268.

Fries, D.M. and von Rohr, P.R., 2009. Liquid mixing in gas-liquid two-phase flow by meandering microchannels. Chem. Eng. Sci. 64, 1326-1335.

Fukano, T., Kariyasaki, A., 1993. Characteristics of gas–liquid two-phase flow in a capillary. Nucl. Eng. Design 141, 59–68.

Garstecki, P., Fuerstman, M.J., Stone, H.A., and Whitesides, G.M., 2006. Formation of droplets and bubbles in a microfluidic tjunction - scaling and mechanism of break-up. Lab Chip 6, 693–693.

Hassan, I., Vaillancourt, M., and Pehlivan, K., 2005. Two-phase flow regime transitions in microchannels: a comparative experimental study. Microscale Thermophys. Eng. 9, 165-182.

Huh, C., Kim, J., Kim, M.H., 2007. Flow pattern transition instability during flow boiling in a single microchannel. Int. J. Of Heat and Mass Trans. 50, 1049-1060.

Kawahara, A., Chung, P.Y., and Kawaji, M., 2002. Investigation of two-phase flow pattern void fraction and pressure drop in a microchannel. Int. J. Multiphase Flow 28 (9), 1411-1435.

Kirpalani, D.M., Patel, T., Mehrani, P., Macchi, A., 2008. Experimental analysis of the unit cell approach for two-phase flow dynamics in curved flow channels. Int. J. Of Heat and Mass Trans. 51, 1095-1103.

Laborie, C., Cabassud, L., Durand-Bourlier, and Laine, J. M, 1999. Characterisation of gas–liquid two-phase flow inside capillaries. Chem. Eng. Sci. 54, 5723–5735.

Liu, H., Vandu, C. O., and Krishna, R, 2005. Hydrodynamics of Taylor flow in vertical capillaries: flow regimes, bubble rise velocity, liquid slug length and pressure drop. Ind. Eng. Chem. Res. 44, 4884–4897.

Martin, J., Oshkai, P., Djilali, N., 2005. Flow structures in a U-shaped fuel cell flow channel: quantitative visualization using particle image velocimetry. J. Of Fuel Cell Sci. and Tech. 2, 70-80.

Menech, M.D., Garstecki, P., Jousse, F., and Stone, H.A., 2008. Transition from squeezing to dripping in a microfluidic T-shaped junction. J Fluid Mech. 595, 141–161.

Mishima, K, Hibiki, T., Nishihara, H., 1995. Some characteristics of air–water two-phase flow in small diameter tubes. Proc 2nd Int. Conf. Multiphase Flow, Vol. 4, April 3–7, 1995, Tokyo, Japan, pp. 39– 46.

Mishima, K., Hibiki, T., 1996. Some characteristics of air–water two-phase flow in small diameter vertical tubes. Int. J. Multiphase Flow 22, 703–712.

Nisisako, T., Torii, T., and Higuchi, T., 2002. Droplet formation in a microchannel network. Lab Chip 2, 24–26.

Niu, H., Pan, L., Su, H., Wang, S., 2009. Flow patern, pressure drop, and mass transfer in a gas-liquid concurrent two-phase flow microchannel reactor. Ind. Eng. Chem. Res. 48, 1621-1628.

Qian, D. and Lawal, A, 2006. Numerical study on gas and liquid slugs for Taylor flow in a T-junction microchannel. Chem. Eng. Sci. 61, 7609–7625.

Shekarriz, R., 2000. Challenges in thermal systems miniaturization. Heat Transfer Eng. 21, 1–2.

Suo, M., Griffith, P., 1964. Two-phase flow in capillary tubes. J. Basic Eng. 86, 576–582.

Thorsen, T., Roberts, R., Arnold, F., and Quake, S., 2001. Dynamic pattern formation in a vesicle-generating microfluidic device. Phys. Rev. Lett. 86, 4163–4166.

Tice, J.D., Song, H., Lyon, A.D., and Ismagilov, R.F., 2003. Formation of droplets and mixing in multiphase microfluidics at low values of the Reynolds and the capillary numbers. Langmuir 19, 9127-9133

Triplett, K.A., Ghiaasiaan, S.M., Adbel-Khalik, S.I., Sadowski, D.L., 1999a. Gas–liquid two-phase flow in microchannels. Part I: Two-phase flow patterns. Int. J. Multiphase Flow 25, 377–394.

Triplett, K.A., Ghiaasiaan, S.M., Adbel-Khalik, S.I., LeMouel, A., and McCord, B.N. 1999b. Gas–liquid two-phase flow in microchannels. Part II: void fraction and pressure drop. Int. J. Multiphase Flow 25, 395–410.

Wang, C., Chen, I.Y., Yang, Y., and Chang, Y., 2003. Two-phase flow pattern in small diameter tubes with the presence of horizontal return bend. Int. J. Heat Mass Transfer 46, 2975–2981.

Wang, C., Chen, I.Y., Yang, Y., Chang, Y., and Hu, R., 2004. Influence of horizontal return bend on the two-phase flow pattern in small diameter tubes. Exp. Therm. Fluid Sci. 28, 145–152.

Wang, C., Chen, I.Y., and Huang, P., 2005. Two-phase slug flow across small diameter tubes with the presence of vertical return bend. Int. J. Heat Mass Transfer 48, 2342–2346.

Xiong, R., Chung, J.N., 2007. Flow characteristics of water in straight and serpentine micro-channels with miter bends. Exp. Therm. And Fluid Sci. 31, 805-812.

Xu, J.H., Luo, G.S., Li, S.W., and Chen, C.G., 2006a. Shear force induced monodisperse droplet formation in a microfluidic device by controlling wetting properties. Lab Chip 6, 131-136.

Xu, J.H., Li, S.W., Tan, J., Wang, Y.J., and Luo, G.S., 2006b. Preparation of highly monodisperse droplet in a T-junction microfluidic device. AIChE J 52(9), 3005-3010.

Xu, J.H., Li, S.W., Tan, J., Wang, Y.J., and Luo, G.S., 2006c. Controllable preparation of monodisperse O/W and W/O emulsions in the same microfluidic device. Langmuir 22(19), 7943-7946.

Xu, J.H., Li, S.W., Tan, J., and Luo, G.S., 2008. Correlations of droplet formation in T-junction microfluidic devices: from squeezing to dripping. Microfluid Nanofluid 5, 711-717.

Yang, C.Y., Shieh, C.C., 2001. Flow pattern of air–water and two-phase R-134a in small circular tubes. Int. J. Multiphase Flow 27, 1163–1177.

Zhao, T.S., Bi, Q.C., 2001. Co-current air–water two-phase flow patterns in vertical triangular microchannels. Int. J. Multiphase Flow 27, 765–782.

Chapter 3

Single and two-phase pressure drop characteristics in serpentine mini-channels

A.A. Donaldson [1,2], D.M. Kirpalani [1], A. Macchi [2]

1 Institute for Chemical Process and Environmental Technology
National Research Council Canada
M-12, 1200 Montreal Road
Ottawa, Ontario, K1A 0R6, Canada

2 Dept. of Chemical and Biological Engineering
University of Ottawa
161 Louis Pasteur Street
Ottawa, Ontario, K1N 6N5, Canada

Abstract

Experimental investigation of single and two-phase flow in mini-channel serpentine systems is performed with a focus on determining the effects of flow patterns and radius of curvature of the serpentine on two-phase pressure drop. Single phase friction factors are compared to conventional theory for straight channels and fully developed flow in helical coils, and are subsequently employed in the prediction of two-phase pressure losses using separated flow models. Empirical correlations for two-phase pressure drop are proposed for the straight and serpentine configurations, leading to the identification of five operating regions in the serpentine geometry, each with distinct pressure drop characteristics.

Two of the identified operating regions corresponded to bubbly and unstable-annular flow, while the remaining three are characterized by the extent of bubble deformation and breakup occurring within the serpentine. Previously reported work (Chapter 2) identified $We_{LG}L_C$ as a suitable parameter for capturing the effects of curvature on the initiation of bubble deformation and breakup, where L_C is the characteristic length for curved geometries encountered in the Dean number for single phase flow. The boundaries between the three regions occur at $We_{LG}L_C$ = 2.7 and 15.5, respectively corresponding to the onset of mild cap deformation, and the conditions at which continuous bubble breakup is observed.

Keywords: Circular mini-channel, Serpentine, pressure drop, two-phase flow, segmented flow model.

3.1 Introduction

The pressure drop of confined gas-liquid flow in straight mini-scale contactors and reactor systems (diameter, $d \sim 1$mm) has been investigated extensively in the past for a variety of cross-sectional geometrical shapes and lengths (Triplett *et al.*, 1999; Kawahara *et al.*, 2002; Kreutzer *et al.*, 2005a,b; Angeli and Gavriilidis, 2008; Niu *et al.*, 2009). While conducted with model fluids, air and water, these studies are often extended to process fluids for engineering applications. Fundamental studies of this nature usually produce semi-empirical expressions, valid for specific flow patterns and operating conditions, providing insight into the hydraulic behaviour of two-phase mixtures flowing through a straight channel (Triplett *et al.*, 1999; Kawahara *et al.*, 2002; Angeli and Gavriilidis, 2008, Niu *et al.*, 2009). With the continued development of new applications for process flow systems at this scale, the incorporation of complex downstream phase contactors that enhance heat and mass transfer is inevitable. In our previous work (Chapter 2), the impact of a planar serpentine configuration on the two-phase flow pattern generated by a cross-flow T-junction was studied for two radiuses of curvature and a range of operating conditions. Limited information is available in literature regarding two-phase pressure drop in serpentine configurations operated at low velocities (Kulkarni & Kalyani 2009; Tung *et al.* 2009; Fries & von Rohr 2009); no applicable correlations were found for the geometric configurations, transitional flow patterns and elevated velocities present in this work.

Planar serpentine mixing arrangements are found in many industrial applications involving mini-channels; including compact heat exchangers, turbines, mini/micro reactors and fuel cells (Martin *et al.*, 2005; Xiong and Chung, 2007; Huh *et al.*, 2007). Noted for their ability to enhance heat transfer and radial mixing in single phase flow through the

formation Dean vortices, serpentine geometries are frequently used to increase the reaction time within a given geometric footprint by connecting long mini-channels with alternating U-shaped return bends. While previous studies have characterized the variation in flow patterns and pressure drop resulting from a single return bend (Idelchik, 1986; Wang *et al.*, 2003, 2004, 2005; Kirpalani *et al.*, 2008), their applicability to serpentine passive mixers consisting of consecutive alternating bends is limited, where the curvature-induced secondary flows have not fully dissipated before entering the next 180° bend.

In this work, water (single phase) and air-water (two-phase) flow was examined in straight and serpentine systems. Bubbly, plug, unstable plug and slug flow patterns were generated by a cross-flow T-junction and introduced into straight and planar serpentine arrangements to study the impact of bubble / slug length, radius of curvature, and flow pattern transitions on pressure drop across the serpentine unit cells. The objectives of this study were to: (a) determine the single phase friction factor for water flowing through the serpentine unit cells; (b) assess the capability of separated flow models for predicting two-phase pressure drop in the presence of flow pattern transitions, curvature and elevated Weber numbers; and (c) provide a semi-empirical model capable of predicting the pressure drop within the serpentine unit cells.

3.2 Experimental configuration

Five geometries were manufactured from cast acrylic to allow for the measurement of the pressure drop across a straight channel and a series of serpentine unit cells. For each geometry, semi-circular grooves were CNC-machined into two 9.5 mm thick acrylic plates to create mirror patterns that formed the straight and serpentine channels when bonded together using dichrolormethane (solvent). The flow path of the straight geometry consists of a cross-

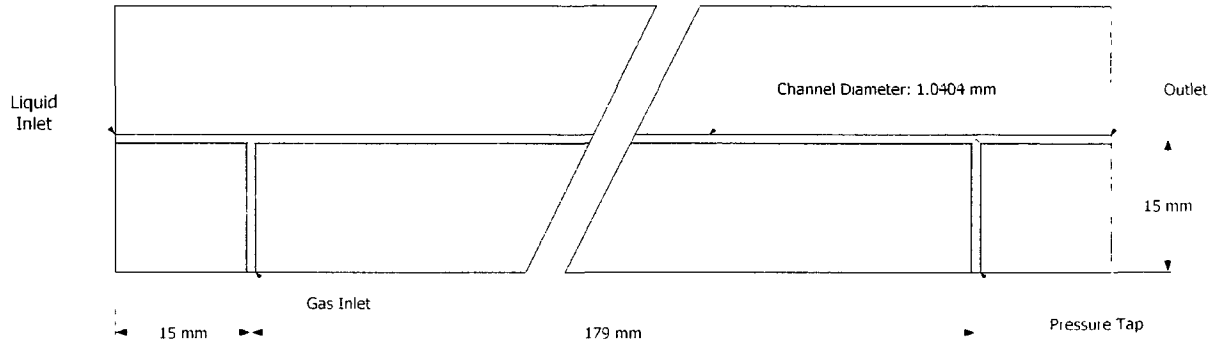

Figure 3.1 Schematic of straight geometry.

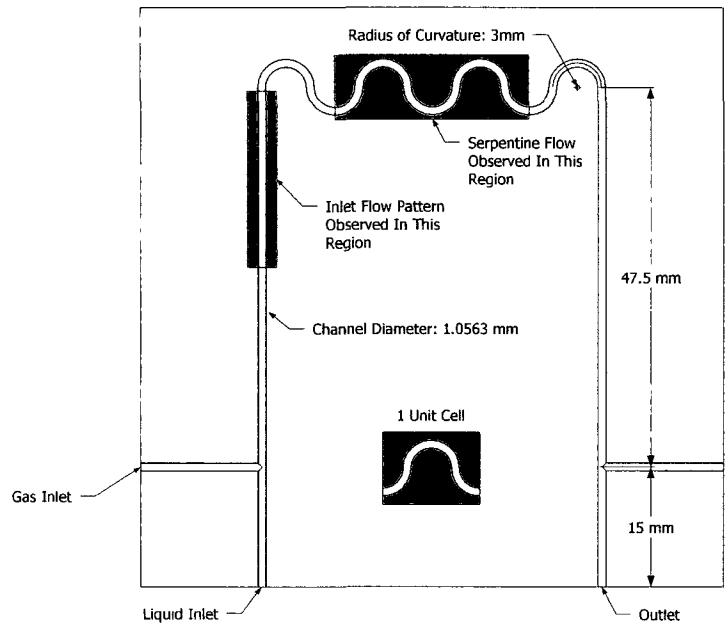

Figure 3.2 Schematic of geometry with r_c = 3 mm and 3.5 repeating serpentine unit cells.

flow T-junction contactor for blending the two phases, followed by a straight length of $L_{Channel}$ = 179mm. At the exit, an additional T-junction was fabricated to monitor the outlet pressure. The serpentine geometries are similar in design, consisting of a cross-flow T-junction contactor followed by a L_{inlet} = 47.5 mm straight channel where the gas-liquid flow pattern is further developed. The straight channel leads to a series of N_{UC} serpentine unit

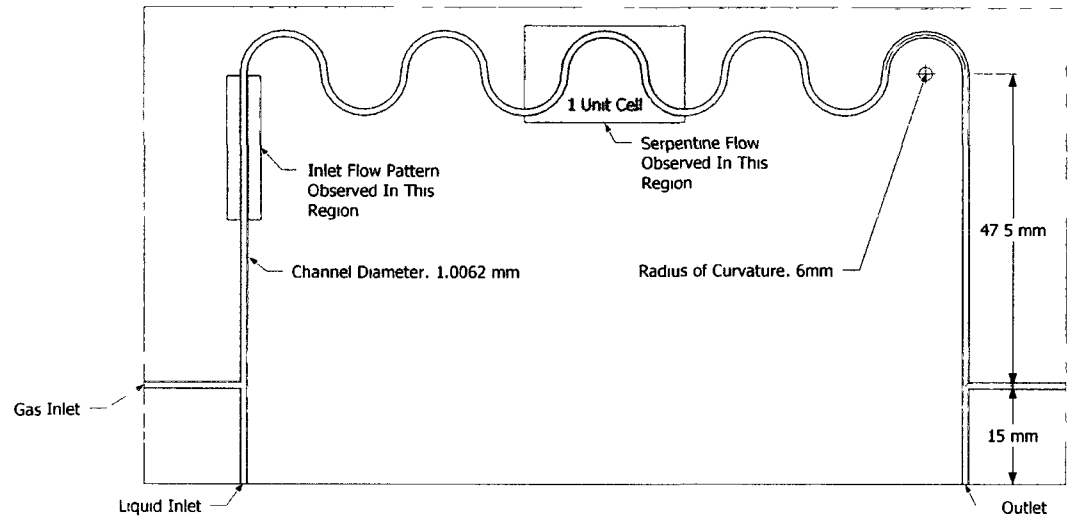

Figure 3.3 Schematic of geometry with r_c = 6 mm and 4.5 repeating serpentine unit cells.

cells with a radius of curvature, r_c, of 3 mm or 6 mm. Exit flow effects from the geometry were reduced by adding an L_{outlet} = 47.5 mm straight length after the last semi-circular curve of the serpentine, followed by an additional T-junction for monitoring the outlet pressure. CNC-machining of the acrylic plates introduced minimal groove depth variation. Schematics of the fabricated straight and serpentine geometries (r_c = 6mm, N_{UC} = 4.5; r_c = 3 mm, N_{UC} = 3.5) and their dimensions are provided in Figs. 3.1 through 3.3.

The experimental setup, shown in Fig. 3.4, illustrates the operation of the mini-channels for air-water mixtures. The gas (dry air) was supplied from a cylinder through a pressure reducing valve (PRV) and a needle valve used to regulate flow. The gas flow rate, at standard conditions, was measured using an electronic mass flow meter (Omega FMA-1812). Pressure was measured at the gas inlet and channel outlet using a water manometer at low flow rates (0-11 kPa, 0-1.6 psig), and a pressure transducer at high flow rates (PSI-Tronix 68920-30, 0-30psig). De-ionized water was introduced using a magnetically driven low flow rate gear-controlled pump (Micropump Series 200 P35, 1.17 mL/rev, 4.2 bar max

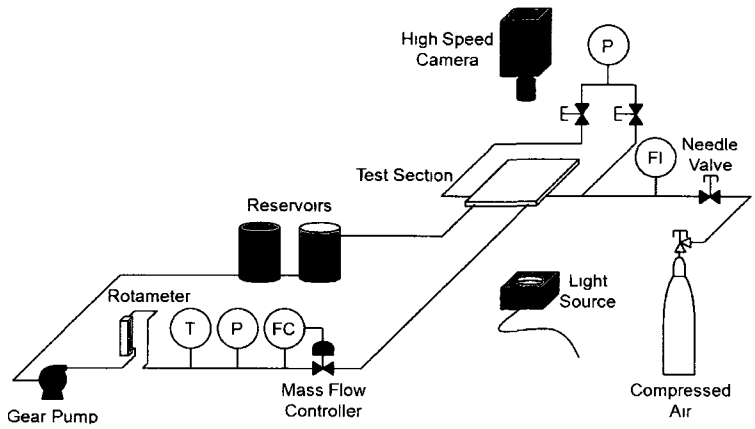

Figure 3.4 Experimental configuration.

ΔP) regulated using an electronic mass flow controller (Omega FLV-4619A). The liquid temperature was also monitored at the mass flow controller to determine the liquid viscosity at each operating condition.

3.3 Single phase pressure drop

Single phase pressure drop experiments were carried out with deionized water for the straight channel, a serpentine channel with r_c = 6 mm and N_{UC} = 4.5, and three serpentine channels with r_c = 3 mm (N_{UC} = 2.5, 3.5 and 4.5). Measurement of the inlet and outlet pressures observed for each geometry at $350 < \mathrm{Re}_L = \rho_L U_L d/\mu_L < 3900$ were obtained for four repeated experiments: three at the onset of this study, and one following the completion of the last multi-phase experiment to confirm repeatability. The straight channel provided a comparison to existing correlations for pressure drop in round tubes, while the serpentine channels allowed for the effects of curvature and the number of repeating unit cells to be explored.

3.3.1 Straight channel pressure drop

The friction factor in the straight geometry, f_S, was determined directly from the measured pressure drop across the channel length, $-\Delta P$.

$$f_S = -\Delta P \frac{2}{\rho_L U_L^2} \frac{d}{L_{Channel}} \tag{3.3.1}$$

A comparison of the resulting values to laminar and turbulent theory for smooth circular tubes is provided in Fig. 3.5; where in laminar flow, $f_S = 64/\mathrm{Re}_L$, and in turbulent flow, $f_S = 0.3164\,\mathrm{Re}^{-0.25}$. The sudden increase in f_S at $Re_L \sim 2300$ is consistent with the typical onset of the transition regime in circular pipes, necessitating the use of an interpolating function to connect the laminar and turbulent regimes. A form of linear interpolation was applied to f_S in this region, resulting in the following relationship for $2300 < Re_L < 8000$.

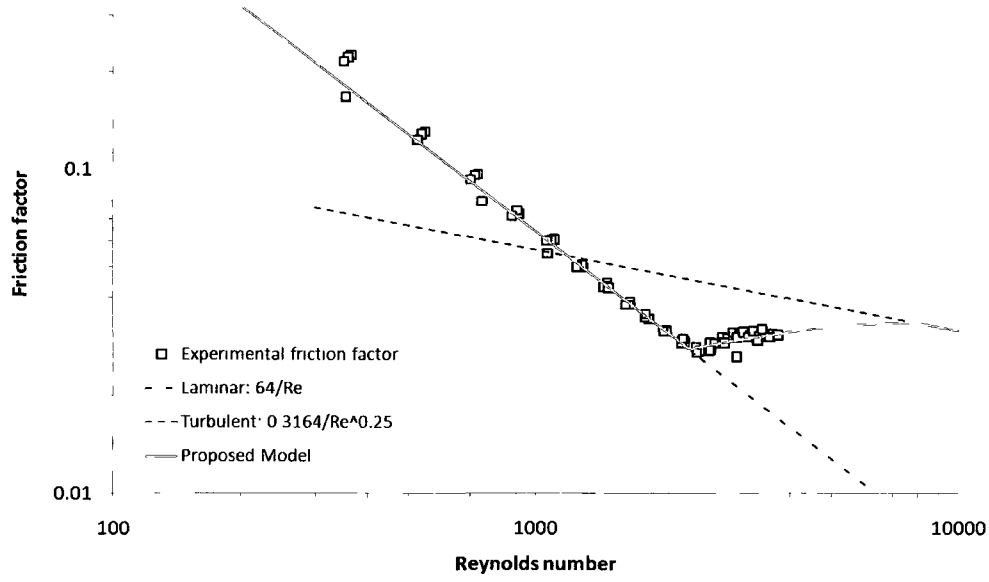

Figure 3.5 Comparison of experimentally obtained friction factors for single phase flow through the straight geometry and conventional correlations for circular pipes.

$$f_S = \frac{\mathrm{Re}_L - 2300}{5700}\left(0.3164\,\mathrm{Re}_L^{-0.25} - 64/2300\right) + 64/2300 \qquad (3.3.2)$$

Note that single phase measurements were carried out for $Re_L < 3900$, well below the values of Re_{LG} which could be observed near the exit of the channel in multi-phase flow at the highest gas and liquid flow rates ($Re_{LG} \sim 7200$). Unfortunately, measurement of the pressure drop at higher flow rates was prevented by limitations of the geometry and pump head used, necessitating the extrapolation of f_S at $Re_L > 3900$. As the variation in f_S predicted by Eq. (3.3.2) is minimal within the transition region, the error introduced by extrapolation should not significantly impact the two-phase pressure drop analysis discussed in section 3.4.

3.3.2 Serpentine channel pressure drop

Single phase pressure drop measurements were obtained for each of the four serpentine geometries (r_c = 6 mm, N_{UC} = 4.5; r_c = 3mm, N_{UC} = 2.5, 3.5, and 4.5), encompassing frictional pressure losses resulting from the $L_{inlet} = L_{outlet}$ = 47.5 mm inlet and outlet sections and N_{UC} serpentine unit cells. The friction factor within the serpentine channel, f_{serp}, was determined by assuming the instantaneous formation of a fully developed flow at the inlet of the first unit cell and at the exit of the last unit cell; thus resulting in a constant f_s and f_{serp} within the outlet length and serpentine channels, respectively.

$$f_{serp} = \frac{d}{N_{UC}(2\pi r_c)}\left(-\Delta P \frac{2}{\rho_L U_L^2} - f_S \frac{L_{inlet} + L_{outlet}}{d}\right) \qquad (3.3.3)$$

For all of the conditions tested, the friction factor within the serpentine was greater than that of the straight channel, producing a smooth transition from laminar to turbulent flow (Figs. 3.6 and 3.7). The change in f_{serp} with an increase in N_{UC} for r_c = 3 mm was minimal, well within the potential variations arising from experimental error in pressure drop measurements and flow control. This suggests that a fully developed flow pattern is

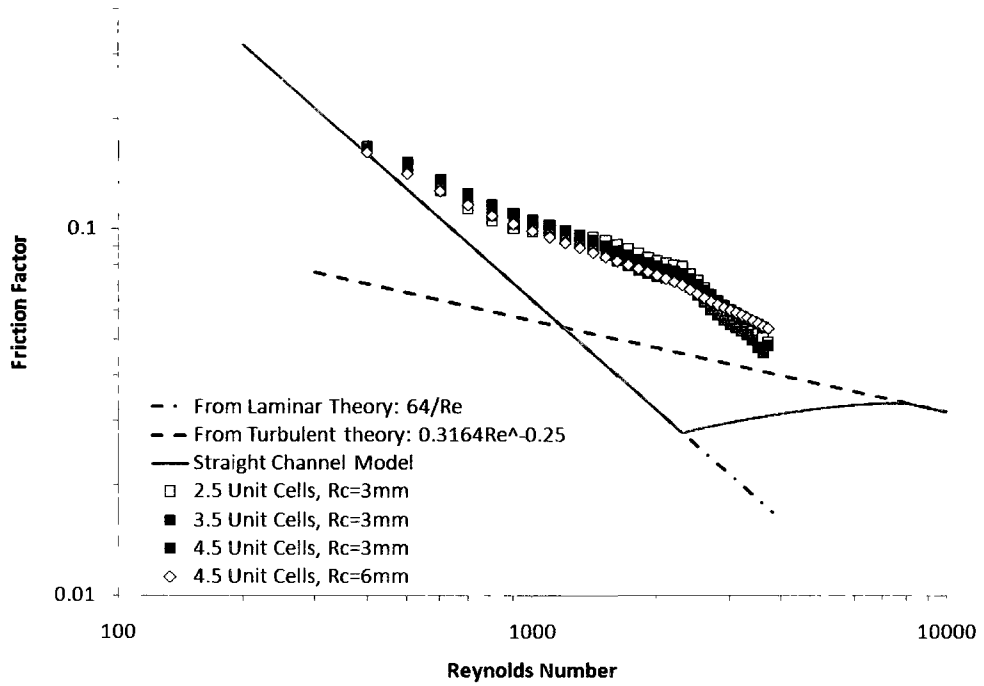

Figure 3.6 Comparison of experimentally obtained friction factors for single phase flow through the serpentine geometries and conventional correlations for circular pipes, log-log axis.

achieved within a single unit cell length for r_c = 3 mm. The change in f_{serp} with radius of curvature was surprisingly small, where the friction factor for the r_c = 6 mm geometry, $f_{serp,6mm}$, was only slightly less than that observed for r_c = 3 mm and N_{UC} = 4.5, $f_{serp,3mm}$. Since $f_{serp,6mm}$ is within the observed variation of the 3 mm friction factor data, the effects of radius of curvature in helical coils was explored to determine if the obtained values are reasonable.

The friction factor in a helical coil, $f_{helical}$, represents the maximum value that would be expected in a serpentine geometry, where the alternating curves in the serpentine disrupt the formation of Dean vortices and dampen secondary flow. The well known correlation proposed by Mishra & Gupta (1979) was used as a basis for assessing the calculated values

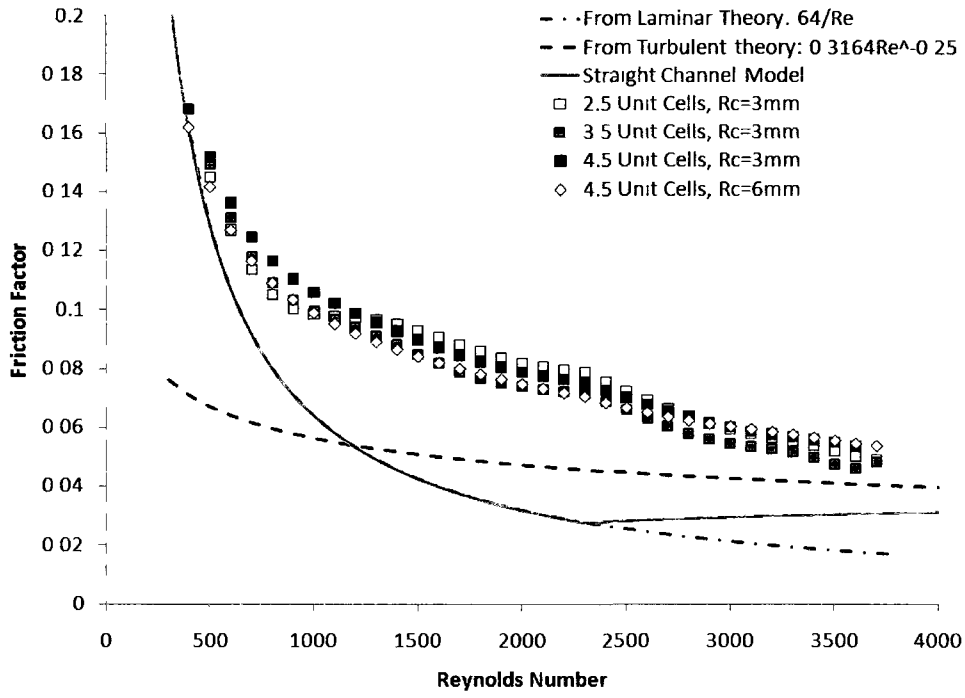

Figure 3.7 Comparison of experimentally obtained friction factors for single phase flow through the serpentine geometries and conventional correlations for circular pipes.

of f_{serp} in the laminar regime for curved flow, $Re_L < 20000(0.5d/r_c)^{0.32}$, where the Dean number is defined as $De = \mathrm{Re}_L(d/2r_c)^{0.5}$.

$$f_{helical} = \frac{64}{\mathrm{Re}_L}\left[1 + 0.03(\log De)^{1.5}\right] \tag{3.3.4}$$

As seen in Fig. 3.8, the values of f_{serp} fell between f_S and $f_{helical}$ due to the presence of curvature inversions in the serpentine geometry. While the effects of r_c are not as pronounced as those predicted by Eq. (3.3.4) for helical coils, the behavior of f_{serp} is consistent with a geometric configuration that is a blend between straight and curved channels.

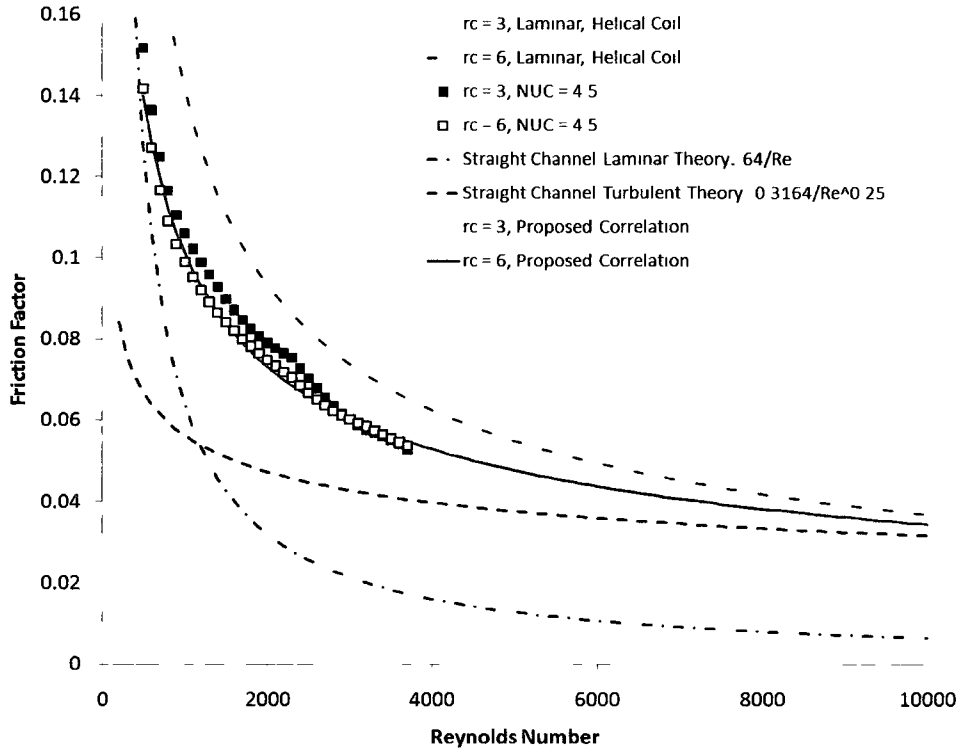

Figure 3.8 f_{serp}, f_S and $f_{helical}$ vs. Reynolds number for r_c = 3 mm and r_c = 6 mm.

For the purpose of estimating the two-phase pressure drop through the serpentine unit cells, simple power law correlations were obtained from the experimental data for f_{serp} in the r_c = 3 mm and r_c = 6 mm geometries.

$$f_{serp,3mm} = 3.505\,\mathrm{Re}_L^{-0.5039} \tag{3.3.5}$$

$$f_{serp,6mm} = 2.565\,\mathrm{Re}_L^{-0.4679} \tag{3.3.6}$$

The resulting predictions for $f_{serp,3mm}$ and $f_{serp,6mm}$ are included in Fig. 3.8, extrapolating well to higher Reynolds numbers while maintaining the intermediate position between f_s and $f_{helical}$. Note that in Figs. 3.6 to 3.8, the peaks observed in the experimental values at $\mathrm{Re_L}$ = 2300 have no physical significance, and are the result of Eq. 3.3.2 being used while removing the inlet and outlet pressure drop contributions.

3.4 Two-phase pressure drop

3.4.1 Homogeneous fluid and separated flow models

The design and optimization of two-phase flow in mini-scale systems requires an accurate prediction of the pressure drop resulting from flow through the geometry. Two-phase pressure drop models currently available in literature typically fall into one of two categories: Homogeneous fluid models or separated flow models (Balasubramaniam *et al.* 2006). In homogeneous fluid models, the two-phase mixture is treated as a single fluid with suitably averaged physical properties of the individual phases. The pressure drop is determined from the contributions of frictional losses, flow acceleration and hydrostatic head, all of which are evaluated using the averaged properties of the homogeneous mixture. Separated flow models consider the two phase mixture as two separate flow streams with cross-sectional areas equivalent to their respective phase holdups. Interaction parameters are then applied to account for heat, mass and momentum transfer between the two distinct phases. The well known Lockhart-Martinelli correlation is one such model, but is not considered in this work in preference for the correlation proposed by Kreutzer *et al.* (2005a) for idealized Taylor flow, depicted in Fig. 3.9.

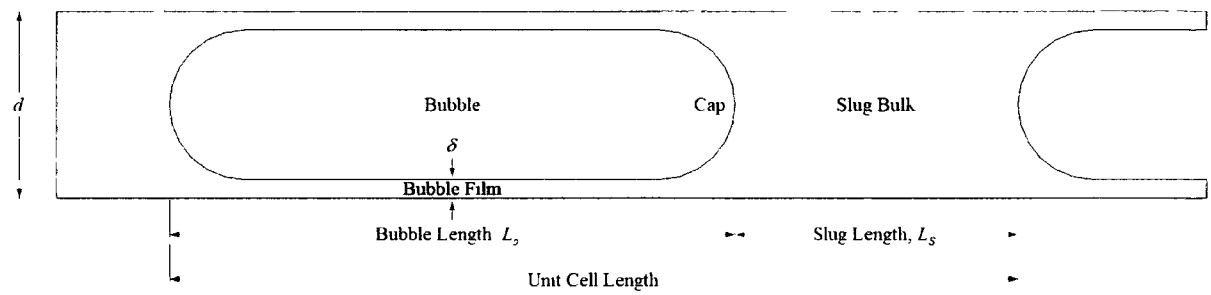

Figure 3.9 Schematic of idealized Taylor flow, where shaded regions represent the liquid phase.

In their work, Kreutzer *et al.* (2005a) explored the validity of friction factor correlations at different combined phase Reynolds, capillary and Weber numbers: $\mathrm{Re}_{LG} = \rho_L(U_L + U_G)d/\mu_L$, $Ca_{LG} = \mu_L(U_L + U_G)/\sigma$, and $We_{LG} = \rho_L(U_L + U_G)^2 d/\sigma$. For a given friction factor, f, the pressure drop per unit cell length was determined and compared to experimental and numerical results:

$$\frac{-\Delta P}{(L_S + L_b)} = \frac{L_S}{(L_S + L_b)} \frac{\rho_L(U_L + U_G)^2}{2d} f \tag{3.4.1}$$

For $We_{LG} << 1$, Kreutzer *et al.* (2005a) confirmed the applicability of Bretherton's correlation for the friction factor (Bretherton 1961), which can be combined with Stokes-flow lubrication solutions to yield the following expression for f:

$$f = \frac{64}{\mathrm{Re}_{LG}} \left[1 + \frac{d}{L_S} \frac{7.16(3Ca_{LG})^{2/3}}{32Ca_{LG}} \right] \tag{3.4.2}$$

The two mechanisms contributing to pressure loss across a unit cell are viscous shear within the liquid slug, and the pressure drop across the bubble due to Laplace terms and, to a lesser extent, frictional losses along the length of the bubble film.

For $We_{LG} = O(1)$ and $Re_{LG} = O(100)$, inertial effects can no longer be ignored and the friction factor can be approximated using the correlation proposed by Kreutzer *et al.* (2005a).

$$f = \frac{64}{\mathrm{Re}_{LG}} \left[1 + a_1 \frac{d}{L_S} \left(\frac{\mathrm{Re}_{LG}}{Ca_{LG}} \right)^{1/3} \right] \tag{3.4.3}$$

Where values of a_1 = 0.17 and 0.07 were proposed for predicting experimentally and numerically derived pressure drops, respectively. To our knowledge, the applicability of Eq. (3.4.3) at the larger We_{LG} and Re_{LG} encountered in this work has yet to be confirmed in published literature. For the purpose of this study, a_1 is set equal to 0.17 and Eq. (3.4.3) is

modified under the assumption that the slug friction factor will be equivalent to that observed in the single phase measurements, f_S, while the bubble film will continue to be laminar:

$$f = f_S + a_1 \frac{64}{\mathrm{Re}_{LG}} \frac{d}{L_S} \left(\frac{\mathrm{Re}_{LG}}{Ca_{LG}} \right)^{1/3} \tag{3.4.4}$$

3.4.2 Inlet bubble and slug size distribution

The pressure-drop correlation proposed by Kreutzer *et al.* (2005a) for the two-phase flow in straight channels requires information regarding both the bubble and slug lengths within the geometry. In our previous work (Chapter 2), the bubble lengths generated by the cross-flow T-junction were correlated using a modified form of the scaling laws proposed by Xu *et al.* (2008) for square micro-channels, resulting in the following expression for $L_{b,in}/d$, valid for $0.0035 < Ca_L = \mu_L U_L / \sigma < 0.025$, $0.0015 < Ca_{G,\mu_L} = \mu_L U_G / \sigma < 0.03$, and $545 < \mathrm{Re}_{LG} < 4675$:

$$\frac{L_{b,in}}{d} = \max \begin{cases} 0.844 Ca_{G,\mu_L}^{0.285} Ca_L^{-0.384} & (Bubbly) \\ 9.721 Ca_{G,\mu_L}^{1.232} Ca_L^{-1} & (Plug / Unstable\ \ Plug) \end{cases} \tag{3.4.5}$$

A comparison of the $L_{b,in}$ predicted by Eq. (3.4.5) to experimentally measured values is provided in Fig. 3.10 for the r_c = 3 mm and r_c = 6 mm serpentine systems.

The average liquid slug length, L_S, was also measured at equivalent conditions. As shown in Fig. 3.11, the slug length generated by the cross-flow T-junction varied significantly, having a mean length comparable to the channel diameter for the entire range of operating conditions. This is of significant importance for the prediction of the two-phase pressure drop, as the liquid circulation pattern in such small slugs may not resemble Hagen-Poiseuille flow and the Laplacian contributions from the bubble may be significant.

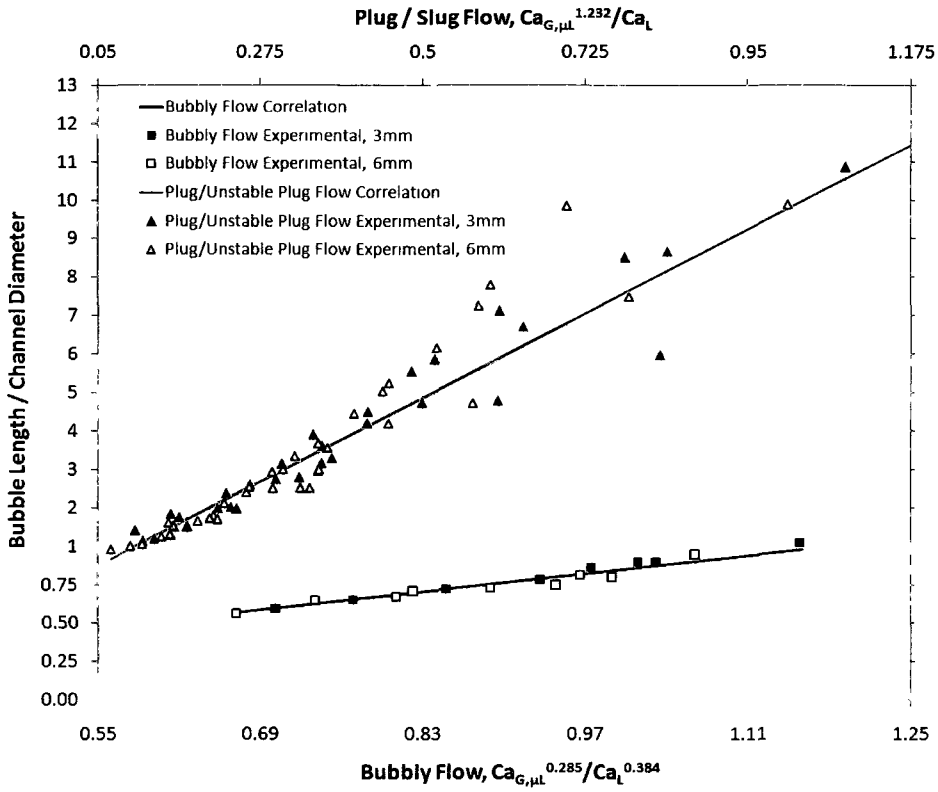

Figure 3.10 Comparison of the average bubble size predicted by Eq. (3.4.5) and experimentally obtained values. Error bars represent one standard deviation, obtained from number frequency distributions of the measured bubble length.

When predicting the two-phase pressure drop, two approaches were taken for estimation of the liquid slug length: Approximation from the gas holdup, and arbitrary selection. The first of these methods required the approximation of the bubble film thickness, δ, to accurately determine the remaining fraction of the liquid contained within the slug. For this purpose, the correlation proposed by Aussilous and Quéré (2000) for $10^{-3} < Ca_b = \mu_L U_b / \sigma < 1.4$ was used:

$$\frac{2\delta}{d} = \frac{1.34 Ca_b^{2/3}}{1 + 3.34 Ca_b^{2/3}} \tag{3.4.6}$$

Where the bubble velocity, U_b, was estimated using the correlation of Liu *et al.* (2005).

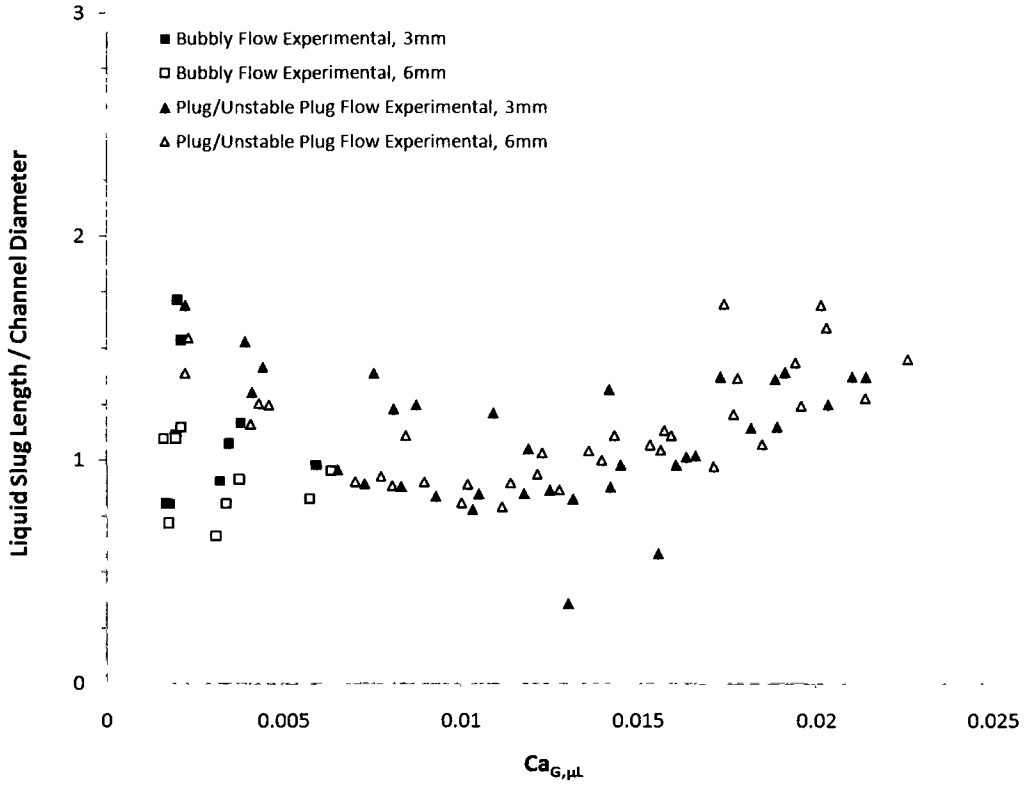

Figure 3.11 Average liquid slug length and variation exiting the cross-flow T-junction. Error bars represent one standard deviation, obtained from number frequency distributions of the slug length.

$$U_b = \frac{U_L + U_G}{1 - 0.61 Ca_{LG}^{0.33}} \tag{3.4.7}$$

Knowing δ, the inlet slug length was determined from a volume balance of the liquid phase:

$$L_{S,in} = \frac{4}{\pi d^2}\left(V_{b,in}\frac{U_L}{U_G} - V_{film} - V_{cap} \right) \tag{3.4.8}$$

Where the inlet bubble volume, $V_{b,in}$, bubble film volume, V_{film}, and liquid volume adjacent to the bubble caps, V_{cap}, is defined as:

$$V_{b,in} = \frac{\pi}{4}\left(L_{b,in} - d + 2\delta\right)\left(d - 2\delta\right)^2 + \frac{\pi}{6}\left(d - 2\delta\right)^3 \tag{3.4.9}$$

$$V_{film} = \frac{\pi}{4}\left(L_b - d + 2\delta\right)\left[d^2 - \left(d - 2\delta\right)^2\right] \tag{3.4.10}$$

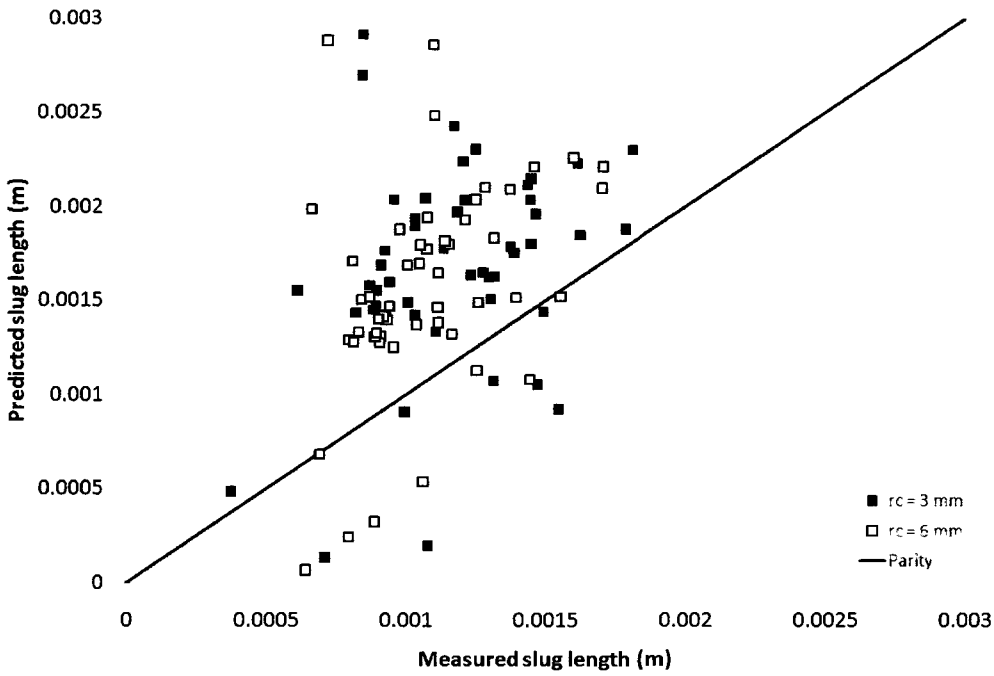

Figure 3.12 Comparison of measured slug length to that predicted using the bubble length and gas holdup. Error bars represent one standard deviation of the measured average slug length.

$$V_{cap} = \frac{\pi}{4} d^2 (d - 2\delta) - \frac{\pi}{6} (d - 2\delta)^3 \tag{3.4.11}$$

As seen in Fig. 3.12, the slug lengths predicted by this method were typically higher than those observed experimentally, and significantly under-predicted the lengths for large gas holdups. The second approach, arbitrary selection, involved assigning a single slug length to all operating conditions, where an average value of L_S/d = 1.045 was observed for both the r_c = 3 mm and r_c = 6 mm geometries (Fig. 3.11).

3.4.3 Two-phase pressure drop in a straight channel

The pressure drop in the straight channel was numerically determined using Eqs. (3.4.1) and (3.4.4), integrated along the length of the channel, $L_{channel}$, using the ideal gas law

to account for compressibility of the gas. Defining $f_{straight}$ as the friction factor predicted by Eq. (3.4.4) and using the proposed model for f_S outlined in section 3.3.1:

$$\Delta P = -\int_0^{L_{channel}} \frac{L_S}{(L_S + L_b)} \frac{\rho_L (U_L + U_G)^2}{2d} f_{straight}\, dx \tag{3.4.12}$$

For a given inlet absolute pressure, P_{in}, and superficial gas and liquid velocities at process conditions, U_G and U_L, the average inlet bubble length was determined from Eq. (3.4.5). The inlet slug length was set to $L_S = 1.045d$ based on experimentally observed values. An explicit Euler's method was applied to integrate the pressure drop along the length of the channel, where a step size of $L_{channel}/1000$ was sufficient to obtain consistent results.

At each step along the channel length, the expansion and acceleration of the gas bubble relative to conditions at the inlet would be determined, and subsequently used to re-evaluate V_b, U_G, Re_{LG}, Ca_{LG}, U_b, Ca_b, δ, L_b, V_{film}, V_{cap}, L_S, f, and the pressure drop per unit length. For an absolute pressure at the current position, P_i, the bubble volume and gas velocity were calculated assuming ideal gas expansion with negligible viscous heating:

$$V_b = V_{b,in}\left(\frac{P_{in}}{P_i}\right) \tag{3.4.13}$$

$$U_G = U_{G,in}\left(\frac{P_{in}}{P_i}\right) \tag{3.4.14}$$

The remaining values were determined in order using Eqs. (3.4.7), (3.4.6), (3.4.10), (3.4.11), (3.4.8), and (3.4.4).

The pressure differences estimated for the 179 mm straight channel length were consistently higher than experimentally obtained values (Fig. 3.13) when $a_1 = 0.17$ was used. For the purpose of correlating the experimental data, an additional multiplier, b_1, was

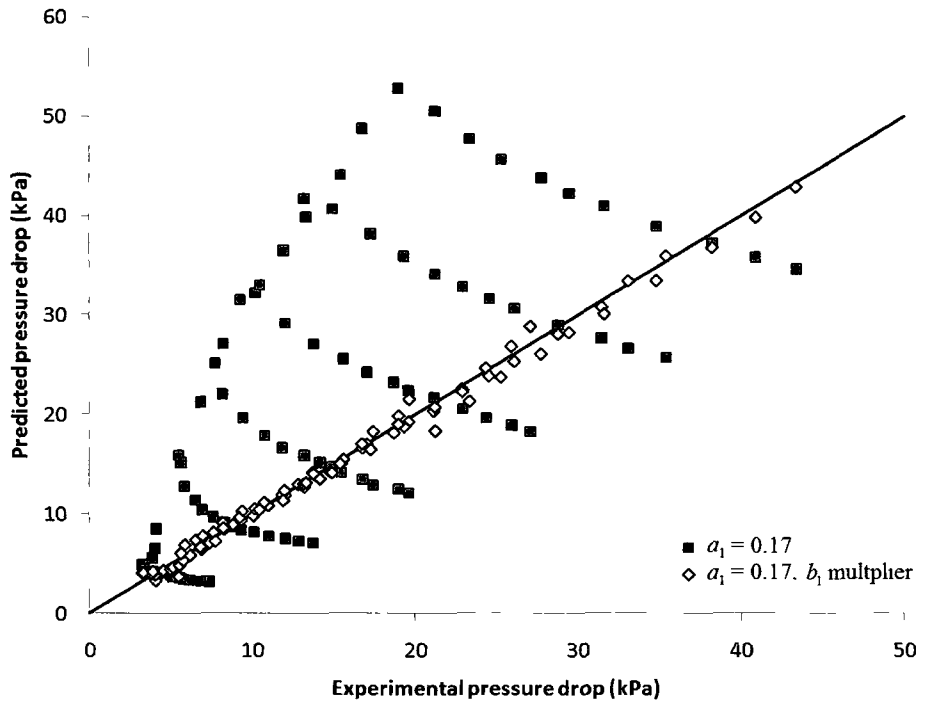

Figure 3.13 Comparison of predicted and measured pressure drop along a 179mm straight channel.

introduced for the Laplacian contributions as a method of accounting the variation in cap shape and film thickness observed at higher We_{LG}.

$$f = f_S + b_1 a_1 \frac{64}{\mathrm{Re}_{LG}} \frac{d}{L_S} \left(\frac{\mathrm{Re}_{LG}}{Ca_{LG}} \right)^{1/3} \tag{3.4.15}$$

At each of the operating conditions tested, the value of b_1 which equated the predicted and observed pressure drops was determined. A dependency between b_1, We_{LG} and the gas phase holdup was identified and described by the following expressions for plug/unstable plug flow:

$$b_1 = -0.13621 + 1.1953\,\varepsilon_G - 0.002815\,We_{LG} + 0.01285\,\varepsilon_G We_{LG} \tag{3.4.16}$$

Note that the gas phase holdup was approximated as the ratio of the superficial gas velocity to the combined velocities of the gas and liquid phases. For bubbly flow, a constant value of b_1 = 0.106134 was observed whenever the bubble length was less than the $(L_b/d)_{Transition}$ proposed in Chapter 2:

$$\varepsilon_G = \frac{U_G}{U_L + U_G} \tag{3.4.17}$$

$$\left(\frac{L_b}{d}\right)_{Transition} = \frac{\left(1 - 0.61 Ca_{LG}^{0.33}\right)^{2/3} + 2Ca_{LG}^{2/3}}{\left(1 - 0.61 Ca_{LG}^{0.33}\right)^{2/3} + 3.33 Ca_{LG}^{2/3}} \tag{3.4.18}$$

While the pressure drop predicted by Eq. (3.4.15) was closer to experimentally observed values than those predicted by Eq. (3.4.4) (Fig. 3.13), the proposed b_1 multiplier has limited potential for generalization beyond this study. Nonetheless, Eq. (3.4.15) provides insight into the applicability of Eq. (3.4.4) at elevated We_{LG}, and the potential source of the model's deviation from experimental measurements under these conditions.

Consider slug flow operating at high values We_{LG} and Re_{LG}. Based on Eq. (3.4.6), the film thickness surrounding the gas bubble increases substantially with Ca_{LG}, possibly leading to an increase in the frictional pressure losses along the length of the bubble film. The liquid slug length observed for these conditions was also comparable to the channel diameter, and would likely contain intense circulation patterns with a higher rate of energy dissipation than that observed in fully developed Hagen-Poiseuille flow. Both of these factors would lead to an increase in the frictional contribution to pressure drop per unit cell length, which can be achieved in Eqs. (3.4.12) and (3.4.15) by increasing either L_S or b_1. Meanwhile, bubble grouping and coalescence during the transition from plug to unstable

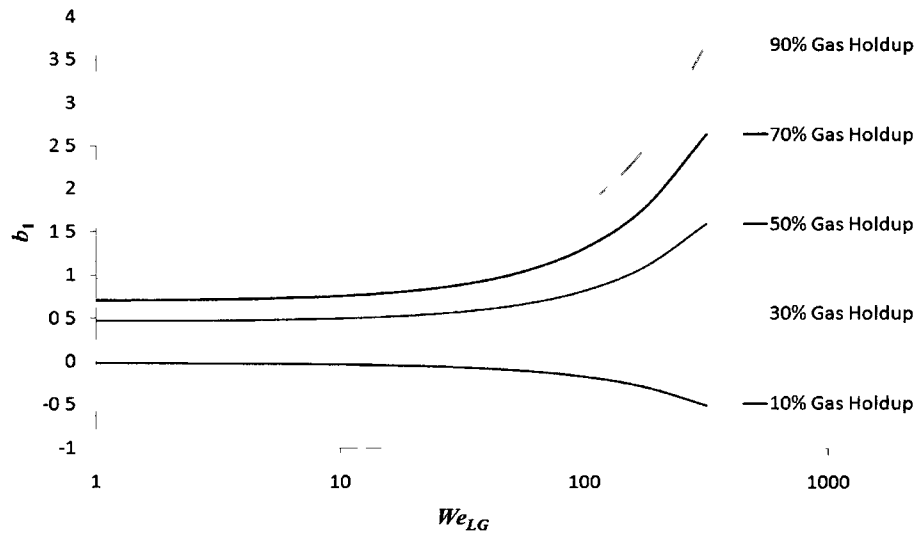

Figure 3.14 Dependence of b_1 on We_{LG} and gas holdup for a straight channel.

plug and slug flow at higher gas flow rates would increase the Laplacian contributions to pressure drop.

For the operating conditions encountered in this study, b_1 typically increased with We_{LG} and ε_G (Fig. 3.14), except in the presence of low gas phase holdups where bubbly flow was more likely to occur. The subsequent analysis of pressure drop in the serpentine geometry uses Eq. (3.4.12), (3.4.15) and (3.4.16) to account for the pressure drop along the inlet and outlet straight channel lengths when determining the total pressure drop across the serpentine unit cells.

3.4.4 Two-phase pressure drop in serpentine channels

Two-phase flow experiments were carried out for the r_c = 6 mm, N_{UC} = 4.5 and r_c = 3 mm, N_{UC} = 3.5 serpentine geometries for gas and liquid flow rates ranging from 10 to 180 cm^3/min STP and 15 to 95 cm^3/min, respectively. At each operating condition, the inlet and outlet pressures were recorded (P_{in} and P_{out}), along with the inlet bubble and slug size distributions and flow pattern variations within the serpentine (discussed in section 3.4.2 and

Chapter 2). This information was subsequently used in conjunction with Eqs. (3.4.15) and (3.4.16) to predict the pressure drop along the inlet and outlet straight channel lengths, resulting in an estimate for the pressure drop across the serpentine unit cells.

Consider a serpentine geometry operating at U_L and U_G, having an inlet and outlet pressure of P_{in} and P_{out}. The pressure at the inlet of the serpentine unit cells, $P_{serp,in}$, can be determined using the methodology outlined in section 3.4.3, where Eq. (3.4.5) is used to predict the inlet bubble length and a constant slug length of $L_s = 1.045d$ is applied:

$$P_{serp,in} = P_{in} - \int_0^{L_{inlet}} \frac{L_S}{(L_S + L_b)} \frac{\rho_L (U_L + U_G)^2}{2d} f_{straight}\, dx \tag{3.4.19}$$

The pressure at the outlet of the serpentine can be similarly determined by integrating from the exit of the outlet straight channel, back to the exit of the last unit cell. Using the inlet bubble and slug lengths, Eqs. (3.4.13) and (3.4.14) are applied to determine the bubble volume and gas velocitiy at the exit of the geometry. After the subsequent determination of L_s, L_b, and $f_{straight}$, the pressure at the outlet of the serpentine can be found:

$$P_{serp,out} = P_{out} + \int_0^{L_{outlet}} \frac{L_S}{(L_S + L_b)} \frac{\rho_L (U_L + U_G)^2}{2d} f_{straight}\, dx \tag{3.4.20}$$

With the inlet and outlet pressures of the serpentine unit cells known, the pressure drop predicted by Eq. (3.4.12) can be assessed for different values of r_c and expressions for f.

The pressure drop estimates obtained through the direct application of Eq. (3.4.4) are shown in Figs. 3.15 and 3.16, where f_S was determined from Eqs. (3.3.5) and (3.3.6) for r_c = 3 mm and r_c = 6 mm, respectively. The predicted pressure drop was significantly higher than that observed experimentally for both geometries, especially in the bubbly flow regime

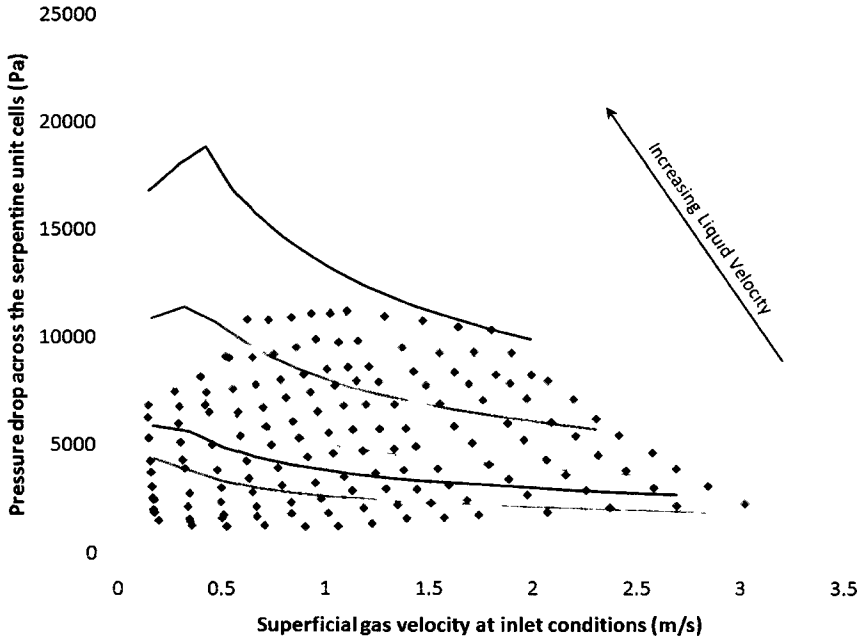

Figure 3.15 Predicted pressure drop obtained using Eq. (3.4.4) with $a_1 = 0.17$ for $r_c = 3$ mm.

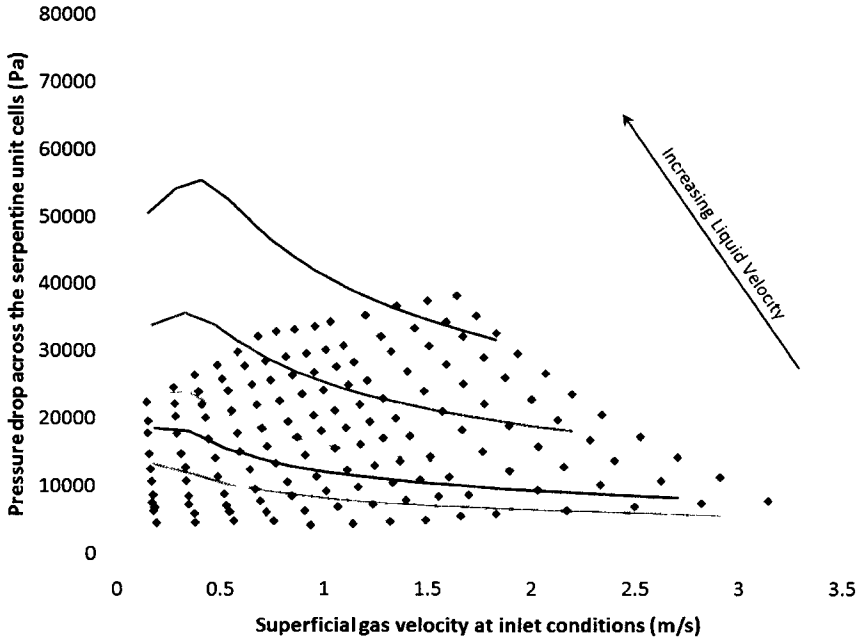

Figure 3.16 Predicted pressure drop obtained using Eq. (3.4.4) with $a_1 = 0.17$ for $r_c = 6$ mm.

where Laplacian contributions are less than predicted by Eq. (3.4.4) for idealized Taylor flow.

As discussed in Chapter 2, the serpentine geometry can have a significant effect on the flow pattern distribution: causing bubble grouping and coalescence, separation of the bubble film from the channel wall, and deformation and breakup of the leading and trailing interfaces. While Eqs. (3.3.5) and (3.3.6) account for the increased frictional pressure losses due to secondary flow formation in single phase flow, the vortices structures in two phase flow can vary significantly due to confinement of the liquid slug by the two bubbles. Separation of the bubble film from the channel wall creates liquid regions with decreased secondary flows and reduces the length of the liquid slugs, both of which contribute to a reduction in f. Meanwhile, deformation and breakup of the interface can notably effect the Laplacian contributions to pressure drop within a single unit cell. For the purpose of correlating the pressure drop in the serpentine channel, an additional multiplier, c_1, was introduced for as a method of accounting for the serpentine-induced flow pattern transitions.

$$f = f_S + c_1 a_1 \frac{64}{\mathrm{Re}_{LG}} \frac{d}{L_S} \left(\frac{\mathrm{Re}_{LG}}{Ca_{LG}} \right)^{1/3} \tag{3.4.21}$$

At each of the operating conditions tested, the value of c_1 which equated the predicted and experimentally observed pressure drops was determined. Including bubbly flow, five operating regions were identified (Fig. 3.17) based on the flow pattern present and the dependence of c_1/L_C on U_G/U_L and $We_{LG}L_C$, where $L_C = 0.5d / r_c$ is the dimensionless characteristic length parameter of the serpentine geometry. For the bubbly flow regime, c_1/L_C was a linear function of the gas holdup, We_{LG} and L_C.

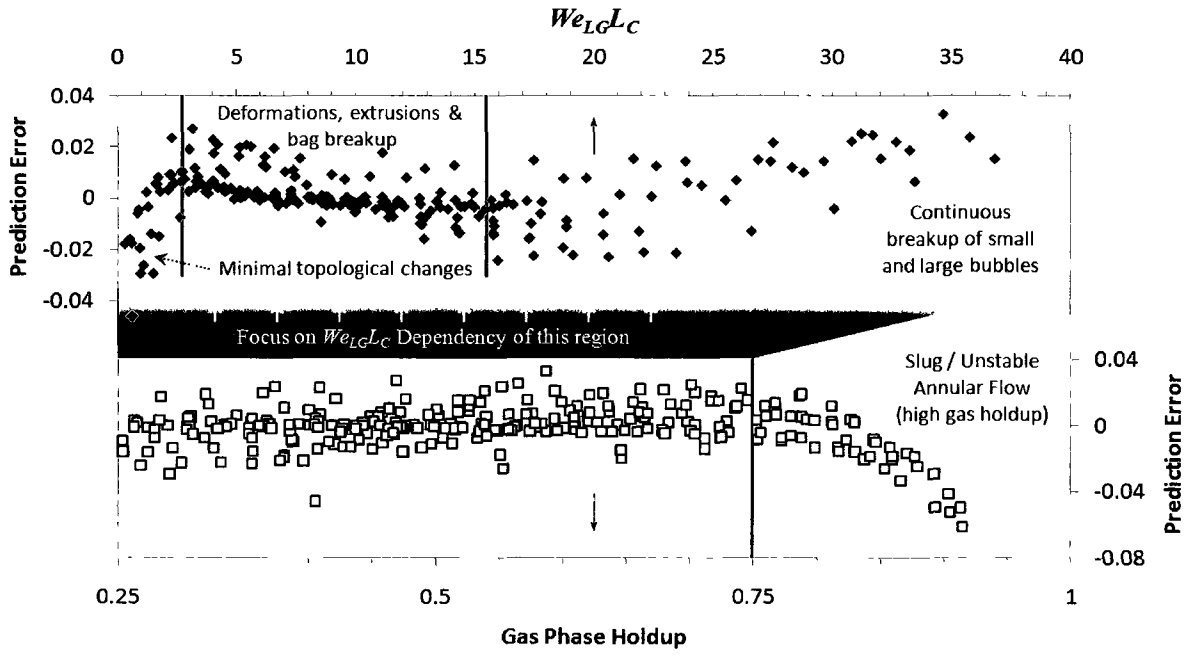

Figure 3.17 Four regimes of plug/slug flow in serpentine channels, identified by the variation in error associated to pressure drop predictions made using a single set of C_A through C_E to fit all of the experimental data.

$$\frac{c_1}{L_C} = -1.07761 - 0.65941\varepsilon_G - 0.0044We_{LG} + 2.4628L_C \tag{3.4.22}$$

A generalized expression was used to correlate the remaining four regimes, Eq. (3.4.23), where each regime was distinguished by a sudden change in the trend of prediction errors obtained from fitting all of the experimental data with a single set of parameters (Fig. 3.17).

$$\begin{aligned}\log(c_1 L_C) = C_A + C_B \log(\varepsilon_G) + C_C \log(We_{LG} L_C) \\ + C_D \log(\varepsilon_G)\log(We_{LG} L_C) + C_E \log(L_C)\end{aligned} \tag{3.4.23}$$

The boundaries and fitted parameters, C_A through C_E, are given in Table 3.1 for the entire data set and individual regimes.

Table 3.1 Fitted parameters and boundary conditions for each of the four regimes identified for plug/unstable plug/slug flow.

Regime	$We_{LG}L_C$	ε_G	C_A	C_B	C_C	C_D	C_E	# of c_1 values
Fit to all Data (regime identification)	N/A	N/A	-0 5739	1 1314	0 37971	0 39583	0 50951	272
Minimal topological changes	< 2 7		-0 1502	1 0283	0 21014	1 54363	0 87277	27
Deformations, extrusions & bag breakup	> 2 7, < 15 5	< 0 75	-0 5988	2 1332	0 24771	-0 7670	0 38947	141
Continuous breakup of small and large bubbles	> 15		-0 4550	0 2249	0 25343	0 75203	0 58746	58
Slug / unstable annular flow, high ε_G	N/A	> 0 75	-0 7081	1 4636	0 48082	0 97814	0 36673	46

The five flow regimes (bubbly flow, and the four regimes identified in Fig. 3.17 and Table 3.1) are separated by either critical values of $We_{LG}L_C$, or a predominance of one phase over the other. For bubbly flow, the liquid phase holdup is typically quite high, with the serpentine shape having the greatest effect on c_1. In contrast, the slug/unstable annular flow regime occurred for gas holdups exceeding 0.75, where the presence of multiple interfaces and shorter bubble lengths resulted in values of c_1 between 1 and 2.5. Although the three regimes dependent on $We_{LG}L_C$ were identified from trend deviations in the prediction error resulting from the use of parameters fitted to all of the experimental data, the boundary values correspond to changes in the extent of deformation and breakup within the serpentine geometry (see Fig. 2.15 in Chapter 2).

For $We_{LG}L_C < 2.7$, only mild deformations and wave instabilities were observed on the leading and trailing edges of the bubble as it traveled through the serpentine. Under these conditions, c_1 was primarily dependent on the gas phase holdup, ranged from 0.1 to 0.85 as

the gas holdup increased from 0.25 to 0.7. For $2.7 < We_{LG}L_C < 15.5$, bubbles undergo increasingly severe deformations, eventually leading to breakup at $We_{LG}L_C \sim 10$. While small satellites are broken off from extruded regions of bubbles between $We_{LG}L_C$ =10 and 15, they are typically not large enough in size to significantly affect Laplacian contributions and the flow patterns within the liquid slugs. It is not until $We_{LG}L_C \sim 15$ that a continuous string of breakup and sizeable bubble formation is observed, at which point the value of c_1 is increasingly dependent on the serpentine geometry, relative lengths of the bubble and slug, and secondary flow strength within the liquid phase.

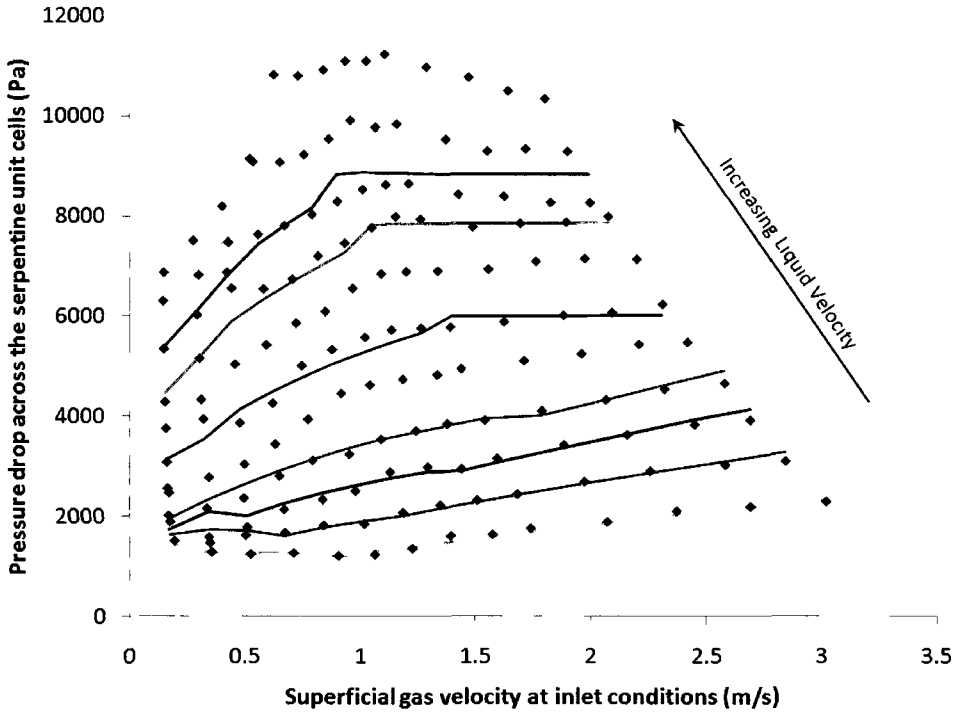

Figure 3.18 Predicted pressure drop obtained for r_c = 3 mm using Eq. (3.4.12), a_1 = 0.17, and c_1 determined from Eqs. (3.4.22) and (3.4.23).

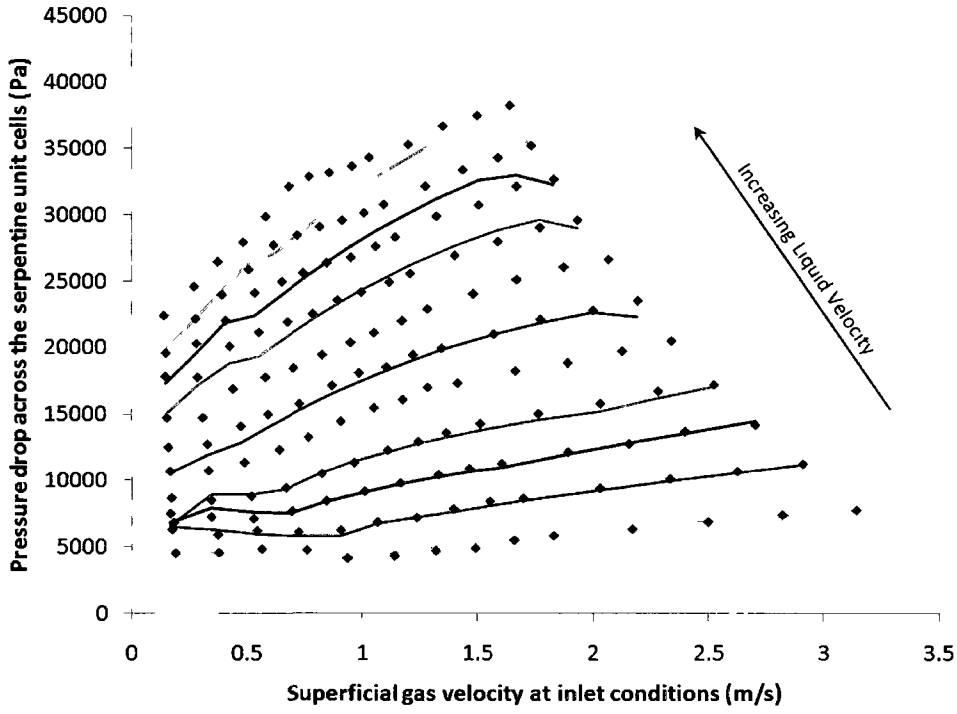

Figure 3.19 Predicted pressure drop obtained for r_c = 6 mm using Eq. (3.4.12), a_1 = 0.17, and c_1 determined from Eqs. (3.4.22) and (3.4.23).

The pressure drops predicted by Eq. (3.4.12) agreed well with experimental values (Figs. 3.18 and 3.19) when Eqs. (3.4.23) and (3.4.22) were used for the plug/unstable-plug/slug flow regime and bubbly flow regime, respectively.

Due to the highly empirical nature of the methodology applied to predict pressure drop within the serpentine channel, generalization of Eqs. (3.4.22) and (3.4.23) beyond the scope of this work may be limited. Assuming that experimental error associated with flow control and pressure drop measurements were negligible, the elimination of inlet and outlet contributions using the correlation proposed in section 3.4.3 and the variability in bubble and slug lengths generated by the cross-flow T-junction makes Eqs. (3.4.22) and (3.4.23) highly geometry-dependent. Although the L_b/d and L_S/d generated within the r_c = 3mm, N_{UC} = 3.5

and r_c = 6mm, N_{UC} = 4.5 were shown to be similar (section 3.4.2), the c_1 values are inevitably affected by the bubble and slug length variability which can differ significantly for other contactor configurations.

Combined with previous work on flow pattern transitions within the serpentine channel (Chapter 2), the boundaries for the different pressure drop regimes further justifies the use of $We_{LG}L_C$ to characterize the interaction between the bubble interface and curvature induced secondary flows. However, as neither the channel diameter nor process fluids have been significantly varied over the course of this work, it is possible that the selected dimensionless parameters and resulting c_1 values may not fully account for their effects on the flow behavior within the serpentine geometry.

3.5 Conclusions

In this work, curvature-induced variations in pressure drop were studied for water and air/water flow in d = 1 mm circular serpentine mini-channels with r_c = 3 mm and 6 mm, operating at $350 < \mathrm{Re}_L < 3900$ and $500 < \mathrm{Re}_{LG} < 7200$.

Single phase experiments carried out in straight and serpentine geometries provided the friction factors for a two-phase separated flow model. In the straight channel, the pressure drop was well defined by laminar theory ($f = 64/Re_L$) up to Re_L = 2300, at which point Eq. (3.3.2) was used to describe the transitional regime to turbulence. The friction factor within the serpentine unit cell was consistent for the three geometries with r_c = 3 mm and variable N_{UC}, decreasing slightly as r_c was increased to 6 mm. The magnitude and behavior of the serpentine friction factors for both values of r_c was accurately correlated using a simple power model, with values between that of a straight channel and that of fully developed flow in a helical coil with equivalent r_c.

The two-phase pressure drop model proposed by Kreutzer *et al.* (2005a) for straight channels and $We_{LG} \sim O(1)$ was extended to increasing values of We_{LG} through the use of the b_1 multiplier. When bubbly flow was present, the Laplacian pressure term in Eq. 3.4.4 was consistently reduced by 90%, but could not be ignored for the current channel dimensions and operating conditions. In plug, unstable plug, slug and unstable annular flow, b_1 typically increased with gas holdup and We_{LG}, but remained less than 1 for $We_{LG} < 10$.

A similar approach was taken for the prediction of multi-phase flow in the serpentine geometry, resulting in the identification of five regions of pressure drop behavior characterized by either a high volume fraction of one phase, or critical values of 2.7 and 15.5 for $We_{LG}L_C$. These values correspond to flow transition boundaries between different extents of bubble deformation and breakup within the serpentine, where: minimal deformation was observed for $We_{LG}L_C < 2.7$; continuous breakup and large satellite bubble formation was observed for $We_{LG}L_C > 15.5$; and intermediate values corresponded to conditions of moderate deformation and breakup of the bubble cap, where any satellite bubbles forming have a minimal effect on circulation within the liquid slug and negligible pressure drops. Empirical correlations for f in each region were developed and discussed, followed by estimates of the pressure drop across the $r_c = 3$ mm, $N_{UC} = 3.5$ and $r_c = 6$ mm, $N_{UC} = 4.5$ geometries.

Although generalization of the reported values for the fitted parameters in Eq. (3.4.23) is limited, identification of five regions for pressure drop behavior in the serpentine geometry could have important implications to mini-scale multi-phase application design. The interaction between pressure drop and flow pattern transitions within the serpentine unit cell will be similar for geometries with comparable geometric configurations and process fluids.

Acknowledgements

One of the authors (A.A. Donaldson) would like to acknowledge the support of the National Research Council of Canada (NRC) and the Natural Sciences and Engineering Research Council of Canada (NSERC).

Nomenclature

a_1	Empirical constant for Eq. (3.4.4)
b_1	Laplacian multiplier for two-phase flow in a straight channel
$C_{A,B,C,D,E}$	Empirical constants for Eq. (3.4.23)
Ca_b	Bubble capillary number
Ca_{G,μ_L}	Modified gas phase capillary number
Ca_L	Liquid phase capillary number
Ca_{LG}	Combined phase capillary number
c_1	Laplacian multipler for two-phase flow in a serpentine channel
d	Diameter [m]
De	Dean number
f	Friction factor
$f_{helical}$	Single phase friction factor in a helical coil
f_S	Single phase friction factor
f_{serp}	Single phase friction factor in the serpentine
$f_{serp,3mm}$	Single phase friction factor in the r_c = 3 mm serpentine
$f_{serp,6mm}$	Single phase friction factor in the r_c = 6 mm serpentine

$f_{straight}$	Single phase friction factor in the straight channel
L_b	Current bubble length [m]
$L_{b,in}$	Bubble length initially generated by the cross-flow T-junction [m]
L_C	Dimensionless characteristic length for curved geometries
$L_{Channel}$	Total length of the channel (straight geometry) [m]
L_{inlet}	Length of the straight inlet section [m]
L_{outlet}	Length of the straight outlet section [m]
L_S	Current slug length [m]
$L_{S,in}$	Slug length initially generated by the cross-flow T-junction [m]
N_{UC}	Number of repeating serpentine unit cells in series
ΔP	Differential pressure [Pa]
P_t	Absolute pressure at the current point in the geometry [Pa]
P_{in}	Absolute pressure at the inlet of the geometry [Pa]
P_{out}	Absolute pressure at the outlet of the geometry [Pa]
$P_{serp,in}$	Absolute pressure at the inlet of the first serpentine unit cell [Pa]
$P_{serp,out}$	Absolute pressure at the outlet of the last serpentine unit cell [Pa]
r_c	Radius of curvature of the serpentine [m]
Re_L	Liquid phase Reynolds number
Re_{LG}	Combined phase Reynolds number
U_b	Bubble velocity [m s^{-1}]
U_G	Superficial gas velocity [m s^{-1}]
U_L	Superficial liquid velocity [m s^{-1}]
V_b	Current bubble volume [m^3]

$V_{b,in}$ Bubble volume at the geometry inlet [m^3]

V_{cap} Current volume of the liquid surrounding the hemi-spherical caps [m^3]

V_{film} Current bubble film volume [m^3]

We_{LG} Combined phase Weber number

δ Bubble film thickness [m]

ε_G Gas phase holdup

μ_L Current bubble volume [kg m^{-1} s^{-1}]

ρ_L Liquid phase density [kg m^{-3}]

σ Surface tension [N m^{-1}]

References

Angeli, P., and Gavriilidis, A., 2008. Hydrodynamics of taylor flow in small channels: a review. Proc. IMechE Vol. 222 Part C: J. Mech. Eng. Sci., 737-751.

Aussilous, P. and Quéré, D., 2000. Quick deposition of a fluid on the wall of a tube. Phys. Fluids 12(10), 2367-2371.

Balasubramaniam, R., Rame, E., Kizito, J., Kassemi, M., 2006. Two phase flow modeling: Summary of flow regimes and pressure drop correlations in reduced and partial gravity. NASA/CRV-2006-214085.

Bretherton, F.P., 1961. The motion of long bubbles in tubes. J. of Fluid Mech. 10,166 –168.

Fries, D.M. and von Rohr, P.R., 2009. Liquid mixing in gas-liquid two-phase flow by meandering microchannels. Chem. Eng. Sci. 64, 1326-1335.

Huh, C., Kim, J., Kim, M.H., 2007. Flow pattern transition instability during flow boiling in a single microchannel. Int. J. Of Heat and Mass Trans. 50, 1049-1060.

Idelchik, I.E., 1986. Handbook of Hydraulic Resistance, 2nd ed.; Hemisphere: New York, p 640.

Kawahara, A., Chung, P.Y., and Kawaji, M., 2002. Investigation of two-phase flow pattern void fraction and pressure drop in a microchannel. Int. J. Multiphase Flow 28 (9), 1411-1435.

Kirpalani, D.M., Patel, T., Mehrani, P., Macchi, A., 2008. Experimental analysis of the unit cell approach for two-phase flow dynamics in curved flow channels. Int. J. Of Heat and Mass Trans. 51, 1095-1103.

Kreutzer, M.T., Kapteijn, F.,Moulijn, J.A., Kleijn, C.R., and Heiszwolf, J.J., 2005a. Inertial and interfacial effects on pressure drop of Taylor flow in capillaries. AIChE J. 105, 667–672.

Kreutzer, M., Kapteijn, F., Moulijn, J., Heiszwolf, J.J., 2005b. Multiphase monolith reactors: Chemical reaction engineering of segmented flow in microchannels. Chemical Engineering Science 60 (22), 5895–5916.

Kulkarni, A.A., and Kalyani, V.S., 2009. Two-phase flow in minichannels: hydrodynamics, pressure drop, and residence time distribution. Ind. Eng. Chem. Res. 48, 8193-8204.

Liu, H., Vandu, C. O., and Krishna, R, 2005. Hydrodynamics of Taylor flow in vertical capillaries: flow regimes, bubble rise velocity, liquid slug length and pressure drop. Ind. Eng. Chem. Res. 44, 4884–4897.

Martin, J., Oshkai, P., Djilali, N., 2005. Flow structures in a U-shaped fuel cell flow channel: quantitative visualization using particle image velocimetry. J. Of Fuel Cell Sci. and Tech. 2, 70-80.

Mishra, P., and Gupta, S.N., 1979. Momentum transfer in curved pipes, 1: Newtonian fluids; 2: Non-Newtonian fluids. Ind. Eng. Chem. Process Des. Dev., 18, 130-142.

Triplett, K.A., Ghiaasiaan, S.M., Adbel-Khalik, S.I., LeMouel, A., and McCord, B.N. 1999. Gas–liquid two-phase flow in microchannels. Part II: void fraction and pressure drop. Int. J. Multiphase Flow 25, 395–410.

Tung, K-Y, Li, C-C, Yang, J-T, 2009. Mixing and hydrodynamic analysis of a droplet in a planar serpentine micromixer. Microfluid Nanofluid 7, 545-557.

Wang, C., Chen, I.Y., Yang, Y., and Chang, Y., 2003. Two-phase flow pattern in small diameter tubes with the presence of horizontal return bend. Int. J. Heat Mass Transfer 46, 2975–2981.

Wang, C., Chen, I.Y., Yang, Y., Chang, Y., and Hu, R., 2004. Influence of horizontal return bend on the two-phase flow pattern in small diameter tubes. Exp. Therm. Fluid Sci. 28, 145–152.

Wang, C., Chen, I.Y., and Huang, P., 2005. Two-phase slug flow across small diameter tubes with the presence of vertical return bend. Int. J. Heat Mass Transfer 48, 2342–2346.

Xiong, R., Chung, J.N., 2007. Flow characteristics of water in straight and serpentine micro-channels with miter bends. Exp. Therm. And Fluid Sci. 31, 805-812.

Xu, J.H., Li, S.W., Tan, J., and Luo, G.S., 2008. Correlations of droplet formation in T-junction microfluidic devices: from squeezing to dripping. Microfluid Nanofluid 5, 711-717.

Chapter 4

Numerical simulation of inter-phase mass transfer for idealized Taylor flow:

A comparison of numerical frameworks and the effects of cap deformation in elevated shear

A.A. Donaldson [1,2], A. Macchi [2*], D.M. Kirpalani [1]

1 Institute for Chemical Process and Environmental Technology
National Research Council Canada
M-12, 1200 Montreal Road
Ottawa, Ontario, K1A 0R6, Canada

2 Dept. of Chemical and Biological Engineering
University of Ottawa
161 Louis Pasteur Street
Ottawa, Ontario, K1N 6N5, Canada

* Corresponding author: Arturo Macchi, Tel: +1 (613) 562-5800 x6939,
e-mail: Arturo.macchi@uottawa.ca

Abstract

Four numerical frameworks are derived to investigate the impact of underlying assumptions on the predicted mass transfer between a Taylor bubble and liquid slug in circular capillaries. The separate influences of bubble velocity and film length, slug length, and bubble film thickness on k_La were compared to empirical predictions by Bercic & Pintar (1997) and CFD simulations by van Baten & Krishna (2004). Reasonable agreement was obtained using the Slug Film model, which accounted for diffusion-limited mass transfer between the slug film and circulating bulk without the need for an iterative numerical solution. Subsequent investigation of the relative contributions of film and mass transport for industrially relevant conditions suggest that both mechanisms need to be accounted for during the prediction of k_La.

With the importance of mass transfer through the bubble cap confirmed, conservative estimates were obtained for the enhancement of $k_{L,cap}a_{cap}$ due to curvature-induced secondary flow and cap deformation in a planar serpentine passive mixing arrangement. A 2 to 7% increase in mass transfer was predicted using the Slug Film model; however, experimental values are expected to be significantly higher in actual applications where the contact time between a liquid packet and bubble surface will be shorter than assumed by this analysis.

Keywords: Taylor flow, mass transfer coefficient, film, cap, bubble deformation, serpentine.

4.1 Introduction

Monolith reactors and capillary micro-reactors continue to receive attention from both industry and academia due to their low pressure drop, high mass transfer rates and ease of scale-up when compared to conventional reactor technology (Edvinsson & Cybulski 1995; Nijhuis *et al.* 2001; Stankiewicz 2001; Kreutzer 2003; Shao *et al.* 2010). Commonly considered for heat and mass transfer limited reactions such as hydrogenations (Edvinsson & Cybulski 1995; Edvinsson *et al.* 1995; Nijhuis *et al.* 2003), hydrodesulphurization (Irandoust & Gahne 1990), oxidations (Klinghoffer *et al.* 1998) and Fischer-Tropsch synthesis (de Deugd *et al.* 2003a,b), the monolith reactor's performance is highly dependent on the liquid-phase mass transfer coefficient, $k_L a$. Accurate predictions of this value are instrumental to the design and optimization of these systems.

The Taylor flow pattern illustrated in Fig. 4.1 is frequently observed in mini and micro-scale two-phase flow, consisting of alternating gas bubbles and liquid slugs flowing concurrently along a capillary length. While a multitude of numerical frameworks and empirical correlations are available in literature to describe mass transfer between the bubble, bubble film, liquid slug bulk and liquid slug film for both reacting and non-reacting systems (Irandoust & Andersson 1988; Irandoust *et al.* 1992; Bercic & Pintar 1997; van Baten & Krishna 2004; Vandu *et al.* 2005; Nedeltchev *et al.* 2007; Zheng *et al.* 2007; Pohorecki 2007); there continues to be a broad range of assumptions applied in the regression of mass transfer data making it difficult to compare results from different sources of literature. One parameter which is of significant interest in these studies is the relative magnitude of film and cap mass transport, which dictates the efficacy of passive mixing arrangements as a method of improving inter-phase mass transfer through the introduction of secondary flows

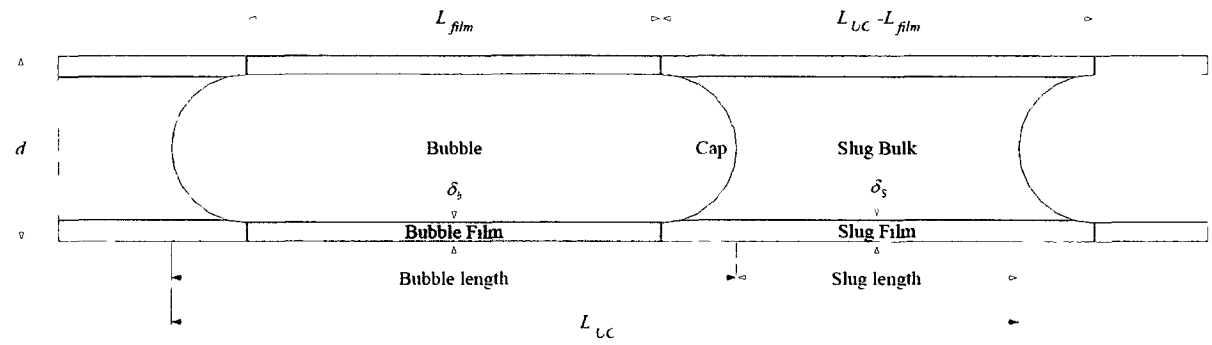

Figure 4.1 Schematic of idealized Taylor flow, where shaded regions represent the liquid phase. For a moving frame of reference, the velocity at the capillary wall is set to $-U_b$, corresponding to movement from left to right.

and redistribution of the film and cap area via bubble breakup (Kirpalani *et al.* 2008; Fries & van Rohr 2009). If film transport is the dominant mechanism of mass transfer, then the cap deformation and secondary flows observed in many passive mixing arrangements would have a minimal impact on the overall k_La.

This work explores the effects of different simplifying assumptions on the predicted behavior of the volumetric gas-liquid mass transfer coefficient and the ratio of film to cap mass transfer for idealized Taylor flow. The resulting numerical frameworks are used to investigate the dependency of k_La on the characteristic parameters of Taylor flow, while determining the conditions under which film or cap mass transfer can reasonably be neglected. A brief analysis of the potential mass transfer implications of bubble deformation due to curvature-induced secondary flow is discussed for a planar serpentine mixer configuration to determine its suitability for enhancing mass transport in mini and micro-scale reactors.

4.2 Homogeneous mixture model for idealized Taylor flow

Inter-phase mass transfer in Taylor flow involves complex interactions between a bubble's surface, the lubricating liquid film, and internal circulation within the liquid slug. Homogeneous mixture models attempt to simplify these interactions into a single term, $k_L a(1-C_S)$, where C_S is the dimensionless cup-mixed average concentration within the liquid normalized against the saturation concentration of the gas phase within the liquid, and $k_L a$ is a weighted mass transfer term accounting for the different mass transfer mechanisms and specific surface area per unit cell volume. An example of one such model is that proposed by van Baten & Krishna (2004) and applied by Vandu *et al.* (2005) for gas-liquid mass transfer in square and circular capillaries.

$$k_L a = k_{L,cap} a_{cap} + k_{L,film} a_{film} \tag{4.2.1}$$

The specific cap and film area per unit cell volume, a_{cap} and a_{film}, are determined based on the assumption of spherical caps for the leading and trailing bubble surfaces and a negligible film thickness relative to the bubble radius:

$$a_{cap} = \frac{A_{cap}}{V_{UC}} = \frac{\pi d^2}{0.25\pi d^2 L_{UC}} = \frac{4}{L_{UC}} \tag{4.2.2}$$

$$a_{film} = \frac{A_{film}}{V_{UC}} = \frac{\pi d L_{film}}{0.25\pi d^2 L_{UC}} = \frac{4}{d}\frac{L_{film}}{L_{UC}} \tag{4.2.3}$$

The cap mass transfer coefficient can be determined from the Higbie penetration model provided the gas diffusivity within the liquid, D, is known and a reasonable approximation can be obtained for the contact time of a liquid packet travelling across the cap of a bubble, $t_{C,cap}$.

$$k_{L,cap} = 2\sqrt{\frac{D}{\pi t_{C,cap}}} \tag{4.2.4}$$

In their work, van Baten & Krishna (2004) assumed a contact length equivalent to half the bubble circumference and a packet velocity equivalent to the bubble velocity, U_b, thus yielding an estimate for $k_{L,cap}$:

$$k_{L,cap} = \frac{2\sqrt{2}}{\pi}\sqrt{\frac{DU_b}{d}} \tag{4.2.5}$$

A contact length equivalent to $0.5\pi d$ is likely an overestimate considering a liquid packet will travel from the nose of the cap to the film (or vice versa), corresponding to only 1/4th of the bubble's circumference or $0.25\pi d$. A packet velocity of U_b may also be an overestimate, and can be replaced by the liquid velocity at the centerline of the slug predicted by Thulasidas *et al.* (1997):

$$U_{centerline} = 2(U_L + U_G) - U_b \tag{4.2.6}$$

Though $U_{centerline}$ and U_b are approximately equal at low capillary numbers, there can be a significant discrepancy as $Ca_{LG} = \mu(U_L + U_G)/\sigma$ increases.

Applying the shorter contact length and the centerline velocity results in an alternative expression for $k_{L,cap}$:

$$k_{L,cap} = \frac{4}{\pi}\sqrt{\frac{D[2(U_L + U_G) - U_b]}{d}} \tag{4.2.7}$$

The film mass transfer coefficient can also be determined directly from the Higbie penetration model, using L_{film} as the contact length and U_b as the packet velocity:

$$k_{L,film} = 2\sqrt{\frac{DU_b}{\pi L_{film}}} \tag{4.2.8}$$

While this approach is simple to apply, its validity starts to decrease with longer contact times when interactions between the liquid packet and the film bulk can no longer be neglected. Mass transport theory for laminar falling films is thus applied in determining

$k_{L,film}$. Based on Pigford's work on transient mass transfer for laminar falling films (summarized in Sherwood *et al.* 1975), and Thulasidas *et al.*'s (1995) characterization of bubble-train flow in capillaries; the mass transfer coefficient can be evaluated for both short and long contact times as:

$$k_{L,film} = \begin{cases} 2\sqrt{\dfrac{D}{\pi t_{C,film}}}\dfrac{\ln(1/\Delta)}{(1-\Delta)} & for \quad Fo < 0.1 \\ 3.41\dfrac{D}{\delta_b} & for \quad Fo > 1.0 \end{cases} \tag{4.2.9}$$

Where $\Delta = 0.7857\exp(-5.212Fo) + 0.1001\exp(-39.21Fo) + 0.0360\exp(-105.6Fo) + ...$

The Fourier number, $Fo = Dt_{C,film}/\delta_b^2$, acts as an indicator of the contact time between the bubble and film. Values of $Fo < 0.1$ correspond to short contact times, while values of $Fo > 1$ correspond to long contact times where the film approaches saturation. The film contact time can be approximated as $t_{C,film} = L_{film}/U_b$, while the thickness of the bubble film, δ_b, can be determined from the correlation of Aussilous & Quéré (2000) for $10^{-3} < Ca_b = \mu U_b/\sigma < 1.4$:

$$\frac{2\delta_b}{d} = \frac{1.34Ca_b^{2/3}}{1+3.34Ca_b^{2/3}} \tag{4.2.10}$$

Note that many of these correlations require knowledge of the bubble velocity, U_b, before either $k_{L,cap}$ or $k_{L,film}$ can be determined. For the remainder of this analysis, the bubble velocity is approximated using the correlation proposed by Liu *et al.* (2005):

$$U_b = \frac{U_L + U_G}{1-0.61Ca_{LG}^{0.33}} \tag{4.2.11}$$

Combining Eqs. (4.2.1) through (4.2.11) produces a homogeneous mixture model theoretically capable of describing the effects of L_{film}, L_{UC}, Ca_{LG}, D and d on inter-phase

mass transfer. In addition to providing estimates for k_La, the relative contributions of film and cap mass transfer can be assessed, thereby identifying the dominant mass transfer mechanism and the potential effects of flow pattern modifications on overall mass transport.

There are a number of key limitations to this approach which must be considered during application. Since the average liquid phase concentration is used to determine the driving force for mass transfer, concentration polarization near the interface is unaccounted for, potentially resulting in overestimates of mass transport. Likewise, the use of the unit cell volume when determining a_{cap} and a_{film} requires division of the resulting k_La by the liquid phase holdup, $1-\varepsilon_G$, when approximating the change in concentration within the liquid phase:

$$\frac{dC_S}{dt} = \frac{k_{L,cap}a_{cap} + k_{L,film}a_{film}}{1-\varepsilon_G}\left(1-C_S\right) \tag{4.2.12}$$

4.3 Numerical simulation of inter-phase mass transfer

A diverse collection of numerical frameworks and assumptions appear in previous literature for predicting inter-phase mass transfer in idealized Taylor flow (Irandoust & Andersson 1988; Irandoust *et al.* 1992; Bercic & Pintar 1997; van Baten & Krishna 2004; Vandu *et al.* 2005; Nedeltchev *et al.* 2007; Zheng *et al.* 2007; Pohorecki 2007). The complexity of each approach has ranged from simple homogeneous mixture models to detailed computational fluid dynamic (CFD) simulations, all with the intent of quantifying the effects of bubble and slug length, velocity, channel diameter and fluid properties on mass transfer. The range of assumptions applied in each of these studies has led to inconsistencies in the reported dependence of mass transfer on the aforementioned parameters, as well as the

relative importance of transfer across the bubble film and cap. A systematic analysis of the impact of common assumptions on mass transfer predictions would provide a basis for comparing previous literature, and a guideline for the minimum numerical complexity required to capture the mass transfer dynamics in two-phase flow.

The following three models represent numerical frameworks with levels of complexity between the two extremes: the homogeneous mixture model and full CFD implementation. The first model, referred to as the perfectly mixed model, assumes that the entire liquid slug is perfectly mixed and the liquid film from the preceding bubble circulates into the body of the slug. The second model, referred to as the slug film model, assumes that a film surrounds the perfectly mixed liquid slug, whereby mass transfer between this film and the bulk is diffusion limited. The final model, the circulating slug model, partitions the liquid slug into 7 regions. The regions near the bubble cap are assumed to be perfectly mixed, while scalar transport equations are solved for the remaining regions based on the analytical solution proposed by Thulasidas *et al.* (1997) for the velocity profile in a liquid slug.

4.3.1 Perfectly mixed model

Similar to the homogeneous mixture models, the perfectly mixed model operates under the assumption that a single concentration can be used for the liquid slug. As such, it is reflective of very long liquid slugs, where the dissolved species in the concentrated film has time to fully diffuse into the slug bulk. Figure 4.2 illustrates the region over which a mass balance is performed to derive the numerical model.

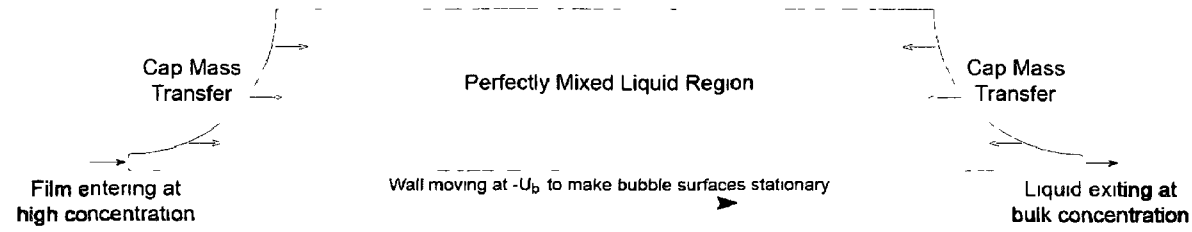

Figure 4.2 Liquid flow region used in the derivation of the perfectly mixed model.

As with most numerical simulations of Taylor flow, stationary interfaces are obtained by applying a moving frame of reference with a velocity equivalent to U_b. Defining the bulk concentration as C_S, and the film concentration entering the mixed region, C_{film}, the mass balance over the liquid slug is expressed as:

$$V_{slug}\frac{dC_S}{dt} = k_{L,cap}A_{cap}(1-C_S)+(C_S-C_{film})Q_{film,ref} \tag{4.3.1}$$

Note that in the derivation of the mass balance and subsequent equations, flow from left to right has a negative sign. The liquid slug volume and cap area can be determined once the thickness of the bubble film is calculated from Eq. (4.2.10):

$$V_{slug} = \pi d^2(L_{UC}-L_{film})-\pi(d-2\delta_b)^3/6 \tag{4.3.2}$$

$$A_{cap} = \pi(d-2\delta_b)^2 \tag{4.3.3}$$

The volumetric flow rate of the bubble film is approximated from a mass balance across two channel cross-sections: one within the bubble, and the other within the liquid slug. Using the relations of Thulasidas *et al.* (2005), Q_{film} is calculated as:

$$Q_{film} = \frac{\pi}{4}\left\{(U_L+U_G)d^2-U_b(d-2\delta_b)^2\right\} \tag{4.3.4}$$

Correcting for the moving frame of reference, the volumetric flow rate of the film used in the perfectly mixed model is determined:

$$Q_{film,ref} = \frac{\pi d^2}{4}\{(U_L + U_G) - U_b\} \tag{4.3.5}$$

With V_{slug}, A_{cap} and $Q_{film,ref}$ known, the only parameters remaining are C_{film} and $k_{L,cap}$, with the latter approximated from Eq. (4.2.7).

Determination of a reasonable value for C_{film} is non-trivial due to the time dependence of the bulk concentration entering the bubble film and the non-uniform radial velocity profile within the film. The concentration exiting the liquid film at the current time, t, is the result of mass transfer to liquid entering the bubble film at time, $t - t_{C,film}$, with a concentration of $C_{film\ in}$. For the purpose of maintaining computational simplicity for the perfectly mixed model, a minimal variation in C_S was assumed over an elapsed time of $t_{C,film}$ ($C_{film\ in} = C_S$), and the Higbie penetration theory from the homogeneous mixture model was applied to determine the flux into the bubble film. When determining $k_{L,film}$ from Eq. (4.2.9), the value of $t_{C,film}$ must be corrected to account for the average velocity in the bubble film:

$$t_{C,film} = \frac{\pi}{4}\frac{\left(d^2 - (d-\delta_b)^2\right)L_{film}}{-Q_{film,ref}} = \frac{\left(1-(1-\delta_b/d)^2\right)}{U_b - (U_L + U_G)}L_{film} \tag{4.3.6}$$

Based on these assumptions, an analytical expression for C_{film} was derived:

$$C_{film} = 1 - (1 - C_S)\exp\left[\pi(d - 2\delta_b)\frac{k_{L,film}L_{film}}{Q_{film,ref}}\right] \tag{4.3.7}$$

Incorporating this expression into the overall mass balance for the mixed liquid region yields:

$$\frac{dC_S}{dt} = \left\{\frac{k_{L,cap}A_{cap}}{V_{slug}} + \frac{Q_{film,ref}}{V_{slug}}\left(\exp\left[\pi(d-2\delta_b)\frac{k_{L,film}L_{film}}{Q_{film,ref}}\right] - 1\right)\right\}(1 - C_S) \tag{4.3.8}$$

Note that the cap mass transfer term is unchanged from that of the homogeneous mixture model, while the film mass transport term is modified to account for the difference in

concentration driving force within the bubble film region. Subsequent determination of the analytical solution for C_S is trivial, and is given below for an initial value of $C_S = 0$.

$$\ln(1-C_S) = -\left\{\frac{k_{L,cap}A_{cap}}{V_{slug}} + \frac{Q_{film,ref}}{V_{slug}}\left(\exp\left[\pi(d-2\delta_b)\frac{k_{L,film}L_{film}}{Q_{film,ref}}\right]-1\right)\right\}t \qquad (4.3.9)$$

As shown in section 4.4, the perfectly mixed model provides a better approximation of mass transport to the bubble film, but the mass transfer driving force is still overestimated and the instantaneous mixing of the bubble film with the liquid slug ignores the time required for diffusion from the liquid film to the bulk of the slug. Regressions of experimental data using this model would fail to account for the effects of liquid slug length, and would consistently underestimate $k_{L,cap}$ and $k_{L,film}$ due to the overestimation of the driving force.

4.3.2 Slug film model

The slug film model is an extension of the perfectly mixed model, whereby the liquid slug is described as a perfectly mixed core surrounded by a thin film. This approach attempts to account for the effects of the liquid slug length while still avoiding the need for a iterative numerical solution. Figure 4.3 illustrates the regions over which mass balances are performed.

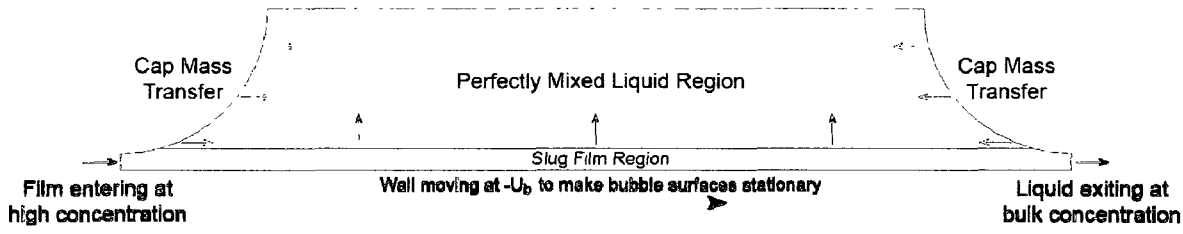

Figure 4.3 Liquid flow regions used in the derivation of the slug film model.

Liquid flowing from the bubble film no longer mixes with the circulating bulk of the liquid slug. Instead, it continues to travel into the slug film region where diffusive transport occurs with the slug bulk. Similar to the perfectly mixed model, there would be time delays associated to the concentrations entering and exiting the bubble and slug films. For computational simplicity, the variation in concentration within these time periods is assumed to be negligible. As a result, the concentration entering the slug film, $C_{S,film\ in}$, is assumed equal to the concentration leaving the bubble film, C_{film}. Likewise, the concentration entering the bubble film, $C_{film\ in}$, is assumed equal to the concentration leaving the slug film, $C_{S,film\ out}$.

Falling film theory is applied to both the bubble and slug films. The outlet concentration for the bubble film is easily obtained as in the perfectly mixed model.

$$C_{film} = 1 - \left(1 - C_{S,film\ out}\right)\exp\left[\pi\left(d - 2\delta_b\right)\frac{k_{L,film}L_{film}}{Q_{film,ref}}\right] \tag{4.3.10}$$

Where the contact time used in the determination of $k_{L,film}$ is that of Eq. (4.3.6). A similar solution can be obtained for $C_{S,film\ out}$, provided the slug bulk concentration, C_S, is assumed to remain fairly constant for the purpose of estimating the concentration driving force.

$$C_{S,film\ out} = C_S - \left(C_S - C_{film}\right)\exp\left[\pi\left(d - 2\delta_S\right)\frac{k_{L,slug\ film}\left(L_{UC} - L_{film}\right)}{Q_{film,ref}}\right] \tag{4.3.11}$$

Note that the length of the film is assumed equal to the slug length and the axial bubble cap lengths combined, or the difference between the unit cell length and bubble film length, $L_{UC} - L_{film}$.

The thickness of the film in the liquid slug, δ_S, is determined such that the flow rate in the film is equivalent to $Q_{film,ref}$. This is expressed in mathematical form as:

$$\int_{r=d/2-\delta_S}^{r=d/2} 2\pi U(r) r dr = Q_{film,ref} \tag{4.3.12}$$

Where $U(r)$ is the axial velocity at a radial distance, r, from the channel's center. Using the analytical solution for $U(r)$ proposed by Thulasidas *et al.* (1997), the value of δ_S which satisfies Eq. (4.3.12) is given by:

$$U(r) = 2(U_L + U_G)\left(1 - \frac{4r^2}{d^2}\right) - U_b \tag{4.3.13}$$

$$\delta_S = \frac{d}{2}\left(1 - \sqrt{2 - \frac{U_b}{U_L + U_G}}\right) \tag{4.3.14}$$

For the determination of $k_{L,slug\ film}$, the contact time is based on the slug film length and average velocity:

$$t_{C,slug\ film} = \frac{V_{slug\ film}}{-Q_{film,ref}} = \frac{\left(1-(1-\delta_S/d)^2\right)}{U_b - (U_L + U_G)}(L_{UC} - L_{film}) \tag{4.3.15}$$

Where $V_{slug\ film} = \pi/4\left(d^2 - (d-2\delta_S)^2\right)(L_{UC} - L_{film})$.

The overall mass balance for the perfectly mixed slug region requires an approximation of mass transport through the bubble caps and the boundary between the slug body and film. Mass transport through the bubble caps is determined from penetration theory, as was done in the homogeneous and perfectly mixed models. Mass transfer through the film is more difficult to estimate, as there are multiple concentration dependencies. One possible solution involves averaging the fluxes which would be necessary for the concentration drop predicted by Eq. (4.3.11) to occur.

$$\left(\frac{dC_S}{dt}\right)_{film\ transport} = (C_{film} - C_{S,film\ out})\frac{-Q_{film,ref}}{V_{slug} - V_{slug\ film}} \tag{4.3.16}$$

In order to express Eq. (4.3.16) solely as a function of C_S, C_{film} and $C_{S,film\ out}$ must be eliminated using Eqs. (4.3.10) and (4.3.11). Inter-substitution results in the following expressions:

$$C_{S,film\ out} = \frac{C_S(1-[B])+[B](1-[A])}{1-[B][A]} \tag{4.3.17}$$

$$C_{film} = \frac{(1-[A])+[A](1-[B])C_S}{1-[A][B]} \tag{4.3.18}$$

Where

$$[A] = \exp\left[\pi(d-2\delta_b)\frac{k_{L,film}L_{film}}{Q_{film,ref}}\right] \tag{4.3.19}$$

$$[B] = \exp\left[\pi(d-2\delta_S)\frac{k_{L,slug\ film}(L_{UC}-L_{film})}{Q_{film,ref}}\right] \tag{4.3.20}$$

Substituting into Eq. (4.3.16) yields the contribution of film mass transport to the temporal change of C_S:

$$\left(\frac{dC_S}{dt}\right)_{film\ transport} = (1-C_S)\frac{(1-[A])(1-[B])}{(1-[B][A])}\frac{-Q_{film,ref}}{V_{slug}-V_{slug\ film}} \tag{4.3.21}$$

The overall change in C_S with respect to time can subsequently be determined:

$$\frac{dC_S}{dt} = \left\{\frac{k_{L,cap}A_{cap}}{V_{slug}-V_{slug\ film}} - \left[\frac{(1-[A])(1-[B])}{1-[B][A]}\right]\frac{Q_{film,ref}}{V_{slug}-V_{slug\ film}}\right\}(1-C_S) \tag{4.3.22}$$

For which the analytical solution is given for an initial value of $C_S = 0$ (no dissolved gas):

$$\ln(1-C_S) = -\left\{\frac{k_{L,cap}A_{cap}}{V_{slug}-V_{slug\ film}} - \left[\frac{(1-[A])(1-[B])}{1-[B][A]}\right]\frac{Q_{film,ref}}{V_{slug}-V_{slug\ film}}\right\}t \tag{4.3.23}$$

The slug film model provides the ability to determine the effect of liquid slug length on film mass transfer, albeit with a number of assumptions regarding the temporal variation in concentrations over a timeframe comparable to the contact times, $t_{C,film}$ and $t_{C,slug\,film}$. The concentration driving force between the slug bulk and the film and cap regions is still over-estimated due to the perfectly mixed assumption for the slug bulk; however, it is closer to actual conditions than the perfectly mixed model. The slug film model represents one of the more comprehensive numerical frameworks for which a computationally simplistic analytical solution can be obtained. Subsequent elimination of assumptions necessitates the use of iterative solutions, eventually leading to full CFD simulations.

4.3.3 Circulating slug model

The circulating slug model is an intermediate step between highly simplified Taylor flow representations and full CFD simulations requiring the solution of the Navier-Stokes and convection-diffusion scalar transport equations. The model is designed based on analytical solutions for developed flow within the bubble film and liquid slug, and the use of perfectly mixed regions to transition between the fully developed flow patterns. While the proposed approach does avoid the Navier-Stokes equation, it still requires the numerical solution of scalar transport equations describing mass transport in the slug film and bulk, and bubble film.

Figure 4.4 illustrates the different regions of the idealized Taylor flow pattern, and the general discretization strategy used within each region. Three grid resolution parameters were utilized to ensure consistency between each of the regions: Number of radial cells within the film region, $N_{film,radial}$; number of radial cells within the slug bulk, $N_{bulk,radial}$; and number of axial cells per channel diameter length, N_{axial}, applicable to both the slug and

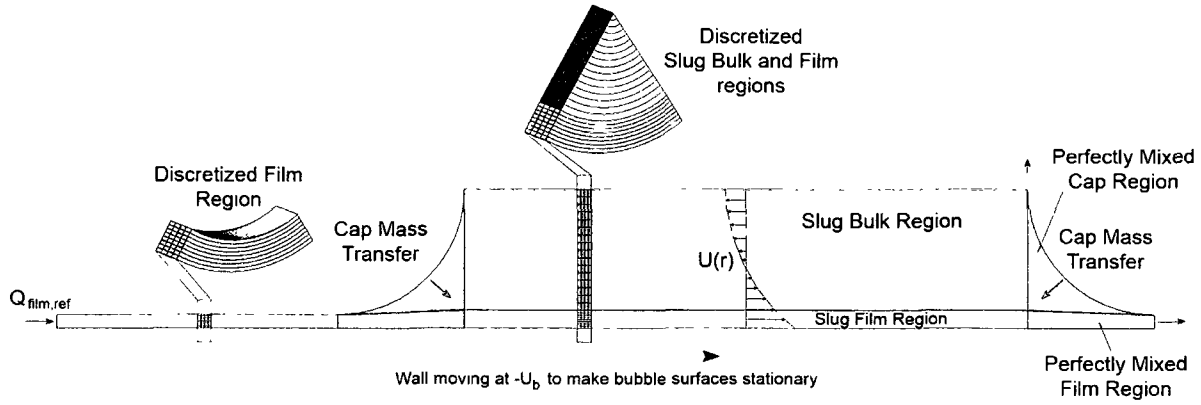

Figure 4.4 Liquid flow regions used in the derivation of the circulating slug model.

bubble regions. The radial cell widths were determined such that the cross-section for flow was equivalent for each cell within a given region. Additional constraints were placed on the radial cells within the slug bulk, such that the forward flowing and backward flowing sub-regions contained an equal number of cells.

The velocity profile within the slug region (slug bulk and slug film) was determined from Eq. (4.3.13) for $U(r)$, proposed by Thulasidas *et al.* (1997). The velocity profile within the bubble film, $U_{film}(r)$ was assumed to be parabolic, with a maximum velocity at the film's surface equivalent to $1.5Q_{film}L_{film}/V_{film} - U_b$:

$$U_{film}(r) = \frac{1.5Q_{film}L_{film}}{V_{film}}\left[1 - \frac{(r - 0.5d + \delta_b)^2}{\delta_b^2}\right] - U_b \qquad (4.3.24)$$

The predicted profile is consistent with the classical solution for falling films (Sherwood *et al.* 1975), and closely matches CFD results presented by van Baten & Krishna (2004).

For the bubble film region, the following scalar transport equation was applied in conjunction with the boundary conditions and indexing structure described in Figure 4.5. Note that $U_{film,j}$ is negative for flow from left to right, and that an upwind scheme is applied.

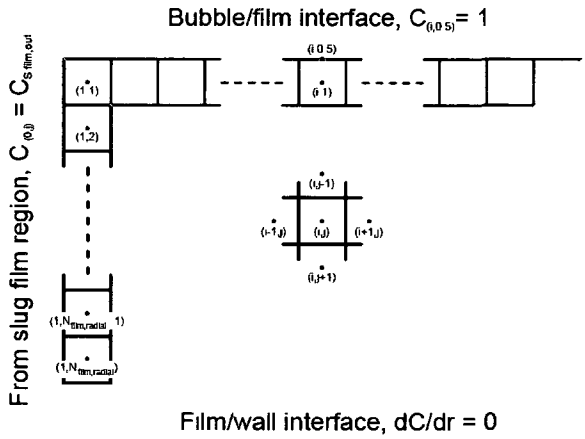

Figure 4.5 Circulating slug model indexing structure and boundary conditions applied within the bubble film.

$$V_{b,(i,j)}\frac{dC_{film,(i,j)}}{dt} = U_{film,j}A_{b,conv,j}\left(C_{film,(i,j)} - C_{film,(i-1,j)}\right) + D\left[\frac{A_{b,diff,j-0.5}}{L_{b,diff,j-0.5}}\left(C_{film,(i,j-1)} - C_{film,(i,j)}\right) - \frac{A_{b,diff,j+0.5}}{L_{b,diff,j+0.5}}\left(C_{film,(i,j)} - C_{film,(i,j+1)}\right)\right] \quad (4.3.25)$$

For i = 1 to $N_{axial}(L_{film}/d)$ and j = 1 to $N_{film,radial}$, the parameters required for the solution of the concentration within each cell of the film, $C_{film,(i,j)}$, are the convection and diffusion areas, $A_{b,conv,j}$ and $A_{b,diff,j}$, the diffusion lengths, $L_{b,diff,j}$, and the integrated axial velocity, $U_{film,j}$, and the cell volumes, $V_{b,(i,j)}$.

$$A_{b,conv,j} = \pi\left(r_{b,j+0.5}^2 - r_{b,j-0.5}^2\right) \quad (4.3.26)$$

$$A_{b,diff,j} = 2\pi r_{b,j}\frac{d}{N_{axial}} \quad (4.3.27)$$

$$L_{b,diff,j} = \begin{cases} 0.25\left(r_{b,2.5} - r_{b,0.5}\right) & for \quad j = 0.5 \\ 0.5\left(r_{b,j+1} - r_{b,j-1}\right) & for \quad j \geq 1.5 \end{cases} \quad (4.3.28)$$

$$U_{film,j} = \frac{1.5Q_{film}L_{film}}{V_{film}}\left[1 - \frac{(0.5d - \delta_b)^2}{\delta_b^2} - \frac{(0.5d - \delta_b)^2}{2\delta_b^2}\frac{\left(r_{b,j+0.5}^3 - r_{b,j-0.5}^3\right)}{\left(r_{b,j+0.5}^2 - r_{b,j-0.5}^2\right)} + \frac{\left(r_{b,j+0.5}^2 + r_{b,j-0.5}^2\right)}{2\delta_b^2}\right] - U_b \quad (4.3.29)$$

$$V_{b,(i,j)} = \pi\left(r_{b,j+0.5}^2 - r_{b,j-0.5}^2\right)\frac{d}{N_{axial}} \tag{4.3.30}$$

Where the radial positions of cell faces, r_j, are determined by:

$$r_{b,j} = \frac{1}{2}\sqrt{\frac{j-0.5}{N_{film,radial}}\left[d^2 - (d-2\delta_b)^2\right] + (d-2\delta_b)^2} \tag{4.3.31}$$

A similar approach was taken in the slug body and film, resulting in the following scalar transport equation and associated parameters. Note that the $i+sign(U_{slug,j})$ subscript in the convection term enforces an upwind scheme for convective mass transport, where *sign*() returns either 1 or -1 depending on value of $U_{slug,j}$.

$$V_{S,(i,j)}\frac{dC_{slug,(i,j)}}{dt} = U_{slug,j}A_{S,conv,j}\left(C_{slug,(i,j)} - C_{slug,(i+sign(U_{slug,j}),j)}\right) + D\left[\frac{A_{S,diff,j-0.5}}{L_{S,diff,j-0.5}}\left(C_{slug,(i,j-1)} - C_{slug,(i,j)}\right) - \frac{A_{S,diff,j+0.5}}{L_{S,diff\ j+0.5}}\left(C_{slug\ (i,j)} - C_{slug,(i,j+1)}\right)\right] \tag{4.3.32}$$

$$A_{S,conv,j} = \pi\left(r_{S,j+0.5}^2 - r_{S,j-0.5}^2\right) \tag{4.3.33}$$

$$A_{S,diff,j} = 2\pi r_{S,j}\frac{d}{N_{axial}} \tag{4.3.34}$$

$$L_{S,diff,j} = \begin{cases} 0.25\left(r_{S,2.5} - r_{S,0.5}\right) & for \quad j = 0.5 \\ 0.5\left(r_{S,j+1} - r_{S,j-1}\right) & for \quad j \geq 1.5 \end{cases} \tag{4.3.35}$$

$$U_{slug,j} = 2\left(U_L + U_G\right)\left[1 - \frac{2}{d^2}\left(r_{S,j+0.5}^2 + r_{S,j-0.5}^2\right)\right] - U_b \tag{4.3.36}$$

$$V_{S,(i,j)} = \pi\left(r_{S,j+0.5}^2 - r_{S,j-0.5}^2\right)\frac{d}{N_{axial}} \tag{4.3.37}$$

$$r_{S,j} = \begin{cases} \frac{1}{2}\sqrt{\frac{j-0.5}{N_{bulk,radial}}(d-2\delta_S)^2} & for \quad j < N_{bulk,radial} \\ \frac{1}{2}\sqrt{\frac{j-0.5-N_{bulk,radial}}{N_{film,radial}}\left[d^2 - (d-2\delta_S)^2\right] + (d-2\delta_S)^2} & for \quad j > N_{bulk,radial} \end{cases} \tag{4.3.38}$$

Within the combined slug cap and film region, the axial and radial cell indices ranged from $i = 1$ to $N_{axial}L_{slug}/d$ and from $j = 1$ to $N_{bulk,radial} + N_{film,radial}$, respectively. The following boundary conditions were applied to account for the flow direction of the circulating slug, symmetry along the centerline of the channel, and interaction with the mixed region transitions between the bubble film and slug bulk/film regions.

$$C_{slug,(0,j)} = \begin{cases} C_{S,cap,in} & for \quad j \le N_{bulk,radial} \\ C_{S,film,in} & for \quad j > N_{bulk,radial} \end{cases}$$

$$C_{slug,(1+N_{axial}L_{slug}/d,j)} = C_{S,cap,out}$$

$$\left.\frac{dC}{dr}\right|_{r=0,r=d/2} = 0$$

The only remaining expressions required to complete the circulating slug model are the mass balances on the mixed slug inlet and outlet cap and film regions. Note that the cap mass transfer coefficient, $k_{L,cap}$, is approximated from Eq. (4.2.7).

$$V_{S,cap,in}\frac{dC_{S,cap,in}}{dt} = \sum_{j=1}^{N_{bulk,radial}/2} U_{slug,j}A_{S,conv,j}C_{slug,(1,j)} + \sum_{j=N_{bulk,radial}/2+1}^{N_{bulk,radial}} U_{slug,j}A_{S,conv,j}C_{S,cap,in} + \frac{DA_{cap,film}}{L_{diff,cap,film}}\left(C_{S,film,in} - C_{S,cap,in}\right) + k_{L,cap}A_{cap}\left(1 - C_{S,cap,in}\right) \tag{4.3.39}$$

$$V_{S,film,in}\frac{dC_{S,film,in}}{dt} = -\sum_{j=1}^{N_{film,radial}} U_{film,j}A_{b,conv,j}C_{film,(N_{axial}L_{film}/d,j)} + \sum_{j=N_{bulk,radial}+1}^{N_{bulk,radial}+N_{film,radial}} U_{slug,j}A_{S,conv,j}C_{S,film,in} + \frac{DA_{cap,film}}{L_{diff,cap,film}}\left(C_{S,cap,in} - C_{S,film,in}\right) \tag{4.3.40}$$

$$V_{S,cap,out}\frac{dC_{S,cap,out}}{dt} = -\sum_{j=1}^{N_{bulk,radial}/2} U_{slug,j}A_{S,conv,j}C_{S,cap,out} - \sum_{j=N_{bulk,radial}/2+1}^{N_{bulk,radial}} U_{slug,j}A_{S,conv,j}C_{slug,(N_{axial}L_{slug}/d,1)} + \frac{DA_{cap,film}}{L_{diff,cap,film}}\left(C_{S,film,out} - C_{S,cap,out}\right) + k_{L,cap}A_{cap}\left(1 - C_{S,cap,out}\right) \tag{4.3.41}$$

$$V_{S,film,out}\frac{dC_{S,film,out}}{dt} = \sum_{j=1}^{N_{film,radial}} U_{film,j}A_{b,conv,j}C_{S,film,out} - \sum_{j=N_{bulk,radial}+1}^{N_{bulk,radial}+N_{film,radial}} U_{slug,j}A_{S,conv,j}C_{slug,(N_{axial}L_{slug}/d,j)} + \frac{DA_{cap,film}}{L_{diff,cap,film}}\left(C_{S,cap,out} - C_{S,film,out}\right) \tag{4.3.42}$$

For each of these equations, the film and cap volumes and mass transfer areas for the inlet and outlet regions are equivalent, and can be expressed as:

$$V_{S,film,out} = V_{S,film,in} = \pi\left[\left(d\delta_b - \delta_b^2\right)\left(0.5d - \delta_b\right) + \left(\delta_S - \delta_b\right)\left(0.5d - \delta_b\right)^2 - \left(\delta_S - \delta_b\right)^2\left(0.5d - \delta_b\right)/3\right] \tag{4.3.43}$$

$$V_{S,cap,out} = V_{S,cap,in} = \frac{\pi}{4}\left[d^2 - \left(d - 2\delta_b\right)^2\right] - V_{S,film,in} \tag{4.3.44}$$

$$A_{cap,film} = \pi\left[\left(d - 2\delta_b\right)^2 - \left(\delta_S - \delta_b\right)\left(d - 2\delta_b\right)/2\right] \tag{4.3.45}$$

$$A_{cap} = \frac{\pi}{2}\left(d - 2\delta_b\right)^2 \tag{4.3.46}$$

The circulating slug model was implemented in Matlab®, using a Runge-Kutta-Fehlberg method for temporal discretization (ode45). The flux of gas dissolving into the bubble film and mixed cap region were monitored at each time step, and subsequently used to determine the overall k_La:

$$k_L a = \frac{\left(Cap\ Flux \times Cap\ Area\right) + \left(Bubble\ Film\ Flux \times Film\ Area\right)}{1 - C_{reference}} \frac{1}{V_{reference}} \tag{4.3.47}$$

The reference concentration and volume, $C_{reference}$ and $V_{reference}$, have varied in existing literature, significantly affecting the magnitude of the resulting k_La values. In van Baten & Krishna's work (2004), $V_{reference}$ was equated to the unit cell volume, $0.25\pi d^2 L_{UC}$, and a cup-mixed concentration was determined at the center of the liquid slug using the velocity field in the reference frame:

$$C_{reference} = \frac{\sum_{J=1}^{N_{bulk,radial}+N_{film,radial}} V_{S,J} U_{slug,J} C_{slug,(0.5 N_{axial} L_{film}/d,J)}}{\sum_{J=1}^{N_{bulk,radial}+N_{film,radial}} V_{S,J} U_{slug,J}} \tag{4.3.48}$$

While Eq. (4.3.48) provides an accurate estimate of the average concentration experienced by the bubble within the moving frame of reference, it is difficult to directly compare to

experimental data where the concentration measured at a channel's outlet is reflective of the cup-mix concentration in a stationary frame of reference. For the purpose of comparing the results obtained from circulating slug model to published data, the following reference concentration was used:

$$C_{reference} = \frac{\sum_{J=1}^{N_{bulk,radial}+N_{film,radial}} V_{S,J}\left(U_{slug,J}+U_b\right)C_{slug,(0.5N_{axial}L_{film}/d,J)}}{\sum_{J=1}^{N_{bulk,radial}+N_{film,radial}} V_{S,J}\left(U_{slug,J}+U_b\right)} \tag{4.3.49}$$

Likewise, a reference volume equivalent to the liquid volume is typically applied when regressing experimental data (Bercic & Pintar 1997), whereby $V_{reference} = 0.25(1-\varepsilon_G)\pi d^2 L_{UC}$.

As the circulating slug approach requires discretization of the bubble film and slug regions, the minimum grid resolution needed for mesh-independent solutions was determined. The concentration profile and k_La were calculated using different values of N_{axial}, $N_{bulk,radial}$ and $N_{slug,radial}$ for the following simulation parameters: L_{UC}=0.005 m,

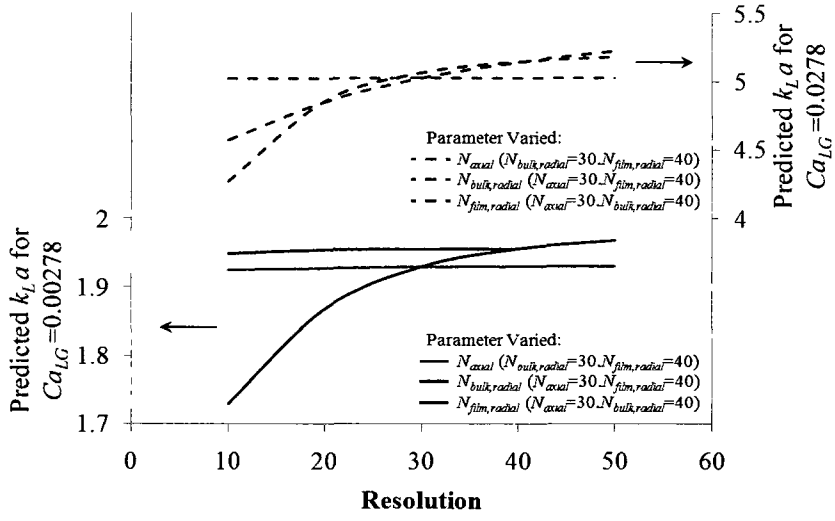

Figure 4.6 Variation in k_La predicted by the circulating slug model with increased mesh resolution.

L_{film}=0.003 m, d=1 mm, D=2x10^{-9} m^2/s, and two capillary numbers, Ca_{LG}=0.00278 and Ca_{LG} =0.0278. Based on the variation in the predicted k_La (Fig. 4.6), values of N_{axial} = 30, $N_{bulk,radial}$ = 40 and $N_{slug,radial}$ = 40 were used for all of the subsequent simulations.

4.4 Results and discussion

4.4.1 Numerical approximations of k_La

In their work on gas-liquid mass transfer in 1.5, 2.5 and 3.1mm diameter capillaries, Bercic & Pintar (1997) derived an empirical correlation for the average k_La measured during methane absorption into water along a 1.12m capillary length.

$$k_La = 0.111\frac{(U_G + U_L)^{1.19}}{[(1-\varepsilon_G)L_{UC}]^{0.57}} \tag{4.4.1}$$

The values of k_La used to derive this correlation were obtained for long gas bubbles ($Fo > 1$), using the liquid concentration exiting the capillary length, C_{exit}:

$$k_La = \frac{U_L + U_G}{1.12}\ln\left(\frac{1}{1-C_{exit}}\right) \tag{4.4.2}$$

A comparison between Eq. (4.4.1) and the instantaneous k_La values predicted by the four models discussed in this work was carried out to gauge the performance of each numerical framework. For the homogeneous mixture, perfectly mixed and slug film model, a direct comparison is possible. For the circulating slug model, simulations were carried out and the average k_La was determined from Eq. (4.4.2) using the cup-mix concentration, Eq. (4.3.49), for C_{exit}. The results are provided in Fig. 4.7 for $0.03 \le U_L + U_G \le 0.45$ m/s, $0.09 \le \varepsilon_G \le 0.9$, $L_{UC} = 0.017, 0.057, 0.11, 0.22$ m, and d = 1.5, 2.5 and 3.1 mm; assuming values of D = 2 x 10^{-9} m^2 s^{-1}, $\sigma = 0.072$ N m^{-1} (assumed equivalent to air/water), and a liquid viscosity of $\mu = 0.00089$ kg m^{-1} s^{-1}.

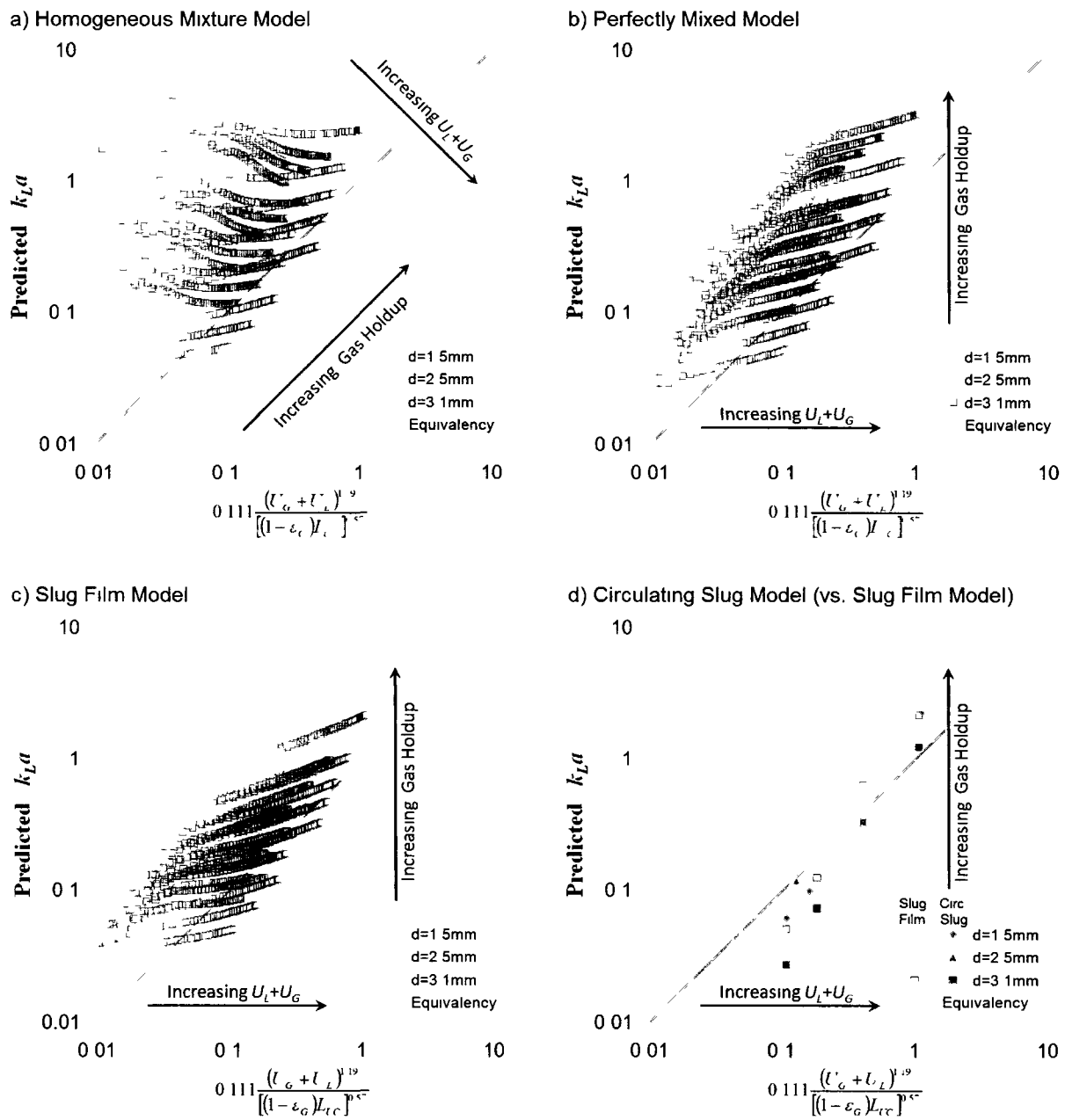

Figure 4.7 Comparison of Bercic & Pintar (1997) correlation to k_La values predicted by the four models discussed in this work.

The homogeneous mixture model, Fig. 4.7(a), overestimates k_La for the majority simulated conditions, eventually performing better as *Fo* decreased below 1. This was to be expected considering the concentration driving force used in Eq. (4.4.2), where Bercic &

Pintar (1997) assumed an identical driving force for both cap and film mass transport. If the concentration rise within the bubble film is not accounted for, a reduction in $k_{L,film}$ is needed to achieve the same flux through the interface. As a result, many of the k_La values predicted by Eq. (4.4.1) will be lower than those obtained from the homogeneous mixture model. While specific conditions could be selected to obtain similar estimates (low gas holdup and high velocities, leading to a reduction in *Fo* and less concentration polarization in the bubble film), the general trend in data was inconsistent with that of Bercic & Pintar (1997).

The perfectly mixed model, Fig. 4.7(b), also yielded higher k_La values than Eq. (4.4.1) at equivalent conditions, but started showing improved agreement since the concentration rise in the bubble film was accounted for. The continued discrepancy between predicted k_La values was attributed to the absence of a resistance term for mass transfer from the slug film to the slug bulk, and over-estimation of the concentration driving force across the bubble cap. Both the homogeneous mixture model and perfectly mixed model assume that the primary resistance to mass transfer is across the interface of the bubble, despite the fact that transfer between slug film and bulk is diffusion limited. For short liquid slugs, there may be insufficient time for the species dissolved in the film to fully equilibrate with the slug bulk, creating a slug-length dependency for mass transport. A concentration gradient will also exist within the internal recirculation patterns of the liquid slug, whereby the liquid contacting the slug film and bubble cap is at a higher concentration than the average. All of these factors would contribute to an increase in k_La values relative to experimental measurements derived from Eq. (4.4.2).

The slug film model incorporated the additional resistance term needed to account for diffusion limited mass transport between the slug film and bulk. Subsequent k_La predictions, Fig. 4.7(c), were closer in magnitude to those of Bercic & Pintar (1997) when compared to

both the homogeneous mixture model and perfectly mixed model. Nonetheless, the predicted k_La continued to exceed that determined from Eq. (4.4.1).

The impact of assumptions applied in the development of the slug film model was assessed by comparing predicted k_La values to those obtained using the circulating slug model, Fig. 4.7(d). One of the key limitations of the slug film model is the assumption that the slug concentration does not vary appreciably within a time scale comparable to $t_{C,film}$ and $t_{C,slug\ film}$. This assumption is avoided in the circulating slug model through discretization of the bubble film and slug and the subsequent solution of scalar transport equations. As can be seen in Fig. 4.7(d), the k_La predicted by the circulating slug model (closed symbols) is consistently lower than those predicted by the slug film model (open symbols). Such a discrepancy is to be expected considering the length and extended contact time of the liquid slugs involved, for which C_S cannot be assumed constant.

All of the aforementioned simulations were completed for gas and liquid bubble lengths many times that of the channel diameter. Industrially practical unit cell lengths are typically much smaller, ranging from 0.005 to 0.0015 m where k_La values are higher and $Fo < 0.1$. CFD simulations were performed in this operating region by van Baten & Krishna (2004) to determine the effects of U_b, L_{UC}, L_{film}, D, d, and δ_b on the overall mass transport coefficient. A similar analysis was completed for the four models presented here, and compared to the CFD results reported by van Baten & Krishna (2004). It should be noted that for these simulations, δ_b and U_b were explicitly set, U_{LG} was determined from the velocity profiles reported in their work, and all k_La values were normalized against a reference volume equivalent to the unit cell volume.

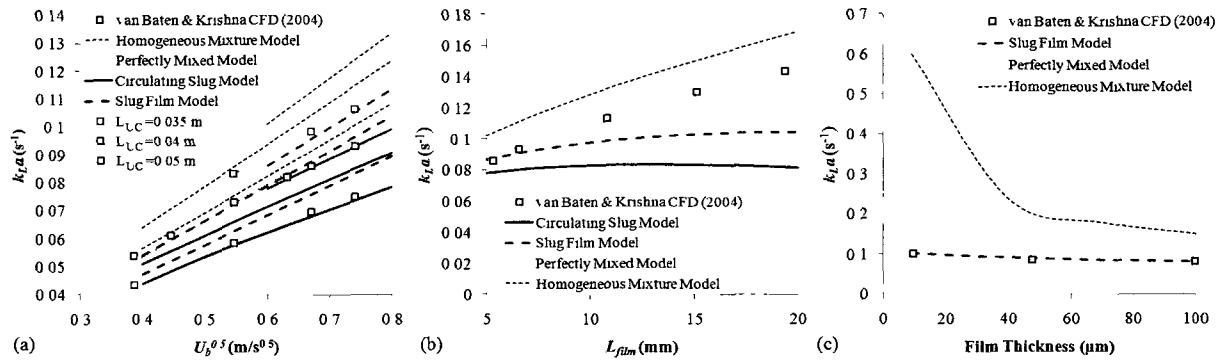

Figure 4.8 Comparison of CFD results by van Baten & Krishna (2004) to k_La values predicted by the four models discussed in this work. Unless otherwise specified simulations were carried out at L_{UC}=0.04m, d=3mm, L_{film}=5.321mm, D=1x10-9m^2/s, U_b=0.45m/s, and $\delta_b = 45\mu m$.

Figures 4.8(a) through 4.8(c) compare the predicted k_La values to those reported by van Baten & Krishna (2004) for specific variations in U_b, L_{UC}, L_{film} and δ_b. There are three significant observations which can be made from these results: the slug film model showed reasonable agreement with the CFD results for variations in U_b, L_{UC} and δ_b; the circulating slug model underestimated most values of k_La; and despite repeated validation of the homogeneous mixture model, the level of agreement reported by van Baten & Krishna (2004) could not be reproduced.

Another phenomenon of interest was the discrepancy between film length dependence of k_La predicted by the CFD results and those predicted by the slug film and circulating slug models. As the length of the bubble film increases, $k_{L,film}a_{film}$ will also increase at a rate proportional to $L_{film}^{0.5}$. However, as L_{film} increases for a set L_{UC}, the length of the slug film must decrease accordingly, causing a similar reduction in $k_{L,slug\ film}a_{slug\ film}$. When the two lengths are comparable (L_{film}=20mm), the variations in $k_{L,film}a_{film}$ and $k_{L,slug\ film}a_{slug\ film}$ are of a similar order of magnitude, resulting in minimal

variations in the overall k_La with changes in L_{film}. While this was observed for both the slug film and circulating slug model, the CFD results reported by van Baten & Krishna (2004) did not appear to capture this interplay between bubble and slug film lengths.

In summary, the homogeneous mixture model and perfectly mixed model consistently over predicted mass transfer in idealized Taylor flow, and failed to account for the effects of slug length on the overall k_La. The slug film model provides an analytical expression which accurately captures many of the parametric dependencies reported by van Baten & Krishna (2004), while avoiding the numerical complexity and time commitments associated to CFD simulations. While the circulating slug model provided insight into some of the interactions between the bubble film, slug film and slug bulk; the increased complexity associated to its implementation would only be justified for long slug film contact times, where the assumptions used in deriving the slug film model are no longer appropriate.

4.4.2 Film vs. cap mass transfer

The ratio of film and cap mass transfer is an important parameter in determining if inter-phase mass transport can be improved through redistribution of cap and film area via bubble breakup and flow pattern transitions. In the CFD simulations of van Baten & Krishna (2004), film mass transfer typically accounted for 60% of the overall transfer between the bubble and liquid slug. In a subsequent experimental analysis of gas-liquid flow in a vertical capillary, Vandu *et al.* (2005) used a variation of the homogeneous mixture model to simulate mass transfer while assuming a dominance of film transport. As part of their analysis, the slug film contact time was identified as an appropriate indicator of the dominance of film mass transport. For values of $\sqrt{(U_L+U_G)/(L_{UC}-L_{film})}$ greater than

3 $s^{-0.5}$, the film contact times are fairly short, increasing the relative magnitude of film mass transfer (compared to mass transfer through the bubble caps). For values less than 3 $s^{-0.5}$, the long film contact times resulted in a reduced relative magnitude of film mass transfer. While this criteria does capture the reduced importance of film mass transport when long contact times are present, it fails to account for the reduction in mass transfer which would be observed when there is insufficient contact time for mass transport to occur between the bubble, bubble film, slug film and slug body.

The slug film model was used to explore the impact of key design parameters on the relative ratio of film and cap mass transport. From Eq. (4.3.22), the ratio of film to cap mass transport can be expressed as:

$$R_{film/cap} = \frac{-\left[\frac{(1-[A])(1-[B])}{1-[B][A]}\right] Q_{film,ref}}{k_{L,cap} A_{cap}} \tag{4.4.3}$$

By combining Eqs. (4.2.7), (4.2.9), (4.2.10), (4.2.11), (4.3.5), (4.3.6), (4.3.14), (4.3.15), (4.3.19) and (4.3.20), an expression for $R_{film/cap}$ was derived which was only a function of four dimensionless parameters: Ca_{LG}, L_{film}/d, $(L_{UC} - L_{film})/d$, and a Peclet number accounting for the effects of diffusivity, $Pe = d(U_L + U_G)/D$:

$$R_{film/cap} = \frac{\pi}{16}\left[\frac{(1-[A])(1-[B])}{1-[B][A]}\right]\sqrt{Pe\left(\frac{0.61Ca_{LG}^{0.33}}{1-1.22Ca_{LG}^{0.33}}\right)\left(\frac{0.61Ca_{LG}^{0.33}}{1-0.61Ca_{LG}^{0.33}}\right)} \tag{4.4.4}$$

Where:

$$[A] = \exp\left[-4\sqrt{\frac{4}{\pi Pe}\left(\frac{1-0.61Ca_{LG}^{0.33}}{0.61Ca_{LG}^{0.33}}\right)\left(\frac{1+4Ca_b^{2/3}+4Ca_b^{4/3}}{2.68Ca_b^{2/3}+7.1556Ca_b^{4/3}}\right)\frac{L_{film}}{d}[k]_{L,film}}\right] \tag{4.4.5}$$

$$[B]=\exp\left[-4\sqrt{\frac{4}{\pi Pe}\left(\frac{1-0.61Ca_{LG}^{0.33}}{0.61Ca_{LG}^{0.33}}\right)\left(\frac{1-1.22Ca_{LG}^{0.33}}{0.61Ca_{LG}^{0.33}}\right)\frac{(L_{UC}-L_{film})}{d}}[k]_{L,slug\ film}\right] \tag{4.4.6}$$

$$[k]_{L,film}=\begin{cases}\dfrac{\ln(1/\Delta)}{(1-\Delta)} & for \quad Fo_{film}<0.1\\ 1.705\dfrac{d}{\delta_b}\sqrt{\dfrac{4}{Pe}\left(\dfrac{1-0.61Ca_{LG}^{0.33}}{0.61Ca_{LG}^{0.33}}\right)\left(1-\left(\dfrac{1+2Ca_b^{2/3}}{1+3.34Ca_b^{2/3}}\right)^2\right)\dfrac{L_{film}}{d}} & for \quad Fo_{film}>1.0\end{cases} \tag{4.4.7}$$

$$[k]_{L,slug\ film}=\begin{cases}\dfrac{\ln(1/\Delta)}{(1-\Delta)} & for \quad Fo_{slug\ film}<0.1\\ 1.705\dfrac{d}{\delta_S}\sqrt{\dfrac{4}{Pe}\dfrac{(L_{UC}-L_{film})}{d}} & for \quad Fo_{slug\ film}>1.0\end{cases} \tag{4.4.8}$$

Note that δ_b/d, δ_S/d and Fo for the bubble and slug film can be determined once Ca_{LG} is known.

The sensitivity of $R_{film/cap}$ to each of the dimensionless parameters was explored for $10^{-4} \le Ca_{LG} \le 1$, $0.1 \le (L_{UC}-L_{film})/d-1 \le 10$, and $0.1 \le L_{film}/d \le 10$. For simplification purposes, a constant diffusivity was selected and Pe determined for a 1mm channel diameter and the physical properties of an air/water system (D = $2\text{x}10^{-9}$ m^2/s, $\sigma = 0.072$ N/m, $\mu = 0.001$ kg/(m s)). The resulting variations in percentage total mass transfer attributed to the film are shown in Figs. 4.9 through 4.11 for a broad range of Ca_{LG}, L_{film} and $(L_{UC}-L_{film})/d-1$ values.

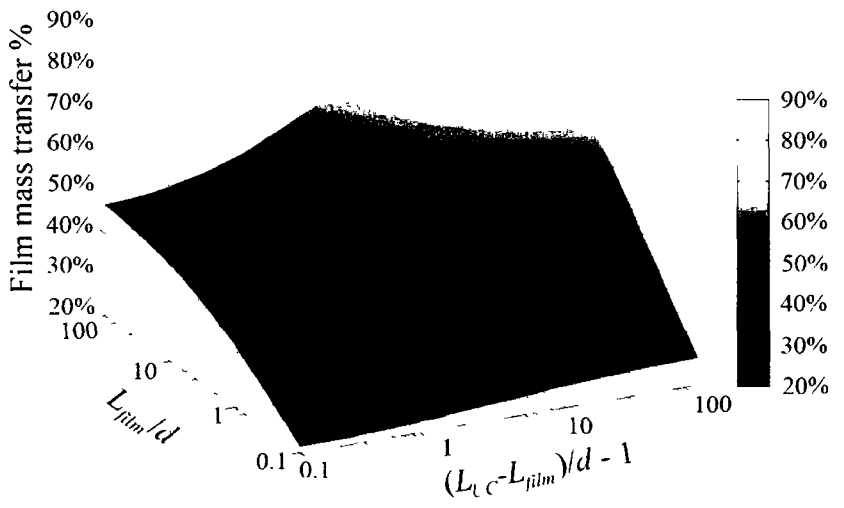

Figure 4.9 Percentage of total mass transport attributed to the film at different bubble and slug film lengths for $D = 2\text{x}10^{-9}$ m^2/s, $Ca_{LG} = 0.004$, $d = 1$ mm, $\sigma = 0.072$ N/m, and $\mu = 0.001$ kg/(m s).

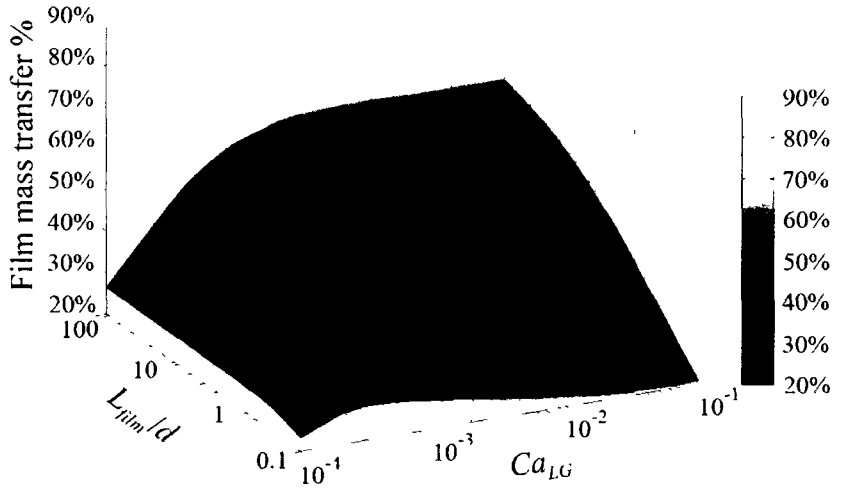

Figure 4.10 Percentage of total mass transport attributed to the film at different bubble film lengths and capillary numbers for $D = 2\text{x}10^{-9}$ m^2/s, $(L_{UC} - L_{film})/d - 1 = 3$, $d = 1$ mm, $\sigma = 0.072$ N/m, and $\mu = 0.001$ kg/(m s).

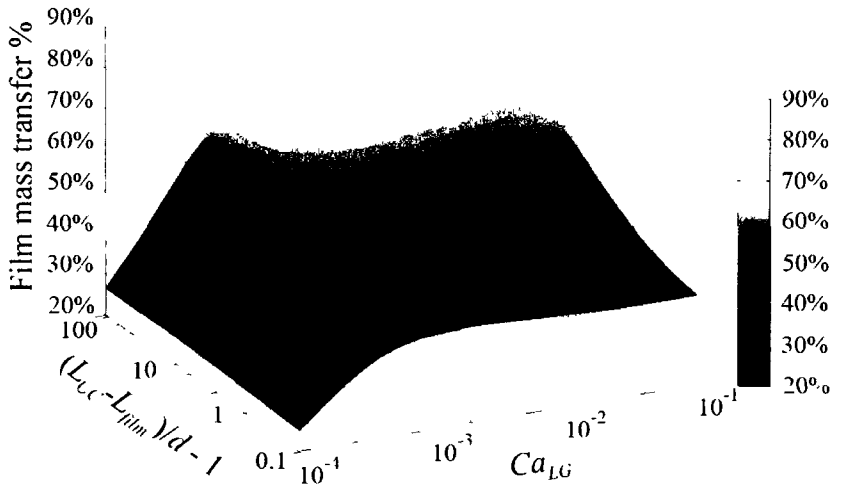

Figure 4.11 Percentage of total mass transport attributed to the film at different bubble film lengths and capillary numbers for D = 2x10^{-9} m^2/s, L_{film}/d = 8, d = 1 mm, $\sigma = 0.072$ N/m, and $\mu = 0.001$ kg/(m s).

The effects of bubble and slug film length at a $Ca_{LG} = 0.004$ are illustrated in Fig. 4.9, where an increase in either parameter corresponds to an increased importance of film mass transport. It is important to note that at this capillary number, neither film or cap mass transport becomes dominant enough to neglect either of the mechanisms. The interplay between capillary number and bubble film length is shown in Fig. 4.10 for a slug film length of approximately 4d, or $(L_{UC} - L_{film})/d - 1 = 3$. Two interesting observations can be made from this graph: the film contribution to total mass transport is almost independent of bubble film length at low capillary numbers, where the thin bubble film and long contact times would lead to rapid saturation; and there is a maximum film contribution at Ca_{LG}~0.0003 for L_{film}/d=0.1, ranging to Ca_{LG}~0.006 for L_{film}/d=100. The location of the maximum film

contribution represents the point at which an increase in the velocity results in insufficient contact time for mass transfer between the slug film and bulk. At this point, increasing Ca_{LG} will enhance cap mass transfer to a greater magnitude than film mass transfer, resulting in the observed leveling-off/drop in percentage contribution to total mass transport. Fig. 4.11 confirms this behavior, whereby the film mass transfer contribution becomes almost independent of Ca_{LG} at values comparable to the maximums observed in Fig. 4.10. As the slug film length increases, the minimum contact time required for transfer to the slug bulk is reached at greater values of Ca_{LG}.

To obtain a better understanding of the interplay between the four dimensionless parameters and the relative contributions of film and cap mass transport, the film mass transfer percentage, $R_{film/cap}/(R_{film/cap}+1)$, was determined for two channel diameters (1mm and 3mm) over a broad range of Ca_{LG}, $(L_{UC} - L_{film})/d - 1$ and L_{film}/d values. The results are plotted in Fig. 4.12 as contours in 3D space, where four film mass transfer percentage contours were used in each figure: 33%, 50%, 66% and 80%. The variation in contours for the two different diameters is minimal, with a slight increase in film mass transfer observed in the 3mm channel at lower capillary numbers. This would indicate the Peclet number has a minimal effect on the relative ratio of film to cap mass transport, but still impacts the overall k_La. Both the bubble and slug film lengths have a similar impact on the relative importance of film mass transport, consistent with Fig. 4.9. Perhaps of greatest importance is the relative equivalency of film and cap mass transport for a wide range of operating conditions. The bubble and slug films need to be on the order of 50 channel diameters in length before the cap mass transport could be reasonably neglected (i.e. film mass transport accounting for over 80% of the total mass transfer).

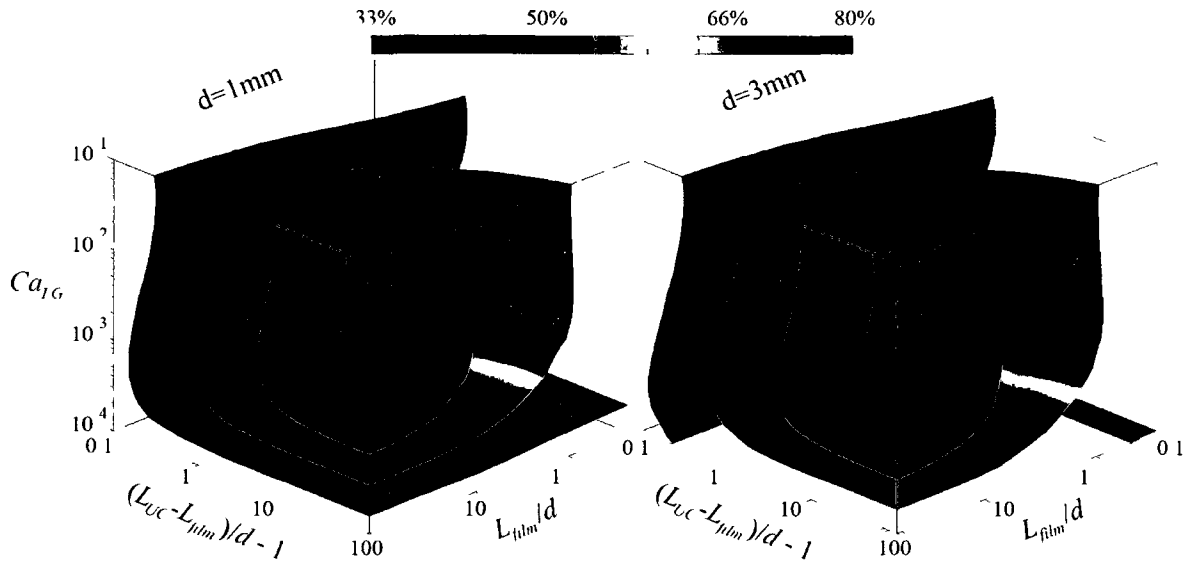

Figure 4.12 Contours of percentage film contributions to total mass transport in 1mm (left) and 3mm (right) circular capillaries for D=2x10^{-9} m^2/s, $\sigma = 0.072$ N/m, and $\mu = 0.001$ kg/(m s)

4.4.3 Effects of deformation on cap mass transfer

From Eqs. (4.2.7) and (4.2.8), the mass transfer coefficient for the cap typically exceeds that of the film for any value of $L_{film} > \pi d/4$. As a result, methods of increasing the cap area per unit cell volume could lead to significant enhancements in overall mass transport provided $k_L a$ was not dominated by film contributions.

Most methods of increasing cap area involve the introduction of high shear regions to deform/break the leading and trailing edges of the bubble interface, thereby reducing the slug film length and increasing U_L+U_G . The previously mentioned criteria for film transfer dominated flow, $\sqrt{(U_L+U_G)/(L_{UC}-L_{film})}$, would indicate that operating under the conditions necessary to induce bubble deformation and breakup would actually lead to a dominance of film mass transport, making modifications to the cap area irrelevant. The slug film model demonstrated that cap and film contributions to mass transfer remain comparable

even at elevated capillary numbers, prompting a brief analysis of the potential effects of elevated shear on mass transfer across the bubble's cap.

Taylor bubbles flowing in circular capillaries are commonly assumed to have hemi-spherical caps in contact with the liquid slugs. In an effort to characterize the effects of shear on this cap region, the applicability of droplet in shear theory was assumed. Consider the classical solution for the extent of deformation of a spherical droplet in simple shear at low shear capillary numbers and viscosity ratios, $Ca_{shear} < 0.5$ (Taylor 1932, 1934; Cox 1969; Rallison 1981; Pozrikidis 1993; Loewenberg & Hinch 1996):

$$Ca_{shear} = \frac{d[\nabla U(r)]\mu}{\sigma} = \frac{l-b}{l+b} \tag{4.4.9}$$

For a given viscous shear capillary number, Ca_{shear}, the major, l, and minor, b, axis lengths of an initially spherical droplet deforming into a prolate ellipsoid can be approximated assuming conservation of volume during deformation.

$$l = \frac{d}{2}\left(\frac{1+Ca_{Shear}}{1-Ca_{Shear}}\right)^{2/3} \tag{4.4.10}$$

$$b = \frac{d}{2}\sqrt{\frac{d}{2l}} \tag{4.4.11}$$

When Higbie penetration theory is applied, $k_{L,cap}A_{cap}$ is dependent on the surface area of the cap, A_{cap}, the bubble's axial perimeter, P, and the velocity of the liquid packet travelling along the bubble's surface, U_{packet}.

$$k_{L,cap}A_{cap} \propto \frac{A_{cap}}{\sqrt{P}}\sqrt{U_{packet}} \tag{4.4.12}$$

The axial perimeter and surface area of a prolate ellipsoid can be approximated as:

$$A_{cap} = 2\pi\left[b^2 + l^2\frac{\arccos(b/l)}{\tan(\arccos(b/l))}\right] \tag{4.4.13}$$

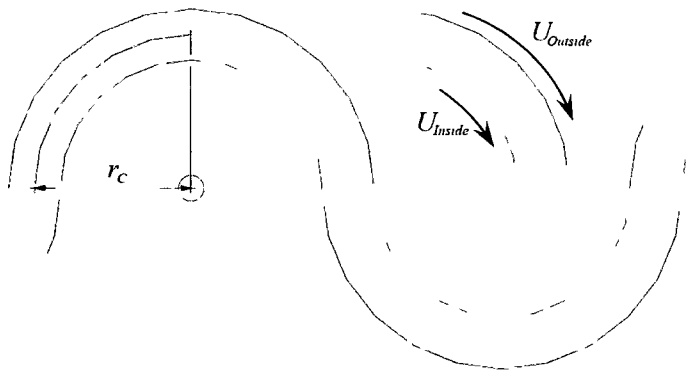

Figure 4.13 Serpentine geometry illustrating the bend radius of curvature, r_c, and localized stationary frame of reference.

$$P = \pi\left[3(l+b) - \sqrt{(3l+b)(l+3b)}\right] \tag{4.4.14}$$

Thus, the only information needed to determine the impact of droplet deformation in shear on mass transfer is an approximation of U_{packet} for a set Ca_{shear}.

Consider a 2D serpentine geometry (Fig. 4.13) with bends having a radius of curvature, r_c. A stationary frame of reference could be established in a localized area of the bend by applying velocities of U_{Inside} and $U_{Outside}$ on the inner and outer walls of the geometry. The magnitudes of U_{Inside} and $U_{Outside}$ are determined by assuming a constant linear residence time for each surface, whereby $U_{Outside}$ is greater than U_{Inside} due to the increased length of the outer wall. For the purpose of defining a relationship between U_L+U_G and Ca_{shear}, deformation of the bubble cap within this localized area will be considered equivalent to that of a droplet suspended between two moving plates, with a shear rate equivalent to $(U_{Outside} - U_{Inside})/d$.

$$U_{Inside} = \frac{L_{Inside}}{t_{flow}} = (U_L + U_G)\left(1 - \frac{d}{2r_c}\right) \tag{4.4.15}$$

$$U_{Outside} = \frac{L_{Outside}}{t_{flow}} = (U_L + U_G)\left(1 + \frac{d}{2r_c}\right) \tag{4.4.16}$$

$$Ca_{shear} = \frac{d}{2r_c} Ca_{LG} \tag{4.4.17}$$

In reality, shear rates along the interface would be much higher due to the presence of curvature induced secondary flows, resulting in conservative estimates for the potential increase in k_La. With this in mind, the packet velocity was set equal to that at $r = r_c+d/4$ to reflect the increased velocities and refreshment rate of the interface.

$$U_{Packet} = (U_L + U_G)\left(1 + \frac{d}{8r_c}\right) \tag{4.4.18}$$

With expressions for A_{cap}, P and U_{packet} defined for deforming bubble caps in a serpentine arrangement, the effects geometry and deformation were explored. For a system with physical properties consistent with air and water, the ratio of the serpentine $k_{L,cap}A_{cap}$ to the straight channel $k_{L,cap}A_{cap}$ is shown in Fig. 4.14 for $0.001 < Ca_{LG} < 0.1$ and $1 < r_c/d < 6$.

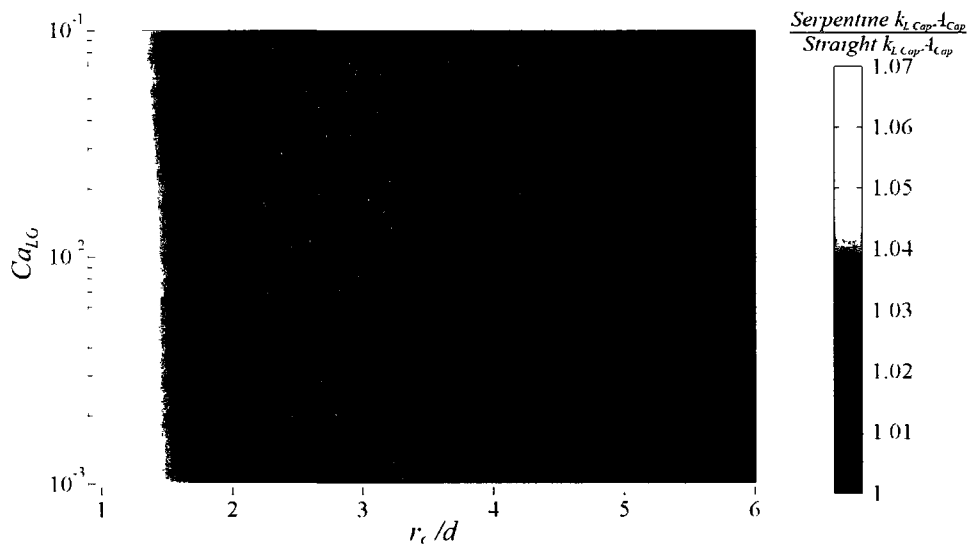

Figure 4.14 Predicted enhancement of $k_{L,cap}A_{cap}$ due to shear-induced deformation of air/water flow within a serpentine geometry.

The current analysis predicts a 1% to 7% increase in $k_{L,cap}A_{cap}$ with the introduction of curvature, where r_c/d has the greatest impact on the observed mass transfer enhancement. The reduction in the serpentine to straight $k_{L,cap}A_{cap}$ ratios as Ca_{LG} increases is due to the interaction between $A_{cap}P^{-0.5}$ and $U_{packet}^{0.5}$ predicted by Higbie penetration theory. Figure 4.15 illustrates the variation in $A_{cap}P^{-0.5}$ at the aforementioned conditions. The introduction of deformation results in a decrease in $A_{cap}P^{-0.5}$, correspond to a longer packet contact length per unit surface area. As a conservative estimate for the packet velocity was used, the net effect of increasing Ca_{LG} for a set r_c/d is a slight increase in the packet contact time and a corresponding decrease in $k_{L,cap}A_{cap}$. In an actual serpentine geometry, significant secondary flows form in both the axial and radial direction (Fries & von Rohr 2009) resulting in a packet contact time proportional to the eddy dimensions and rotation rate. As a result, the contact time would decrease and the enhancement to $k_{L,cap}A_{cap}$ would be significantly greater than predicted here.

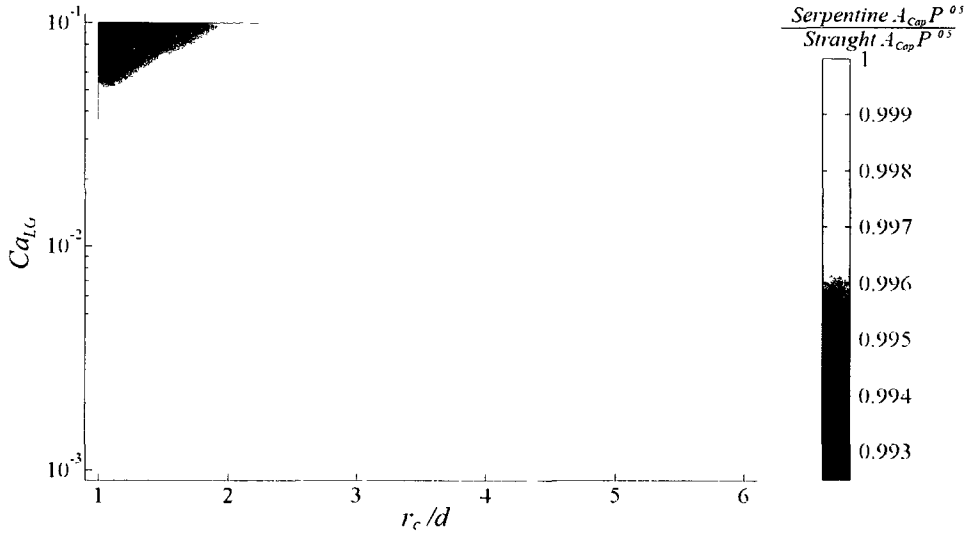

Figure 4.15 Variation in path length per unit surface area due to shear-induced deformation of air/water flow within a serpentine geometry.

4.5 Conclusions

In this work, four models predicting the overall inter-phase mass transfer coefficient for idealized Taylor flow were derived and the impacts of underlying assumptions discussed for a range of operating conditions. While simple to implement, the homogeneous mixture and perfectly mixed models frequently overestimated k_La and mass transfer when the cup-mixed concentration of the liquid slug was used to determine the concentration driving force. The inclusion of mass transfer resistance between the slug film and bulk in the slug film model significantly improved estimates of k_La when compared to the experimental data of Bercic & Pintar (1997) and the CFD results of van Baten and Krishna (2004), while still having an analytical solution for the temporal evolution of C_S. The circulating slug model represented an intermediate step between the slug film model and a full CFD simulation of mass transport, producing k_La estimates slightly lower than those of the slug film model, but with similar trends in the dependence of mass transport on the characteristic parameters of ideal Taylor flow.

Thus, the ratio of film to cap mass transfer was explored for a broad range of operating conditions using the slug film model to determine the conditions, if any, in which either film or cap mass transfer can be ignored. For unit cell lengths practical in industrial applications, film mass transport accounted for 50 to 66% of the overall mass transport even at high capillary numbers. With the importance of cap mass transfer confirmed, a conservative analysis of the potential enhancement to $k_{L,cap}A_{cap}$ was completed for a planar serpentine geometry. A 1 to 7% increase was predicted for the simplifying assumptions used, and is expected to be higher in an actual system where curvature-induced secondary flows would significantly decrease the packet contact time for the cap.

For the range of conditions discussed here, Eq. (4.3.23) is recommended for practical estimation of $k_L a$. The use of this correlation requires the estimation of additional properties relative to the homogeneous mixture model and perfectly mixed models, but yields results comparable to CFD simulations without the need for an iterative solution.

Acknowledgements

One of the authors (A.A. Donaldson) would like to acknowledge the support of the National Research Council of Canada (NRC) and the Natural Sciences and Engineering Research Council of Canada (NSERC).

Nomenclature

$A_{b,conv,J}$ Area open to convective flow in computational cell (i,j) in the bubble film [m^2]

$A_{b,diff,J}$ Area open to diffusion in computational cell (i,j) in the bubble film [m^2]

a_{cap} Cap interfacial area per unit volume [m^{-1}]

A_{cap} Cap interfacial area [m^2]

a_{film} Bubble film interfacial area per unit volume [m^{-1}]

A_{film} Bubble film interfacial area [m^2]

$A_{S,conv,J}$ Area open to convective flow in computational cell (i,j) in the slug [m^2]

$A_{S,diff,J}$ Area open to diffusion in computational cell (i,j) in the slug [m^2]

$[A]$ Exponential term for bubble to bubble film mass transfer

b Minor axis length of a deforming droplet [m]

$[B]$ Exponential term for slug film to slug bulk mass transfer

Ca_b Capillary number, based on U_b

Ca_{LG} Capillary number, based on U_L+U_G

Ca_{Shear} Capillary number for a droplet in simple shear flow

C_{exit} Concentration exiting a given capillary length

C_{film} Concentration exiting the bubble film

$C_{film,(i,j)}$ Concentration within computational cell (i,j) in the bubble film

$C_{reference}$ Reference concentration used to determine k_La in the circulating slug model

$C_{slug,(i,j)}$ Concentration within computational cell (i,j) in the slug

C_S Cup-mixed average concentration

$C_{S,cap,in}$ Concentration within the mixed cap region in contact with the slug film inlet

$C_{S,cap,out}$ Concentration within the mixed cap region in contact with the slug film outlet

$C_{S,film\ in}$ Concentration entering the slug film from the bubble film

$C_{S,film\ out}$ Concentration exiting the slug film

d Capillary diameter [m]

D Diffusivity [$m^2\ s^{-1}$]

Fo Fourier Number

i Axial index used in circulating slug model

j Radial index used in circulating slug model

k_L Overall mass transfer coefficient [$m\ s^{-1}$]

$k_{L,cap}$ Gas bubble to slug bulk mass transfer coefficient (via the cap) [$m\ s^{-1}$]

$k_{L,film}$ Gas bubble to bubble film mass transfer coefficient [$m\ s^{-1}$]

$k_{L,slug\ film}$ Slug body to slug film mass transfer coefficient [$m\ s^{-1}$]

$[k]_{L,film}$ Dimensionless bubble film mass transfer coefficient multiplier

$[k]_{L,slug\ film}$ Dimensionless bubble film mass transfer coefficient multiplier

l Major axis length of a deforming droplet [m]

$L_{b,diff,j}$ Diffusion length between cells (i,j-0.5) and (i,j+0.5) in the bubble film [m]

$L_{diff,cap,film}$ Diffusion length between the mixed cap and film regions [m]

L_{film} Bubble film length [m]

L_{Inside} Inside wall length of a single bend in a serpentine configuration [m]

$L_{Outside}$ Outside wall length of a single bend in a serpentine configuration [m]

$L_{S,diff,j}$ Diffusion length between cells (i,j-0.5) and (i,j+0.5) in the slug [m]

L_{UC} Unit cell length [m]

N_{axial} Axial cells per diameter length along the bubble film and slug

$N_{film,radial}$ Number of radial cells within the bubble and slug film regions

$N_{bulk,radial}$ Number of radial cells within the slug bulk region

P	Axial perimeter of a deforming droplet
Pe	Peclet number
Q_{film}	Volumetric flow rate of the film in the stationary reference frame [$m^3\ s^{-1}$]
$Q_{film,ref}$	Volumetric flow rate of the film in the moving reference frame [$m^3\ s^{-1}$]
r	Radial position from the capillary's centerline [m]
r_{bJ}	Radial position of cell center of cell (i,j) in the bubble film [m]
r_c	Radius of curvature of a single bend in a serpentine configuration [m]
$R_{film/cap}$	Ratio of film to cap mass transfer
r_{SJ}	Radial position of cell center of cell (i,j) in the slug [m]
t	Time [s]
$t_{C,cap}$	Cap contact time [s]
$t_{C,film}$	Bubble film contact time [s]
$t_{C,slug\,film}$	Slug film contact time [s]
t_{flow}	Average residence time of two-phase flow in a serpentine bend [s]
U_b	Bubble velocity [$m\ s^{-1}$]
$U_{film,J}$	Axial velocity in computational cell (i,j) in the bubble film [$m\ s^{-1}$]
U_G	Superficial gas velocity [$m\ s^{-1}$]
U_{Inside}	Inside wall velocity required for a stationary frame of reference [$m\ s^{-1}$]
U_L	Superficial liquid velocity [$m\ s^{-1}$]
$U_{Outside}$	Outside wall velocity required for a stationary frame of reference [$m\ s^{-1}$]
U_{packet}	Velocity of a liquid packet travelling along a bubble's surface [$m\ s^{-1}$]
$U_{slug,J}$	Axial velocity in computational cell (i,j) in the slug [$m\ s^{-1}$]
$U(r)$	Axial velocity at position r [$m\ s^{-1}$]

$\nabla U(r)$ Velocity gradient in simple shear flow [s^{-1}]

$V_{b,(i,j)}$ Volume of computational cell (i,j) in the bubble film [m^3]

V_{film} Bubble film volume [m^3]

$V_{reference}$ Reference volume used to determine k_La in the circulating slug model [m^3]

V_{slug} Volume of the slug bulk [m^3]

$V_{slug\,film}$ Volume of the slug film [m^3]

$V_{S,(i,j)}$ Volume of computational cell (i,j) in the slug [m^3]

V_{UC} Unit cell volume [m^3]

δ_S Slug film thickness [m]

δ_b Bubble film thickness [m]

Δ Delta parameter for determining $k_{L,film}$ and $k_{L,S,film}$

ε_G Gas phase holdup

μ Liquid phase viscosity [kg m^{-1} s^{-1}]

σ Surface tension [N m^{-1}]

References

Aussillous, P., Quere, D., 2000. Quick deposition of a fluid on the wall of a tube. Physics of fluids 12, 2367–2371.

Bercic, G. & Pintar, A., 1997. The role of gas bubbles and liquid slug lengths on mass transport in Taylor flow through capillaries. Chem. Eng. Sci. 52, 3709-3719.

Cox, R.G., 1969. The deformation of a drop in a general time-dependent fluid flow. J. Fluid Mech. 37, 601-623.

Edvinsson, R.K., Cybulski, A., 1995. A comparison between the monolithic reactor and the trickle-bed reactor for liquid-phase hydrogenations. Catalysis Today 24, 173–179.

Fries, D.M. and von Rohr, P.R., 2009. Liquid mixing in gas-liquid two-phase flow by meandering microchannels. Chem. Eng. Sci. 64, 1326-1335.

Irandoust, S., Andersson, B., 1988. Mass-transfer and liquid-phase reactions in a segmented 2-phase flow monolithic catalyst reactor. Chem. Eng. Sci. 43, 1983–1988.

Irandoust, S., Ertle, S., Andersson, B., 1992. Gas–liquid mass-transfer in Taylor flow through a capillary. Canadian J. of Chem. Eng. 70, 115–119.

Kirpalani, D.M., Patel, T., Mehrani, P., Macchi, A., 2008. Experimental analysis of the unit cell approach for two-phase flow dynamics in curved flow channels. Int. J. Of Heat and Mass Trans. 51, 1095-1103.

Kreutzer, M.T., 2003. Hydrodynamics of Taylor flow in capillaries and monolith reactors. Ph.D. Thesis, Delft University of Technology, Delft, The Netherlands.

Liu, H., Vandu, C.O., Krishna, R., 2005. Hydrodynamics of Taylor flow in vertical capillaries: flow regimes, bubble rise velocity, liquid slug length and pressure drop. Ind. & Eng. Chem. Res., 44 (14), 4884-4897.

Loewenberg, M. & Hinch, E.J., 1996. Numerical simulations of concentrated emulsions. J. Fluid Mech. 321, 395-419.

Nedeltchev, S., Jordan, U., Schumpe, A., 2007. Correction of the penetration theory based on mass-transfer data from bubble columns operated in the homogenous regime under high pressure. Chem. Eng. Sci. 62, 6263-6273.

Nijhuis, T.A., Kreutzer, M.T., Romijn, A.C.J., Kapteijn, F., Moulijn, J.A., 2001. Monolithic catalysts as more efficient three-phase reactors. Catalysis Today 66, 157–165.

Pohorecki, R., 2007. Effectiveness of interfacial area for mass transfer in two-phase flow in microreactors. Chem. Eng. Sci. 62, 6495-6498.

Pozrikidis, C., 1993. On the transient motion of ordered suspensions of liquid drops. J. Fluid Mech. 246, 301-320.

Rallison, J.M., 1981. A numerical study of the deformation and burst of a viscous drop in general shear flows. J. Fluid Mech. 109, 465-482.

Shao, N., Gavrilidis, A., Angeli, P., 2010. Mass transfer during Taylor flow in microchannels with and without chemical reaction. Chem. Eng. J. Article in press.

Sherwood, T.K., Pigford, R.L., Wilke, C.R., 1975. Mass Transfer. Mc-Graw Hill, New York, SA.

Stankiewicz, A., 2001. Process intensification in in-line monolithic reactor. Chem. Eng. Sci. 56, 359–364.

Taylor, G.I., 1932. The viscosity of a fluid containing small drops of another fluid. Proc. R. Soc. London Ser. A 138, 41-48.

Taylor, G.I., 1934. The formation of emulsions in definable fields of flow. Proc. G. Soc. London Ser. A 146, 790-796.

Thulasidas, T.C., Abraham, M.A., Cerro, R.L., 1995. Bubble-train flow in capillaries of circular and square cross-section. Chem. Eng. Sci. 50, 183–199.

Thulasidas, T.C., Abraham, M.A., Cerro, R.L., 1997. Flow patterns in liquid slugs during bubble-train flow inside capillaries. Chem. Eng. Sci. 52, 2947-2962.

van Baten, J.M. & Krishna, R., (2004). CFD simulations of mass transfer from Taylor bubbles rising in circular capillaries. Chem. Eng. Sci. 59, 2535-2545.

Vandu, C.O., Liu, H., Krishna, R., 2005. Mass transfer from Taylor bubbles rising in single capillaries. Chem. Eng. Sci. 60, 6430-6437.

Zheng, D., He, X., Che, D., 2007. CFD simulations of hydrodynamic characteristics in gas-liquid vertical upward slug flow. Int. J. of Heat and Mass Trans. 50, 4151-4165.

Chapter 5

Diffuse interface tracking of immiscible fluids: Improving phase continuity through free energy density selection

A.A. Donaldson [1,2], D.M. Kirpalani [1,*], A. Macchi [2]

Submitted to Int. J. of Multiphase Flow, August, 2010.

1 Institute for Chemical Process and Environmental Technology
National Research Council Canada
M-12, 1200 Montreal Road
Ottawa, Ontario, K1A 0R6, Canada

2 Dept. of Chemical and Biological Engineering
University of Ottawa
161 Louis Pasteur Street
Ottawa, Ontario, K1N 6N5, Canada

* Corresponding author: Deepak Kirpalani, Tel: +1 (613) 991-6958, Fax: +1 (613) 991-2384, e-mail: Deepak.kirpalani@nrc-cnrc.gc.ca

Abstract

Originally developed for modeling near-critical fluid mixtures with high inter-phase miscibility, diffuse interface (DI) tracking methods are frequently extended to immiscible two-phase systems involving moving contact lines and extensive morphological changes. For computational simplicity, the double-well function describing miscible fluids is adopted as the bulk free energy density, with spontaneous drop shrinkage and loss of phase continuity reported. These losses are limited through constraints placed on the interfacial width and mobility parameter. With some exceptions highlighted in this work, the increased computational cost associated with minimizing the interfacial width has limited DI methods to 2D planar and axi-symmetric flow.

In this work, a temperature-variant simplified energy density function (TVSED) is proposed to examine the effect of the metastable thermodynamic region on phase continuity. By varying a non-dimensional reduced temperature parameter, T_R, free energy analysis and scalar transport simulations are performed for simplified energy densities ranging from the double-obstacle (T_R = 0) to the double-well function (T_R = 1). A correlation between spontaneous drop shrinkage and the choice of energy function is derived, where continuity losses are minimized in the absence of a metastable thermodynamic region (T_R = 0).

Pressure rise, collapsing column and droplet in shear simulations performed at T_R = 0 and T_R = 1 are compared to results obtained using a volume-of-fluid (VOF) based solver. In each case, continuity is maintained at T_R = 0 due to the presence of a large spinodal thermodynamic region, whereas the large metastable region of the more commonly used double-well function (T_R = 1) promoted inter-mixing in the bulk phases. Comparable solutions are obtained from the T_R = 0 and VOF simulations, closely approximating those

reported in literature. At $T_R = 1$, continuity losses introduced significant discrepancies, diluting the inertia transferred between impacting fluids and under-predicting deformation in shear.

The proposed implementation addresses the fundamental source of perceived continuity losses in the DI approach and eliminates the spontaneous drop shrinkage phenomenon, relaxing the associated constraints on the mobility parameter and interfacial width. The comparable performance of $T_R = 0$ and VOF simulations is a promising indication of the potential for application to complex 3D flows at reduced mesh resolution relative to existing DI methods.

Keywords: Diffuse-interface method; Phase-field; Interface tracking; Cahn-Hilliard free energy theory; continuity; spontaneous drop shrinkage; critical drop radius.

5.1 Introduction

Over the last decade, the diffuse interface (DI) method for multi-phase computational fluid dynamics (CFD) has been applied successfully to a variety of physical systems involving extensive topological changes and length scales commensurate with the thickness of the interface. Following the early stages of development (refer to the review by Anderson *et al.* 1998), applications of the DI method have generally followed the works of Jacqmin (1999) and Badalassi *et al.* (2003), with modifications made to incorporate high density ratio fluids (Inamuro *et al.* 2004; Yuan & Schaefer 2006; Takada & Tomiyama 2006; Ding *et al.* 2007) and multi-component systems (Kim 2007). Extensions of the DI method to incompressible two-phase flow have provided insight into a variety of flow phenomena, including the impact (Khatavkar *et al.* 2007) and spreading (Ding *et al.* 2007) of droplets on treated surfaces, and droplet breakup in micro-fluidic geometries (De Menech 2006). Despite the continued evolution of the DI method, a number of inherent limitations exist due to the nature of the Cahn-Hilliard dynamics governing interfacial transport: spontaneous drop shrinkage and a perceived loss of continuity (Yue *et al.* 2007), increased grid resolution requirements relative to sharp interface tracking methods, and limited applicability to complex geometries due to spatial discretization requirements.

The interface between fluids in the DI method is described as a finite region across which physical and thermodynamic properties are resolved. Transport of this region is governed by the convective Cahn-Hilliard equation (Cahn & Hilliard 1958, 1959), where the equilibrium profile of the order parameter used to delineate between phases is maintained through the minimization of free energy. Restorative diffusive fluxes are driven by gradients in the chemical potential, which are governed by the function selected to describe the bulk free energy density (Jacqmin 1999). The double-well function is commonly used for its

numerical simplicity, approximating the van der Waals Equation of State for highly-miscible mixtures near the critical point. When the location of an interface is visualized by a contour of the volume fraction ($\phi = 0.5$), a gradual loss of continuity is observed. This perceived continuity loss is caused by a combination of three mechanisms: energy exchange between the interface and bulk that results in spontaneous drop shrinkage (Yue *et al.* 2007); initial conditioning and curvature induced losses due to discrepancies between the one-dimensional and actual equilibrium profile; and interfacial smearing during advection (Jacqmin 1999; Yue *et al.* 2004; Feng *et al.* 2005). While global continuity of ϕ is maintained, the loss of continuity of the volume bounded by the $\phi = 0.5$ contour can lead to the incorrect interpretation of results, poor resolution of surface forces across an interface, variations in the physical properties of the bulk fluids as the phases interpenetrate, and the disappearance of small droplets.

With a few exceptions discussed by Zhou *et al.* (2010), the mesh resolution necessary to mitigate the aforementioned limitations has led to the use of 2D planar or axisymmetric geometries in the majority of reported literature. Nonetheless, many engineering problems involve complex 3D geometries and multi-phase flow where 2D and 3D dynamics differ significantly (viscous encapsulation, spray formation, multi-phase micro-fluidic contactors). The inherent ability of the DI method to regularize singular events such as breakup, coalescence and moving contact lines has led to several attempts at 3D implementation within a framework that is practical both in complexity and computational cost (Badalassi *et al.* 2003; Jacqmin 2004; Zhou *et al.* 2010). Each of these implementations has attempted to either minimize the number of cells across the interface using high-order and spectral discretization, or minimize the total mesh size through adaptive mesh refinement in the

vicinity of the interface. The first approach has limited application in complex geometries, where the order of the spatial discretization techniques used is limited on unstructured meshes. The second approach requires additional cells across the interface to accurately resolve free energy variations and surface force contributions given the reduced order of the spatial discretization schemes available on unstructured meshes common to adaptive mesh refinement algorithms. Additional strategies have been suggested to minimize the perceived continuity loss, including guidelines for selecting the mobility parameter governing the magnitude of diffusive fluxes (Yue *et al.* 2007), and limiting the width of the interfacial region (Jacqmin 1999). While each of the reported approaches improved control over the extent of continuity loss within a quiescent system, such approaches may require significant mesh refinement. Additionally, such methods do not consider the mechanisms responsible for continuity loss in convective flow.

Alternative energy functions for partially miscible or immiscible fluids are available in previous literature, such as the double-obstacle function (Langer *et al.* 1975; Oono & Puri 1988) or equations of state (Yuan & Schaefer 2006; Takada & Tomiyama 2006). These functions typically have a larger spinodal thermodynamic region and smaller metastable region, limiting the extent of phase inter-mixing and improving the rate at which the equilibrium profile of the order parameter is restored when deformed. Aside from the limitations in applying an energy function for highly miscible fluids to describe the interaction of two immiscible fluids, the increased numerical complexity associated with the implementation of alternative energy functions has resulted in the continued use of the double-well function in most recent applications (Anderson *et al.* 1998; Jacqmin 1999; Badalassi *et al.* 2003; De Menech 2006; Ding *et al.* 2007; Kim 2007; Zhou *et al.* 2010). In order to apply the DI approach to 3D simulations of fluid flow through complex geometries,

the mechanisms responsible for continuity loss must be addressed without incurring excessive computational cost through mesh refinement.

In this work, a temperature-variant simplified energy density function (TVSED) is proposed for describing a range of simplified energy density expressions transitioning from the double-well to the double-obstacle function. Through the variation of a parameter akin to the reduced temperature, the effects of the metastable thermodynamic region and inter-phase miscibility on spontaneous drop shrinkage and loss of continuity are explored. In order to maintain a numerical complexity comparable to that of approaches using the double-well function, a modified form of the Cahn-Hilliard equation is proposed in conjunction with a diffusive flux limiting methodology, minimizing variations of the order parameter that are beyond the bulk phase values. The proposed method is then applied to two-phase benchmark cases to compare the relative performance of the double-well function and an energy function with no metastable region.

5.2 Free Energy Theory for Interface Tracking

In the DI method, the equilibrium state of a binary mixture is governed by the minimization of the Helmholtz free-energy, $H[\phi]$, defined using the Ginzburg-Landau functional as:

$$H[\phi]=\int_V \frac{\lambda}{\varepsilon^2}\left\{f(\phi)+\frac{\varepsilon^2}{2}|\nabla\phi|^2\right\}dV \tag{5.2.1}$$

Where λ is the mixing energy density, ε is the capillary width of the interface, $f(\phi)$ is the bulk free energy density, and $0.5\varepsilon^2|\nabla\phi|^2$ is the excess free energy due to the presence of an interface. Generalized expressions for ε and λ can be derived from free energy

considerations for any energy density function, $f(\phi)$, with minimum energy states normalized to $\phi = 0, 1$:

$$\varepsilon = \sqrt{2}\psi\left[\int_{\varphi}^{1-\varphi} \frac{d\phi}{\sqrt{f(\phi)-f(0)-\phi(f(1)-f(0))}}\right]^{-1} \tag{5.2.2}$$

$$\lambda = \frac{\varepsilon\sigma}{\sqrt{2}}\left[\int_{0}^{1} \sqrt{f(\phi)-f(0)-\phi(f(1)-f(0))}d\phi\right]^{-1} \tag{5.2.3}$$

Where ψ is the thickness of the interface on the computational domain, σ is the surface tension, and φ is the filtering parameter governing the extent of the interfacial region ($\varphi \le \phi \le 1-\varphi$), commonly set at $\varphi = 0.05$ for the double-well function.

The physical basis of an energy density's thermodynamic properties can have a significant effect on the computational behaviour of the interface, controlling separation dynamics and the extent of inter-mixing between phases. As a result, the proposition of a new form of $f(\phi)$ must begin with a review of the origins, advantages and limitations of energy density functions currently applied to the DI method.

5.2.1 Equations of state (EOS)

Equations of state of varying complexity are available in scientific literature for describing the energy variation during phase change, including the relatively simple van der Waal's equation (vdW) and the more complex Peng-Robinson expression. When implemented in the phase-field approach, EOS are commonly applied to a second virtual system (Inamuro *et al.* 2004; Seta & Kono 2004; Takada & Tomiyama 2006), where the value of the phase variable corresponds to the molar density of the mixture, Φ.

$$f(\Phi) = -\frac{1}{V}\int P(a_{EOS}, b_{EOS}, V_{EOS}, T)dV = -\Phi\int P\left(a, b, \frac{1}{\Phi}, T\right)d\left(\frac{1}{\Phi}\right) \tag{5.2.4}$$

The EOS parameters for attraction, a_{EOS}, repulsion, b_{EOS}, and temperature, T, govern the critical properties of the fluid system, the order of magnitude of Φ, and thermodynamic miscibility between phases. For the vdW EOS, the bulk free energy density function can be expressed as:

$$f_{vdW}(\Phi) = \Phi RT \ln\left(\frac{\Phi}{1-b_{EOS}\Phi}\right) - a_{EOS}\Phi^2 \tag{5.2.5}$$

In Eq. (5.2.5), the minimum energy states correspond to the bi-nodal points, Φ_A and Φ_B, for which the double tangent condition is satisfied (Yuan & Schaefer 2006). To simplify implementation, the molar density can be defined as a linear function of the volume fraction, ϕ, of phase A, $\Phi = (\Phi_A - \Phi_B)\phi + \Phi_B$, thereby normalizing the energy minima to correspond with $\phi = 0, 1$.

EOS-based energy density functions have a clear thermodynamic basis and enable the variation of inter-phase miscibility through the temperature parameter, T. However, they introduce additional complexities during implementation. Depending on temperature and EOS parameters used, Φ_A and Φ_B can differ by many orders of magnitude and become difficult to accurately resolve. The value of ϕ is also subject to the stability constraint of $\phi > \Phi_B/(\Phi_B - \Phi_A)$, where the disparity between molar densities increases as the reduced temperature approaches zero, $T_R = T/T_C \to 0$, forcing $\Phi_B/(\Phi_B - \Phi_A) \to -0$. At low reduced temperatures, even small variations in ϕ below zero necessitates the use of polynomial approximations of $f(\phi)$ for values of ϕ below the stability limit.

Frequently employed in Lattice-Boltzmann models (Yuan & Schaefer 2006), EOS-based functions are avoided in Eulerian interface tracking studies due to the added

complexity of implementation resulting from the variable minimum energy states and stability constraints on ϕ (Takada & Tomiyama 2006). Instead, simplified expressions are generally used to approximate the free energy variation at specific thermodynamic conditions.

5.2.2 Simplified energy density functions

Conventional DI methods have employed simplified energy density functions as approximations for $f(\phi)$. These functions are characterized by quadratic expressions with well-defined bi-nodal values, for which analytical solutions exist for the one-dimensional equilibrium profile of the phase variable, ϕ.

The double-well function, shown in Eq. (5.2.6), is the simplest of the non-singular approximations for $f(\phi)$.

$$f(\phi) = 0.25\phi^2(1-\phi)^2 \tag{5.2.6}$$

Originally developed as an approximation of the van der Waals equation at near-critical conditions, it was adopted by a number of interface tracking algorithms due to its numerical simplicity (Anderson *et al.* 1998; Jacqmin 1999; Badalassi *et al.* 2003; De Menech 2006; Ding *et al.* 2007; Kim 2007). For the simple case of a planar interface separating two phases, the one-dimensional equilibrium profile can be derived from energy-minimization considerations, and expressed as:

$$\phi = 0.5 + 0.5\tanh\left(\frac{x}{\sqrt{2}\varepsilon}\right) \tag{5.2.7}$$

Where the capillary width and mixing energy density are defined as:

$$\varepsilon = \frac{\psi}{2\sqrt{2}}\operatorname{arctanh}(1-2\varphi) \tag{5.2.8}$$

$$\lambda = \frac{3}{2\sqrt{2}}\varepsilon\sigma \tag{5.2.9}$$

The double-well function is representative of the thermodynamics for near-critical phenomena involving highly miscible fluids and large interfacial widths. As the DI method has evolved into a generalized interfacial tracking technique, this expression has been increasingly adopted for immiscible fluid systems. As a result, phase inter-mixing due to high miscibility and poor separation dynamics has introduced continuity losses in dynamic simulations.

Alternative energy density expressions for immiscible fluid systems have been proposed in the past, such as the double-obstacle function for immiscible fluids (Langer *et al.* 1975; Oono & Puri 1988).

$$f(\phi) = \begin{cases} 0.5\phi(1-\phi) & 0 < \phi < 1 \\ \infty & \phi \geq 1, \phi \leq 0 \end{cases} \tag{5.2.10}$$

Or the following function having square-root behaviour in the bulk phases:

$$f(\phi) = |\phi|^{3/2}|1-\phi|^{3/2} \tag{5.2.11}$$

These expressions were mentioned by Jacqmin (1999), and dismissed due to the additional numerical complexity arising in the treatment of the bulk phases. In an effort to characterize the importance of $f(\phi)$ to phase continuity in the DI method, a temperature-variant simplified energy density function is proposed in § 2.3. Using this expression, these simplified energy density functions can be examined on a common framework through the variation of a dimensionless reduced temperature parameter, T_R.

5.2.3 Temperature-variant simplified energy density (TVSED)

The following function is proposed as a simplified energy density expression possessing well-defined bi-nodal points and a temperature dependency similar to that of the van der Waals equation of state.

$$f(\phi)=|\phi(1-\phi)|^{1+T_R} \tag{5.2.12}$$

As the reduced temperature varies from $T_R=1$ at the critical point to $T_R=0$ for immiscible fluids, $f(\phi)$ transitions from the double-well to the double-obstacle function within the $0<\phi<1$ region. From free energy considerations, the one-dimensional equilibrium profile, capillary width and mixing energy density can be derived and expressed as:

$$x=\varepsilon 2^{T_R-0.5}(1-2\phi)\,{}_2F_1\left[\frac{1}{2},\frac{1+T_R}{2};\frac{3}{2};(1-2\phi)^2\right] \tag{5.2.13}$$

$$\varepsilon=\frac{\psi}{2^{T_R+0.5}(1-2\varphi)\,{}_2F_1\left[\frac{1}{2},\frac{1+T_R}{2};\frac{3}{2};(1-2\varphi)^2\right]} \tag{5.2.14}$$

$$\lambda=\sigma\varepsilon 2^{T_R+0.5}\left[\,{}_2F_1\left[\frac{1}{2},-\frac{(1+T_R)}{2};\frac{3}{2};1\right]\right]^{-1} \tag{5.2.15}$$

Where ${}_2F_1[a_1,a_2;b_1;z]$ is the hypergeometric function:

$${}_2F_1[a_1,a_2;b_1;z]=1+\sum_{k=0}^{\infty}c_k \qquad \frac{c_k}{c_{k-1}}=\frac{(k+a_1)(k+a_2)}{(k+b_1)(k+1)}z\ , \quad c_{-1}=1 \tag{5.2.16}$$

The equilibrium ϕ profile can be approximated at intermediate values of T_R through the linear interpolation of the analytical solutions at $T_R=1$ and $T_R=0$.

$$\phi = 0.5 + 0.5\left[T_R \tanh\left(\frac{1}{\sqrt{2}\varepsilon_{T_R=1}}x\right) + (1-T_R)\sin\left(\min\left\{\max\left\{\frac{\sqrt{2}}{\varepsilon_{T_R=0}}x, -\frac{\pi}{2}\right\}, \frac{\pi}{2}\right\}\right)\right] \quad (5.2.17)$$

$$\varepsilon_{T_R=1} = \frac{\psi}{2\sqrt{2}\,\text{arctanh}[1-2\varphi]} \quad (5.2.18)$$

$$\varepsilon_{T_R=0} = \frac{\psi}{\sqrt{2}\,\arcsin[1-2\varphi]} \quad (5.2.19)$$

The added computational expense of evaluating the hypergeometric functions during initialization was insignificant when compared to that of the main simulation.

5.2.4 Normalized excess free energy comparison

The form of the simplified and EOS-based energy density functions can be compared through the use of a normalized excess free energy function, $F(\phi)$, derived from the chemical potential.

$$F(\phi) = \frac{f(\phi) - f(0) - \phi[f(1) - f(0)]}{f(\phi_{Center}) - f(0) - \phi_{Center}[f(1) - f(0)]} \quad (5.2.20)$$

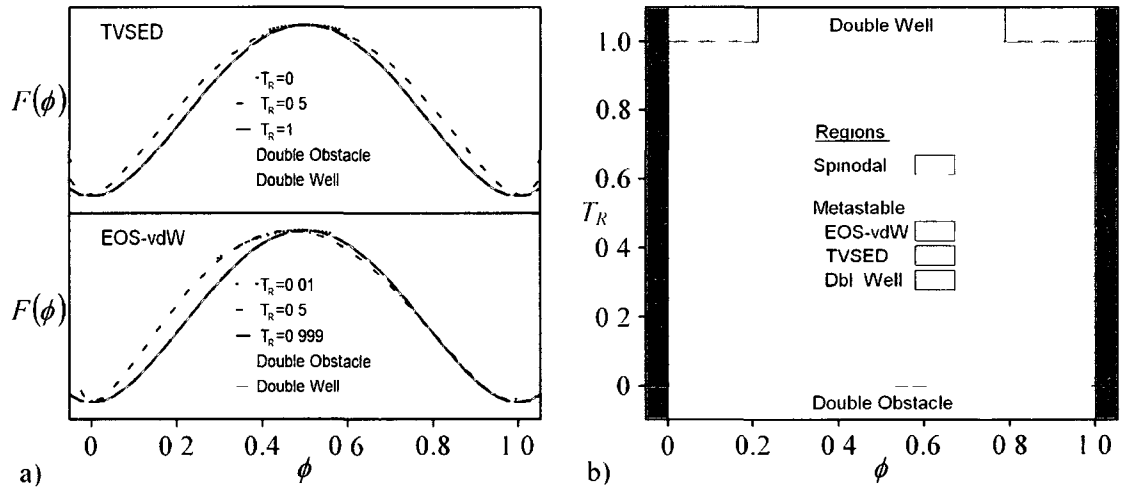

Figure 5.1 Normalized excess free energy (a) and thermodynamic regions (b) for the double-well, double-obstacle, vdW EOS (a = 1, b = 1), and TVSED energy functions.

The value of ϕ_{Center} is such that $f'(\phi_{Center}) = f'(0) = f'(1)$ for $0 < \phi_{Center} < 1$. Normalized excess free energies for the EOS-based, simplified, and TVSED energy functions are shown in Fig. 5.1(a), along with the corresponding thermodynamic regions as a function of T_R in Fig. 5.1(b).

The convergence of the double-well and EOS-based $F(\phi)$ as the temperature approaches the critical point confirms it's applicability to highly miscible systems. As $T_R \to 0$, the metastable region gradually recedes for both the EOS-based and TVSED $F(\phi)$, corresponding to a reduction in inter-phase miscibility and improved separation dynamics. At the lower limit, the spinodal region spans the entire range of interfacial values of ϕ, coinciding with the double-obstacle function describing immiscible fluids.

5.3 Equations of motion

5.3.1 Convective Cahn-Hilliard equation

The transport and reconstruction of the diffuse interface between two fluids, denoted A and B, is governed by the convective Cahn-Hilliard equation (Cahn and Hilliard 1958, 1959):

$$\frac{\partial \phi}{\partial t} + \nabla \cdot (\mathbf{u}\phi) + \nabla \cdot (\Gamma J) = 0 \tag{5.3.1}$$

Similar to sharp interface methods, the volume fraction of phase A is frequently applied as the order parameter delineating between phases, ϕ.The temporal evolution of ϕ is dependent on convective transport due to the divergence-free volume-averaged velocity, $\mathbf{u}$, and diffusive transport due to gradients in the chemical potential, $\mu = -\delta H[\phi]/\delta\phi$. The magnitude of the diffusive term is controlled by the mobility parameter, Γ, and the diffusive volumetric flux, J, which is a function of the gradient of the chemical potential. The non-

dimensional form of Eq. (5.3.1) incorporates the mobility parameter into a Péclet number, necessitating the selection of a characteristic velocity. In this work, an alternative approach is proposed for the TVSED to address the numerical instabilities that arise in the treatment of the bulk phases for $T_R < 1$.

When interfacial diffusion is dominant over bulk diffusion (Langer et al., 1975), the mobility is defined as a function of the order parameter, $\Gamma = \Gamma_C \left| \phi(1-\phi) \right|$, in which the critical mobility, Γ_C, governs the temporal stability of diffusive transport. Through an analogy to convective transport, a diffusive Courant number, C_Γ, is proposed to determine a suitable value for Γ_C given the characteristic grid cell length and time step, Δx and Δt respectively.

$$C_\Gamma = \Delta t \max\left\{ \frac{1}{\Delta x} \frac{\Gamma J}{\phi} \right\} \tag{5.3.2}$$

The advantage of this approach becomes apparent for the non-dimensional form of Eq. (5.3.1), where the time scale of diffusive transport is no longer coupled to a characteristic velocity through the Péclet number. In the DI method, the Péclet number represents the ratio of the diffusive time scale, $\varepsilon^2 L_c^2 / (\lambda \Gamma_C)$, to the convective time scale, L_c / U_c, which varies considerably depending on the selected length and velocity scales. In contrast, the diffusive Courant number represents the ratio of the time step to the diffusion-based cell residence time, with no direct dependence on the convective time scale. A local estimate of the Péclet number can be obtained from the ratio of C_Γ to the convective Courant number, C_U, yielding the local ratio of the diffusive and convective time scales.

To determine the magnitude of Γ_C and diffusive transport, the diffusive flux is calculated from the gradient of the chemical potential:

$$J = -\nabla\mu = \frac{\lambda}{\varepsilon^2}\left(\varepsilon^2\nabla\left(\nabla^2\phi\right) - f''(\phi)\nabla\phi\right) \tag{5.3.3}$$

The restorative diffusivity, $f''(\phi)$, is determined from the second derivative of $f(\phi)$ with respect to ϕ. For the TVSED, $f''(\phi)$ has the following form:

$$f''(\phi) = (1+T_R)\{T_R - (4T_R+2)[\phi(1-\phi)]\}\left|\phi(1-\phi)\right|^{T_R-1} \tag{5.3.4}$$

For values of $T_R < 1$, $f''(\phi)$ is numerically unstable in the bulk regions where $\phi(1-\phi) = 0$. This instability can be eliminated through a combination and rearrangement of the diffusive flux and mobility to obtain the following expression for ΓJ :

$$\Gamma J = \Gamma_C \frac{\lambda}{\varepsilon^2} pos[\phi(1-\phi)]\{[\phi(1-\phi)]\varepsilon^2\nabla\left(\nabla^2\phi\right) - \zeta(\phi)\nabla\phi\} \tag{5.3.5}$$

In which $pos[\phi(1-\phi)] = 1$ for $\phi(1-\phi) \geq 0$ and zero for negative values. The diffusivity, $\zeta(\phi)$, is defined as:

$$\zeta(\phi) = (1+T_R)\{T_R - (4T_R+2)[\phi(1-\phi)]\}\left|\phi(1-\phi)\right|^{T_R} \tag{5.3.6}$$

Incorporating Eq. (5.3.5) into the expression for C_Γ and rearranging for the critical mobility at $\phi = 0.5$ yields:

$$\Gamma_C = \frac{C_\Gamma}{\Delta t}\frac{\varepsilon^2}{2\lambda}\left[\max\left\{\frac{1}{\Delta x}\left(\frac{\varepsilon^2}{4}\nabla\left(\nabla^2\phi\right) + \frac{(1+T_R)}{2^{2T_R+1}}\nabla\phi\right)\right\}\right]^{-1} \tag{5.3.7}$$

Through the use of Eqs. (5.3.1), (5.3.5) and (5.3.7), the proposed TVSED function can be implemented as a diffuse interface tracking algorithm for which phase miscibility is varied to determine the effects on continuity.

5.3.2 Momentum equation

The incompressible Navier-Stokes equation and continuity equation can be expressed for a two-phase mixture with variable viscosity and density as:

$$\rho\frac{\partial \mathbf{u}}{\partial t} + \rho\mathbf{u}\cdot\nabla\mathbf{u} = -\nabla p + \nabla\cdot\left(\eta\left(\nabla\mathbf{u} + \nabla\mathbf{u}^{\mathrm{T}}\right)\right) + F_S + \rho g \tag{5.3.8}$$

$$\nabla\cdot\rho\mathbf{u} = 0 \tag{5.3.9}$$

Where p and g are the pressure and acceleration due to gravity, F_S is the surface force which is discussed in more detail in § 5.4, and ρ and η are the density and dynamic viscosity, defined as a function of the order parameter and the bulk-phase values:

$$\rho(\phi) = \rho_A\phi + \rho_B(1-\phi) \tag{5.3.10}$$

$$\eta(\phi) = \eta_A\phi + \eta_B(1-\phi) \tag{5.3.11}$$

5.4 Numerical procedure

5.4.1 Temporal discretization and solution procedure

Numerical simulations carried out using OpenFOAM, an open-source math-based solver for computational fluid dynamics on unstructured meshes, employed a staggered grid approach with scalar variables and fluxes defined at cell centres and cell faces respectively. The time stepping procedure was based on a multi-step approach solving Eqs. (5.3.1) and (5.3.8) consecutively. Equation (5.3.1) was solved using a 4^{th} order explicit Runge-Kutta (ERK4) method, and the results used to solve Eq. (5.3.8) without strictly enforcing the incompressibility constraint Eq. (5.3.9). The uncorrected velocity field was then projected onto the space of discrete divergence-free vector fields, and the pressure updated at each time step via the PISO algorithm.

The procedure for advancing a single time step from the current time, t_n, to a new time, $t_{n+1} = t_n + \Delta t$, is outlined below.

Step 1: Solve the Cahn-Hilliard Equation:

For each advancement in time, the evolution of ϕ from its current value, ϕ_n, to its new value, ϕ_{n+1}, was determined using a 4th order Runge-Kutta technique. This technique requires the determination of four temporal slope functions ($k_{\phi,1}$, $k_{\phi,2}$, $k_{\phi,3}$ and $k_{\phi,4}$), where each $k_{\phi,i}$ is calculated from Eq. (5.3.1) using the velocity field at the current time step, $\mathbf{u}_n$.

$$k_{\phi,i} = -\nabla \cdot (\Gamma J_i) - \nabla \cdot (\mathbf{u}_n \phi_i) \tag{5.4.1}$$

For i = 1, ϕ_1 is set equal to ϕ_n, and is used to determine Γ_C from Eq. (5.3.7). ΓJ_1 is subsequently calculated from Eq. (5.3.5) using ϕ_1 and the diffusive flux limiting technique described in §4.2. The value of $k_{\phi,1}$ is then determined from Eq. (5.4.1). Before proceeding to the calculation of $k_{\phi,2}$, the contribution to mass flux through each cell face is estimated for the current step in the ERK4 method for subsequent use when solving the momentum equation.

$$[\rho \mathbf{u}]_i = (\rho_A - \rho_B)[\Gamma J_i + Flux(\mathbf{u}_n \phi_i)] \tag{5.4.2}$$

The mass flux contribution, $[\rho \mathbf{u}]_i$, accounts for the flux of the density difference between cells. If $[\rho \mathbf{u}]_i$ is not explicitly determined for each step in the ERK4 method, the mass flux resulting from diffusive fluxes will not be accounted for in the momentum equation.

For subsequent values of $i = 2 \rightarrow 4$, $\Gamma_C, \Gamma J_i$, $[\rho \mathbf{u}]_i$ and $k_{\phi,i}$ are evaluating using the new value of ϕ_i determined from Eq. (5.4.3).

$$\phi_i = \phi_n + \Delta t\left[0.75 + 0.25\left(\frac{i-3.5}{|i-3.5|}\right)\right]\left(k_{\phi,i-1}\right) \tag{5.4.3}$$

Following the calculation of each $k_{\phi,i}$, the value of ϕ_{n+1} is determined from $\phi_{n+1} = \phi_n + \Delta t\left[\left(k_{\phi,1} + k_{\phi,4}\right)/6 + \left(k_{\phi,2} + k_{\phi,3}\right)/3\right]$, and the total mass flux contribution for the current time step, $[\rho\mathbf{u}]_n$, is determined from $[\rho\mathbf{u}]_n = \left([\rho\mathbf{u}]_1 + [\rho\mathbf{u}]_4\right)/6 + \left([\rho\mathbf{u}]_2 + [\rho\mathbf{u}]_3\right)/3$.

Step 2: Solve the momentum equation:

With the value of ϕ_{n+1} and $[\rho\mathbf{u}]_n$ known, the momentum equation is solved using the PISO algorithm to determine $\mathbf{u}_{n+1}$. Excluding the pressure gradient term, Eq. (5.3.8) is used to determine the uncorrected velocity, $\mathbf{u}^*$.

$$\rho(\phi_{n+0.5})\frac{\mathbf{u}^* - \mathbf{u}_n}{\Delta t} + [\rho\mathbf{u}]_n \cdot \nabla\mathbf{u}^* = \nabla\cdot\left(\eta(\phi_{n+0.5})\left(\nabla\mathbf{u}^* + \nabla\mathbf{u}^{*\mathrm{T}}\right)\right) + F_S + \rho(\phi_{n+0.5})g \tag{5.4.4}$$

In this equation, the surface force, F_S, density, $\rho(\phi_{n+0.5})$, and viscosity, $\eta(\phi_{n+0.5})$, are evaluated based on an intermediate value of ϕ: $\phi_{n+0.5} = 0.5(\phi_n + \phi_{n+1})$. Once $\mathbf{u}^*$ is known, the pressure field at the new time step, p_{n+1}, is estimated through the solution of the Poisson equation:

$$\nabla\cdot\left(\frac{\Delta t}{\rho(\phi_{n+0.5})}\nabla p_{n+1}\right) = \nabla\cdot\mathbf{u}^* \tag{5.4.5}$$

Finally, the corrected velocity field at the new time step is determined:

$$\mathbf{u}_{n+1} = \mathbf{u}^* - \frac{\Delta t}{\rho(\phi_{n+0.5})}\nabla p_{n+1} \tag{5.4.6}$$

5.4.2 Limiting diffusive flux to prevent non-physical variations in ϕ

Variations in ϕ outside of the meaningful range of values frequently occur in the DI method due to discretization errors at the edges of the interface. The double-well function limits these variations; however, additional consideration is required for the double-obstacle

function and TVSED function when $T_R < 1$. An adjustment method was employed to limit the fluxes through cell faces which resulted in values of $\phi < 0$ or $\phi > 1$. To maintain global continuity of ϕ, the algorithm was applied following the determining ΓJ_i from Eq. (5.3.5), prior to solving for $k_{\phi,i}$ and $[\rho \mathbf{u}]_i$. The procedure for correcting the diffusive fluxes for a given step, *i*, in the ERK4 method is provided below:

1) Calculate ΓJ_i from Eq. (5.3.5), storing the values on the faces of the cells.

2) Determine the value of ϕ_{i+1} that would result if convective transport were ignored and no flux limiting were applied: $\phi_{i+1} = \phi_i - \Delta t\left[0.75 + 0.25\left(\frac{i-2.5}{|i-2.5|}\right)\right](\nabla \cdot \Gamma J_i)$.

3) Identify cells where $\phi_{i+1} < 0$, and determine which cell faces have fluxes exiting the cell. This is done in OpenFOAM by creating a binary filter which is equal to 1 for all cells having a value of $\phi_{i+1} < 0$, and interpolating the filter to the cell face using an upwind scheme based on ΓJ_i. Defining the binary filter as $Filter_{Low} = if(\phi_{i+1} < 0, 1, 0)$, the change in ϕ resulting from fluxes exiting the cell face, $\Delta\phi_{Low}$, can be determined for the step from ϕ_i to ϕ_{i+1}:

$$\Delta\phi_{Low} = -\Delta t\left[0.75 + 0.25\left(\frac{i-2.5}{|i-2.5|}\right)\right]\nabla \cdot \left[\text{interpolate}(Filter_{Low})_{upwind,\ \Gamma J \text{ as vector}}(\Gamma J_i)\right].$$

4) Identify cells where $\phi_{i+1} > 1$, and determine which cell faces have fluxes entering the cell. This is done in OpenFOAM by creating a binary filter which is equal to 1 for all cells having a value of $\phi_{i+1} > 1$, and interpolating the filter to the cell face using a downwind scheme based on ΓJ_i. Defining the binary filter as $Filter_{High} = if(\phi_{i+1} > 1, 1, 0)$, the change in ϕ resulting from fluxes entering the cell

face, $\Delta\phi_{High}$, can be determined for the step from ϕ_t to ϕ_{t+1}:

$$\Delta\phi_{High} = -\Delta t\left[0.75 + 0.25\left(\frac{t-2.5}{|t-2.5|}\right)\right]\nabla\cdot\left[\text{interpolate}\left(Filter_{High}\right)_{downwind,\ \Gamma J\ as\ vector}\left(\Gamma J_t\right)\right].$$

5) Calculate the correction factors for ΓJ_t from $Filter_{Low}$, $Filter_{High}$, $\Delta\phi_{Low}$, and $\Delta\phi_{High}$:

$$Factor_{Low} = \min\left[\max\left[\left(Filter_{Low}\right)\left(\phi + \Delta\phi_{Low}\right)/\Delta\phi_{Low}, -2\right], 3\right]$$

$$Factor_{High} = \min\left[\max\left[\left(Filter_{High}\right)\left(\phi + \Delta\phi_{High} - 1\right)/\Delta\phi_{High}, -2\right], 3\right]$$

A correction factor of zero indicates that no change to the flux is required. A correction factor of 1 will set the entering or exiting flux to zero. It is possible to have correction factors greater than 1 or less than zero, indicating that an increase or reversal of the flux would be required to obtain a value of ϕ_{t+1} between zero and one. For this algorithm, correction factors were limited to a minimum and maximum of -2 and 3, enabling the algorithm to increase or reverse the flux as necessary while avoiding large changes to ΓJ_t.

6) Adjust the diffusive flux using the calculated correction factors:

$$\Gamma J_{t,adjusted} = \Gamma J_t\left(1 - \text{interpolate}\left[Factor_{Low}\right]_{upwind,\ \Gamma J\ as\ vector} - \text{interpolate}\left[Factor_{High}\right]_{downwind,\ \Gamma J\ as\ vector}\right)$$

7) Solve for the current value of $k_{\phi,t}$ and $[\rho\mathbf{u}]$ using the adjusted flux, $\Gamma J_{t,adjusted}$.

5.5 Results and discussion

5.5.1 Spontaneous shrinkage of quiescent droplets

When implemented with the double-well function, the DI method is subject to spontaneous drop shrinkage, whereby the Cahn-Hilliard dynamics reduces the total free energy in a system through an exchange between interfacial and bulk energies (Yue *et al.* 2007). As a result of this exchange, the interfacial position of a droplet with initial radius, r_0, shifts to a lower radius, r, until the total free energy is minimized. Through the analysis

of free energy variation with droplet radius, Yue *et al.* (2007) proposed an expression for a critical initial radius, r_C, for which a droplet with $r_0 < r_C$ will eventually disappear:

$$r_C \approx \left(\frac{\sqrt{6}}{8\pi} V\varepsilon \right)^{1/3} \tag{5.5.1}$$

Derived for the double-well function, r_C is dependent on the volume of the computational domain, V, and the capillary width, $\varepsilon = \psi / 4.164$.

A similar analysis was completed for the TVSED function. For a given droplet radius, the total free energy can be derived through the integration of $H[\phi]$ over the computational domain:

$$H(r,T_R) = 2\pi r\sigma + \frac{\lambda}{\varepsilon^2}\left\{ [1+\partial\phi](1-[1+\partial\phi])^{T_R+1}\pi r^2 + |[\partial\phi](1-[\partial\phi])|^{T_R+1}\left(V-\pi r^2\right)\right\} \tag{5.5.2}$$

In this equation, $\partial\phi$ represents the shift in the bulk value of ϕ and can be expressed as:

$$\partial\phi = \frac{\pi\left(r_0^2 - r^2\right)}{V} \tag{5.5.3}$$

Neglecting $\partial\phi$ terms of order greater than two, the temperature-dependent total free energy can be simplified and approximated as:

$$H(r,T_R) \approx 2\pi r\sigma + \frac{\lambda}{\varepsilon^2}\frac{\pi^{T_R+1}}{V^{T_R}}\left|r_0^2 - r^2\right|^{T_R+1} \tag{5.5.4}$$

The surface tension, σ, is obtained from Eq. (5.2.15). The critical radius corresponds to the value of r for which $\partial H(r,T_R)/\partial r = 0$ at the inflection point of $H(r,T_R)$, determined to be $r_i = r_0/\sqrt{2T_R+1}$ for a 2D droplet through the solution of $\partial^2 H(r_i,T_R)/\partial r^2 = 0$. Solving for the critical radius at $r = r_i$:

$$r_c = \left[\frac{\sqrt{1+2T_R}}{\sqrt{2}(T_R+1)} \left(\frac{1+2T_R}{4T_R} \frac{V}{\pi} \right)^{T_R} \varepsilon \, {}_2F_1\left[\frac{1}{2}, -\frac{(1+T_R)}{2}; \frac{3}{2}; 1 \right] \right]^{\frac{1}{2T_R+1}} \tag{5.5.5}$$

The critical radius of a 3-dimensional droplet can also be derived, for which $r_i = r_0(3T_R+1)^{-1/3}$:

$$r_c = \left[\frac{\sqrt{2}(1+3T_R)^{\frac{1}{3}}}{(1+T_R)} \left(\frac{1+3T_R}{T_R} \frac{V}{8\pi} \right)^{T_R} \varepsilon \, {}_2F_1\left[\frac{1}{2}, -\frac{(1+T_R)}{2}; \frac{3}{2}; 1 \right] \right]^{\frac{1}{3T_R+1}} \tag{5.5.6}$$

The variation of $H(r,T_R)$ with T_R for a droplet with initial radius $r_0 = 0.1\,\text{m}$, $\psi = 0.04164\,\text{m}$, $\sigma = 0.05\,\text{N m}^{-1}$ and $V = 4\,\text{m}^3$ is illustrated in Fig. 5.2. Under these conditions, the critical droplet radius at $T_R = 1$ is $r_C = 0.157\,\text{m}$. As expected, the droplet would vanish at $T_R = 1$ due to the absence of a minimum energy state at a radius above the

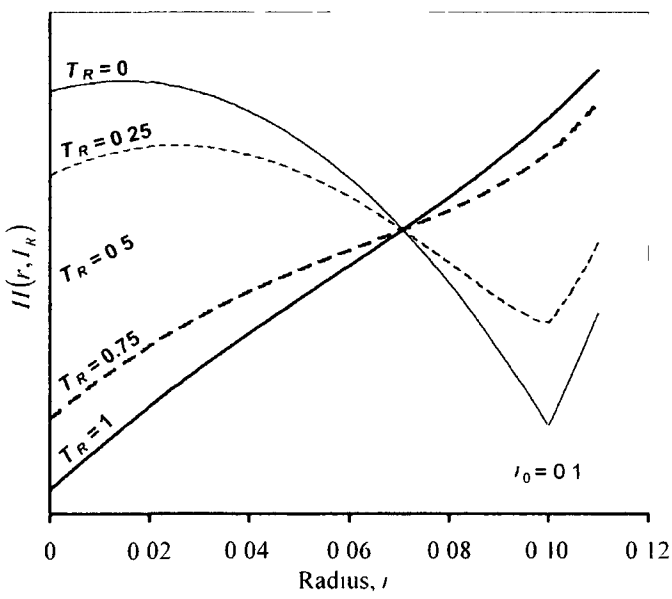

Figure 5.2 Temperature dependency of the radial variation in total free energy for a 2-D droplet with initial radius, r_o = 0.1 m. $\psi = 0.04164\,\text{m}$, σ = 0.05 n m^{-1}.

inflection point in $H(r,T_R)$. As T_R decreases, a minimum energy state is introduced above the inflection point in Fig. 5.2, limiting the extent of drop shrinkage. At $T_R = 0$, the initial and minimum energy states converge, eliminating the mechanism responsible for the spontaneous drop shrinkage phenomenon. This result illustrates that the shrinkage phenomena greatly depends on the choice of energy function rather than being an inherent characteristic of Cahn-Hilliard dynamics.

5.5.2 Metastable thermodynamics and phase separation

As an interface tracking technique, the phase-field approach relies on the competing mechanisms of diffusive transport to maintain the equilibrium profile for ϕ. The separation dynamics governing the reconstruction of an interface are dependent on the thermodynamic regions of the energy density function. Rapid phase separation occurs within the spinodal region while gradual phase separation or mixing can occur in the metastable region. When the interfacial profile deviates from the equilibrium profile during convection, the leading and trailing edges of the interface are subject to metastable dynamics that may result in insufficient restorative diffusive fluxes for preventing the formation of a metastable mixture in the bulk phases. As the continuity in the phase-field approach is commonly defined by the region within a $\phi = 0.5$ contour, the gradual inter-penetration of the phases and formation of metastable mixtures results in a loss of phase continuity. This phenomenon has frequently been reported in simulations adopting the double-well function (Jacqmin 1999; Yue *et al.* 2004, 2007), even in the case where relaxed solutions for ϕ were used as initial conditions to avoid spontaneous drop shrinkage.

To illustrate the effect of the thermodynamic region on phase separation, spinodal decomposition simulations were carried out on a 128x128 grid with cyclic boundary

conditions using the TVSED function at $T_R = 0$ and $T_R = 1$. An initial distribution of ϕ within the metastable region of $T_R = 1$ ($0 \le \phi < 0.21$) was used to represent a highly diffuse mixture, similar to what might be found at the trailing edge of a skewed interface. As seen in Fig. 5.3, separation of the initial ϕ distribution into distinct droplets was achieved for $T_R = 0$ (no metastable region), whereas a metastable mixture was formed for $T_R = 1$.

Another example illustrating the poor separation dynamics of the double-well function involves the absorption of a smaller droplet by a larger adjacent droplet via transfer of ϕ through the metastable region. To examine this test case, two droplets with initial radii of 12 and 24 cells were placed at (x,y) = (64,32) and (64,84) respectively on a 128x128 computational domain with $\varphi = 0.05$, $\psi = 6$ cells, $C_\Gamma = 0.001$, $\Delta t = 0.001$ s and $\sigma = 1$ N m^{-1}. Fig. 5.4 illustrates the initial, transient and final interfacial profiles for simulations carried out at $T_R = 0$ and $T_R = 1$ until steady-state solutions were obtained. As shown in Fig. 5.4, he smaller droplet was gradually absorbed by the larger droplet at $T_R = 1$. During the droplet

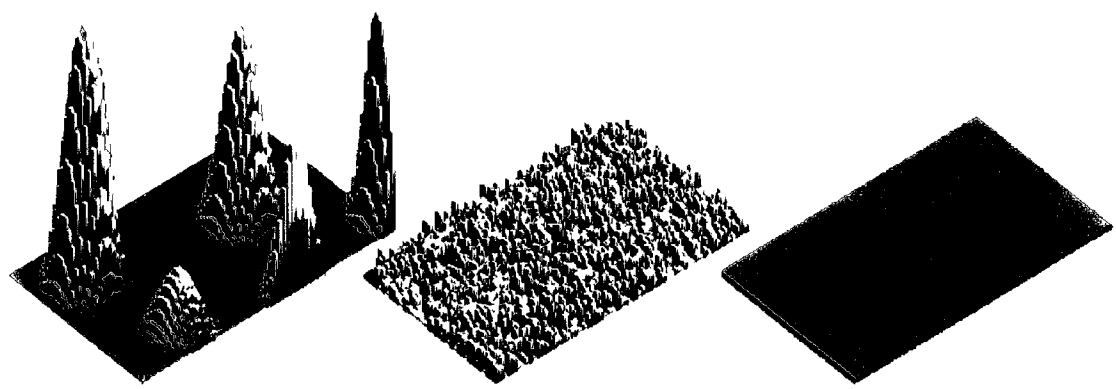

Figure 5.3 Phase separation of an initially random distribution of ϕ in the meta-stable region (middle) for T_R = 0 (left) and T_R = 1 (right).

absorption, the two adjacent interfaces were connected by a mixture within the metastable thermodynamic region, having typical values of ϕ less than 0.01. The total free energy of the system was then minimized by a diffusive flux of ϕ through this region, resulting in the gradual absorption of the smaller droplet. In the case of $T_R = 0$, this metastable mixture was absent, and the two drops remain in their original condition throughout the simulation.

The resulting simulations illustrate the importance of the choice of energy function for interface tracking applications, in which the formation of metastable mixtures could have a significant impact on the validity of the results obtained. The remainder of this discussion focuses on comparing the solutions obtained using $T_R = 0$ and $T_R = 1$ for a number of cases commonly used to validate interface tracking capabilities, free surface flows, pressure force approximation and shear stress. These comparisons are presented to highlight the potential

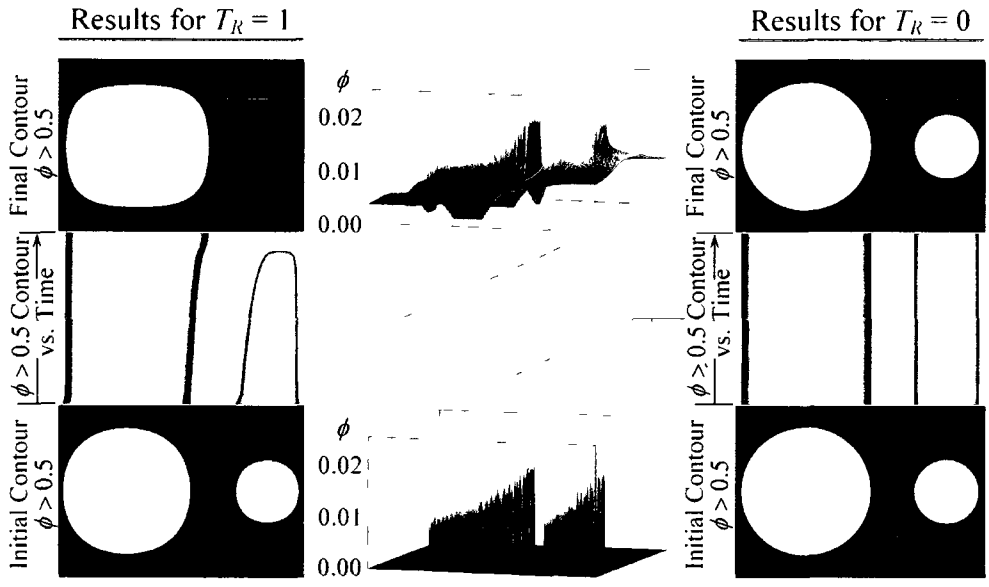

Figure 5.4 Effect of T_R on the non-physical adsorption of an adjacent droplet arising from transport through the meta-stable region. Transient behaviour and ϕ profiles obtained for simulation parameters: $\varphi = 0.05$, $\psi = 6$ cells, $C_\Gamma = 0.001$, $\Delta t = 0.001$ s and $\sigma = 1\,\mathrm{N\,m^{-1}}$.

shortcomings associated with the use of the double-well function, and to demonstrate the benefits of alternative energy expressions (such as the proposed TVSED function) in the framework common to diffuse-interface tracking applications.

5.5.3 Interface tracking and phase continuity

Of the three mechanisms leading to continuity loss, previous literature has frequently considered only the initial relaxation of the 1D equilibrium profile and the spontaneous drop shrinkage phenomena (Jacqmin 1999; Yue *et al.* 2004; Feng *et al.* 2005). Phase inter-mixing and continuity loss during convection was characterized as an extension of the dynamics governing spontaneous drop shrinkage under quiescent conditions (Yue *et al.* 2007). To explore the effect of the metastable region on phase inter-mixing, diagonal convection simulations were carried out using the TVSED function at $T_R = 0$ and $T_R = 1$.

A circular region with a 16-cell radius was initialized at the centre of a 128x128

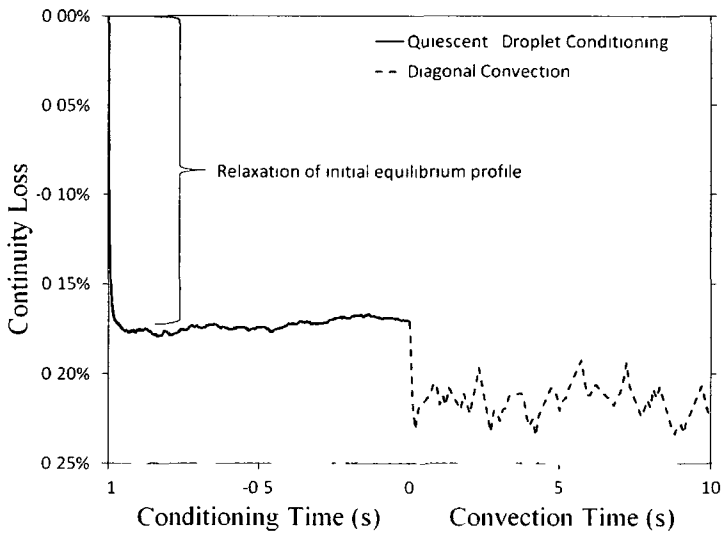

Figure 5.5 Continuity loss of a circular region during relaxation and diagonal convection at $T_R = 0$. Other simulation parameters: 128x128 mesh, r_o = 16 m, $\varphi = 0.05$, $\psi = 6$ m, $C_\Gamma = 0.001$, $C_U = 0.001$, $\sigma = 1\,\mathrm{N\,m^{-1}}$.

cyclic computational domain using Eq. (5.2.17) with $\varphi = 0.05$, $\psi = 6$ cells, $C_\Gamma = 0.001$, $\Delta t = 7.8125 \times 10^{-6}$ s ($C_U = 0.001$), and $\sigma = 1$ N m^{-1}. Applying a quiescent velocity field ($u = v = 0$ m s^{-1}), the initial ϕ profile was conditioned through the solution of Eq. (5.2.1) until a steady-state droplet radius was achieved. The projected area of the computational domain for which $\phi \geq 0.5$ was measured and compared to that of the initialized case to determine the loss of continuity observed. Figures 5.5 and 5.6 show the continuity loss during conditioning for $T_R = 0$ and $T_R = 1$ respectively. For both $T_R = 0$ and $T_R = 1$, a rapid loss of continuity was observed during the first few time steps as the one-dimensional equilibrium profile predicted by Eq. (5.2.17) relaxed to account for grid-dependent discretization error. This initial conditioning resulted in 0.175% and 0.488% continuity loss for $T_R = 0$ and $T_R = 1$ respectively. A steady-state, relaxed solution was obtained for $T_R = 0$ by $t = 1$ s, with a minimal loss in continuity beyond that already observed during the first few time steps.

The simulation for $T_R = 1$ did not reach a fully conditioned solution until $t \cong 950$ s, at which point the total continuity loss was 11.91%. The quiescent simulation results shown in Figs. 5.5 and 5.6 illustrate the elimination of the spontaneous drop shrinkage phenomena at $T_R = 0$, with the only observable continuity loss occurring due to the relaxation of the initial one-dimensional equilibrium profile.

Applying a $u = v = 128$ m s^{-1} velocity profile, continuity loss was monitored during diagonal convection of the fully conditioned $T_R = 0$ and $T_R = 1$ quiescent solutions. As seen in Fig. 5.5, an additional 0.05% of continuity loss was observed during the initial time

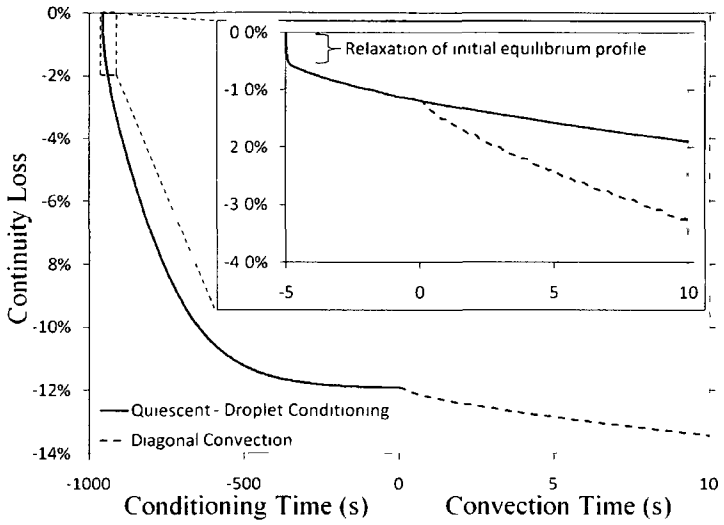

Figure 5.6 Continuity loss of a circular region during partial (inset) and full relaxation, and diagonal convection at T_R = 1. Other simulation parameters: 128x128 mesh, r_o = 16 m, $\varphi = 0.05$, ψ = 6 m, $C_\Gamma = 0.001$, $C_U = 0.001$, $\sigma = 1\,\mathrm{N\,m^{-1}}$.

steps for $T_R = 0$, after which no significant losses occurred. The convection results for $T_R = 1$ (Fig. 5.6) show a gradual loss of continuity with each traversal of the computational domain, despite a steady-state solution having already been obtained under quiescent conditions. To characterize any synergistic effects between spontaneous drop shrinkage and metastable mixing, the simulation was repeated at $T_R = 1$ for the case where the initial system was only partially conditioned ($t_{conditioning} = 5\,\mathrm{s}$). As shown in Fig. 5.7, the overall continuity loss was higher for the partially conditioned solution than the fully conditioned solution. However, when the continuity loss under quiescent conditions for the same time period was accounted for, the remaining convective component of the partially conditioned solution's continuity loss was almost identical to that of the fully conditioned simulation for $T_R = 1$. This confirms that the metastable mixing mechanism responsible for convective

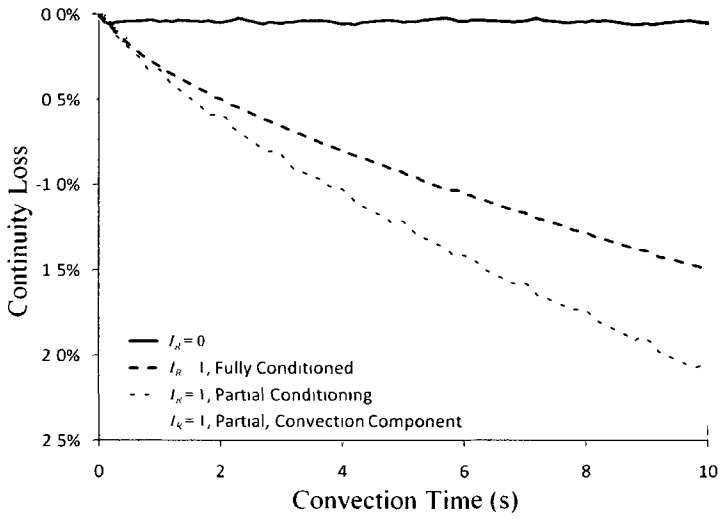

Figure 5.7 Effect of T_R and conditioning on continuity loss during advection for $C_\Gamma = 0.001$. Other simulation parameters: 128x128 mesh, $r_o = 16$ m, $\varphi = 0.05$, $\psi = 6$ m, $C_U = 0.001$, $\sigma = 1\,\mathrm{N\,m^{-1}}$.

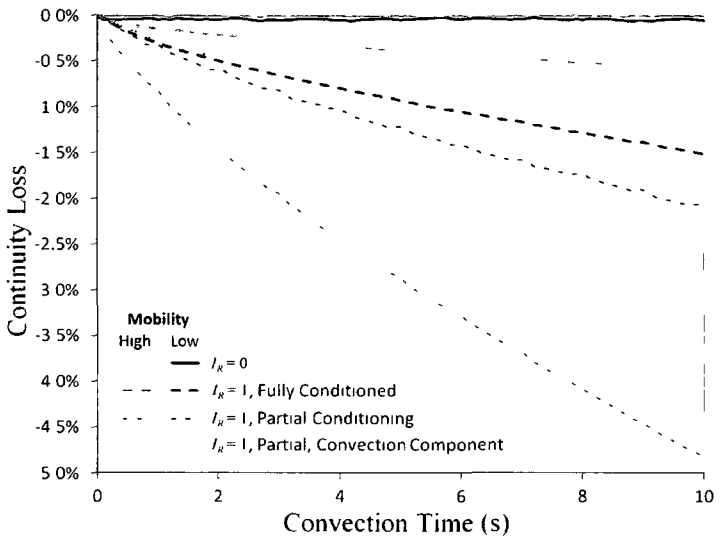

Figure 5.8 Effect of low ($C_\Gamma = 0.001$) and high ($C_\Gamma = 0.01$) mobility on continuity loss during diagonal convection of fully and partially conditioned systems. Other simulation parameters: 128x128 mesh, $r_o = 16$ m, $\varphi = 0.05$, $\psi = 6$ m, $C_U = 0.001$, $\sigma = 1\,\mathrm{N\,m^{-1}}$.

continuity loss is independent of the spontaneous drop shrinkage phenomenon.

The convection simulations were repeated with a mobility courant number of $C_\Gamma = 0.01$ to characterize the effects of increasing the relative magnitude of the diffusive flux on spontaneous drop shrinkage and metastable mixing. As seen in Fig. 5.8, the results for $T_R = 0$ improved slightly, with no continuity loss observed beyond that which had already occurred during initial conditioning. For $T_R = 1$, the convective component of continuity loss improved significantly for both the partially and fully conditioned cases. However, the improvement in the partially conditioned case was offset by the acceleration of spontaneous drop shrinkage, leading to a net increase in continuity loss of 2.75 percentage points over that observed at $C_\Gamma = 0.001$. The increase in C_Γ led to an increase in the magnitude of restorative diffusive fluxes, enhancing the rate at which deformations in the equilibrium profile of ϕ were corrected. As a result, phase inter-penetration between the trailing interface and the surrounding bulk was minimized, thereby limiting the potential for continuity losses arising from the formation of metastable mixtures.

Taking into account the extended length of time required for the $T_R = 1$ simulation to reach a relaxed solution, one might argue that the continuity loss observed in a shorter simulation would be minimal. Yue *et al.* (2007) provided guidelines to this effect, suggesting limits on the mobility and a reduction in the Cahn number to reduce the extent of continuity loss within a given time frame. Even with these guidelines in place, continuity losses above 1% are not uncommon in reported literature (Yue *et al.* 2005, 2007). The use of these guidelines is further limited by the increased grid requirements and smaller time steps needed to avoid interfacial smearing during convection when the mobility and Cahn number are reduced. The proposed TVSED function avoids this issue as $T_R \to 0$, with the only

significant source of continuity loss arising from the initial relaxation of the one-dimensional equilibrium profile.

5.5.4 Spurious currents and pressure rise

The surface force contribution to the momentum equation, F_S, can be approximated from free energy considerations, or through a continuous surface force formulation (CSF). The CSF formulation proposed by Kim (2005) for the DI approach has been applied to a variety of flow systems, approximating F_S as:

$$F_S = -\lambda \nabla \cdot \left(\frac{\nabla \phi}{|\nabla \phi|} \right) |\nabla \phi| \nabla \phi \tag{5.5.7}$$

The efficacy of this formulation can be characterized by the pressure rise across an interface and the magnitude of spurious or parasitic currents, described as fictitious vortices forming at the edges of an interface due to errors in F_S. Kim's formulation has been validated extensively for the double-well function; however, the direct application to the TVSED function is complicated by the increased linearity of the equilibrium profile as $T_R \to 0$. Consider the relative magnitudes of $|\nabla \phi| \nabla \phi$ for an interface at $T_R = 1$ and $T_R = 0$. At $T_R = 1$, it was found that the surface forces are concentrated in the central region, with 92% accounted for within the four central cells of a 6-cell interface. At $T_R = 0$, $|\nabla \phi| \nabla \phi$ is more widely distributed, and 5.2 cells are required to account for the same percentage of surface forces. The wider distribution leads to better estimates of $|\nabla \phi| \nabla \phi$ using lower-order discretization schemes; however, the surface force contributions extend closer to the centre of the radius of curvature, where the reduced tangential linearity of ϕ causes an increase in error associated to the curvature approximation, $\nabla \cdot \left(\nabla \phi / |\nabla \phi| \right)$.

To illustrate this point, pressure rise simulations were carried out at $T_R = 1$ and $T_R = 0$ for cases similar to those of Kim (2005). For a 1 m x 1 m computational domain with zero velocity on the top and bottom walls and periodicity in the x-direction, a droplet with initial radius, $r_o = 0.25$ m, was positioned at the centre of the domain and simulations were carried out for three levels of mesh refinement and interfacial width. The fluid properties and additional model parameters used were: $\rho = 4\,\text{kg m}^{-3}$, $\eta = 1$ Pa s, $C_\Gamma = 0.01$, $\Delta t = 10^{-5}$ s, and $\sigma = 1\,\text{N m}^{-1}$. In dimensionless terms, the relevant parameter is the Ohnesorge number, $Oh = \eta(\sigma\rho r_o)^{-0.5} = 1.6737$. For each refinement level ($h = 1/32,\ 1/64,\ 1/128$), three interfacial widths were used to evaluate the convergence of the spurious currents: $\psi = 0.1875$ m, representing a constant interfacial width; $\psi = 0.1875(32h)$m, representing a constant number of cells within the interface; and $\psi = 0.1875\sqrt{32h}$ m, representing an intermediate between these two extremes. The resulting maximum spurious velocity magnitudes and pressure rise are shown in Tables 5.1(a) and 5.1(b) for $T_R = 1$ and $T_R = 0$ respectively.

The convergence rates at $T_R = 1$ coincided with those reported in Kim's work (2005), where second, zero and first order rates were observed for $\psi = 0.1875$ m, $\psi = 0.1875(32h)$m, and $\psi = 0.1875\sqrt{32h}$ m respectively. Simulation results were obtained at $T_R = 0$, however, the pressure rise approximation errors and spurious current magnitudes exhibited divergent trends. At $\psi = 0.1875$ m, the low tangential linearity of ϕ resulted in an over-estimation of the pressure rise that worsened with mesh refinement. Also, at $\psi = 0.1875(32h)$m the poor resolution of $|\nabla\phi|\nabla\phi$ near the edges of the interface resulted in an increasing spurious

Table 5.1 Maximum velocity and pressure rise obtained after 200 time steps ($\Delta t = 10^{-5}$ s) using Kim's formulation, Eq. (5.5.7), at T_R = 1 (a) and T_R = 0 (b), and using a linearized interfacial profile with n = 1.75, Eq. (5.5.8), at T_R = 0 (c).

	32×32		64×64		128×128	
a) $T_R = 1$, (5.5.7)	$U_{\max}$	ΔP_{error}	$U_{\max}$	ΔP_{error}	$U_{\max}$	ΔP_{error}
$\psi = 0.1875$	3.48×10^{-4}	2.25%	4.21×10^{-5}	1.47%	9.19×10^{-6}	2.06%
$\psi = 0.1875(32h)$	3.48×10^{-4}	2.25%	2.28×10^{-4}	1.66%	1.90×10^{-4}	1.94%
$\psi = 0.1875\sqrt{32h}$	3.48×10^{-4}	2.25%	1.00×10^{-4}	0.57%	4.97×10^{-5}	0.11%
b) $T_R = 0$, (5.5.7)	$U_{\max}$	ΔP_{error}	$U_{\max}$	ΔP_{error}	$U_{\max}$	ΔP_{error}
$\psi = 0.1875$	8.88×10^{-5}	−2.08%	1.48×10^{-5}	2.72%	5.49×10^{-6}	3.92%
$\psi = 0.1875(32h)$	8.88×10^{-5}	−2.08%	1.09×10^{-4}	−0.98%	1.93×10^{-4}	−1.03%
$\psi = 0.1875\sqrt{32h}$	8.88×10^{-5}	−2.08%	1.13×10^{-4}	−0.27%	3.44×10^{-5}	0.37%
c) $n = 1.75$, (5.5.8)	$U_{\max}$	ΔP_{error}	$U_{\max}$	ΔP_{error}	$U_{\max}$	ΔP_{error}
$\psi = 0.1875$	1.37×10^{-4}	−2.27%	2.86×10^{-5}	0.21%	6.91×10^{-6}	1.41%
$\psi = 0.1875(32h)$	1.37×10^{-4}	−2.27%	9.36×10^{-5}	0.39%	9.28×10^{-5}	1.29%
$\psi = 0.1875\sqrt{32h}$	1.37×10^{-4}	−2.27%	4.56×10^{-5}	−0.43%	2.23×10^{-5}	0.06%

current magnitude with mesh refinement. Despite these trends, the results obtained at $T_R = 0$ were found to be more favorable as compared to those at $T_R = 1$, since the spurious current magnitude and pressure rise approximation errors were lower for smaller interfacial widths.

To improve the performance of Kim's formulation at $T_R = 0$, the interfacial profile was linearized and an arbitrary energy function applied for the calculation of $|\nabla\phi|\nabla\phi$. For the $T_R = 0$ equilibrium profile of $\phi = 0.5 + 0.5\sin\left(\min\left(\max\left(\sqrt{2}\,x/\varepsilon, -\pi/2\right), \pi/2\right)\right)$, the linearized order parameter, ϕ', was expressed as $\phi' = \arcsin(2\phi - 1)$. In addition, an arbitrary energy function was applied through the following surface force formulation:

$$F_S = -\lambda'\nabla\cdot\left(\frac{\nabla\phi'}{|\nabla\phi'|}\right)|\nabla\phi'|\nabla\phi'[\phi(1-\phi)]^{2n} \tag{5.5.8}$$

Where n governed the distribution of the surface forces and λ' is a modified mixing energy:

$$\lambda' = \frac{\varepsilon\sigma}{\sqrt{2}}\left[\int_0^1 [\phi(1-\phi)]^{2n-0.5}\, d\phi\right]^{-1} \tag{5.5.9}$$

Values of $n = 0.5$ and $n = 0.75$ approximate the surface force distributions at $T_R = 0$ and $T_R = 1$ respectively. Higher values of n centralize the surface forces, where $n \geq 1.5$ results in greater than 99.9% of the surface forces being accounted for within the $\varphi \leq \phi \leq 1-\varphi$ region. By repeating the pressure rise simulations for $n = 0.5$, 0.75, 1.25 and $n = 1.75$, the impact of centralizing surface forces on spurious current formation and pressure rise approximation error were characterized. At $n = 0.5$ and $n = 0.75$, the results obtained are generally

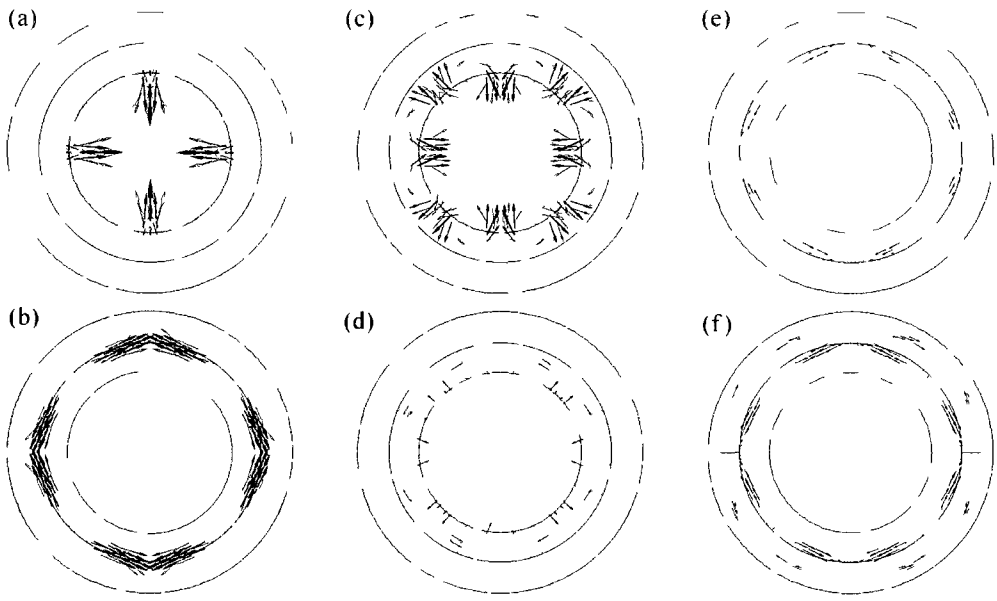

Figure 5.9 Velocity profiles obtained for $h = 1/64$ and $\psi = 0.1875\sqrt{32h}$ m after 200 time steps ($\Delta t = 10^{-5}$ s) using Kim's formulation, Eq. (5.5.7), at $T_R = 0$ (a) and $T_R = 1$ (b), and using Eq. (5.5.8) with $n = 0.5$ (c), $n = 0.75$ (d), $n = 1.25$ (e), and $n = 1.75$ (f). Contours represents $\phi = \varphi$ (outside), 0.5 (center), and $1-\varphi$ (inside)

equivalent to or worse than those of Eq. (5.5.7) for $T_R = 0$. However, as n increased to 1.25 and 1.75, convergence rates and pressure rise error stabilized at all three levels of mesh refinement, yielding a more reliable solution. The results for $n = 1.75$ ($\lambda' = 140\varepsilon\sigma/\sqrt{2}$) are presented in table 5.1(c).

In addition to making convergence rates and pressure rise approximation errors comparable to those of Eq. (5.5.7) at $T_R = 1$, the use of Eq. (5.5.8) resulted in a two-fold reduction in the magnitude of spurious velocity currents. The predominant source of error introduced by Eqs. (5.5.7) and (5.5.8) can be inferred from observation of the location of the maximum spurious currents. Figure 5.9 shows the velocity profiles resulting from Eqs. (5.5.7) and (5.5.8) for the case of $h = 1/64$, $\psi = 0.1875\sqrt{32h}$ m, and varying values of n. Note that for $T_R = 1$ and Eq. (5.5.7), the maximum spurious velocity occurs at the centre of the interface where $|\nabla\phi|\nabla\phi$ is highly non-linear. For $T_R = 0$ and Eq. (5.5.7), the maxima is located at the edge of the interface closest to the centre of the radius of curvature, confirming the transition in dominant error from $|\nabla\phi|\nabla\phi$ to the curvature approximation. The location of the maxima transitions back to the centre of the interface for Eq. (5.5.8) as n increases, with an overall reduction in the spurious current magnitude. Based on these results, subsequent simulations employ Eq. (5.5.7) for $T_R = 1$ and Eq. (5.5.8), $n = 1.75$ for $T_R = 0$.

5.5.5 Free surface flow: collapse of a liquid column

Scientific literature on conventional-scale free surface flows is dominated by sharp-interface tracking techniques, where the low relative magnitude of surface forces does not justify the increased computational cost associated with a DI approach. Nonetheless, the performance of new interface tracking techniques is frequently benchmarked using free

surface flow systems, such as the collapse of a liquid column under gravity (Koshizuka & Oka 1996; Kim & Lee 2003; Sochnikov & Efrima 2003; Yue *et al.* 2003; Bonet *et al.* 2004; Cruchaga *et al.* 2007). Using the experimental data of Cruchaga *et al.* (2007), Koshizuka & Oka (1996) and Martin & Moyce (1952), the interface tracking capabilities of the VOF model built into OpenFOAM and the TVSED function at $T_R = 0$ and $T_R = 1$ were compared for the case of a collapsing column of water with initial width, $L = 0.114$ m, and aspect ratio, $A_R = H / L = 2$.

The computational domain illustrated in Fig. 5.10 was adapted from experiments by Cruchaga *et al.* (2007), in which the flow was described for both the initial collapse and subsequent settling of a column of water. Simulations were performed on a 140×210 mesh with no-slip boundary conditions on the bottom and side walls. Each case was initialized using the 1D equilibrium profile Eq. (5.2.17) and conditioned through the solution of the Cahn-Hilliard equation Eq. (5.3.1) for 1000 time steps with $C_\Gamma = 0.01$. After initial

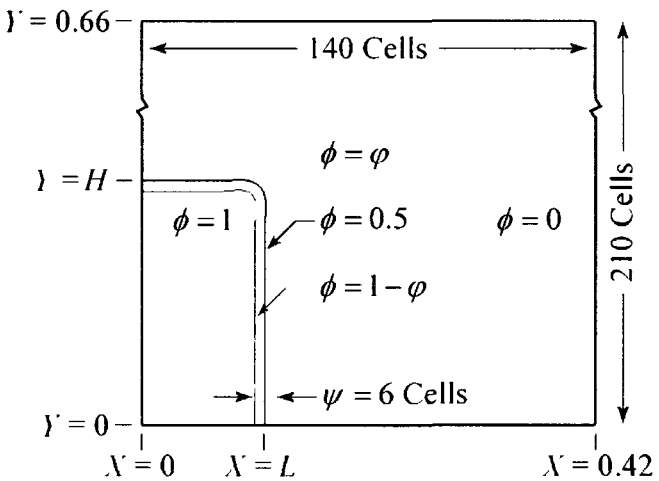

Figure 5.10 Case description of a collapsing column of water ($\phi = 1$) in air ($\phi = 0$) with initial width, $L = 0.114$ m, and aspect ratio, $A_R = H / L = 2$.

conditioning, simulations were carried out with the following fluid properties and parameters: $C_\Gamma = 0.01$, $C_U = \Delta t U/\Delta x = 0.001$, $\rho_{liq} = 1000$ kg m^{-3}, $\eta_{liq} = 0.001$ Pa s, $\rho_{gas} = 1.2$ kg m^{-3}, $\psi = 0.018$ m and $\sigma = 0.072$ N m^{-1}. Simulations were performed at a gas viscosity equal to the liquid viscosity, $\eta_{gas} = \eta_{liq}$ (HV), as suggested by Cruchaga *et al.* (2007), and at the real viscosity of air, $\eta_{gas} = 0.01\eta_{liq}$ (LV). A low value was used for the Courant number, C_U, to minimize temporal discretization error and to maximize the relative magnitude of restorative diffusive fluxes. The results obtained are presented in Figs. 5.11 to 5.14.

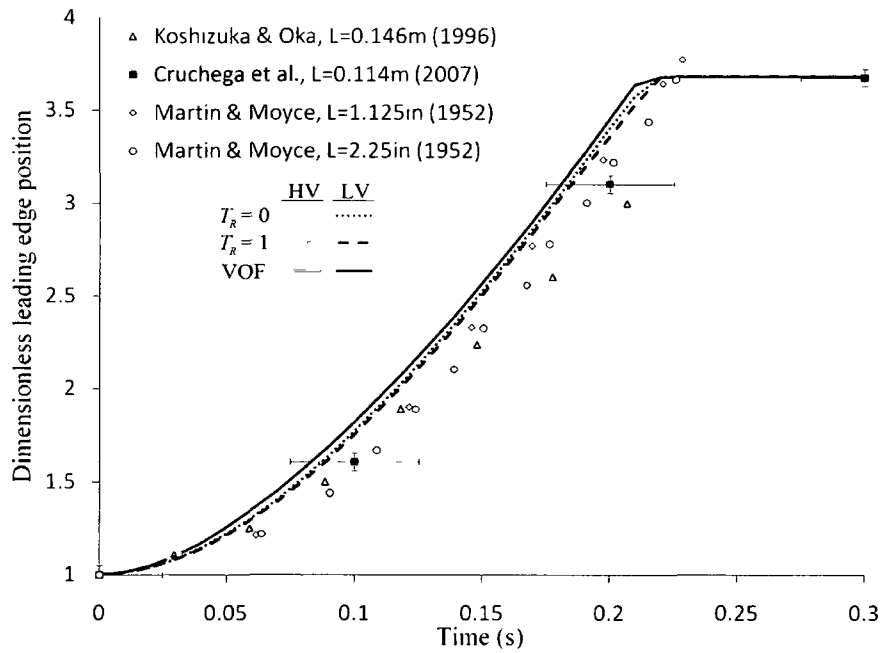

Figure 5.11 Dimensionless leading edge position, X/L, of a collapsing water column with aspect ratio, $A_R = 2$, obtained using the TVSED function and a VOF method with a high air viscosity, 0.001 Pa s (HV), and a low air viscosity, 0.00001 Pa s (LV).

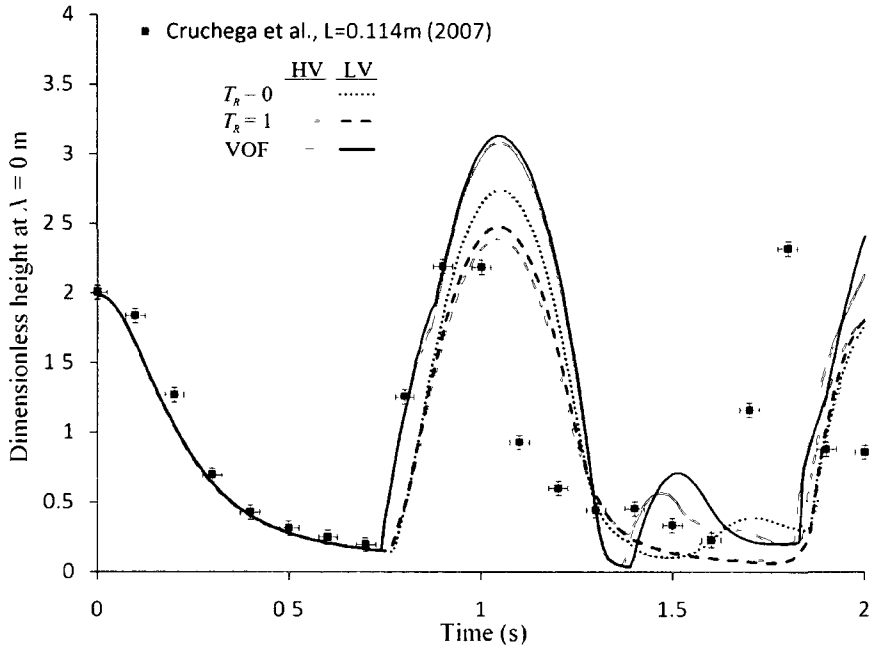

Figure 5.12 Dimensionless height, Y / L, of a collapsing water column at $X = 0$ m.

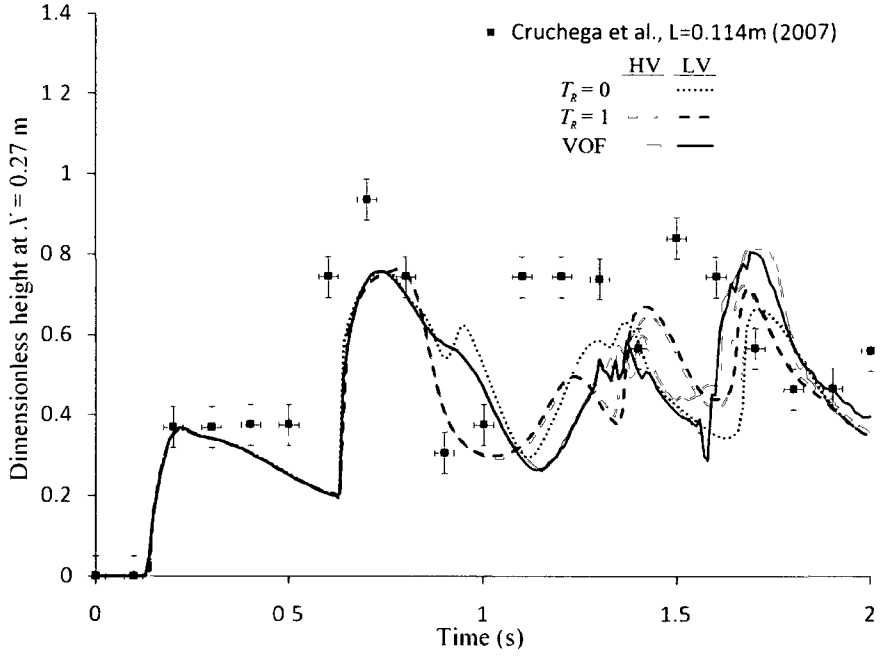

Figure 5.13 Dimensionless height, Y / L, of a collapsing water column at $X = 0.27$ m.

Defined as the point where the $\phi = 0.5$ contour intersects the bottom wall, the predicted leading edge position of the collapsing column was found to be similar for the

VOF, $T_R = 0$ and $T_R = 1$ simulations. The results of each model compared well with experimental data as well as alternative interface tracking techniques reported in literature for the initial collapse of a liquid column with $A_R = 2$ (Martin & Moyce 1952; Takada & Tomiyama 2006; Cruchaga *et al.* 2007). However, following the initial collapse and contact of the leading edge with the wall ($X = 0.42$ m), significant differences were observed between the VOF and TVSED predictions. Using the VOF model as a benchmark, the results for $T_R = 0$ were consistently closer than those of $T_R = 1$. The position of the leading edge in Fig. 5.11 was higher at $T_R = 0$ due to a degree of inter-mixing at $T_R = 1$ in the high curvature region near the top-corner of the column.

In Fig. 5.12, the peak heights for $T_R = 0$ were closer to those of the VOF model near $t = 1$ s, with both simulations predicting an intermediate peak just before the large

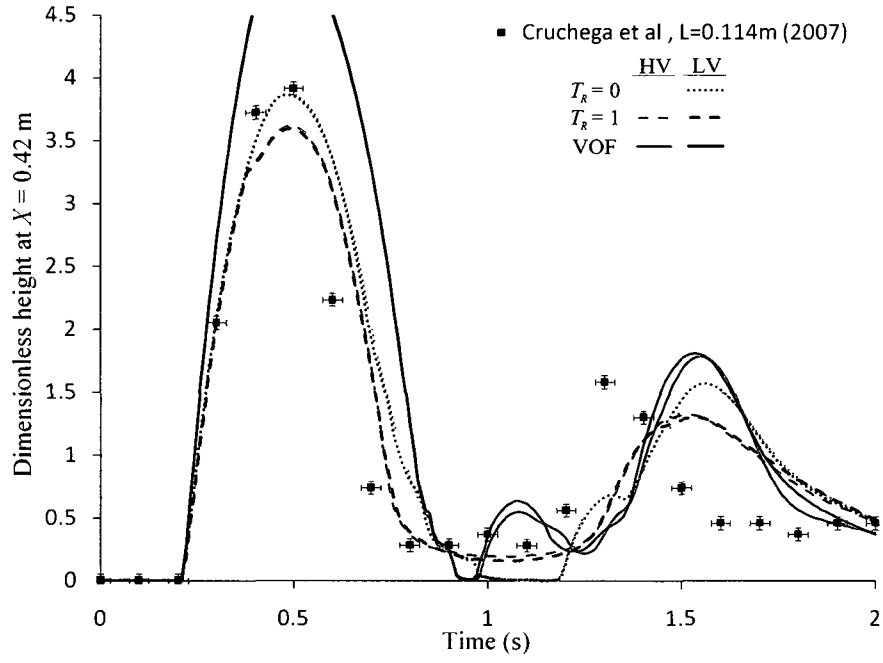

Figure 5.14 Dimensionless height, Y / L, of a collapsing water column at $X = 0.42$ m.

peak at $t = 2$ s. The VOF and $T_R = 0$ simulations both predicted a greater dimensionless height close to $t = 1$ in Fig. 5.13 due to a recession of the interface from the wall at $X = 0.42$ m. Such similarities were also observed in Figs. 5.14 and 5.15, whereas the results for $T_R = 1$ differed due to spontaneous drop shrinkage and shearing of the interface after $t \cong 0.4$ s.

As shown in Fig. 5.15, the VOF method predicted the formation of a thin column of droplets that eventually fall and impact with the interface at the base of the wall. Similar results were obtained for $T_R = 0$, where the small droplets observed in the VOF simulation appeared as a partial interface along the wall since the grid resolution was insufficient to resolve each droplet. The eventual impact of the droplets caused the interface to recede away from the base of the wall, corresponding to the minima shown in Fig. 5.14 near $t = 1$ s. Despite the formation of a partial interface along the wall, there was little to no

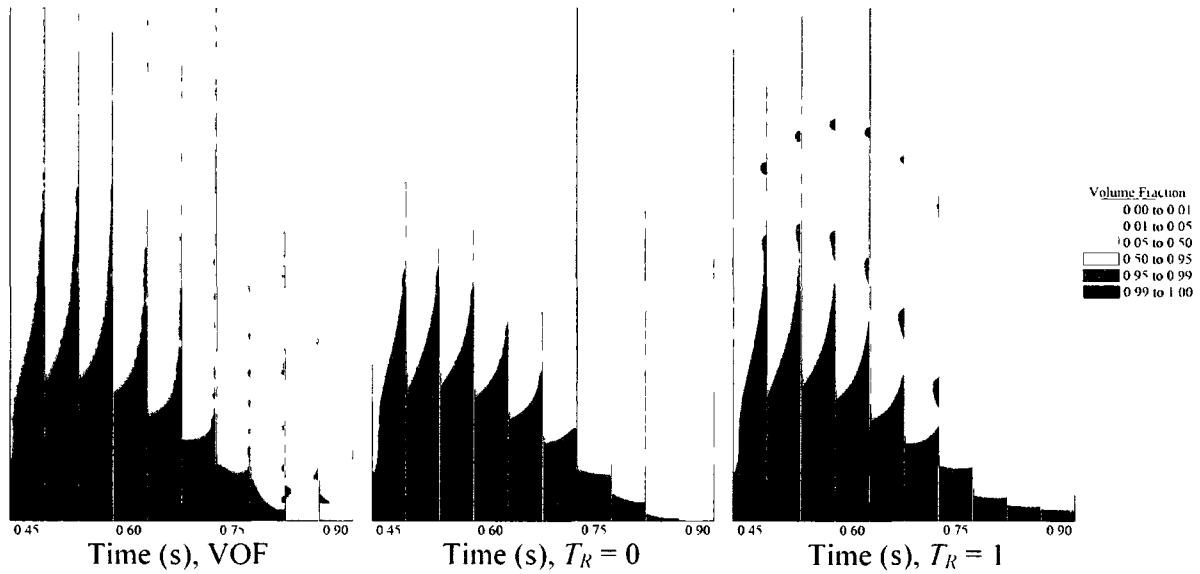

Figure 5.15 Temporal evolution of ϕ following the contact of a collapsing column with a wall at $X = 0.42$ m for VOF (left), $T_R = 0$ (middle) and $T_R = 1$ (right).

smearing of the $0.01 \leq \phi \leq 0.05$ region in the $T_R = 0$ simulations. At $T_R = 1$, significant smearing of this region occurred as the interface travelled up and down the wall, introducing small gradients in ϕ in the gas phase that caused the formation of large vortices. The vortices generated instabilities as the liquid travelled up the wall, resulting in the formation of the single satellite droplet shown in Fig. 5.15. The droplet then proceeded to gradually disappear due to spontaneous drop shrinkage, forming a metastable mixture while still suspended above the main fluid interface. The density of this mixture eventually caused it to fall to the base of the geometry; however, the mass was diluted until the inertia of the mixture impacting the liquid phase was insufficient to cause a recession from the wall.

In the experiments of Cruchaga *et al.* (2007), a recession of the interface from the wall was not recorded near $t = 1$. The $T_R = 1$ simulation was also found to predict this behaviour, but the similarity was solely due to spontaneous drop shrinkage, not the physical properties of the system. Nonetheless, the results from $T_R = 1$ did provide insight into the source of the subsequent discrepancies between the experimental and numerical results shown in Figs. 5.13 and 5.14. As the interface receded from the wall, surface forces and inertia from droplet impacts resulted in an increase in the dimensionless height at $X = 0.27$ m, leading to the over-prediction observed in Fig. 5.13 near $t = 1$ s for both the VOF and $T_R = 0$ simulations. Combined with the error introduced by a delay due to increased droplet falling times, the simulations only possessed qualitative similarities to experimental data following the initial impact of the leading edge with the wall at $X = 0.42$ m. While discrepancies between the numerical predictions and experimental data can be partially accounted for by the absence of turbulence, wall friction, and vertical shear induced by the

removal of the initial obstruction, the inclusion of these factors was not required to successfully highlight the effects of the energy function on flow predictions.

The results shown in Figs. 5.11 to 5.15 illustrate the performance similarities of the VOF model and TVSED function at $T_R = 0$ for the case of flow with minimal curvature, negligible surface forces, and little to no viscous shear acting on the interface. As curvature and surface forces are introduced, spontaneous drop shrinkage is expected to be more significant at $T_R = 1$, with viscous shear compounding the problem by shearing off the $0 \le \phi \le 0.05$ region. Such a system represents a worst-case scenario for continuity loss, and is embodied in the simulation of a droplet in simple shear flow.

5.5.6 Droplet in shear

The deformation of a droplet in low Reynolds number simple shear flow has been studied extensively in literature for Newtonian fluids (see reviews by Acrivos 1983; Rallison 1984; and Stone 1994). In a surfactant free system operated at low Reynolds numbers, the droplet shape and orientation are dependent on the viscosity ratio of the droplet and suspending medium, $\lambda_\eta = \eta_d / \eta_s$, and the capillary number, Ca, representing the ratio of viscous (shear) force to surface force. For low viscosity ratios, $\lambda_\eta \to 0$, and small deformations, $Ca << 1$, the final deformation of a droplet is solely a function of Ca:

$$D \cong Ca = \frac{r_o G \eta_s}{\sigma} \tag{5.5.10}$$

Where r_o is the initial bubble radius, G is the shear rate, η_s is the suspending fluid viscosity and σ is the surface tension. The dimensionless deformation parameter, $D = (l-b)/(l+b)$, is generally used to quantify the degree of deformation for elliptical droplets, where l and b are the lengths along the major and minor axes. This relationship has been confirmed for

$Ca \ll 1$ and $\lambda_\eta \ll 1$ both experimentally and computationally (Taylor 1932, 1934; Cox 1969; Rallison 1981; Pozrikidis 1993; Loewenberg & Hinch 1996).

At higher capillary numbers, $Ca \gg 1$, Hinch & Acrivos (1980) assumed that the droplet had a circular cross section, and used slender body theory to predict l/r_o for a 3D droplet:

$$\frac{l}{r_o} \cong 3.45 Ca^{1/2} \tag{5.5.11}$$

Hence, the deformation parameter can then be estimated by fitting the predicted value of l to an ellipsoid, calculating the corresponding minor axis length which would result in a conserved droplet volume:

$$D \cong \frac{(l/r_o)-1}{(l/r_o)+1} \tag{5.5.12}$$

Experiments carried out by Canedo *et al.* (1993) found that Eq. (5.5.11) resulted in an over-prediction of droplet deformation due to the presence of an elliptical droplet cross section. For the range of capillary numbers evaluated ($3 < Ca < 50$), they found their deformation data for 3D droplets was well described by:

$$\frac{l}{r_o} = 3.1 Ca^{0\,43} \tag{5.5.13}$$

For intermediate capillary numbers and $\lambda_\eta = \mathrm{O}(10^{-7})$, Rust and Manga (2002) confirmed the validity of Eq. (5.5.10) up to $Ca \cong 0.5$, and Eq. (5.5.11) for $Ca > 1$. At values of Ca between 0.5 and 1, the majority of measured deformations were below those predicted by Eqs. (5.5.10), (5.5.11) and (5.5.13).

Two-dimensional simulations were carried out within this intermediate capillary number range to maximize viscous shear and droplet deformation, while avoiding the

prohibitive mesh resolution required to capture the extremities of a droplet at high capillary numbers. The parameters used for the VOF and TVSED cases were based on the experimental values reported by Rust & Manga (2002) for an air bubble suspended in corn syrup: $\rho_s = 1360\,\text{kg m}^{-3}$, $\eta_s = 137\,\text{Pa s}$, $\rho_d = 1.2\ \text{kg m}^{-3}$, $\eta_d = 10^{-5}\,\text{Pa s}$ and $\sigma = 0.082\,\text{N m}^{-1}$. A droplet with radius, $r_o = 0.001$ m, was initialized in the centre of a 0.01 m x 0.006 m 2D computational domain using Eq. (5.2.17), and conditioned for 1000 time steps through the solution of Eq. (5.3.1) with $C_\Gamma = 0.01$. Following the initial conditioning, a steady-state solution was obtained for a shear rate of $G = 0.38481\ \text{s}^{-1}$ with $C_U = 0.005$, corresponding to a capillary number of $Ca = 0.6429$. Mesh independence was confirmed for $T_R = 0$ through the comparison of results obtained at three mesh resolutions: 160x96 cells, $\psi = 0.000375$ m; 320x192 cells, $\psi = 0.0001875$ m; and 640x384 cells, $\psi = 9.375\times10^{-5}$ m.

The deformation parameter and angle of deformation at each mesh resolution is provided in Table 5.2, where a 1% variation in the predicted values is observed when the mesh resolution is doubled from 320x192 cells to 640x384 cells. Under these conditions,

Table 5.2 Mesh dependence of the deformation parameter and the angle between the major droplet axis and x-axis at $t = 9$ seconds for $T_R = 0$.

Mesh Resolution:	160 x 96 $\psi = 0.000375$	320 x 192 $\psi = 0.0001875$	640 x 384 $\psi = 9.375\times10^{-5}$
Deformation:	0.5068	0.5899	0.5826
Angle:	23.40	20.36	20.59

both Eqs. (5.5.10) and (5.5.11) predicted a deformation parameter of $D = 0.6429$, Eq. (5.5.13) predicted a value of $D = 0.6082$, and the analysis of Rust and Manga's data (2002) yielded an experimental value of $D \cong 0.5853$.

The transient behaviour of the deformation parameter obtained with a 320x192 mesh resolution is illustrated for a 2D droplet in Fig. 5.16 for the VOF model and TVSED function at $T_R = 0$ and $T_R = 1$. All three models yielded similar results for the initial deformation, with deviations occurring as significant curvature was introduced on the elongated ends of the air bubble. The VOF model yielded a final deformation of $D = 0.611$, close to that predicted by Eq. (5.5.13), while the deformations predicted at $T_R = 0$ and $T_R = 1$ were $D = 0.587$ and $D = 0.557$ respectively. The results for the TVSED function approximate the empirical data from Rust & Manga (2002), where both $T_R = 0$ and $T_R = 1$

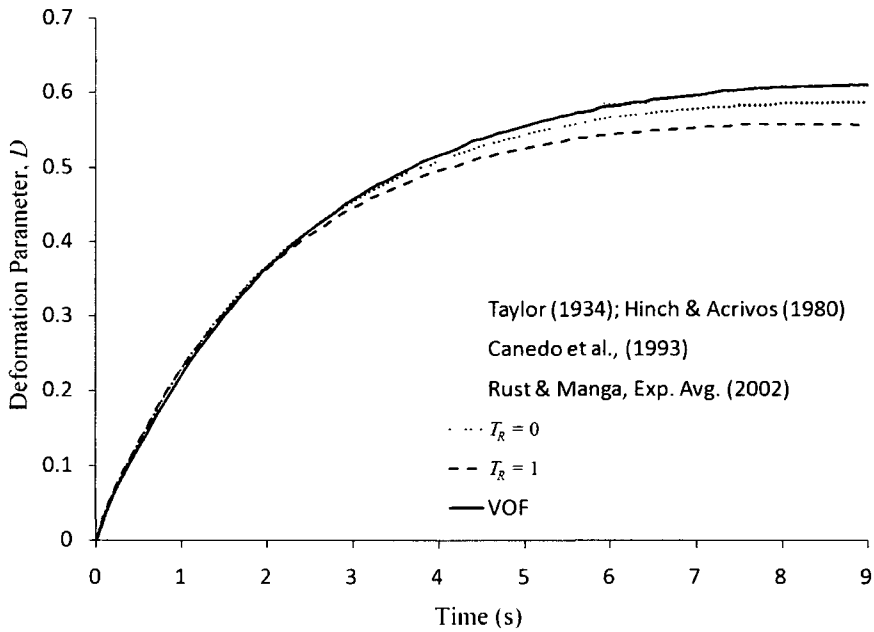

Figure 5.16 Predicted deformation of an air droplet suspended in corn syrup due to simple shear: $r_o = 0.001\,\text{m}$, $\lambda_\eta = 7.3\times10^{-8}$, $Ca = 0.6429$, $\text{Re} = 3.82\times10^{-6}$.

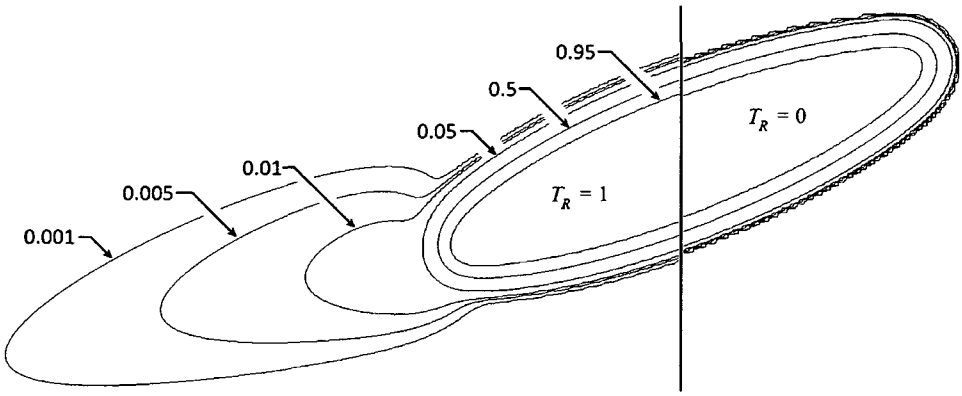

Figure 5.17 Contours of ϕ at $t = 9$ s for the simulation of an air bubble under shear, carried out using the TVSED function at $T_R = 0$ (right) and $T_R = 1$ (left).

yielded values of D below those predicted for 3D droplets by Eqs. (5.5.10), (5.5.11) and (5.5.13). The source of the discrepancy between the $T_R = 0$ and $T_R = 1$ results can be determined from the distribution of ϕ within the computational domain. The contours of ϕ at $t = 9$ s are shown in Fig. 5.17 for $T_R = 1$ (left) and $T_R = 0$ (right). As the droplet deformed, shear along the edges of the interface smeared the $0 \le \phi \le 0.05$ region in the $T_R = 1$ simulation, causing a loss in continuity and an apparent decrease in the equivalent initial drop radius, r_o. As a reduction in r_o leads to lower values of Ca, the continuity loss resulted in a lower prediction of the deformation parameter. The $T_R = 0$ simulation was a true representation of a conservative diffuse interface model, where the $0 \le \phi \le 0.05$ region remained intact and the equivalent initial radius remained constant.

After the bubble reached a stable shape in each simulation, the shear flow was removed and the bubble was allowed to relax to its original shape. Figure 5.18 illustrates the variation in the bubble shape during relaxation by plotting the normalized major axis length, $(l - r_o)/(l_o - r_0)$, versus t/τ, where l_o is the initial major axis length of the deformed bubble,

and τ is the surface tension time scale or characteristic relaxation time (Toramaru 1988; Guido & Greco 2001):

$$\tau = \frac{r_o \eta_s}{\sigma} \tag{5.5.14}$$

For an air bubble in corn syrup, $\tau \cong 1.67$ s. Rust & Manga (2002) also provided an exponential fit for their experimental data, where the shape of a relaxing droplet was approximated by:

$$\frac{l - r_o}{l_o - r_o} = e^{-0.67(t/\tau)} \tag{5.5.15}$$

The variation in bubble shape for $T_R = 0$ was almost identical to experimental values reported for similar initial radii. While the VOF model closely matched Eq. (5.5.15) during

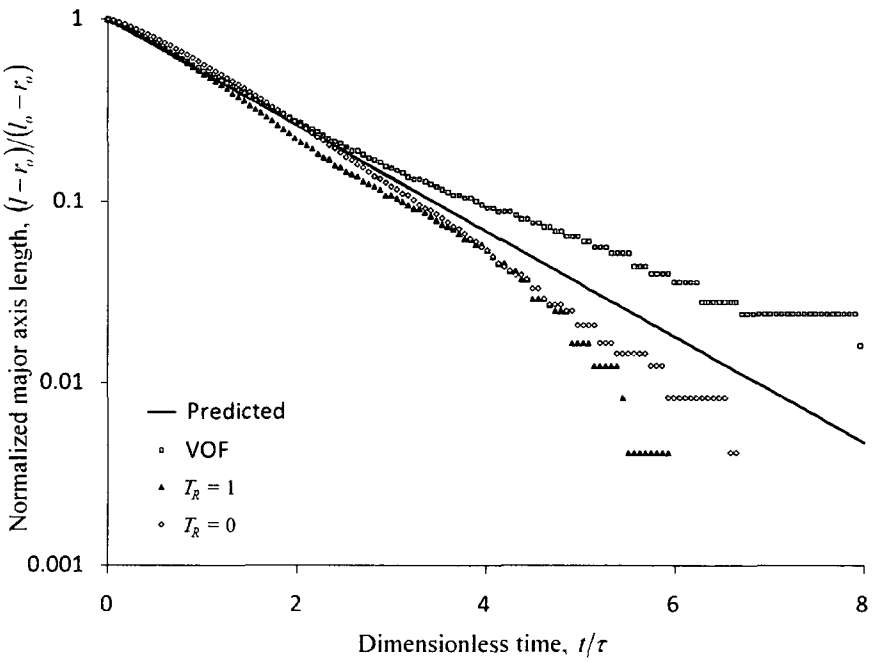

Figure 5.18 The relaxation of an air bubble's shape after shear flow is ceased for VOF and TVSED simulations: $r_o = 0.001$ m, $\lambda_\eta = 7.3 \times 10^{-8}$, $Ca = 0.6429$, $\mathrm{Re} = 3.82 \times 10^{-6}$. Predicted values are based on the empirical fit to experimental data reported by Rust & Manga (2002).

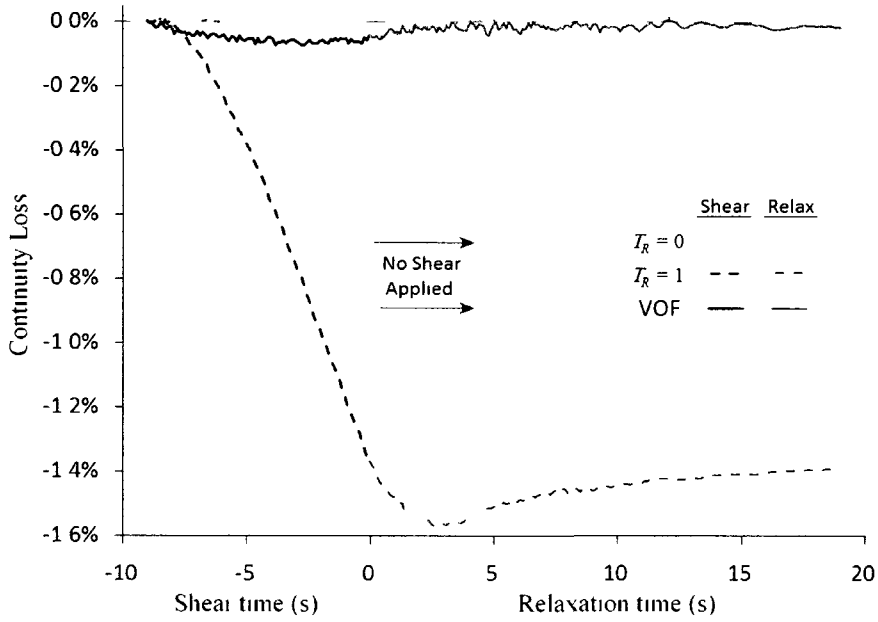

Figure 5.19 Continuity loss during droplet deformation in shear and subsequent relaxation for VOF and TVSED based simulations of an air bubble suspended in corn syrup.

the initial relaxation, the formation of spurious velocity currents resulted in a slower relaxation rate as the droplet neared its original shape. For $T_R = 1$, the relaxation rate was slightly over-predicted due to smearing of the interface and continuity loss as the initially rapid contraction of the bubble occurred. The smeared region was eventually restored, where the slower relaxation rate from $t/\tau = 2$ to 4 was the result of a gradual reversal of the continuity loss observed shortly after shear flow was removed. This behaviour can be seen in Fig. 5.19, where the percentage continuity loss of the $T_R = 1$ simulation is reduced from 1.56 % at $t = 2\tau$ to 1.48% at $t = 4\tau$, representing approximately 50% of the continuity loss that occurred after the shear flow was removed. It is noteworthy that continuity loss was negligible throughout deformation and relaxation at $T_R = 0$, highlighting the advantages of $T_R = 0$ over $T_R = 1$ for simulating shear flow.

5.6 Concluding Remarks

The computational study of two-phase fluid mechanics often requires the tracking of fluid interfaces to resolve the interactions between phases leading to breakup and coalescence, phase transitions, and inter-phase mass and energy exchange. As an interface tracking technique, the DI approach offers many advantages when tracking such phenomena, at the expense of increased computational cost arising from greater mesh refinement. With few exceptions, the mesh resolution needed to resolve free energy variations across an interface and to control continuity losses from phase inter-penetration has limited the DI approach to 2D and axisymmetric flow in simple geometries.

This paper explored the energy dependency of the three mechanisms responsible for continuity loss for a range of quadratic simplified energy densities described by the TVSED function. The existing limitations of the DI approach were illustrated through the solution of three scalar transport benchmark cases solved at $T_R = 0$ and $T_R = 1$: perceived continuity loss of a quiescent droplet (§5.5.1), spontaneous merging of adjacent droplets (§5.5.2), and continuity loss during scalar transport (§5.5.3). In brevity, free energy analysis and scalar transport simulations in §5.5.1 and §5.5.3 illustrated the elimination of spontaneous drop shrinkage as $T_R \to 0$, where interfacial smearing during convection was significantly reduced due to the absence of a metastable thermodynamic region. The independence of spontaneous drop shrinkage and convective smearing was confirmed through diagonal convection simulations of partially and fully relaxed initial conditions, as illustrated by the overlap of convective continuity losses shown in Fig. 5.8. At $T_R = 0$, continuity loss was minimized, the adsorption of adjacent droplets through the metastable region was eliminated,

and the mobility parameter could be selected based on temporal stability constraints instead of continuity-based constraints.

Three typical two-phase flow benchmark simulations were solved to compare the performance of the proposed DI method at $T_R = 0$ and $T_R = 1$ to that of the VOF approach. From the pressure rise simulations in §5.5.4, the need for a modified surface force term was identified for $T_R = 0$, leading to the proposed linearization and centralization technique which significantly improved the performance of Kim's model (2005) at $T_R = 0$. The collapsing column simulation shown in Fig. 5.15 illustrated the similarities between VOF and $T_R = 0$ results with minimal mesh refinement, while providing a clear example of spontaneous drop shrinkage impacting interfacial behaviour at $T_R = 1$. Finally, simulations of droplet deformation and relaxation in simple shear flow highlighted the performance improvements of the proposed approach. At $T_R = 1$, continuity losses caused by portions of the interface shearing away resulted in an under-prediction of the deformation parameter and an inconsistent droplet relaxation rate. In contrast, continuity was conserved at $T_R = 0$, with the predicted droplet deformation and relaxation rates in reasonable agreement with empirical data reported by Rust & Manga (2002).

This work has focused on eliminating the continuity-loss mechanisms responsible for the constraints placed on the mobility parameter and interfacial width, thereby reducing the mesh requirements in 2D and 3D simulations and improving the overall performance of the DI method. As such, the relative performance of the proposed implementation has been discussed for each two-phase benchmark case, rather than the detailed physics involved. Nonetheless, the proposed TVSED function was implemented and validated in a fully

parallelized math-based 3D unstructured mesh solver with adaptive meshing capabilities, and can be easily extended to multi-phase flow in complex 3D geometries.

Acknowledgements

One of the authors (A.A. Donaldson) would like to acknowledge the support of the National Research Council of Canada (NRC) and the Natural Sciences and Engineering Research Council of Canada (NSERC).

Nomenclature

a_{EOS} van der Waals attraction parameter

a_1, a_2 Hypergeometric function parameter

A_R Column aspect ratio

b_{EOS} van der Waals repulsion parameter

b_1 Hypergeometric function parameter

C_Γ Diffusive Courant number

C_U Convective Courant number

$f(\phi)$ Free energy density function

$f'(\phi)$ First derivative of $f(\phi)$ with respect to ϕ

$f''(\phi)$ Second derivative of $f(\phi)$ with respect to ϕ

${}_2F_1$ Hypergeometric function

$F(\phi)$ Normalized excess free energy

F_S Surface force contribution [kg m^{-2}]

g Acceleration due to gravity [m s^{-2}]

$H[\phi]$ Helmholtz free energy function [kg m^2 s^{-2}]

J Diffusive flux [kg m^{-2} s^{-2})]

$k_{\phi,J}$ Temporal slope function for ERK4 method [s^{-1}]

L Initial column width [m]

n Surface force modifier

p Pressure [Pa]

R Universal gas constant

r_c Critical radius [m]

r_i Inflection point radius [m]

r_o Initial drop radius [m]

t Time [s]

T Absolute temperature [K]

T_C Critical temperature [K]

T_R Reduced temperature

$\mathbf{u}$ Volume averaged velocity [m s^{-1}]

V Volume of the computational domain [m^3]

x Radial position in 1-D equilibrium profile [m]

X Horizontal position [m]

Y Vertical position [m]

Δx Grid cell characteristic length [m]

φ Filtering parameter

Γ Mobility [m^3 s kg^{-1}]

Γ_C Critical mobility [m^3 s kg^{-1}]

ε Capillary width [m]

$\zeta(\phi)$ Modified diffusivity function

η Viscosity [Pa s]

λ Mixing energy density [kg m s^{-2}]

μ Chemical potential [kg m^{-1} s^{-2}]

ρ Density [kg m^{-3}]

σ Surface tension [N m^{-1}]

ϕ Volume fraction

ϕ_{Center} Centre value of the free energy function

Φ Molar density for EOS linearization

ψ Physical thickness of the interface [m]

Subscripts

A Phase A

B Phase B

C Critical

High Filtering and Factor for $\phi > 1$

i Inflection point for critical radius

i Current step in ERK4 technique

Low Filtering and Factor for $\phi < 0$

n Current time step

o Initial

R Reduced

S Surface force

U Convective

Γ Mobility

ϕ Term evaluated for volume fraction

References

Acrivos, A., 1983. The breakup of small drops and bubbles in shear flows. 4th Int. Conf. on Physicochemical Hydrodynamics, Ann. N.Y. Acad. Sci. 404, 1-11.

Anderson, D.M., McFadden, G.B., & Wheeler, A.A., 1998. Diffuse-interface methods in fluid mechanics. Annu. Rev. Fluid Mech. 30, 139-165.

Badalassi, V. E., Ceniceros, H. D., & Banerjee, S., 2003. Computation of multiphase systems with phase-field models. J. Comput. Phys. 190, 371-397.

Bonet J., Kulasegaram S., Rodriguez-Paz M.X., Profit M., 2004. Variational formulation for the smooth particle hydrodynamics (SPH) simulation of fluid and solid problems. Comput Methods Appl. Mech. Eng. 193, 928–948.

Cahn, J. & Hilliard, J., 1958. Free energy of nonuniform system I. J. Chem. Phys. 28, 258.

Cahn, J. & Hilliard, J., 1959. Free energy of nonuniform system III. J. Chem. Phys. 31, 688.

Canedo, E.L., Favelukis, M., Tadmor, Z., & Talmon, Y., 1993. An experimental study of bubble deformation in viscous liquids in simple shear flow. AIChE 39, 553-559.

Cox, R.G., 1969. The deformation of a drop in a general time-dependent fluid flow. J. Fluid Mech. 37, 601-623.

Cruchaga, M.A., Celentano, D.J., & Tezduyar, T.E., 2007. Collapse of a liquid column: numerical simulation and experimental validation. Comput. Mech. 39, 453-476.

De Menech, M., 2006. Modeling of droplet breakup in micro-fluidic T-shaped junction with a phase-field model. Phys. Rev. E 73, 031505.

Ding, H., Spelt, P.D.M. & Shu, C., 2007. Diffuse interface model for incompressible two-phase flows with large density ratios. J. of Comp. Phys. 226, 2078-2095.

Feng, J.J., Liu, C., Shen, J. & Yue, P., 2005. An energetic variational formulation with phase field methods for interfacial dynamics of complex fluids: advantages and challenges. In: Modeling of Soft Matter (ed. Calderer, M.-C.T., Terentjev, E.), Springer, New York. pp. 1-26.

Guido, S. & Greco, F., 2001. Droplet shape under slow steady shear flow and during relaxation. Experimental results and comparison with theory. Rheol Acta 40, 176-184.

Hinch, E.J. & Acrivos, A., 1980. Steady long slender droplets in two-dimensional straining motion. J. Fluid Mech. 98, 305-328.

Inamuro, T., Ogata, T., Tajima, S. & Konishi, N., 2004. A lattice boltzmann method for incompressible two-phase flows with large density differences. J. Comput. Phys. 198, 628-644.

Jacqmin, D., 1999. Calculation of two-phase navier-stokes flows using phase-field modeling. J. Comput. Phys. 155, 96-127.

Jacqmin, D., 2004. Onset of wetting failure in liquid-liquid systems. J. Fluid Mech. 517, 209-228.

Khatavkar, V.V., Anderson, P.D., & Neijer, E.H., 2007. Capillary spreading of a droplet in the partially wetting regime using a diffuse-interface model. J. Fluid Mech. 572, 367-387.

Kim M.S. & Lee W.I., 2003. A new VOF-based numerical scheme for the simulation of fluid flow with free surface. Part I: New free surface-tracking algorithm and its verification. Int J Numer Methods Fluids 42, 765–790.

Kim, J., 2005. A continuous surface tension force formulation for diffuse-interface models. J. Comput. Phys. 204, 784-804.

Kim, J., 2007. Phase-field computations for ternary fluid flows. Comp. Meth. In Appl. Mechanics and Eng. 196, 4779-4788.

Koshizuka S. & Oka Y., 1996. Moving-particle semi-implicit method for fragmentation of incompressible fluid. Nucl Sci Eng 123, 421–434.

Langer, J.S., Baron, M. & Miller, H., 1975. New computational method in theory of spinodal decompositions. Phys. Rev. A 11, 1417.

Loewenberg, M. & Hinch, E.J., 1996. Numerical simulations of concentrated emulsions. J. Fluid Mech. 321, 395-419.

Martin J. & Moyce W., 1952. An experimental study of the collapse of liquid columns on a rigid horizontal plane. Philos Trans R Soc Lond 244, 312–324.

Oono, Y. & Puri, S., 1988. Study of phase-separation dynamics by use of cell dynamical system. I. Modeling. Phys. Rev. A 38, 434.

Pozrikidis, C., 1993. On the transient motion of ordered suspensions of liquid drops. J. Fluid Mech. 246, 301-320.

Rallison, J.M., 1981. A numerical study of the deformation and burst of a viscous drop in general shear flows. J. Fluid Mech. 109, 465-482.

Rallison, J.M., 1984. The deformation of small viscous drops and bubbles in shear flows. Annu. Rev. Fluid Mech. 16, 45-66.

Rust, A.C. & Manga, M., 2002. Bubble shapes and orientations in low Re simple shear flow, J. Colloid Interfacial Science 249, 476-480.

Seta, T. & Kono, K., 2004. Thermal lattice boltzmann method for liquid-gas two-phase flows in two dimensions. JSME Int. J. Series B 47, 572-583.

Sochnikov V. & Efrima S., 2003. Level set calculations of the evolution of boundaries on a dynamically adaptive grid. Int J Numer Methods Eng 56, 1913–1929.

Stone, H.A., 1994. Dynamics of drop deformation and breakup in viscous fluids. Annu. Rev. Fluid Mech. 26, 65-102.

Takada, N. & Tomiyama, A., 2006. A numerical method for two-phase flow based on a phase field model. JSME Int. J. Series B 49, 636-644.

Taylor, G.I., 1932. The viscosity of a fluid containing small drops of another fluid. Proc. R. Soc. London Ser. A 138, 41-48.

Taylor, G.I., 1934. The formation of emulsions in definable fields of flow. Proc. G. Soc. London Ser. A 146, 790-796.

Toramaru, A., 1988. Formation of propagation pattern in two-phase flow systems with application to volcanic eruptions. Geophys. J. R. Ast. Soc. 95, 613-623.

Yuan, P. & Schaefer, L., 2006. Equations of state in a lattice boltzmann model. Phys. of Fluids 18, 042101.

Yue W., Lin C.L. & Patel V.C, 2003. Numerical simulation of unsteady multidimensional free surface motions by level set method. Int J Numer Methods Fluids 42, 853–884.

Yue, P., Feng, J.J., Liu, C. & Shen, J., 2004. A diffuse-interface method for simulating two-phase flows of complex fluids. J. Fluid Mech. 515, 293-317.

Yue, P., Feng, J.J., Liu, C. & Shen, J., 2005. Viscoelastic effects on drop deformation in steady shear. J. Fluid Mech. 540, 427-437.

Yue, P., Zhou, C. & Feng, J.J., 2007. Spontaneous shrinkage of drops and mass conservation in phase-field simulations. J. Comp. Phys. 223, 1-9.

Zhou, C., Yue, P., Feng, J.J., Ollivier-Gooch, C.F., Hu, H.H., 2010. 3D Phase-field simulations of interfacial dynamics in Newtonian and viscoelastic fluids. J. Comput. Phys. 229, 498-511.

5.A Appendix material: Initial conditioning continuity loss

In a previous review of the manuscript contained in chapter 5, one of the reviewers expressed concern over the existence of the spontaneous drop shrinkage phenomenon reported by Yue *et al.* (2007). In the reviewer's response, the observed continuity loss was attributed to the transition from the 1D analytical solution used to initialize each case to the true 2D equilibrium profile of ϕ. The following analysis quantifies the change in the projected area of the $\phi >= 0.5$ region that would occur during this transition, and compares the results to those obtained from the numerical implementation outlined in this manuscript.

5.A.1 Proposed form for the 2D solution

Consider a two-dimensional simulation where a circular region of radius of $r_0 = 16$ is placed at the center of a 128x128 computational domain. The distribution of the order parameter, ϕ, at a given radial position, r, is initialized with the 1D analytical solution for a given interfacial width, ψ, where the following equations apply for $T_R = 0$ and $T_R = 1$: (assuming $\phi = 1$ inside the region)

1D Solution for $T_R = 0$: $$\phi = 0.5 + 0.5\sin\left[\frac{\sqrt{2}}{\varepsilon}(r_0 - r)\right] \qquad \varepsilon = \frac{\psi}{\sqrt{2}\arcsin(1-2\varphi)}$$

1D Solution for $T_R = 1$: $$\phi = 0.5 + 0.5\tanh\left[\frac{1}{\sqrt{2}\varepsilon}(r_0 - r)\right] \qquad \varepsilon = \frac{\psi}{2\sqrt{2}\,\text{arctanh}(1-2\varphi)}$$

For a two-dimensional case, the requirements for equilibrium can be expressed in polar coordinates as:

Requirements for Equilibrium (2D): $$\frac{d^2\phi}{dr^2} + \frac{1}{r}\frac{d\phi}{dr} - \frac{f'(\phi)}{\varepsilon^2} = 0$$

The solution to this second order nonlinear ODE cannot be obtained analytically, and a numerical solution would require two boundary conditions where only one could be defined without affecting the viability of the solution obtained (i.e. the value of ϕ at any other point within the interface is unknown, and the slope is unknown).

An alternative approach to obtaining a solution that satisfies the requirements for equilibrium in 2D involves the modification of the 1D equilibrium profiles. Assuming that the addition of the $\frac{1}{r}\frac{d\phi}{dr}$ term introduces a variable degree of skew into the 2D equilibrium profile relative to the 1D solution, the 2D profile can be approximated by incorporating a radius-dependent multiplication factor, b, into the 1D solution:

For $T_R = 0$: $$\phi = 0.5 + 0.5\sin\left[b\frac{\sqrt{2}}{\varepsilon}\left(r_{0,2D} - r\right)\right]$$

For $T_R = 1$: $$\phi = 0.5 + 0.5\tanh\left[b\frac{1}{\sqrt{2}\varepsilon}\left(r_{0,2D} - r\right)\right]$$

The expressions for ε remain the same as was used for the 1D solutions. While the introduction of b into these equations would affect the true value of epsilon needed to control the interfacial width, this analysis is interested in the 2D solution that would be obtained for a case initialized with the 1D equilibrium profile and epsilon value.

5.A.2 Conditions for equilibrium

Expressions for the derivatives and $f'(\phi)$ for each of the proposed solutions can subsequently be determined:

$$For\ T_R = 0 \quad \begin{cases} \dfrac{d\phi}{dr} = -\dfrac{b}{\sqrt{2}\varepsilon}\cos\left[b\dfrac{\sqrt{2}}{\varepsilon}\left(r_{0,2D} - r\right)\right] \\ \dfrac{d^2\phi}{dr^2} = -\dfrac{b^2}{\varepsilon^2}\sin\left[b\dfrac{\sqrt{2}}{\varepsilon}\left(r_{0,2D} - r\right)\right] \\ f'(\phi) = 1 - 2\phi \end{cases}$$

$$For\ T_R = 1 \quad \begin{cases} \dfrac{d\phi}{dr} = -\dfrac{b}{2\sqrt{2}\varepsilon}\left(1 - \tanh^2\left[b\dfrac{1}{\sqrt{2}\varepsilon}\left(r_{0,2D} - r\right)\right]\right) \\ \dfrac{d^2\phi}{dr^2} = -\dfrac{b^2}{2\varepsilon^2}\left(\tanh\left[b\dfrac{1}{\sqrt{2}\varepsilon}\left(r_0 - r\right)\right] - \tanh^3\left[b\dfrac{1}{\sqrt{2}\varepsilon}\left(r_{0,2D} - r\right)\right]\right) \\ f'(\phi) = 2\phi(1-\phi)(1-2\phi) \end{cases}$$

Substituting these expressions into the requirements for equilibrium and simplifying yields:

$$For\ T_R = 0: \qquad \left(1 - b^2\right)\sin\left[b\frac{\sqrt{2}}{\varepsilon}\left(r_{0,2D} - r\right)\right] - \frac{b\varepsilon}{\sqrt{2}r}\cos\left[b\frac{\sqrt{2}}{\varepsilon}\left(r_{0,2D} - r\right)\right] = 0$$

$$For\ T_R = 1: \qquad \begin{aligned} &\left(b^2 - 1\right)\tanh^3\left[b\frac{1}{\sqrt{2}\varepsilon}\left(r_{0,2D} - r\right)\right] + \frac{b\varepsilon}{\sqrt{2}r}\tanh^2\left[b\frac{1}{\sqrt{2}\varepsilon}\left(r_{0,2D} - r\right)\right] \\ &+\left(1 - b^2\right)\tanh\left[b\frac{1}{\sqrt{2}\varepsilon}\left(r_{0,2D} - r\right)\right] - \frac{b\varepsilon}{\sqrt{2}r} = 0 \end{aligned}$$

Note that in calculating the derivatives, we have assumed that b remains constant for simplicity (as the nature of the dependency of b on the radial position is not trivial). This assumption is fairly accurate near the edges of the interface, where $\frac{1}{r}\frac{d\phi}{dr}$ is minimized and b approaches a constant value. However, this assumption is not valid in the central region of the interface, where the only solution to the requirements for equilibrium derived here is $b = 0$. Fortunately, ϕ in this region is almost linear, allowing for the use of linear interpolation to reconstruct the equilibrium profile.

For a given radial position, r, initial radius $r_{0,2D}$, and epsilon, the value of b satisfying the requirements for equilibrium can be determined through the solution of each non-linear equation. Once b is known at a given radial position, ϕ can be calculated directly. The continuity loss associated to the shift from the 1D to 2D equilibrium profile can then be determined by comparing the radial position of the $\phi = 0.5$ contour when both profiles have the same volume integral of ϕ.

5.A.3 Graphical representation of instability region

Linear interpolation was used to estimate ϕ in the central region of the interface where the method employed in this analysis could not yield an accurate solution. Figure 5.A.1 illustrates the instability in the determined value of ϕ for $T_R = 0$, $\psi = 6$, and the corresponding linear fit within the region. As can be seen, ϕ is fairly linear within the central region.

Note that for $T_R = 0$, the linear fit was constructed from $0.2 \le \phi \le 0.3$ and $0.6 \le \phi \le 0.7$, while for $T_R = 1$, the fit was constructed from $0.25 \le \phi \le 0.35$ and $0.65 \le \phi \le 0.75$.

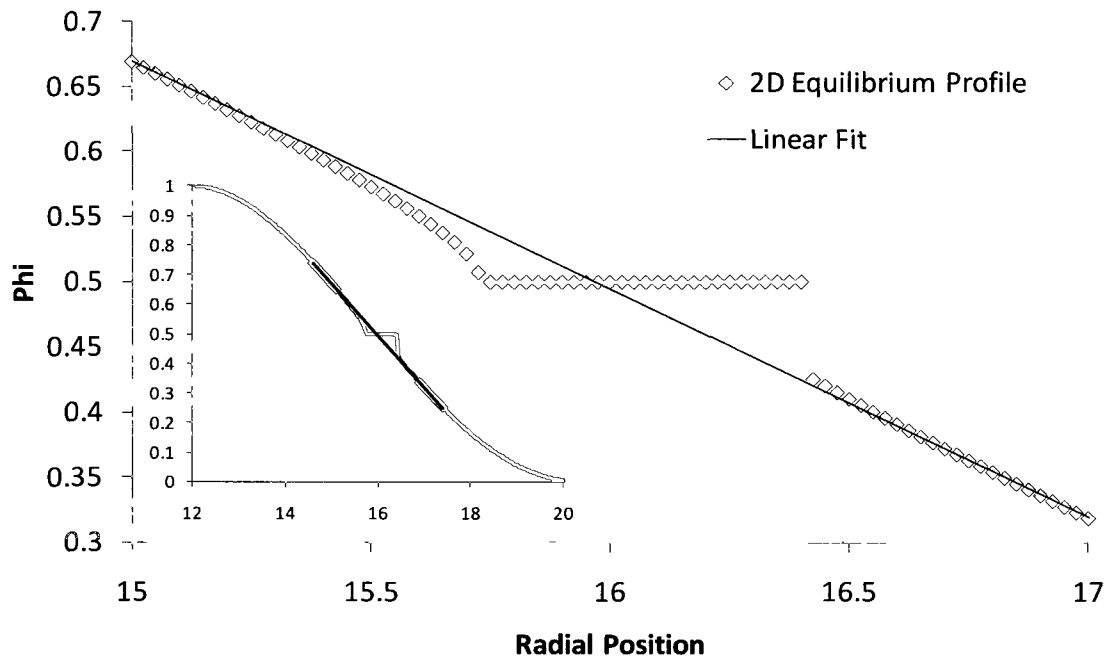

Figure 5.A.1 Linear fit applied in the central region of the 2D equilibrium profile of ϕ

5.A.4 Numerical implementation

An Excel spreadsheet was developed to determine the value of $r_{0,2D}$ that would result in the 2D equilibrium profile having the same volume integral of ϕ as a 1D equilibrium profile of initial radius, $r_0 = 16$.

For a given estimate of $r_{0,2D}$, the value of b was evaluated at radial positions ranging from $0 < r \leq 32$, with each position separated by a user-defined step size, dr. The resulting ϕ profile was integrated using Simpson's 1/3 rule, where for a step size of $dr = 0.1$ the integral is evaluated as:

$$Integral = \frac{2\pi(dr)}{3}\left(32\phi_{r=32} + 4\sum_{r=0\,1,0\,3,0\,5}^{to\ r=31\,9} r\phi_r + 2\sum_{r=0\,2,0\,4,0\,6}^{to\ r=31\,8} r\phi_r\right)$$

This integral was then compared to that obtained from the 1D equilibrium profile, evaluated at the same radial points and integrated using Simpson's 1/3 rule. The value $r_{0,2D}$ was increased if the 2D integral was less than the 1D integral, and decreased if the 2D integral was greater. Once the integrals were evaluated at two different estimates for $r_{0,2D}$, the false-position root-finding method was used to estimate the next value of $r_{0,2D}$.

This process was repeated until the 1D and 2D volume integrals of ϕ were equal, yielding the 2D equilibrium profile that would be obtained when a case was initialized with the 1D analytical solution. The step size, *dr*, was subsequently reduced to check convergence, ranging from $dr = 0.1$ to $dr = 0.05$, $dr = 0.025$, and for one case, $dr = 0.0125$. For each converged solution, the radial position of $\phi = 0.5$ was determined, and the projected area was compared to that of the 1D equilibrium profile.

CFD Simulations were also carried out for $\psi = 6$ and $\psi = 3$ at $T_R = 0$ and $T_R = 1$. The results have been used to validate the analysis proposed here, and to compare the predicted continuity losses to actual values observed in practice.

5.A.5 Results: Validation of the 2D equilibrium profile

In order to validate the 2D equilibrium profile obtained using this analysis, the deviation of the calculated profile from the initial 1D analytical solution was compared to that obtained using CFD simulations completed with two grid resolutions. The results are shown in Fig. 5.A.2 for $T_R = 0$, $\psi = 6$.

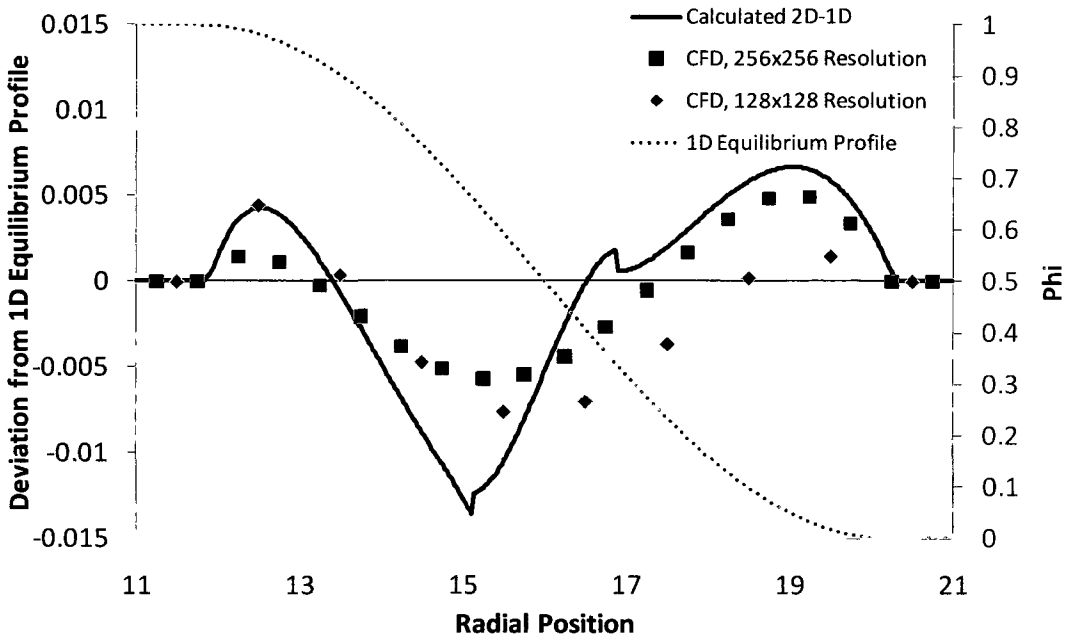

Figure 5.A.2 Comparison of the deviation from the 1D equilibrium profile obtained from CFD simulations and from the proposed analysis.

Note that it would not be possible to accurately validate the 2D profile obtained at $T_R = 1$ for the interfacial widths used, as any results from CFD simulations would be affected by the initial stages of spontaneous drop shrinkage.

The predicted deviation of the 2D equilibrium profile from the 1D analytical solution matched fairly well with the steady-state CFD results obtained at $T_R = 0$. Note that a certain degree of error is present in the central region of the interface, as was expected when b was assumed constant for the purposes of taking the derivative of ϕ.

Regardless, the 2D equilibrium profile predicted by this analysis was close enough to the CFD solution to obtain reasonable approximations for the continuity loss associated to the shift in the equilibrium profile of ϕ when initializing a case using the 1D analytical solution.

5.A.6 Continuity loss results and convergence testing

The variation in calculated continuity gain/loss with a reduction in *dr* (mesh refinement) is given in table 5.A.1, along with the corresponding continuity gain/loss observed in CFD simulations:

Table 5.A.1 Initial gain/loss in continuity resulting from the use of the 1D solution to initialize the equilibrium profile of a 2D droplet.

TVSED: TR=1 (Double Well Function)

	Calculated Continuity Gain				
Thickness	***dr=0.1***	***dr=0.05***	***dr=0.025***	***dr=0.0125***	**CFD Result**
6	0.08000%	0.08199%	0.08280%	---	0.00000%
3	---	0.01989%	0.01986%	---	0.01879%

TVSED: TR=0

	Calculated Continuity Loss				
Thickness	***dr=0.1***	***dr=0.05***	***dr=0.025***	***dr=0.0125***	**CFD Result**
6	-1.35385%	-0.18814%	-0.18828%	---	-0.17934%
3	-0.04518%	-0.04438%	-0.04591%	-0.04590%	-0.00223%

The CFD results were obtained using the numerical implementation outlined in chapter 5. The values given represent the maximum continuity gain ($T_R = 1$) or loss ($T_R = 0$) observed within the first 3 seconds of conditioning time for each simulation carried out on a 128x128 domain with a cell width of 0.5 (256x256 mesh resolution). The selected conditioning time (3 s) was sufficient for the $T_R = 0$ simulations to reach steady-state.

Note that in the case where spontaneous drop shrinkage is eliminated ($T_R = 0$), the results are very close to estimates obtained in this analysis. Likewise, the CFD results and estimated continuity loss were very close for $T_R = 1$, $\psi = 3$. The only significant deviation was for $T_R = 1$, $\psi = 6$, where no continuity gain was observed. This was most likely due to

the initial stages of spontaneous drop shrinkage offsetting the very small continuity gain that would have been observed. In all cases, the maxima and minima were observed within the first time steps of conditioning, after which point either a stable value was observed for the projected area ($T_R = 0$), or a gradual loss of continuity was observed ($T_R = 1$).

5.A.7 Conclusion

In all cases tested for $T_R = 1$, the continuity gain associated to the shift in ϕ from the 1D to the 2D equilibrium profile was not significant when compared to the overall continuity loss observed during conditioning. This clearly illustrates that the spontaneous drop shrinkage phenomenon detailed in the work of Yue *et al.* (2007) does in fact exist, and is not simply the result of using the 1D analytical solution to initialize multi-dimensional simulations. This analysis has also illustrated that the continuity loss observed for $T_R = 0$ is primarily the result of the shift from the 1D to 2D equilibrium profiles, as postulated in §5.5.3.

Chapter 6

Conclusions and future research

6.1 Conclusions

Novel developments in chemical engineering processing are focused on miniaturization of reactor flow systems. As new applications for mini and micro-scale contactors are developed, mixing arrangements commonly employed for single phase flow are being considered in multi-phase systems. The planar serpentine channel is one such arrangement, found in compact heat exchangers, turbines, mini/micro-reactors and fuel cells. While extensive literature is available for configurations with long lengths between alternating 180° return bends, a limited understanding of the hydrodynamics and mass transfer characteristics exists when this distance is reduced. In order to address some of these issues, the flow pattern transitions, pressure drop, potential impact on mass transfer and suitability of common multi-phase CFD approaches were studied in this work. First, the air-water flow pattern generated by a cross-flow T-junction contactor was characterized, and the variation in flow pattern studied for two serpentine geometries with different radii of curvature. Pressure drop in the straight and serpentine sections were measured for single and two-phase flow, and correlated using a modified separated flow model. Mass transfer models of varying numerical complexity were assessed for straight channels, and extended to curved flow to obtain conservative estimates for shear-induced enhancement of inter-phase mass transport. Finally, a diffuse interface CFD approach suitable for tracking topological transitions in surface-tension dominated flow is presented, with a detailed analysis of current limitations and modifications needed to enhance performance when modeling immiscible

fluids. An overall summary of conclusions, describing the findings in this thesis, are presented in this chapter.

The initial formation of two-phase flow patterns in a cross-flow T-junction contactor and the resulting effect on the flow through serpentine geometries was studied to predict the initiation of bubble breakup and/or coalescence in planar serpentine arrangements. An investigation of the flow patterns formed and bubble size distributions generated by the cross-flow T-junction led to the extension of scaling laws derived for square micro T-junctions to circular mini-scale systems; successfully predicting bubble lengths for bubbly and plug/unstable-plug flow at $545 < \mathrm{Re}_{LG} < 4675$, $0.0035 < Ca_L < 0.025$ and $0.0015 < Ca_{G,\mu_L} < 0.03$, and enabling the use of an analytical expression to describe the transition between bubbly and plug flow. Single phase dimensionless analysis for curved geometries was extended to two-phase flow to identify the geometric dependence of critical bubble breakup. Further analysis performed showed that the characteristic length for curved geometries encountered in the Dean number for single-phase flow was suitable for capturing the effects of curvature on the initiation of bubble breakup. A critical value of $We_{LG}L_C = 10$ was identified for predicting bubble breakup inception in the serpentine system, while values of $We_{LG}L_C \approx 3$ and $We_{LG}L_C \approx 15$ corresponded to the initiation of appreciable bubble deformation and continuous breakup of large bubbles, respectively. The mechanisms of bubble coalescence were discussed, and the residence time within each 180° return bend identified as predominant factor affecting bubble grouping due to draining of the liquid slug. To maintain fully developed plug flow, r_c should be minimized whenever curvature is introduced into a design; be it for enhancing radial mixing or increasing the reaction time within a given geometric footprint.

Single and two-phase pressure drop experiments carried out in straight and serpentine geometries provided the friction factors and empirical constants for a two-phase separated flow model. The single-phase friction factor in the straight channel followed laminar theory up to $Re_L = 2300$, at which point the transitional regime to turbulence was observed. For the serpentine unit cell, the magnitude and behavior of the friction factors for both values of r_c was accurately correlated using a simple power model, with values between that of a straight channel and fully developed flow in a helical coil. Two-phase flow pressure drop in the straight channel was well correlated by a We_{LG} and ε_G dependent empirical constant modifying the Laplacian contributions in the separated flow model. A similar approach was taken for the prediction of multi-phase flow in the serpentine geometry, resulting in the identification of five regions of pressure drop behavior characterized by either a high volume fraction of one phase (bubbly or unstable annular flow), or critical values of 2.7 and 15.5 for $We_{LG}L_C$ (plug, unstable plug and slug flow). These values correspond to flow transition boundaries between different extents of bubble deformation and breakup within the serpentine previously observed in Chapter 2. Empirical correlations for f in each region were developed and discussed, followed by estimates of the pressure drop across the $r_c = 3$ mm, $N_{UC} = 3.5$ and $r_c = 6$ mm, $N_{UC} = 4.5$ geometries.

Four numerical frameworks for the prediction of mass transfer in idealized Taylor flow were studied to determine the effects of simplifying assumptions on the overall mass transfer coefficient. While simple to implement, the homogeneous mixture and perfectly mixed models frequently overestimated k_La and mass transfer due to the assumed mixing properties between the slug film and slug bulk. By accounting for mass transfer resistance between these regions, the slug film model was able to reproduce the parametric

dependencies of k_La observed in previous experimental and CFD-based literature, while avoiding the need for an iterative solution. As an intermediate step between the slug film model and a full CFD simulation of mass transport, the circulating slug model produced k_La estimates slightly lower than those of the slug film model. Nonetheless, the parametric dependencies of the predicted mass transfer coefficient were similar. In each of the aforementioned models, neither film nor cap mass transfer could be reasonably neglected for unit cell lengths and gas phase holdups suitable for industrial applications. Subsequent extension of the slug film model to a simplified representation of flow through a curved geometry predicted a 1 to 7% increase in mass transfer relative to a straight channel. Due to the simplifying assumptions applied, the mass transfer enhancement observed experimentally is expected to be higher, where curvature-induced secondary flows would significantly decrease the liquid packet contact time used by Higbie penetration theory in the prediction of k_La.

The CFD analysis of multi-phase flow thorough serpentine mini-channels operating at elevated flow conditions is limited by a lack of interface tracking techniques suitable for modeling complex topological changes within an unstructured mesh at geometric scales where surface forces are dominant. While the diffuse interface approach was identified as a suitable candidate, it is currently limited to highly structured geometries where 2-D axisymmetric meshing can be applied in conjunction with higher-order spatial discretization schemes to mitigate numerical inaccuracies and spontaneous drop shrinkage arising from the continued use of the double-well energy density function. Through the use of the proposed TVSED function, the energy-dependence of current limitations of the diffuse interface approach was investigated, and a numerical methodology developed which eliminates the spontaneous drop shrinkage phenomena. Subsequent validation using traditional benchmark

simulations showed comparable performance between the VOF and proposed approach at conditions where the traditional double-well function failed to accurately capture the interaction between phases. The proposed methodology relaxes numerical constraints on the mobility parameter and Cahn number currently used for the double-well function, decreasing the mesh resolution needed for 3-D simulations and increasing the time step which can be taken without introducing numerical instability.

6.2 Future research

The following recommendations are proposed for further research in the studies of two-phase flow in mini-scale serpentine channels:

- Study the effect of channel diameter and additional radii of curvature to confirm the suitability of $We_{LG}L_C$ for characterizing curvature-induced flow pattern transitions, bubble breakup and pressure drop through the serpentine unit cells.
- Examine alternate gas-liquid and liquid-liquid fluid pairs representative of actual industrial process conditions.
- Experimentally investigate the enhancement of mass transfer within the serpentine geometry operating at elevated Weber numbers. One suggested approach is the use of either reactive absorption or gas phase absorption techniques commonly applied to Taylor flow in straight channels.
- Numerically investigate the local interactions between circulation patterns within the liquid slug and the bubble cap using the VOF and Diffuse Interface CFD approaches; quantifying interfacial shear, temporal variation of cap and film area, and the suitability of the periodic unit-cell approach for modeling fully developed two-phase flow in the serpentine geometry.
- Incorporate additional mass transport equations into the aforementioned CFD simulations to evaluate k_La between the deforming bubble and circulating liquid slug.
- Extend the scope of this study to alternative mixing designs.

Appendix A.1

Manufacturing technique for the serpentine geometries

The following manufacturing technique for producing circular serpentine geometries suitable for visual investigation was developed in collaboration with David Smith at the National Research Council, M-4, 1200 Montreal Rd., Ottawa, Ontario, K1A 0R6.

A.1.1 Geometry specifications

Four geometries were manufactured using the techniques outlined in this appendix for the purpose of studying multi-phase flow through serpentine geometries. Each geometry was constructed of two mirror-patterned acrylic pieces bonded together to form a circular channel cross-section with a desired diameter of $d = 1 \pm 0.0762$ mm. Figure A.1.1 through A.1.3 shows an example of one of the milled acrylic pieces with 3.5 repeating serpentine unit cells and a radius of curvature, r_c = 3mm.

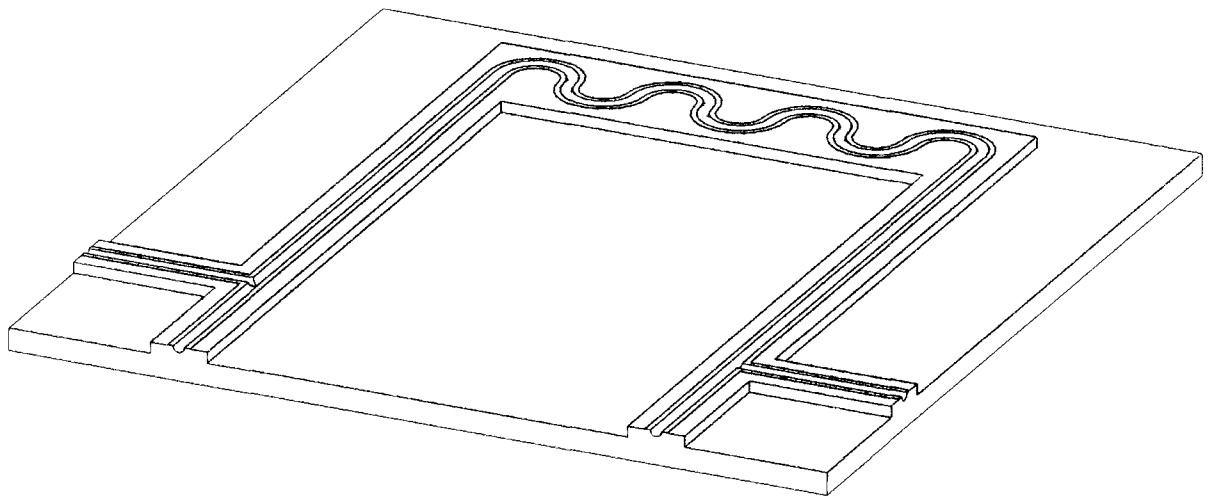

Figure A.1.1 3D representation of a manufactured piece with r_c = 3mm and 3.5 serpentine unit cells.

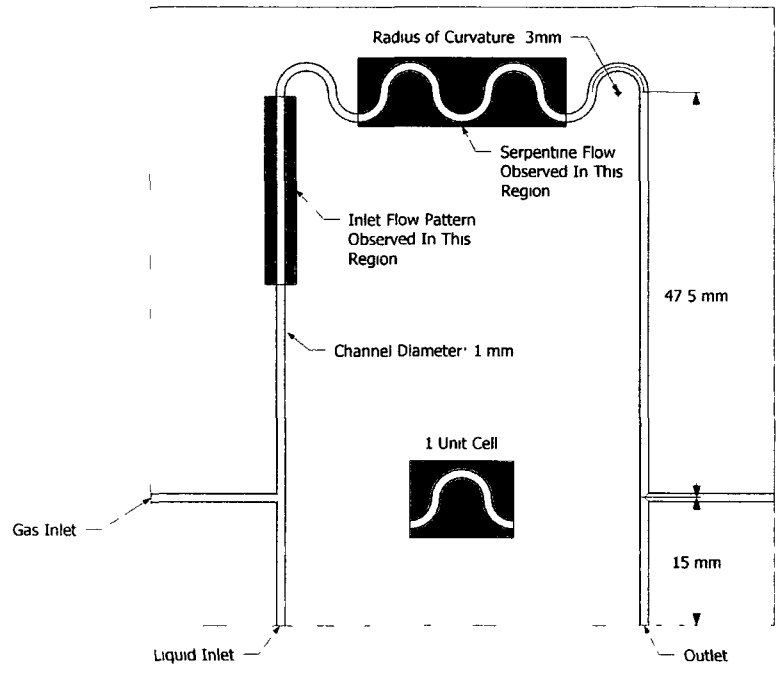

Figure A.1.2 Key geometric parameters of a manufactured piece with r_c = 3mm and 3.5 serpentine unit cells.

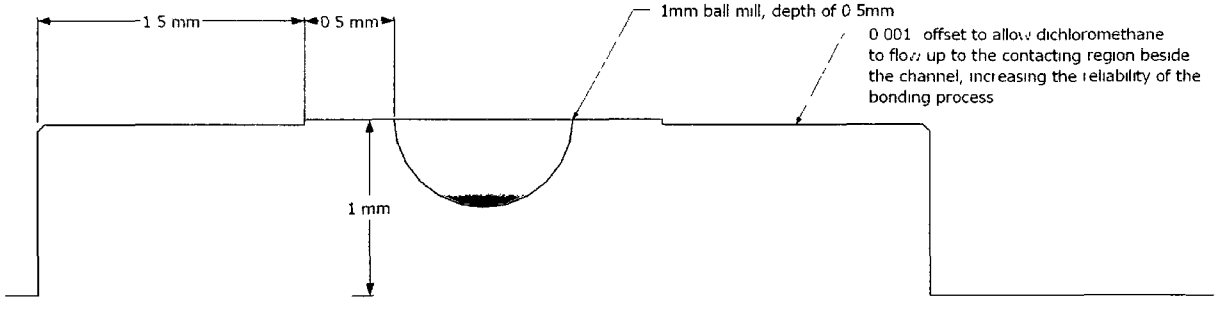

Figure A.1.3 Profile of raised portion of the geometry with a 1 mm grove cut for the flow path.

A.1.2 Materials of construction

All pieces were constructed from 3/8" cast acrylic. Extruded acrylic sheets were avoided due to the inherent stresses present from the extrusion process, which was found to create sufficient warping during manufacturing to significantly affect reproducibility and cutting tolerances.

A.1.3 CNC equipment and cutters

A Hass VF1 CNC machine along with Gibbs machining software were used to design and fabricate each of the geometries. The semi-circular groove was cut with a 1 mm carbide ball endmill, supplied by De Boer (#115-0100-202, #1mm 2F BN). A 2 mm carbide ball endmill was used for a 10mm length at each inlet and outlet for subsequent insertion of tube connectors (Scanivalve TC 063-040 R).

A.1.4 Machining (Courtesy of David Smith)

Machining of each half of a patterned pair needed for the construction of each geometry was completed via the following steps:

1) For a base-plate, a piece of aluminum was inserted into a vice and machined flat
2) Oversized pieces of cast acrylic were then glued onto this flat surface (care had to be taken to ensure that the glue did not interfere with the machined channels.
3) Using a 1/8" endmill , 1mm ball endmill , 2mm ball endmill , ¼" spot drill , 0.180" drill, 6" facemill and a 0.1875" reamer. The parts would be machined as per the program developed for each application.
    a. A "skim cut" was done first, involving the removal of 0.01" of material from the entire piece to create a flat surface.
    b. The 1/8" endmill was used to machine away the material to create a raised portion (approximately 5 mm wide) on which the 1mm and 2mm grooves were then machined. The 1mm to a depth of .5 mm, the 2mm to a depth of 1mm.
    c. The 2 mm groove was used to hold the tube connectors (Scanivalve TC 063-040 R), the 1mm groove was the test area for subsequent experiments.

d. The 0.180" drill and reamer created two holes that are used for location purposes only when bonding the two mirror-patterned pieces together.

e. The ¼" spot drill was used to create a chamfer along the edge of the raised portion. This provided a "V groove" which allowed for better control of the gluing applicator when assembling the two pieces.

4) The part was then cleaned and an inspection then took place.

a. Using a dial indicator with a resolution of 0.0005 and a 0.031 diameter pin, the flatness and depth of the groove were inspected.

b. Holding the indicator in the spindle of the machine, and using the machine controls, the indicator would be moved over the finished surface and any variances noted.

c. If the part's flatness was not within 0.001" then a skim cut of approximately 0.003" was taken off the top face.

d. The groove was inspected by inserting the 0.031 diameter pin into the 1mm wide groove. If machined to the correct depth (0.5 mm.....0.0197") the pin would be protruding above the reference surface by 0.0113". The part would be considered acceptable if the groove was within the tolerance of 0.0205" to 0.019" deep.

e. If the groove was not within the acceptable tolerance, then the reference face would be machined or the depth of the groove would be machined.

f. A number of machining passes were typically required to achieve the desired tolerance for the channel depth.

5) The glue bond to the aluminum base-plate would then be broken by using a soft faced mallet.

6) The mirror image of that part would then be machined using the same procedure as above.

7) Prior to bonding, the parts are washed thoroughly and the mating surfaces hand lapped using emery paper #240. This ensured that the parts were perfectly flat and that the glue would not migrate into the 1mm groove.

A.1.5 Bonding of mirror-patterned pieces

Unlike conventional glued parts, the two pieces needed to be bonded together in such a way as to ensure a strong bond without introducing a gap between the pieces, and without allowing the bonding medium to migrate into the channel. Dichloromethane was subsequently selected as a solvent to melt the contacting surfaces between the two pieces, instantly resulting in a permanent bond which was capable of withstanding pressures up to 30psig without leaking.

The parts needed to be bound together using low normal forces to ensure the glue sealed the contacting surfaces without allowing the glue to enter into the machined 1mm groove. Using a syringe needle with a Teflon extension tube, the solvent was applied along the mating edges of the two parts. The chamfer on the edge helped to guide the Teflon tube and also provided a valley for the glue to collect in.

A.1.6 Testing

The assembled parts were initially tested by inserting the glued assembly into water and injecting air into the grooves. Any large leaks would result in bubble formation along the glued edge, easily detected by visual inspection when the part was under water. If the bond appeared leak-proof, the system was pressurized to 30psi with water and rechecked. Depending on the extent of any leaks present, the part would either be patched or completely re-manufactured.